



University
of Glasgow

<https://theses.gla.ac.uk/>

Theses Digitisation:

<https://www.gla.ac.uk/myglasgow/research/enlighten/theses/digitisation/>

This is a digitised version of the original print thesis.

Copyright and moral rights for this work are retained by the author

A copy can be downloaded for personal non-commercial research or study, without prior permission or charge

This work cannot be reproduced or quoted extensively from without first obtaining permission in writing from the author

The content must not be changed in any way or sold commercially in any format or medium without the formal permission of the author

When referring to this work, full bibliographic details including the author, title, awarding institution and date of the thesis must be given

Enlighten: Theses

<https://theses.gla.ac.uk/>
research-enlighten@glasgow.ac.uk

High Spatial Resolution Microanalysis of Semiconductor Interfaces

by Alastair J. M^CGibbon

submitted for the degree of Ph.D in the University of Glasgow.

May 1989

© 1989 Alastair J. M^CGibbon

ProQuest Number: 10999237

All rights reserved

INFORMATION TO ALL USERS

The quality of this reproduction is dependent upon the quality of the copy submitted.

In the unlikely event that the author did not send a complete manuscript and there are missing pages, these will be noted. Also, if material had to be removed, a note will indicate the deletion.



ProQuest 10999237

Published by ProQuest LLC (2018). Copyright of the Dissertation is held by the Author.

All rights reserved.

This work is protected against unauthorized copying under Title 17, United States Code
Microform Edition © ProQuest LLC.

ProQuest LLC.
789 East Eisenhower Parkway
P.O. Box 1346
Ann Arbor, MI 48106 – 1346



"As your Physics professor, I can't say you've exactly made my day."

Acknowledgements

I would like to thank all those who have helped me throughout the course of this work. Foremost, I must thank Professor J. N. Chapman for his guidance and help in all aspects of this work. Thanks also to Professor R. P. Ferrier for provision of the electron microscope facilities in the Solid State Group at the University of Glasgow. I am grateful to my industrial supervisor, Dr. A. G. Cullis of RSRE, Malvern for many useful discussions. Also at RSRE, I must thank Mr. N. G. Chew for his assistance in teaching me the specimen preparation techniques, and Dr. S. J. Bass and Dr. L. L. Taylor for the provision of multilayer materials.

I would like to thank Dr. W. A. P. Nicholson, Mr. A. Howie and Mr. J. Simms for maintenance of the microscope facilities at Glasgow. I am also grateful to Mr. S. Hefferman and Mr. I. McVicar for assistance in producing the photographic prints and to Mrs. M. Waterson and Miss M. Low for stencilling many of the diagrams in this thesis. Thanks also go to Mr. A. Donald for his help with the ion beam thinner, and to Mr. K. Piechowskiak for his assistance in the course of specimen preparation stages carried out in Electrical Engineering. I would also like to thank all those in the Solid State Group whom I have not mentioned for their invaluable help.

I would like especially to thank my parents for supporting me for another four years.

Finally, I would like to thank SERC and RSRE Malvern for the provision of a CASE award and equipment.

Declaration

This thesis has been written solely by myself and details the research which I have carried out in the Department of Physics and Astronomy at the University of Glasgow. The work described is my own, except otherwise stated. Some of the results from this work have been presented in the following papers:-

Composition Determination in InGaAs/InP Multilayer structures by X-ray Microanalysis in a STEM.

J N Chapman, A J McGibbon, A G Cullis, N G Chew, S J Bass and L L Taylor, 1987 Microscopy of Semiconducting Materials eds. A G Cullis and P D Augustus (Inst. Phys. Conf. Ser. No. 87, Adam Hilger Ltd., Bristol) 649

Microanalysis of III-V Semiconductor Interfaces.

A J McGibbon, J N Chapman, A G Cullis and N G Chew, AEM Proceedings, Manchester 1987, ed. G W Lorimer 219.

High-angle Annular Dark Field Imaging of AlGaAs/GaAs Multilayer Structures.

A J McGibbon, J N Chapman and A G Cullis, EUREM proceedings, York 1988, eds. P J Goodhew and H G Dickinson, 2 403.

X-ray Microanalysis of InGaAs/InP Multilayer Structures grown by MOCVD.

A J McGibbon, J N Chapman, A G Cullis, N G Chew, S J Bass and L L Taylor, J. Appl. Phys. 65 2293 (1989)

Absorption corrections for thin specimens.

K M Khan, W A P Nicholson, J N Chapman and A J McGibbon, in EMAS workshop proceedings (Antwerp,1989)

Corrections for self-absorption in EDX microanalysis of semi-thin specimens.

W A P Nicholson, K M Khan, J N Chapman and A J McGibbon, in SCANNING 89/EM West proceedings (Long Beach, 1989)

This thesis has not been submitted in any previous application for a degree.

Contents

Acknowledgements

Declaration

Summary

Table of frequently used symbols

Chapter 1: Introduction

1.1	Aim of thesis	1
1.2	Compound semiconductor multilayer structures	1
1.3	Material growth techniques	4
1.4	Structural and compositional characterisation techniques	5
1.5	Characterisation of semiconductor multilayers in a STEM	8

Chapter 2: Theoretical considerations

2.1	Introduction	11
2.2	Image formation using high-angle elastically scattered electrons	12
2.2.1	Factors affecting image contrast	13
2.2.2	Quantitative interpretation of high-angle ADF image contrast	16
2.3	Ionisation cross-sections for characteristic x-ray production	21

Chapter 3: Instrumentation

3.1	Introduction	25
3.2	The VG HB5 STEM	25
3.2.1	The Field Emission Gun	26
3.2.2	Pre-specimen Optics	28
3.2.2.1	Instrumentation	28

3.2.2.2	Operating conditions for EDX and high-angle ADFI	29
3.2.2.3	Calculation of the probe current density distribution	30
3.2.3	The Specimen Cartridge	36
3.2.4	Post-specimen Lenses	36
3.2.5	Electron Detectors	
3.2.5.1	The Bright Field Detector	37
3.2.5.2	The Annular Dark Field Detector	37
3.2.5.3	The Diffraction Screen	38
3.2.6	X-ray Detectors	39
3.3	The Link Analytical AN10000	40
3.4	Specimen Preparation	42
3.4.1	Pre-milling Preparation	43
3.4.2	Ion Milling	45

Chapter 4: Considerations for imaging techniques that reveal layer contrast

4.1	Introduction	48
4.2	Structure factor contrast	49
4.3	Attainment of suitable experimental conditions for high-angle ADFI	51
4.4	Acquisition and analysis of high-angle ADF images	54
4.4.1	Profile noise reduction	55
4.4.2	Thickness corrections	55
4.4.3	Simulation of intensity profiles	57

Chapter 5: Considerations for EDX microanalysis

5.1	Introduction	58
5.2	Factors affecting spatial resolution	59
5.3	Determination of suitable specimen thicknesses for EDX microanalysis using Monte Carlo simulations	59
5.4	Simulation of detected signal profiles	64
5.5	Self-absorption of characteristic x-rays	66
5.6	Low energy detector efficiencies	68
5.7	Experimental determination of film thickness	70
5.8	Experimental procedure	72

Chapter 6: Analysis of the AlGaAs/GaAs system grown by MBE

6.1	Introduction	75
6.2	High-angle ADFI	76
6.2.1	Determination of the spatial resolution	76
6.2.2	Quantitative analysis of layer contrast	79
6.3	EDX microanalysis	80
6.3.1	Analysis of spectra	81
6.3.2	Results	86
6.3.2.1	Determination of specimen concentrations	87
6.3.2.2	Beam broadening effects	88
6.3.2.3	Layer centre composition measurements	89
6.4	Comparison of high-angle ADFI with EDX microanalysis	91

Chapter 7: Analysis of the InGaAs/InP system grown by MOCVD at atmospheric pressure.

7.1	Introduction	93
7.2	High-angle ADFI	94
7.2.1	Intensity profile analysis	94

7.2.2 Discussion	96
7.3 EDX microanalysis	97
7.3.1 Analysis of spectra	98
7.3.2 Results	102
7.4 Conclusions	105

Chapter 8: Analysis of the InGaAs/InP system grown by solid source MBE.

8.1 Introduction	108
8.2 High-angle ADFI	109
8.2.1 Intensity profile analysis	109
8.2.2 Discussion	110
8.3 EDX microanalysis	112
8.3.1 Results	113
8.4 Conclusions	116

Chapter 9: Conclusions and future work

9.1 Conclusions	118
9.2 Future work	124

Appendix: Notes on software

A.1 Programs used to calculate probe current density distributions	127
A.2 High-angle ADFI profile analysis programs	129
A.3 Monte Carlo simulations	131
A.4 Analysis programs for series of x-ray spectra	132

References

Summary

The work presented in this thesis is concerned with high spatial resolution characterisation of compound semiconductor multilayer structures. The principal techniques used are high-angle annular dark field imaging (ADFI) and energy dispersive x-ray (EDX) microanalysis. These are both available on a scanning transmission electron microscope (STEM). The motivation for this project is that, to enable a greater understanding of material growth processes and of the electronic and optical properties of semiconductor multilayers, it is desirable to obtain a knowledge of the atomic perfection of, and elemental compositions across, layer interfaces in the materials. This thesis is primarily concerned with the analysis of AlGaAs/GaAs multilayer specimens grown by molecular beam epitaxy (MBE) and InGaAs/InP specimens grown by MBE and by atmospheric pressure metal-organic chemical vapour deposition (MOCVD). A brief description of the material growth processes and a general introduction to the structural and compositional characterisation of semiconductor multilayers is given in chapter 1.

The theoretical bases that underlie the two analytical techniques used in this project are discussed in chapter 2. The chapter describes the way in which elastically scattered electrons can be used to provide compositional information on multilayers using the technique of high-angle ADFI. In preparation for the measurement of elemental compositions using EDX microanalysis, cross sections for the production of characteristic x-ray photons for the elements of interest in this project are calculated.

Experimental procedures and data analysis techniques used in this thesis are established in chapters 3, 4 and 5. A detailed description of the STEM and its associated detectors is given in chapter 3. The discussion includes the calculation of the current density distribution in the electron probe used for each

of the two analytical techniques. Chapter 3 concludes with a description of the technique used to prepare high quality cross-sectional specimens for microanalysis in a STEM. Considerations specific to the analysis of semiconductor multilayers using high-angle ADFI are addressed in chapter 4. Optimised experimental conditions for the technique are established, as is the image analysis technique that is used to yield as much information as possible from the acquired data. Chapter 4 also includes a description of a second composition sensitive imaging technique, namely structure factor contrast imaging which is principally used here for orienting the cross-sectional specimen in the microscope. Considerations relevant to EDX microanalysis of semiconductor multilayers are discussed in chapter 5. This includes a detailed description of a Monte Carlo simulation routine used to help in the interpretation of measured concentration distributions from interface regions.

The application of EDX microanalysis and high-angle ADFI to the characterisation of the materials of interest is described in chapters 6, 7 and 8. In the study of high quality MBE grown AlGaAs/GaAs specimens described in chapter 6, emphasis is given to the development of a results analysis procedure that utilises the full potential of each analytical technique. The investigation of the InGaAs/InP specimens grown by atmospheric pressure MOCVD is described in chapter 7. In this chapter, the procedures developed in chapters 2 to 6 are used to provide as much information as possible on the variation in elemental composition across interfaces and at layer centres in the system. This information is used by material growers to modify and improve atmospheric pressure MOCVD growth techniques. Similar studies are carried out in chapter 8 in the investigation of MBE grown InGaAs/InP specimens.

Finally, in chapter 9, general conclusions are drawn on the work described in this thesis and suggestions are made for future studies of semiconductor multilayers in a STEM.

Table of frequently used symbols

General

Z	Atomic number
\bar{Z}	Mean atomic number
A	Atomic weight
ρ	Density
E_0	Incident electron energy
λ	Wavelength of incident electrons
e	Charge of an electron = $1.602 \times 10^{-19} \text{C}$
m_0	Electron rest mass = $9.109 \times 10^{-31} \text{Kg}$
m	Fast electron mass
h	Planck's constant = $6.626 \times 10^{-34} \text{Js}$
k_B	Boltzmann's constant = $1.38 \times 10^{-23} \text{JK}^{-1}$
a_0	Bohr radius = $5.292 \times 10^{-11} \text{m}$
r_0	Thomas-Fermi radius
θ_D	Debye temperature
θ_B	Bragg angle
α_0	Illumination semi-angle
β_0	Collection semi-angle
I_P	Total electron beam current

Symbols specific to electron probe calculations

r_0	Characteristic radius of electron source
$j(r)$	Radial current density distribution of electron probe
$J(x)$	Linear current density distribution of electron probe
I_0	Primary beam current
C_s	Spherical aberration coefficient

Δz Defocus length

Symbols specific to high-angle ADFI

θ_1 Inner acceptance angle of ADF detector
 θ_2 Outer acceptance angle of ADF detector
 C Layer contrast in high-angle ADF images
 σ_{el} Cross section for the elastic scattering of electrons
 $f(\bar{Z})$ Variation of \bar{Z} across a specimen

Symbols specific to EDX microanalysis

σ_i Total ionisation cross section
 σ_c Characteristic x-ray production cross section/sr
 s_K K-shell partition function
 ω_K K-shell fluorescence yield
 I_K K-shell binding energy

Chapter 1

Introduction

1.1 Aim of thesis

Compound semiconductor multilayer structures display novel electronic properties which have a wide range of applications in the semiconductor industry. Advances in semiconductor growth techniques have enabled the development of multilayer systems which can consist of very well defined layers of different composition. In some cases, the layers can be as narrow as one monolayer. This degree of growth control allows the formation of devices whose electronic properties can be 'tailored' to satisfy pre-determined parameters. The electronic properties of such devices do, however, depend strongly on the structural properties of, and elemental composition across, each interface. These will depend on both the materials used and the semiconductor growth techniques employed. It is necessary, therefore, to use experimental techniques which can provide as much information as possible about such interfaces. The aim of the work described in this thesis is to use analytical techniques available on a modified VG HB5 scanning transmission electron microscope (STEM) to provide compositional information with high spatial resolution on multilayer structures. This information can be used to help in the understanding of the electronic and optical properties of multilayers and to provide information that can enable the improvement of semiconductor growth techniques.

1.2 Compound semiconductor multilayer structures

The growth of multilayer structures by the selective, alternate deposition of

two components was first suggested by Esaki and Tsu (1970). As figure 1.1 illustrates, a multilayer comprises layers of materials of differing compositions grown on a substrate. The substrate is a single crystal and acts essentially as an 'atomic template' for the growth of the new material. Provided that a suitable selection is made of both the growth conditions and the components of the multilayer, the resulting material can be a very high quality single crystal. The most commonly used components in the growth of semiconductor multilayer structures are GaAs and the ternary alloy $\text{Al}_x\text{Ga}_{1-x}\text{As}$. A major advantage of ternary or indeed quaternary semiconductors in multilayers is that their electronic properties such as the band gap (E_g) can be varied by changing the value of x . As a result, the growth of compound semiconductor multilayers has given rise to the development of superlattices or multiple quantum wells. These systems are heterostructures in which the band gap discontinuities are so closely spaced that the bulk optical and transport properties are strongly modified. Figure 1.2 shows a schematic representation of the energy bands in an AlGaAs/GaAs heterostructure. The electronic properties of such structures can be modified to an extent determined by both the thickness of the layers grown and the band gaps of the components used. These properties can be exploited to provide a wide range of new electronic devices such as high mobility electron transistors (HEMTs) for ultra-high speed logic (e.g. Mimura et. al., 1980) and multiple quantum well lasers (e.g. Tsang, 1981). In HEMTS, the charge carriers are, in effect, confined to motion in the plane of the layers and so their mobilities are increased considerably. The development of multiple quantum well lasers enables the fabrication of devices designed to operate at a pre-determined wavelength.

As stated previously, the most commonly used system for multilayer growth is the $\text{Al}_x\text{Ga}_{1-x}\text{As}/\text{GaAs}$ system. An advantage to using this particular configuration is that, irrespective of the value of x selected, the lattice parameter

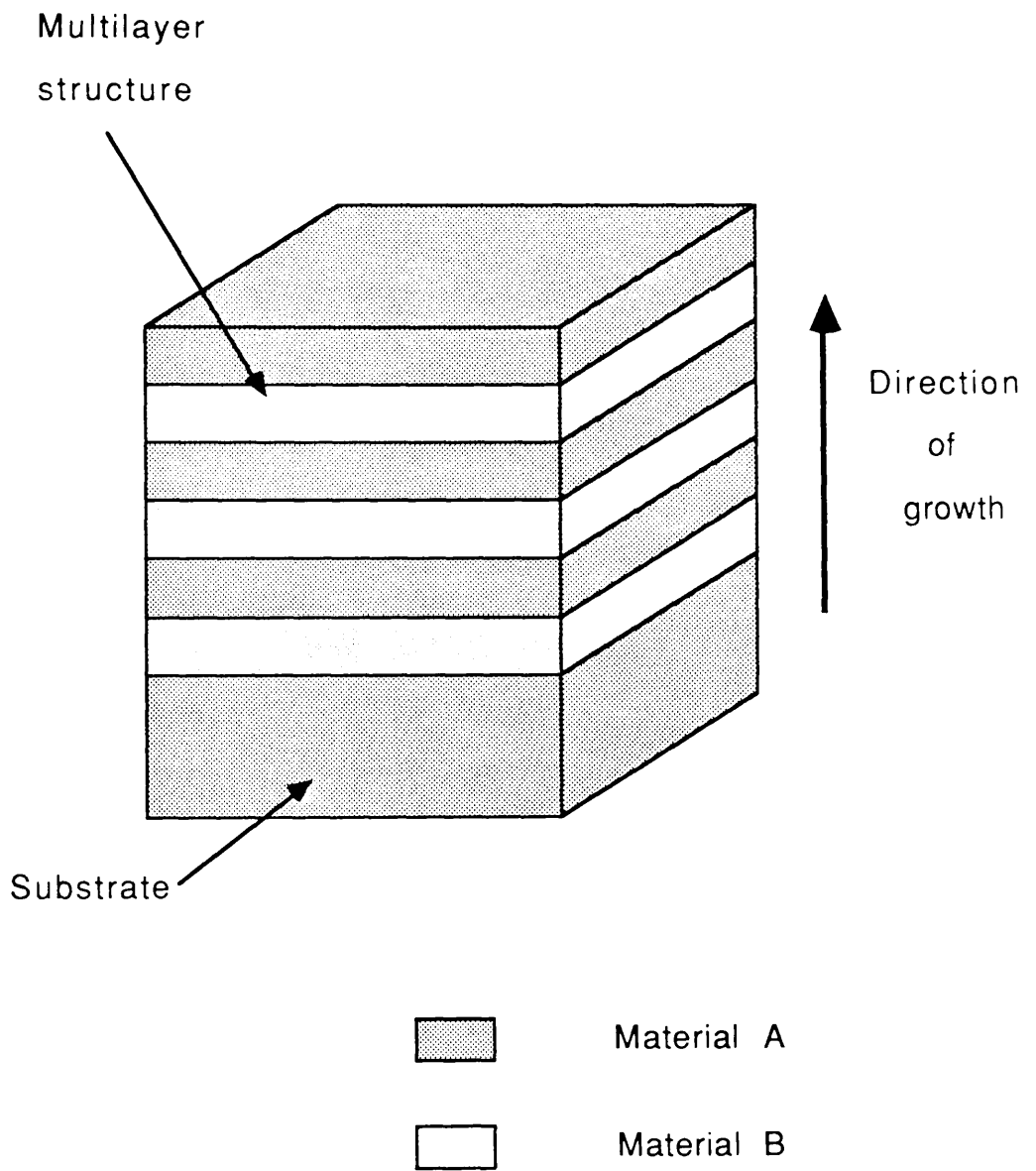


Figure 1.1: Schematic representation of a multilayer structure.

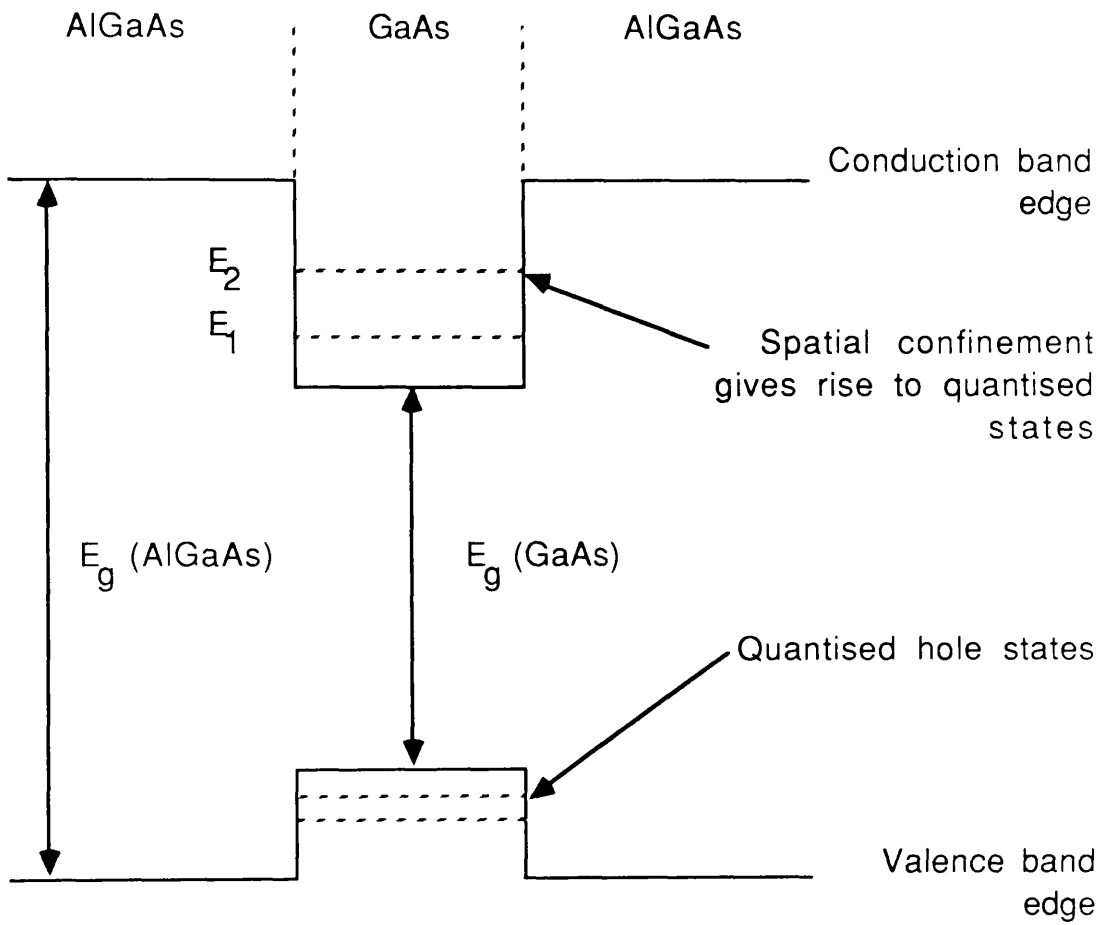


Figure 1.2: Schematic diagram of energy bands in an AlGaAs/GaAs quantum well heterostructure.

of $\text{Al}_x\text{Ga}_{1-x}\text{As}$ is very similar to that of GaAs. Such close 'lattice matching' enables the growth of high quality multilayers with very few misfit dislocations at interfaces. The majority of devices fabricated from the AlGaAs/GaAs system have been used for fast logic and microwave applications. The band gaps in the AlGaAs/GaAs system dictate that optoelectronic devices fabricated from the system operate at wavelengths of typically $<850\text{nm}$. There is, however, a need for devices in optical communication systems that operate at longer wavelengths. Ideally suited to these purposes is the $\text{In}_x\text{Ga}_{1-x}\text{As}/\text{InP}$ system which, depending on the values of well thickness and x , can operate in the wavelength range 1.1 to $1.6\mu\text{m}$ (e.g. Razeghi et. al., 1983; Marsh et. al., 1985). In addition to the AlGaAs/GaAs and InGaAs/InP systems, a wide range of materials can be used in the formation of compound semiconductor multilayers. These include superlattices comprising the quaternary $\text{In}_x\text{Ga}_{1-x}\text{As}_y\text{P}_{1-y}$ and InP (Burgeat et. al., 1981; Twigg et. al., 1987) and those comprising CdTe and InSb (Williams et. al., 1985). Also of interest are, for example, single epitaxial layers of $\text{Cd}_x\text{Hg}_{1-x}\text{Te}$ grown on CdZnTe substrates (Rosbeck and Harper, 1987) and CdTe and $\text{Cd}_x\text{Hg}_{1-x}\text{Te}$ grown on GaAs substrates (Cullis et. al., 1987) which have device applications in the field of infra-red radiation detectors. The superlattices discussed to this point are generally grown to be lattice matched. Recently, however, there has been much interest in the growth of multilayer structures in which the two components are not lattice matched. In such strained layer superlattices (SLSs), the lattice mismatch between the layers is totally accommodated by the strain in the layers so that no misfit defects are generated at the interfaces. Examples of SLSs are $\text{GaAs}_x\text{P}_{1-x}/\text{GaP}$ (Osbourne et. al., 1982), $\text{In}_x\text{Ga}_{1-x}\text{As}/\text{In}_y\text{Ga}_{1-y}\text{As}$ (Osbourne, 1983) and $\text{Ge}_x\text{Si}_{1-x}/\text{Si}$ (Bean et. al., 1984). The work described in this thesis, however, concentrates on InGaAs/InP and AlGaAs/GaAs multilayer systems that have been grown with the intention of being lattice matched.

1.3 Material growth techniques

As stated, the electronic properties of compound semiconductor multilayers depend strongly on the perfection of the atomic arrangements and on the elemental compositions across each interface. It is therefore very important that the growth techniques used in the fabrication of multilayers produce as high quality materials as possible. A number of techniques have been employed with this aim in mind, the most common of which is molecular beam epitaxy (MBE). Conventional MBE involves the generation of molecular beams from solid thermal sources. A schematic diagram illustrating the MBE process is shown in figure 1.3. The molecular beams interact with a heated crystalline substrate in a deposition chamber which is held under high vacuum (total pressure $<10^{-10}$ torr). To enable even deposition of the epilayers, the substrate is heated to temperatures of typically $\sim 600^\circ\text{C}$ and is rotated at a constant frequency. Comprehensive reviews of the technique have been given by Davies and Andrews (1985) and Joyce (1985). The quality of material grown by MBE depend on such factors as the substrate rotation rate and temperature (e.g. Alavi et. al., 1983; Hull et. al., 1986). The AlGaAs/GaAs multilayer system is that most commonly grown by MBE. Difficulties encountered in controlling the flow of P in the MBE deposition chamber to produce lattice matched InGaAs/InP systems have encouraged the development of other growth techniques, the most successful to date being metal-organic chemical vapour deposition (MOCVD). Growth of the InGaAs/InP system by this technique generally involves the reaction of the metal-organic gases trimethyl- or triethyl- indium and trimethyl- or triethyl- gallium with the hydrides arsine (AsH_3) and phosphine (PH_3). The reaction takes place in a chamber containing the substrate. A schematic diagram illustrating the MOCVD process is shown in figure 1.4. In MOCVD, the substrate is placed on a heated susceptor. The hot susceptor has

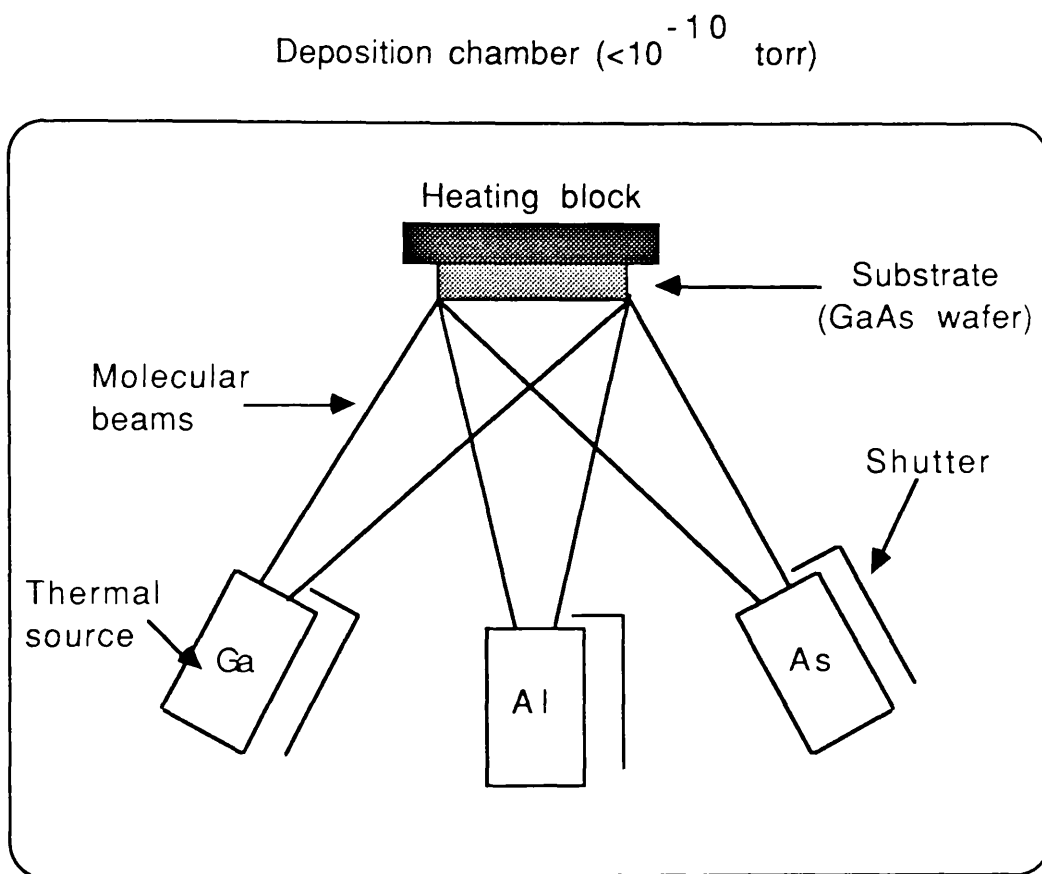


Figure 1.3: Schematic diagram of the MBE process for the growth of AlGaAs on a GaAs substrate.

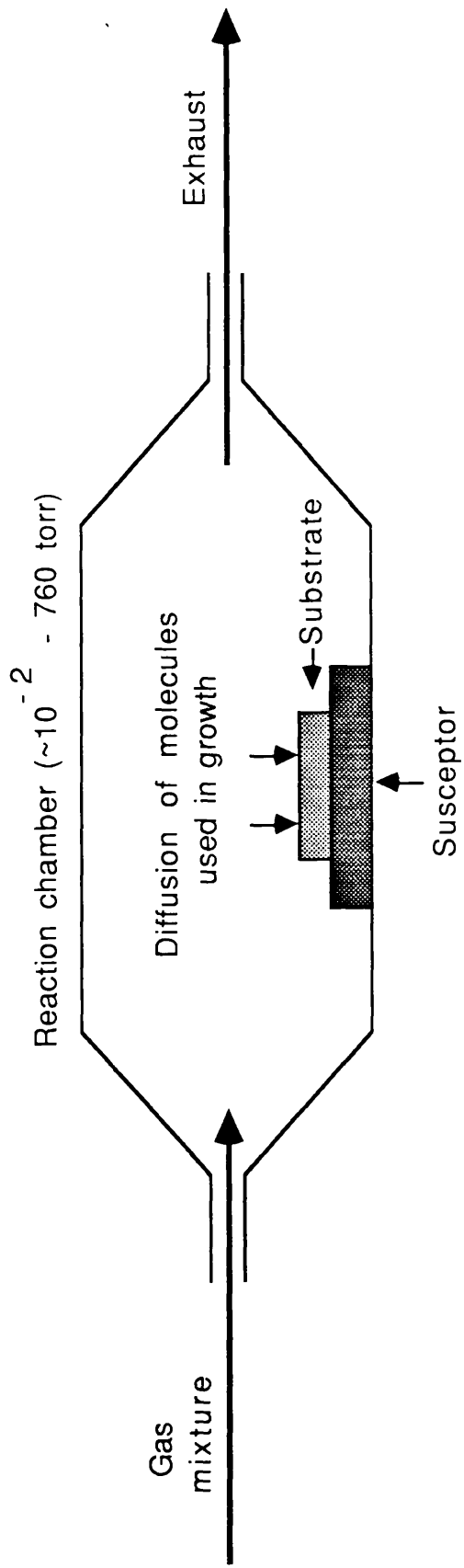


Figure 1.4: Schematic diagram of the MOCVD process.

a catalytic effect on the decomposition of the gases and so material growth primarily takes place at this hot surface. The reactants are transferred to and from the chamber using H_2 as the carrier gas. The use of this gas also avoids the deposition of carbon in the chamber in the course of a reaction. MOCVD can be carried out either at low pressure, typically between 10^{-2} and 300 torr (e.g. Razeghi et. al., 1983, 1986) or at atmospheric pressure (e.g. Bass et. al., 1986, 1987). The technique has also been used in the fabrication of AlGaAs/GaAs multilayers (Griffiths et. al., 1983). In addition to MBE and MOCVD, other techniques that have been employed in the growth of multilayers include chloride vapour phase epitaxy (VPE; Kodama et. al., 1983), hydride VPE (DiGiuseppi, 1983), liquid phase epitaxy (LPE; DiGiuseppi, 1982), gas source MBE (Temkin et. al., 1986) and, most recently, the hybrid technique of metal-organic MBE or chemical beam epitaxy (CBE; Tsang and Schubert, 1986). The growth techniques that are of particular interest to the work carried out in this thesis, however, are atmospheric pressure MOCVD and conventional MBE. Analyses will concentrate on the InGaAs/InP system grown by the former, and both the AlGaAs/GaAs and InGaAs/InP systems grown by the latter.

1.4 Structural and compositional characterisation techniques

It has already been stressed in this chapter that the electronic properties of multilayer structures depend strongly on material quality and hence on the growth techniques employed. It is very important, therefore, to obtain as accurate a knowledge as possible of the crystalline ordering and elemental compositions across the multilayer structures and so enable a greater understanding of growth mechanisms. Consequently, a wide range of experimental techniques have been employed to characterise interfaces in the materials. Surface profiling using analytical techniques such as secondary ion

mass spectrometry (SIMS; e.g. Barnett et. al., 1988), Auger spectroscopy (Cazaux et. al., 1986) and pulsed laser atom probe (PLAP) analysis (e.g. Grovenor et. al., 1987) can provide compositional information on multilayer structures with excellent depth resolution in a direction parallel to that of material growth, but at the expense of lateral resolution as signals are collected from relatively large areas. Such resolution limitations are serious if the techniques are used to examine multilayers which possess defects at interfaces and/or layers of uneven thickness.

Local composition changes in crystals can lead to lattice distortions and the presence of strain. These phenomena can be measured by, for example, ion channeling methods to yield elemental analyses as in the case of InGaAs/InP lattice mismatched structures (Cole et. al., 1986). However, x-ray diffraction analysis is the most commonly employed approach which relies on the measurement of lattice parameter variations. This technique can provide such information as the mean interfacial sharpness in a multilayer structure and has been applied to studies of the InGaAs/InP system (Barnett et. al., loc. cit.). Despite its wide use, it suffers again from limited lateral resolution and relies upon the modelling of diffraction rocking curves based upon idealised specimen structures; as such it is not a direct technique for measuring elemental compositions.

In the field of transmission electron microscopy (TEM), a number of characterisation techniques have been employed to investigate multilayers. The techniques named here utilise the ability of TEM to form high resolution images of suitably prepared multilayer specimens and to form electron diffraction patterns that can yield much useful structural and compositional information. High resolution electron microscopy (HREM) for example, has been used successfully to examine the crystalline ordering at layer interfaces in both lattice matched and mismatched structures (e.g. Humphreys, 1986; Hutchison, 1987). HREM studies of InGaAs/InP multilayers in particular have been carried out by

Chew et. al. (1987) and Mallard et. al. (1987). This technique, however, offers no direct method of measuring elemental compositions. Structure factor imaging (Petroff, 1977) is a composition sensitive technique that is commonly used to image multilayer structures in an electron microscope. It is for this purpose that the technique is employed in this thesis, and a detailed description of the method is given in chapter 4. Structure factor contrast images can also be used, for example, to determine the width of layers and the degree of planarity of the interfaces. Although the technique can provide a qualitative description of compositional changes across the system, detailed and accurate compositional analysis using this technique can be complicated and ambiguous (Boothroyd and Stobbs, 1988; see also chapter 4). Difficulties associated with image interpretation also arise when techniques such as thickness fringe analysis (Kakibayashi and Nagata, 1985, 1986; de Jong et. al., 1988) and δ fringe analysis (Bangert and Charsley, 1989) are used. The former is highly sensitive to changes in material composition and has been used extensively in the study of the AlGaAs/GaAs system. However, it is not an element specific analytical technique and so this adversely affects its application to systems in which the concentrations of more than one element can vary independently. A wealth of information on the structural quality and elemental composition of multilayers is available in convergent beam electron diffraction (CBED) patterns, but the technique of CBED is again not element specific. It has, however, been used successfully to examine the presence of strain in quaternary optical devices (Twigg et. al., 1987) and GeSi/Si SLSs (Humphreys, Eaglesham et. al., 1988). In addition to the above techniques, many other TEM methods have been developed to investigate multilayer systems, including convergent beam imaging (CBIM; Humphreys, Maher et. al., 1988), superlattice reflection imaging (Vincent et. al., 1987) and Fresnel fringe contrast (Ross et. al., 1987).

1.5 Characterisation of semiconductor multilayers in a STEM

The characterisation techniques discussed in the previous section provide important information, both compositional and structural, on semiconductor multilayers. However, the discussion does highlight a need for an analytical procedure that can combine high spatial resolution in two dimensions with direct, quantitative information on elemental compositions in the material. Techniques that are available in scanning transmission electron microscopy (STEM) can fulfill both criteria, and this thesis describes the application of such techniques in investigations to determine elemental compositions across AlGaAs/GaAs and InGaAs/InP multilayer structures as a function of material growth. All experiments described in this thesis were carried out on a Vacuum Generators (VG) HB5 STEM.

In a STEM, an electron beam can be focussed onto a thin (typically <100nm) specimen using one or more magnetic lenses. The beam can either be held stationary or scanned in a raster pattern across the specimen. If a field emission electron source is used, sufficient current can be made available in the probe (which can be ~1nm in diameter) to allow statistically meaningful information to be recorded in relatively short times. The volume of specimen irradiated by the stationary beam can contain of the order of a few thousand atoms and so composition measurements can be made with high spatial resolution.

STEM techniques have been employed in a number of investigations into semiconductor multilayer systems. By developing diffraction pattern recording techniques, for example, Brown et. al. (1988) applied microdiffraction (the technique in which the smallest probe is used to obtain a diffraction pattern) in an investigation into the presence of strain in GeSi/Si SLSS. Petford-Long and Long (1987) showed that electron energy loss spectroscopy (EELS) of

semiconductor multilayers has the potential to provide high spatial resolution quantitative information on elemental compositions. However, to enable EELS analysis of multilayers with sufficient energy resolution and relatively short acquisition times, it is desirable to employ a parallel EELS recording system corrected for some second order aperture aberrations. The acquisition system available in the STEM used in this project is a serial recording system corrected for first order aberrations only. Consequently, this thesis looks towards the use of other analytical techniques to investigate the materials of interest.

The analytical techniques employed in this thesis are energy dispersive x-ray (EDX) microanalysis and high-angle annular dark field imaging (ADFI). Investigations into semiconductor multilayers using EDX microanalysis in a STEM have also been carried out by Bullock et. al. (1986, 1987). EDX microanalysis involves determining information about a specimen from the x-rays produced by the interaction of the electron beam with the atoms in the specimen. The technique enables direct, quantitative measurements to be made of the composition in the volume of specimen excited by the beam. High-angle ADFI involves the detection of electrons that have been elastically scattered on interaction with the specimen. Images of the specimen from the detected signals enable observations to be made on the variation of mean atomic number across the area of specimen scanned by the beam. The theoretical bases underlying EDX microanalysis and high-angle ADFI are described in detail in chapter 2. Although the latter in itself cannot be used to measure the concentrations of specific elements in the material, the high spatial resolution information that it provides can complement that recorded by EDX microanalysis. In this thesis, the complementarity of the two techniques will be exploited to yield as much information as possible about the materials of interest.

To enable the accurate measurement of elemental compositions across semiconductor interfaces, many aspects involved with the development of

experimental procedures and with the correct interpretation of data must be carefully considered. A detailed discussion of such considerations is given in chapters 3, 4 and 5. This includes a description of the instrumentation used and of the methods employed to prepare suitable specimens for examination in the STEM. Also given is a detailed description of the way in which the optimum experimental conditions and procedures for both EDX microanalysis and high-angle ADFI are established. Considerations specific to the interpretation of data acquired using each technique are discussed, as is the way in which theoretical models and simulations can be used as a comparison to experimentally acquired data. Although particular emphasis is given in these chapters to the study of the AlGaAs/GaAs and InGaAs/InP systems, much of the work described can be applied to investigations of III-V semiconductor multilayers in general. In addition, many of the concepts discussed here are relevant to the general study of interfaces using EDX microanalysis and high-angle ADFI.

As stated previously in this chapter, the multilayer systems of particular interest to this thesis are the AlGaAs/GaAs system grown by MBE and the InGaAs/InP systems grown by both MBE and atmospheric pressure MOCVD. A detailed description of the experiments carried out on each system is given in chapters 6, 7 and 8. The main aim of the experiments carried out on the AlGaAs/GaAs system is to experimentally establish the resolution capabilities of both EDX microanalysis and high-angle ADFI when applied to very high quality interfaces. Using this information, together with the analytical procedures established in the opening chapters, the techniques are applied to InGaAs/InP multilayers with the aim of providing detailed information on the variations in elemental composition across each system. Such information will enable a greater understanding of the material growth processes.

Chapter 2

Theoretical Considerations

2.1 Introduction

The two principal analytical techniques employed in this thesis are energy dispersive x-ray (EDX) microanalysis and high-angle annular dark field imaging (ADFI). This chapter describes the principles on which each technique is based, and the way in which each is relevant to the problem of determining elemental compositions across AlGaAs/GaAs and InGaAs/InP multilayer systems.

Section 2.2 describes the underlying principle of high-angle ADFI, namely image formation from high-angle elastically scattered electrons. Included is a discussion of factors other than elastic scattering that can lead to image contrast between layers of different compositions in high quality crystals and their relevance to the experimental conditions employed here. This is followed by a description of theoretical models that are used to determine the probability with which an electron incident on a particular elemental species will be elastically scattered through a pre-determined angular range. This discussion is extended to predict layer contrast in high-angle ADF images of the multilayer systems of interest to this project.

The following section describes the production of characteristic x-rays. From measured x-ray yields, direct information on elemental compositions in materials can be obtained. The description includes the model used to determine characteristic x-ray production cross sections for elemental analysis in EDX. The cross sections are then evaluated for the elements that are present in the materials of interest.

2.2 Image formation using high-angle elastically scattered electrons

Elastic scattering is produced by the coulombic attraction between the negatively charged incident electron and the positively charged atom. Signals collected from electrons scattered through high angles only, result in detected intensities that are predominantly attributable to elastic scattering and display a strong dependence on atomic number Z . Crewe et. al. (1975) demonstrated that such 'Z-contrast' imaging is ideally suited to the scanning transmission electron microscope (STEM) where predominantly elastically scattered electrons can be collected by an annular dark field (ADF) detector. This technique, known as annular dark field imaging (ADFI) led to many subsequent applications (e.g. Isaacson et.al., 1976; Donald and Craven, 1979; Ohtsuki, 1980; Pennycook, 1981). Pennycook et. al. (1986), in a paper describing elemental mapping with elastically scattered electrons, suggested that accurate quantitative information on the mean atomic number \bar{Z} of a specimen could be obtained from high-angle ADF images recorded from an annular detector with inner and outer acceptance angles defined by θ_1 and θ_2 respectively (see also Berger and Pennycook, 1987) . A schematic diagram illustrating the detector/specimen geometry is shown in figure 2.1. The values of θ_1 and θ_2 used for all experiments described in this thesis are 85 and 200mrad respectively. A full description of the detector used in this project and the methods employed to experimentally establish θ_1 and θ_2 is given in chapters 3 and 4.

Following the method outlined by Pennycook et. al., high-angle ADFI can provide important information concerning the variation of \bar{Z} across semiconductor multilayers as a function of material growth. Figure 2.2(b) shows the high-angle ADF image intensity distribution in a direction parallel to that of material growth that would be expected from a system possessing a variation in

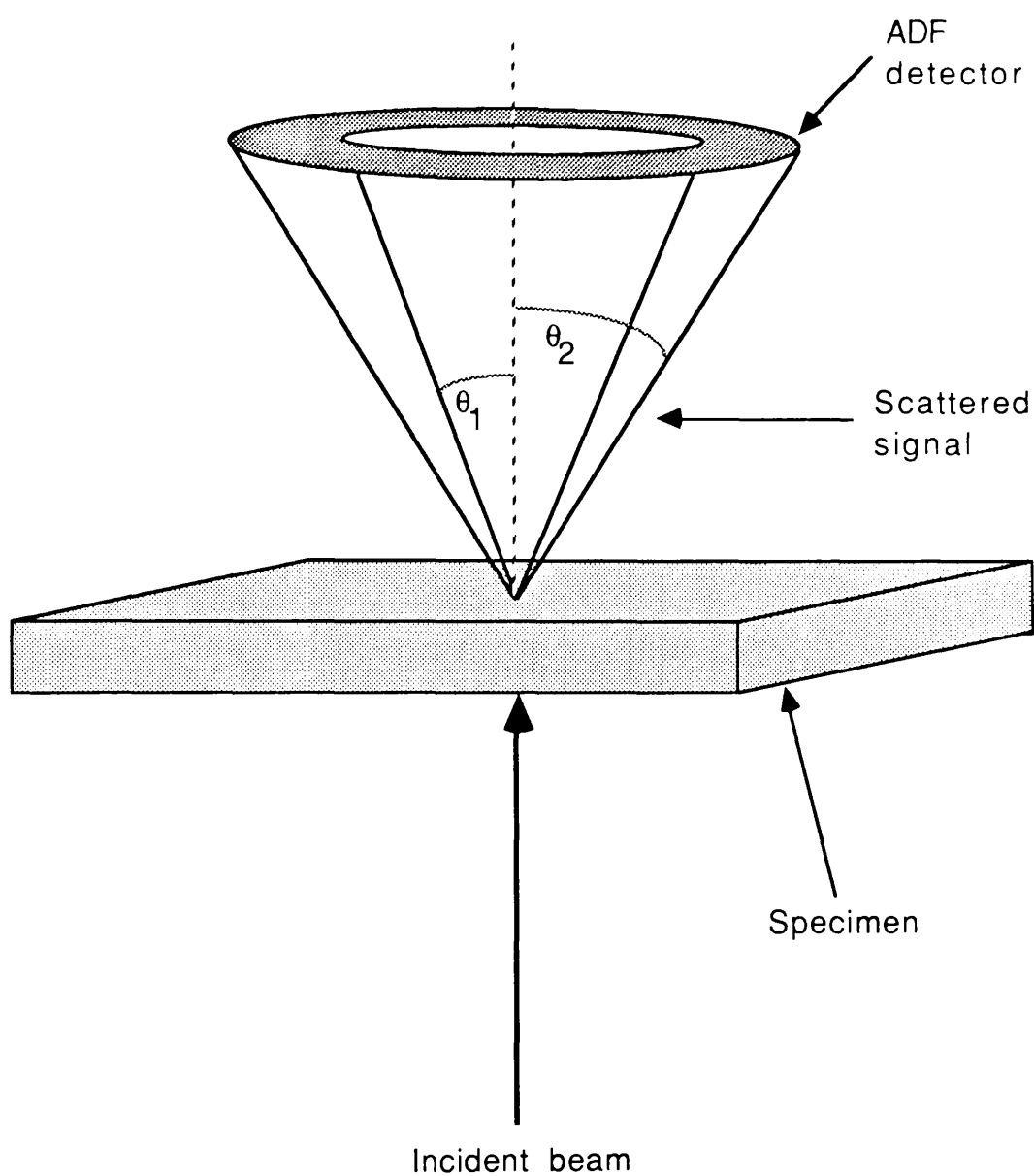


Figure 2.1: Schematic diagram illustrating the detector/specimen geometry for ADF signal collection.

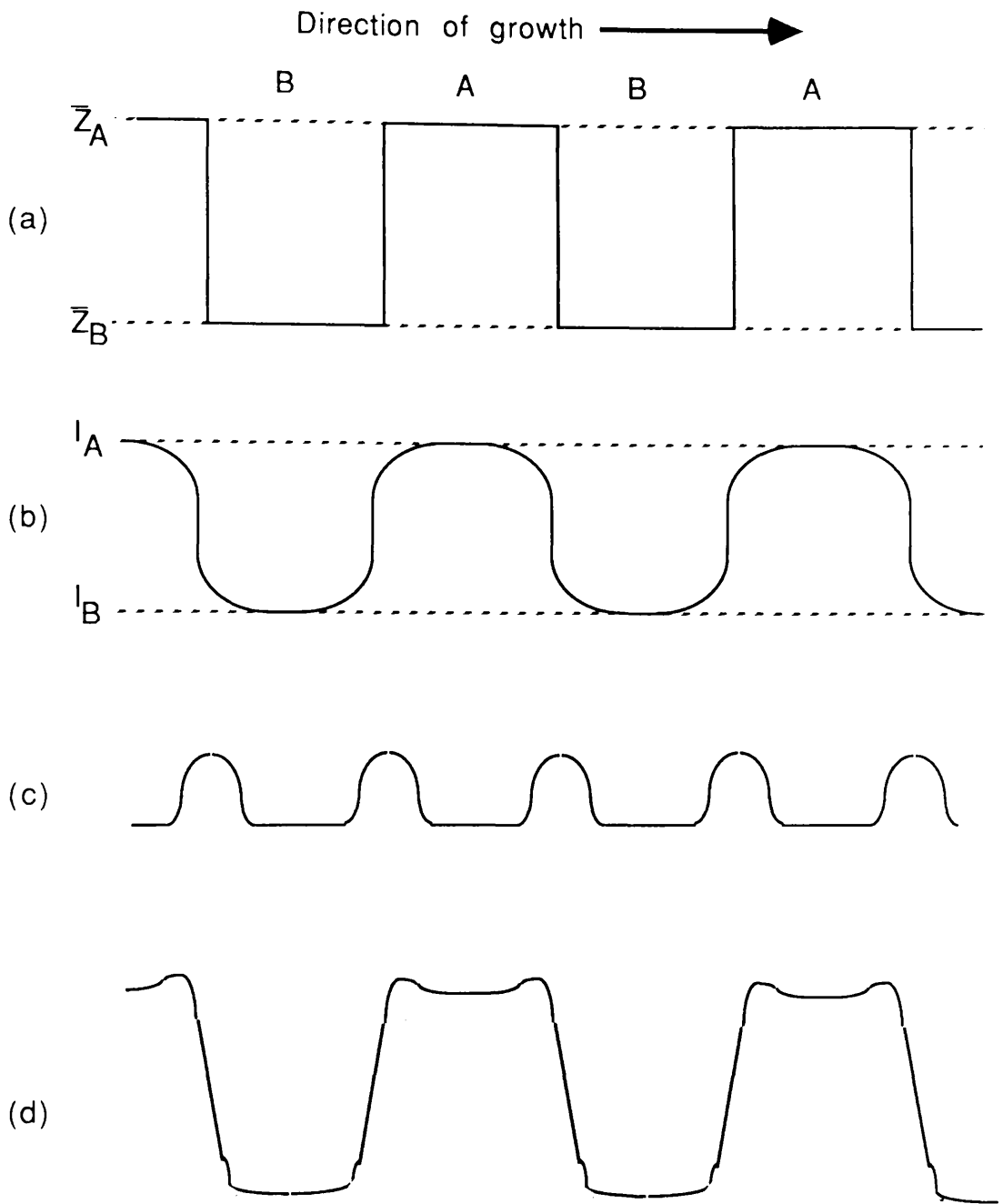


Figure 2.2: (a) Variation in \bar{Z} across a multilayer system.
 (b) Predicted high-angle ADF intensity variation from (a).
 (c) Predicted intensity variation attributable to the presence of strain at interfaces.
 (d) Predicted high-angle ADF intensity variation from (a) in the presence of strain at interfaces.

\bar{Z} as shown in figure 2.2(a). A full discussion on the sources that contribute to the spreading of the detected signal from interface regions is given in chapters 3 and 4. In figure 2.2(b), I_A and I_B are the detected intensities from material A and material B respectively. To enable quantitative analysis of such a profile, the contrast, C , between I_A and I_B must be related to the relative values of \bar{Z} in each layer. C is defined as;

$$C = \frac{I_A - I_B}{I_A} \quad (2.1)$$

Other factors that lead to layer contrast in high-angle ADF images are Bragg scattering of the incident electrons in the crystal, electron channeling and the presence of strain in the material. The influence each effect has on layer contrast under the experimental conditions used in this project are discussed in section 2.2.1. Pennycook et. al. (1986) derived formulae for elastic scattering cross sections over the angular range subtended by the ADF detector. Similar calculations are carried out in section 2.2.2 using three theoretical models. The values of the elastic scattering cross sections for elements of interest to this project are calculated and used to predict the value of C in high-angle ADF images of the InGaAs/InP and AlGaAs/GaAs multilayer systems.

2.2.1 Factors affecting image contrast

The materials investigated in this project were high quality single crystals and so Bragg reflection of incident electrons strongly influenced image contrast by redistributing the scattered intensity over the detector plane. As a result, image contrast becomes strongly dependent on specimen orientation thereby masking \bar{Z} -contrast effects. Bragg scattering contrast can be reduced significantly, however, by avoiding the excitation of low order Bragg reflections

as far as possible and by increasing θ_1 into the angular range where the reflections are strongly attenuated by atomic thermal vibrations (Howie, 1979). For thin crystals (specimens discussed in this thesis have thicknesses in the range 30 to 80nm), the intensity attenuation of Bragg reflection \underline{g} in the (hkl) plane is $\exp(-2M_g)$ (Hall and Hirsch, 1965) where;

$$M_g = 2\pi^2 g^2 \langle u^2 \rangle \quad (2.2)$$

$\langle u^2 \rangle$ is the mean square atomic vibration amplitude. Treacy (1982) showed that for the Bragg reflected intensity to fall to ~2% of the unattenuated value,

$$\theta_1 \geq \frac{2\theta_D \lambda}{h} \left(\frac{m' k_B}{3T} \right)^{\frac{1}{2}} \quad (2.3)$$

where λ is the incident electron wavelength, h is Planck's constant, k_B is Boltzmann's constant, θ_D is the Debye temperature of the material, m' is the atomic mass and T is the crystal temperature. For 100keV electrons incident on a Ge film at room temperature (conditions which simulate closely those used in experiments discussed in this thesis), where $\theta_D=374K$, $\theta_1 \geq 180\text{mrad}$. Treacy adds, however, that if principal Bragg reflections are avoided, the criterion of equation 2.3 is weighted towards lower values of θ_1 and that a lower limit of $\theta_1 \approx 70\text{mrad}$ is found suitable for most materials. Experimental results acquired using $\theta_1=85\text{mrad}$ discussed in later chapters show that detected image intensities can indeed be attributed fully to factors other than Bragg scattering.

High energy electron waves, when entering a crystal, take on the periodicities of the projected potential of the lattice and the incident electron wave redistributes into a series of Bloch wave states (Hirsch et. al., 1977). Bloch wave intensities are at a maximum at different positions within the unit cell. The

relative amplitudes of the Bloch waves are highly sensitive to the direction with which the incident electrons are travelling with respect to the lattice, particularly when close to low order Bragg reflections. Bloch waves travelling or 'channeling' near to strings of atoms are most strongly scattered. Consequently, electron channeling is sensitive to crystal orientation and can influence high-angle ADF image contrast (e.g. Pennycook et. al., 1986; Treacy et.al., 1988). In a manner similar to that used to avoid Bragg scattering contrast, channeling effects can be reduced by avoiding the strong excitation of low order Bragg reflections. In addition, channeling effects are most significant if the incident electron beam can be described as a plane wave. In the experiments discussed here, however, the illumination is highly convergent (chapter 3) and so channeling effects are further reduced.

The relative positions of atoms in regions of strain in a material are not as they would be in a perfect crystal. Such lattice deformation is in essence similar to that produced by thermal vibrations of the crystal. As a result, Treacy et. al. (1988) observed that strain may give rise to an increase in detected ADF intensity that is related to an increase in scattering similar in nature to the thermal diffuse scattering discussed earlier in this section. Following the Treacy argument, the detected intensity distribution from thermal diffuse related scattering alone from a multilayer system undergoing strain at interfaces would be similar to that shown in figure 2.2(c). When the effects of \bar{Z} -contrast from multilayers are taken into consideration, the total detected intensity distribution would resemble in some way that shown in figure 2.2(d). It should be noted that the exact form of such an intensity distribution would depend on the relative contributions of strain and \bar{Z} to signal intensity. The materials examined in this thesis are grown with the intention of being lattice matched, and HREM studies have found that the systems are essentially free from extended crystallographic defects (Chew et. al., 1987). The experimental results discussed later in this

thesis show that, in the majority of specimens examined, interface quality was very high and that such distributions as shown in figure 2.2(d) are, in the main, not observed. In the cases where the presence of strain was indicated, the arguments of Treacy were taken into consideration.

2.2.2 Quantitative interpretation of high-angle ADF image contrast

The detected signal S_Y collected by an ADF detector and attributable to element Y in a specimen is proportional to the number of atoms of Y per unit volume, N_Y , the thickness of the specimen, t , the incident beam current, I_P , and the cross section for elastic scattering into the detector due to Y, $\sigma_{el}(Y)$;

$$S_Y \propto \sigma_{el}(Y)tN_YI_P \quad (2.4)$$

Here, σ_{el} is evaluated for elements of interest to this thesis using three theoretical models. The numerical values of physical constants and parameters used in the calculations are listed in table 2.1.

Evaluation of σ_{el} for a particular element must take into consideration the screening effect of the nucleus by the atomic electrons. A simple way to achieve this is to describe the charge distribution as a single exponential potential (Wentzel, 1927);

$$V(r) = -\frac{Ze^2}{r} \exp\left(-\frac{r}{r_o}\right) \quad (2.5)$$

Symbol	Description	Value
λ	Wavelength of 100keV electrons	$3.7 \times 10^{-12} \text{ m}$
a_0	Bohr radius	$5.29 \times 10^{-11} \text{ m}$
m_0	Electron rest mass	$9.109 \times 10^{-31} \text{ kg}$
m	Fast electron mass	$1.089 \times 10^{-30} \text{ kg}$
θ_1	Inner acceptance angle	85mrad
θ_2	Outer acceptance angle	200mrad
β	v/c	0.548

Table 2.1: Numerical values relevant to the calculation of elastic scattering cross sections.

where e is the charge of the electron, r is the radial distance from the centre of the atom and r_o is the Thomas-Fermi radius where;

$$r_o = 0.885a_oZ^{-\frac{1}{3}} \quad (2.6)$$

a_o is the Bohr radius. Scott (1963) showed that by using the first Born approximation, the differential cross section for elastic scattering, $d\sigma_{el}/d\Omega$, can be expressed in the form;

$$\frac{d\sigma_{el}}{d\Omega} = \left(\frac{m}{m_o}\right)^2 \frac{Z^2\lambda^4}{4\pi^4a_o^2} \frac{1}{\left(\theta^2+\theta_o^2\right)^2} \quad (2.7)$$

Ω is solid angle, m is the fast electron mass, m_o is the electron rest mass, λ is the electron wavelength, θ is the angle through which the electron is scattered and θ_o is the Born screening angle, where;

$$\theta_o = 1.13 \frac{m}{m_o} \frac{\lambda Z^{\frac{1}{3}}}{2\pi a_o} = \frac{1.13Z^{\frac{1}{3}}}{137\beta} \quad (2.8)$$

$\beta = v/c$, the ratio of the electron velocity to that of light. To calculate σ_{el} for scattering into an annular detector, the most convenient method of approach is to express equation 2.7 as the product of the Rutherford cross section $d\sigma_{Ruth}/d\Omega$ and a screening function $q(\theta)$;

$$\frac{d\sigma_{el}}{d\Omega} = \frac{d\sigma_{Ruth}}{d\Omega} q(\theta) \quad (2.9)$$

where;

$$\frac{d\sigma_{\text{Ruth}}}{d\Omega} = \left(\frac{m}{m_o}\right)^2 \frac{Z^2 \lambda^4}{4\pi^4 a_o^2 \theta^4} \quad (2.10)$$

and;

$$q(\theta) = \frac{\theta^4}{\left(\theta^2 + \theta_o^2\right)^2} \quad (2.11)$$

The expression for $d\sigma_{\text{Ruth}}/d\Omega$ breaks down at low values of θ and so must always be used in conjunction with a screening function. Pennycook et. al. (loc. cit.) showed that equation 2.9 can be directly integrated to give σ_{el} for scattering into an annular detector;

$$\sigma_{\text{el}} = \left(\frac{m}{m_o}\right)^2 \frac{Z^2 \lambda^4}{4\pi^3 a_o^2} \left[\frac{1}{\theta_1^2 + \theta_o^2} - \frac{1}{\theta_2^2 + \theta_o^2} \right] \quad (2.12)$$

For the purposes of this discussion, σ_{el} in equation 2.12 is denoted as the Born cross section, $\sigma_{\text{el}}(\text{Born})$.

Moliere (1947) suggested that a better fit to the atomic potential could be obtained by using a sum of three exponentials;

$$V(r) = -\frac{Ze^2}{r} \sum_{i=1}^3 a_i \exp\left[-\frac{b_i r}{r_o}\right] \quad (2.13)$$

where a_1 , a_2 and a_3 have values 0.1, 0.55 and 0.35 respectively and b_1 , b_2 and b_3 have values 6.0, 1.2 and 0.3 respectively. Moliere proposed that his

calculations for $d\sigma/d\Omega$ using the potential in equation 2.13 could be approximated by a simple functional form for $q(\theta)$ similar to that in equation 2.11 where θ_0 is replaced by θ_a ;

$$\theta_a^2 = \theta_0^2 (1.13 + 3.76\alpha^2) \quad (2.14)$$

and;

$$\alpha = \frac{Z}{137\beta} \quad (2.15)$$

σ_{el} can be re-evaluated to give the Moliere cross section, $\sigma_{el}(\text{Moliere})$.

Fleischmann (1960) suggested that a better fit to that of Moliere, especially as a function of increasing Z , is to express $q(\theta)$ as;

$$q(\theta) = \frac{\theta}{\theta + \theta'_a} \quad (2.16)$$

where;

$$\theta'_a = \theta_a e^{\frac{1}{2}} \quad (2.17)$$

Pennycook (loc. cit.) showed that integration of equation 2.9 using this expression of $q(\theta)$ gives the Fleischmann cross section $\sigma_{el}(\text{Fleischmann})$ where;

$$\sigma_{el} = \left(\frac{m}{m_0}\right)^2 \frac{Z^2 \lambda^4}{2\pi a_0^2} \left[\frac{\theta_2 - \theta_1}{\theta_1 \theta_2 \theta'_a} + \frac{1}{(\theta'_a)^2} \log_e \left(\frac{\theta_1}{\theta_2} \cdot \frac{\theta_2 + \theta'_a}{\theta_1 + \theta'_a} \right) \right] \quad (2.18)$$

The numerical values of θ_o , θ_a and θ_a' , and the Born, Moliere and Fleischmann cross sections for elements relevant to this thesis are listed in table 2.2. These values show that the approximations for σ_{el} differ considerably according to the model used.

Of interest to this project is the contrast C (defined in equation 2.1) produced between layers of different compositions in high-angle ADF images of multilayer systems. For GaAs, the detected intensity from elastically scattered electrons can be expressed as;

$$I_{GaAs} = K(\sigma_{el}(Ga) + \sigma_{el}(As)) \quad (2.19)$$

where K is a constant related to factors such as specimen thickness and incident electron beam current (equation 2.4). For $Al_xGa_{1-x}As$, where atoms occupying the group III sublattice sites are assumed to be either Al or Ga, the detected intensity can be expressed in the form;

$$I_{Al_xGa_{1-x}As} = K(x\sigma_{el}(Al) + (1-x)\sigma_{el}(Ga) + \sigma_{el}(As)) \quad (2.20)$$

The detected intensities for InP and $In_xGa_{1-x}As$ are calculated in a similar manner. Using this method, table 2.3 lists the values of C predicted between layers of $In_{0.53}Ga_{0.47}As$ and InP, and $Al_{0.3}Ga_{0.7}As$ and GaAs using the Born, Moliere and Fleischmann cross sections. Also listed are the values of C predicted using the unscreened Rutherford cross section (proportional to \bar{Z}^2) and that predicted from the total elastic scattering cross section, summed over all scattering angles (proportional to $\bar{Z}^{4/3}$; Lenz, 1954). As would be expected, table 2.3 shows that the inclusion of screening effects predicts a level of layer contrast lower than that predicted by unscreened Rutherford scattering. The listed values also show that there is good agreement between the Born, Moliere

Element	θ_o (mrad)	θ_a (mrad)	θ'_a (mrad)	$\sigma_{el} \text{ (} \times 10^{-22} \text{ m}^2 \text{ sr}^{-1} \text{)}$		
				Born	Moliere	Fleischmann
In	55	91	15	1.38	0.81	2.88
P	37	42	69	0.16	0.15	.39
Ga	47	63	104	0.61	0.49	1.39
As	48	66	109	0.68	0.54	1.54
Al	35	39	64	0.12	0.12	.30

Table 2.2: Values of screening angles and elastic scattering cross sections for elements of interest to this thesis. The cross sections were evaluated for 100keV incident electrons, with $\theta_1= 85\text{mrad}$ and $\theta_2 = 200\text{mrad}$.

Materials	Born	Moliere	Fleishmann	\bar{Z}^2	$\bar{Z}^{4/3}$
$\text{Al}_{0.3}\text{Ga}_{0.7}\text{As}/\text{GaAs}$	0.12	0.11	0.11	0.16	0.11
$\text{In}_{0.53}\text{Ga}_{0.47}\text{As}/\text{InP}$	0.09	0.20	0.12	0.24	0.17

Table 2.3: Predicted high-angle ADF layer contrast for the materials of interest to this project using several elastic scattering models.

and Fleischmann calculations as to the predicted contrast between GaAs and $\text{Al}_{0.3}\text{Ga}_{0.7}\text{As}$. For the lattice matched InGaAs/InP system, however, there is a large discrepancy between the contrast predicted by the Moliere calculation compared with those of Born and Fleischmann. All values listed in table 2.3 will be used in future chapters in comparison with the contrast measured from experimentally acquired high-angle ADF images.

2.3 Ionisation cross sections for characteristic x-ray production

Energy dispersive x-ray (EDX) microanalysis is an established technique used to investigate the elemental compositions of specimens in an electron microscope (e.g. Hall and Gupta, 1979; Lorimer, 1983). There are two completely different mechanisms by which x-rays can be produced when electrons with energies of 100keV are incident on a thin foil target; the production of bremsstrahlung photons and that of characteristic photons. The former are produced when electrons are accelerated in the field of the atomic nuclei in the specimen. The photon energy is equal to the difference in energy of the incident and emergent electron, and can have any energy between 0 and T_0 , the energy of the incident electron. The distribution of x-ray intensity varies smoothly with photon energy and, except for an increase in the number of photons produced, does not change significantly as a function of increasing specimen atomic number. Consequently, bremsstrahlung yields no direct information on the composition of the specimen. A discussion on the understanding of the bremsstrahlung component of x-ray spectra is given by Chapman et. al. (1984).

Characteristic photons may be produced when an atom de-excites following the ionisation of an inner atomic shell by an incident electron. The value of T_0 must be greater than the binding energy of the atomic electron. If the de-

excitation occurs by a radiative transition, the energy of the emitted photon is equal to the difference in energy of the two electronic states and is therefore characteristic to the particular atomic species. Consequently, characteristic photons can provide direct information on elemental compositions in specimens.

To enable quantitative microanalysis of specimens using the EDX technique, it is desirable to have as accurate a knowledge as possible of the ionisation cross sections for characteristic photon production. The x-ray spectral lines analysed and used in this thesis to determine elemental compositions in InGaAs/InP and AlGaAs/GaAs systems arise from the Al K, P K, Ga K_{α} , As K_{α} and In L transitions. In all experiments the value of T_0 was 100keV. Table 2.4 lists the energies ($I_{K\alpha}$) of the K_{α} lines for Al, P, Ga and As.

Characteristic photons are emitted isotropically (Berenyi and Hock, 1978) and so ionisation cross sections need not be differential in angle. Such cross sections are often calculated according to a simple functional form. One suitable form is the Bethe model (Bethe, 1930). In this model, the incident electron is described by a plane wave and transfers a given amount of energy and momentum to the target atom at the collision. This transfer can be described in terms of the kinematics of the incident electron and of the generalised oscillator strength of the atom which represents the internal dynamics of the atom. The model calculates the total cross section for transitions into a particular shell by summing over all permitted values of momentum transfer and all possible final energy states for the doubly differential cross section. Using the Bethe model, the total ionisation cross section for K-shell transitions, σ_{iK} , is given by;

$$\sigma_{iK} = 2 \pi e^4 b_K \ln \left(\frac{c_K T_0}{I_K} \right) \frac{1}{T_0 I_K} \quad (2.21)$$

I_K is the K-shell binding energy and b_K and c_K are parameters which may be

Element	I_K (keV)	$I_{K\alpha}$ (keV)	ω_K	s_K	σ_{cK} ($\times 10^{-32} \text{ m}^2 \text{ sr}^{-1}$)
Al	1.56	1.49	0.038	1.0	6.7
P	2.14	2.02	0.058	1.0	6.9
Ga	10.37	9.24	0.528	0.873	6.5
As	11.86	10.53	0.587	0.865	5.9

Table 2.4: Numerical values of parameters used in the calculation of characteristic x-ray production cross sections for K_{α} transitions in elements relevant to this thesis.

evaluated empirically. Following Gray et. al. (1983), the values of b_K and c_K used for all elements of concern here are 0.67 and 0.89 respectively. Equation 2.21 is non-relativistic. Inokuti (1971) published a relativistically corrected form of σ_{iK} ; however it has been observed (e.g. Paterson et. al., 1989) that although relativistic corrections may be necessary for values of $T_0 > 100\text{keV}$, equation 2.21 is found suitable for $T_0 = 100\text{keV}$.

As stated in the description of the Bethe model, the expression for σ_{iK} takes into consideration all transitions to the K-shell. To enable analysis of K_α lines from x-ray spectra that are recorded by detectors that subtend a finite solid angle (see chapter 3), the cross sections for x-ray production per unit solid angle for K_α transitions, σ_{cK} , must be calculated;

$$\sigma_{cK} = \frac{s_K \omega_K \sigma_{iK}}{4\pi} \quad (2.22)$$

ω_K is defined as the fluorescence yield, which is the probability that an x-ray rather than an Auger electron will result following the ionisation of an inner shell electron. s_K , the partition function, is the probability of a transition to the K-shell originating from a particular higher order shell and is defined as;

$$s_K = \frac{N_\alpha}{N_\alpha + N_\beta} \quad (2.23)$$

N_α is the number of transitions from the L-shell and N_β that from the M-shell. Using values given by Gray (1981), table 2.4 lists the values of I_K , s_K and ω_K for the elements of relevance to this thesis. σ_{cK} can be calculated easily by combining equations 2.21 and 2.22;

$$\sigma_{cK} = \frac{\omega_K s_K}{4\pi} \frac{1}{I_K T_0} \ln \left(\frac{0.89 T_0}{I_K} \right) \cdot 8.55 \times 10^{-28} \quad (\text{m}^2 \text{sr}^{-1}) \quad (2.24)$$

where I_K and T_0 are expressed in keV. The numerical values of σ_{cK} for elements of interest here are given in the final column of table 2.4. These values are used in future chapters to determine elemental compositions from experimentally acquired x-ray spectra. It should be noted that composition determination in future chapters does not rely exclusively on the above calculations and that (when available) specimens of known composition are used to verify experimentally the relative efficiencies of x-ray production of the elements.

As will be discussed in chapter 3, x-ray spectra are recorded using a multi-channel analyser which possesses 1024 channels. The energy width of the channels can be either 20 or 40eV. The former value was used for all experiments described in this thesis because the higher energy resolution that this corresponds to is beneficial for analyses of the Al K and P K signals. As a result, the energy range over which spectra are recorded extends to ~20keV. The energy of the In $K_{\alpha 1}$ characteristic photons is 24.2keV and so no In K signal is detected. If channel widths of 40eV were chosen, the number of In K photons detected would be very low, since the detection efficiency for the EDX detector falls below unity in this energy range. Consequently, the In L characteristic signal was used in all calculations of elemental composition. Unlike the K-shell, the L-shell is split into three sub-shells and so the relationship between ionisation and x-ray production is more complicated. Paterson et. al. (1989) described the way in which the Bethe model is applied to the L-shell and compared experimental and calculated K/L cross section ratios. There is, however, a paucity of reliable cross section models for the L-shell and so elemental concentrations are calculated on the basis of data acquired experimentally from specimens of known composition.

Chapter 3

Instrumentation

3.1 Introduction

The aim of this project is to determine, with high spatial resolution, elemental concentrations across layer interfaces in InGaAs/InP and AlGaAs/GaAs multilayer systems. As chapters 1 and 2 have discussed, the experimental techniques of EDX microanalysis and high-angle ADFI that are available in scanning transmission electron microscopy provide an opportunity to realise this aim. The microscope used for all experiments described in this thesis is an extended VG HB5 scanning transmission electron microscope (STEM). To enable the implementation of both experimental techniques, the electron beam-specimen configuration should ideally correspond to that shown in figure 3.1. In this diagram, the size of the beam at the specimen is as small as possible, and the specimen is oriented so that the plane of the layers is parallel to the direction of the incident beam. With particular emphasis on the steps taken to achieve these objectives, section 2 of this chapter describes the HB5 together with its associated detectors. This is followed by a description of the computer and software used to analyse experimental data. The final section gives a detailed description of the technique used to prepare cross-sectional semiconductor specimens that are suitable for microanalysis in the HB5.

3.2 The VG HB5 STEM

In the extended VG HB5 STEM (a schematic diagram of which is shown in figure 3.2), a demagnified image of a high brightness electron source is formed

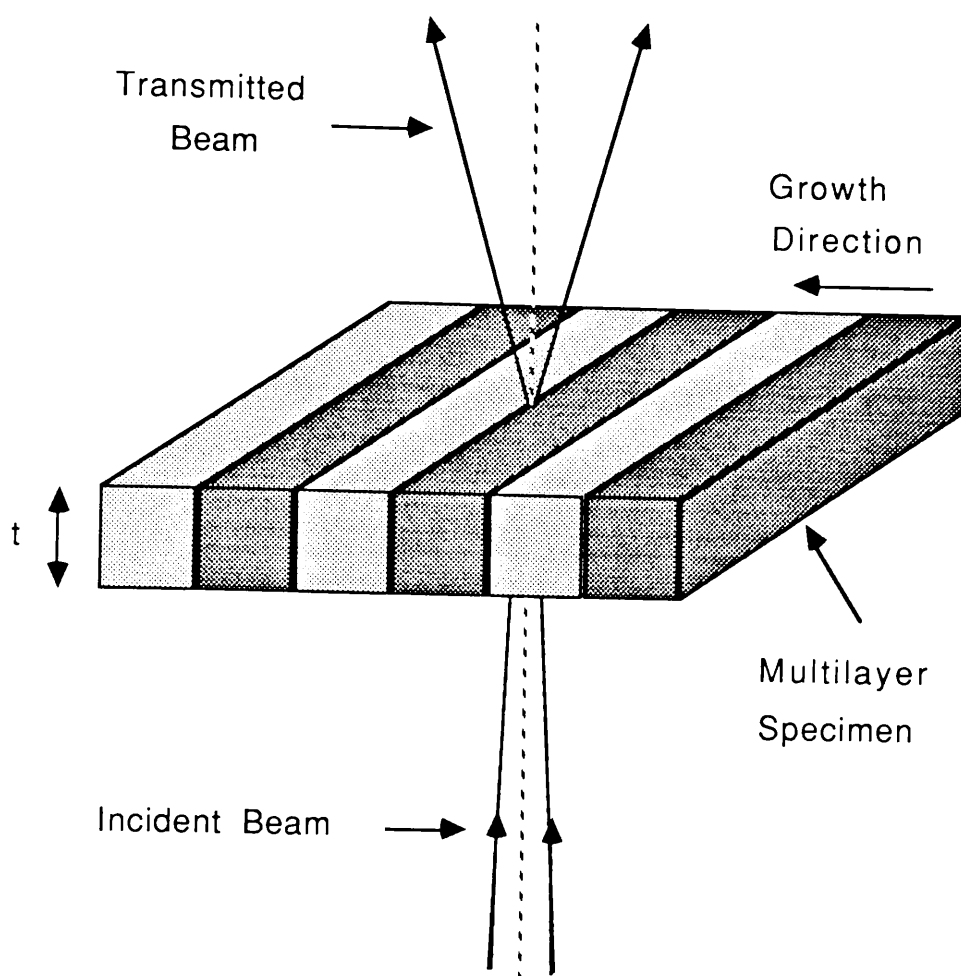


Figure 3.1: Schematic diagram of a cross-sectional multilayer suitable for microanalysis.

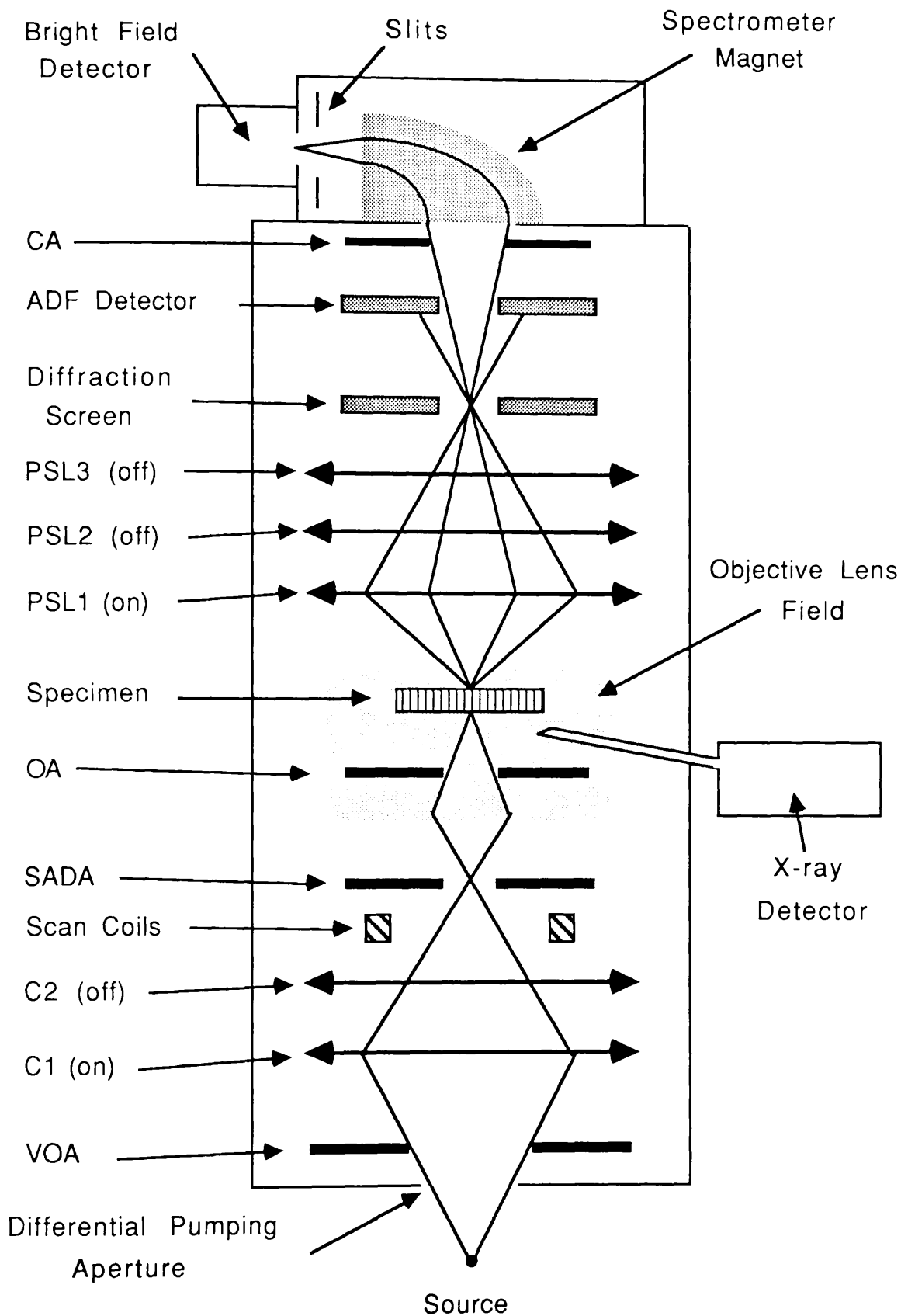


Figure 3.2: Schematic diagram of the VG HB5 STEM.

on a thin specimen. Such an image, known as the probe, can either be held stationary to enable microanalysis on a specific volume of specimen or scanned in a raster pattern across the specimen. The size and current density of the probe is controlled by a pre-specimen electron optical configuration, and the magnification of the final image depends on the size of the specimen area scanned.

A series of post-specimen lenses control the spatial distribution of the transmitted signal enabling illumination of the various electron detectors by specific parts of the signal. Compositional determination of materials by microanalysis is carried out in this instrument by analysing either the electron or characteristic x-ray signals. This section describes the various components in the electron microscope and their interaction. Included is a detailed discussion on probe formation with particular emphasis on the modes of operation used for EDX microanalysis and high-angle ADFI.

3.2.1 The Field Emission Gun

An important factor governing the spatial resolution with which microanalysis is carried out in the HB5 is the probe size at the specimen. For meaningful quantitative analysis of multilayer systems, this should be considerably smaller than the width of each layer. The serial nature of the recording systems used in STEM operation also demand that the probe current be sufficiently high to enable good statistical accuracy using data acquisition times that are as short as possible. Consequently, a very high brightness electron source with a small emitting area is essential.

The gun used in the HB5 is a field emission gun (e.g. Crewe, 1971), the electron source of which is a single crystal tungsten cathode welded onto a

tungsten filament. The radius of the cathode tip is $\sim 100\text{nm}$ and its emitting surface is a (310) face. Electrons are stripped from the surface when a potential difference of $\sim 3\text{kV}$ is applied between the cathode and an extraction anode, creating fields $> 5 \times 10^7 \text{Vcm}^{-1}$ in the source region. A second anode accelerates the electrons up to energies of 100keV . The two anodes act in the same way as an electrostatic lens in that the electrons appear to originate from a virtual source. Measurements by Morrison (1981) found that the virtual source, assumed gaussian in form, has a full-width half-maximum (FWHM) of $\sim 6\text{nm}$. In this chapter, for the purposes of probe calculations, radial gaussian distributions $\beta(r)$ are expressed in terms of the characteristic radius r_0 of the distribution where,

$$\beta(r) = \beta_0 \exp \left[-\frac{r^2}{2(r_0)^2} \right] \quad (3.1)$$

The relationship between r_0 and the FWHM is;

$$\text{FWHM} = 2\sqrt{2\ln 2} r_0 \quad (3.2)$$

The characteristic radius of the virtual source, $r_0(\text{source})$ is 2.5nm . The brightness of the source is $\sim 5 \times 10^9 \text{Acm}^{-2}\text{sr}^{-1}$. The energy distribution of electrons emitted from the source has a full-width half-maximum (FWHM) of $\sim 0.5\text{eV}$. This enables beams with average electron energies of 100keV to be treated as essentially monochromatic.

Efficient operation of the gun requires a vacuum of $< 10^{-10}\text{torr}$ in the vicinity of the source. The column of the HB5 is held at typically $\sim 10^{-9}\text{torr}$, and so a differential pumping aperture separates the gun from the remainder of the microscope. During microscope operation, contaminants accumulate on the

cathode surface. Such material is removed by passing a small current through the tungsten filament ensuring maximum emission current and prolonging the lifetime of the source. This procedure, known as flashing, is carried out at intervals of ~30mins.

3.2.2 Pre-specimen Optics

The numerical values of all parameters relevant to the following discussion are given in table 3.1. More detailed descriptions of the experimental methods employed to determine them are given by Crozier (1985) and Morrison (1981).

3.2.2.1 Instrumentation

The pre-specimen optical configuration in the HB5 is treated as a three lens system, consisting of a double condenser lens (C1 and C2) and the pre-specimen field of the objective lens. Such a configuration allows a high degree of flexibility in probe forming conditions. In image mode (used for both of the principal experimental techniques discussed in this thesis) the probe is focussed at the plane of the selected area diffraction aperture (SADA) by the condenser lenses before the beam enters the objective lens field. In this mode, it was found suitable to use either C1 or C2 with the objective lens. If the source (with characteristic radius $r_o(\text{source})$ defined in equation 3.1) is magnified by a factor M (where $M < 1$ forms a demagnified image with characteristic radius $r_o(\text{probe})$) by the pre-specimen lenses, $r_o(\text{probe})$ can be expressed in the form;

$$r_o(\text{probe}) = Mr_o(\text{source}) = M_C M_{Obj} r_o(\text{source}) \quad (3.3)$$

where M_C and M_{Obj} are the contributions to the source magnification due to

excitation of the condenser and objective lens respectively. Note that, in image mode, $M_C = M_{C1}$ or $M_C = M_{C2}$. The ratio of the image distance to the object distance for C2 is lower than that for C1 and so $M_{C2} < M_{C1}$. This means that a smaller probe is formed at the specimen if C2 is used instead of C1. The total current in the probe, however, is higher when C1 is used in preference to C2. Consequently, the lens configuration employed for a particular experiment will depend on the relative importance of probe size with respect to probe current. The most significant contribution towards the demagnification of the virtual source under conditions used for both EDX microanalysis and high-angle ADFI is made by the pre-specimen field of the objective lens, where $M_{Obj} \approx 0.03$.

In addition to the SADA, the apertures situated in the pre-specimen region of the column are the objective aperture (OA) and the virtual objective aperture (VOA). Both the total current and the current density distribution of the probe are a function of the probe-defining aperture size and hence illumination semi-angle (α_0). The value of α_0 can be defined by either the OA or the VOA. The latter is situated before the first condenser lens in a plane approximately conjugate to that occupied by the former. In a similar manner to the choice of condenser lens excitations, experimental aims will govern the choice of objective aperture.

The specimen is located within the objective lens field. Focussing of the probe at the specimen plane can occur in two ways; either by adjustment of the objective lens setting or by leaving this at a set excitation, moving the specimen by means of a z-shift facility to as near to the in-focus position as possible then using the objective lens for fine-focussing only. The latter method is preferred for microscope operation as this enables a set optical configuration to be maintained.

3.2.2.2 Operating conditions for EDX and high-angle ADFI

An important consideration for EDX microanalysis is that the intensity of x-rays emanating from the specimen is sufficient to enable good statistical accuracy in the characteristic peaks of interest without unduly lengthening the times over which spectra are acquired. As will be discussed in chapter 5, effects in addition to probe size (such as beam spreading in the specimen) can limit the spatial resolution of the technique. With this in mind, C1 and the objective lens are used to project the image of the source onto the specimen. In this configuration, the total probe current is 0.2nA (Crozier, 1985). When the OA is used to define the probe convergence angle, because of its proximity to the specimen and the EDX detector, there is a substantial extraneous contribution to spectra generated by electrons backscattered from the aperture. To reduce this effect, the VOA is used in preference. Using the probe current density distribution calculations described in section 3.2.2.3, the 100 μ m VOA ($\alpha_0=11$ mrad) was found to give the smallest coherent probe. As EDX spectra are usually recorded with the beam held stationary, it should not strike the edge of even the smallest SADA, which in turn should not give rise to any stray radiation. Such radiation emanating from the VOA will, however, not pass through the SADA and so this aperture is inserted during the acquisition of each x-ray spectrum.

The cross-section values (calculated in chapter 2) for high-angle ADFI are several orders of magnitude greater than those for x-ray generation and so it is possible to use a smaller probe containing less current. Consequently, C2 and the objective lens are employed thereby minimising incoherent probe contributions. The probe defining aperture chosen for this technique, is again that which gives the smallest coherent probe. Using the calculations described in section 3.2.2.3, the 50 μ m OA ($\alpha_0=9.2$ mrad) was found to be most suitable.

3.2.2.3 Calculation of the probe current density distribution

Analysis and interpretation of results from both experimental techniques discussed in this thesis require that the radial current density distributions in the probe, defined by $j_o(r)$ be known up to radii of at least 1nm. This section gives estimates of such distributions for conditions suitable for EDX microanalysis and high-angle ADFI following a wave-optical approach outlined by Mory et al. (1985) and Colliex and Mory (1983). The description of this method refers to figure 3.3 (a schematic diagram representing the formation of the wave function from a monochromatic point source) and table 3.1. The program that calculates $j_o(r)$ was written in QL Super-Basic for use on a Sinclair QL minicomputer and is entitled 'J_Dist_Overall'. A complete listing of the program is given in appendix A1. Calculations are performed in two stages:

1. Estimation of the radial current density distribution $j_{mono}(r)$ on the specimen from a monochromatic point source. The principal parameters used here are the illumination semi-angle α_o , the defocus length Δz and the spherical aberration coefficient of the objective lens C_s .

2. Calculation of $j_o(r)$ from a monochromatic extended source. This considers the effect of incoherent contributions due to the finite size of the reduced image of the virtual source.

As discussed earlier in this section, polychromatic effects in probe formation caused by a finite distribution of electron energies emitted from the source are very small for the gun used in the HB5 and can be disregarded.

Calculation of $j_{mono}(r)$ is based on an expression for the complex amplitude of the waveform in the objective exit pupil ($G(\underline{\alpha})$). Using the general diffraction theory developed in Born and Wolf (1959);

$$G(\underline{\alpha}) = A(\underline{\alpha})\exp(iW(\underline{\alpha})) \quad (3.4)$$

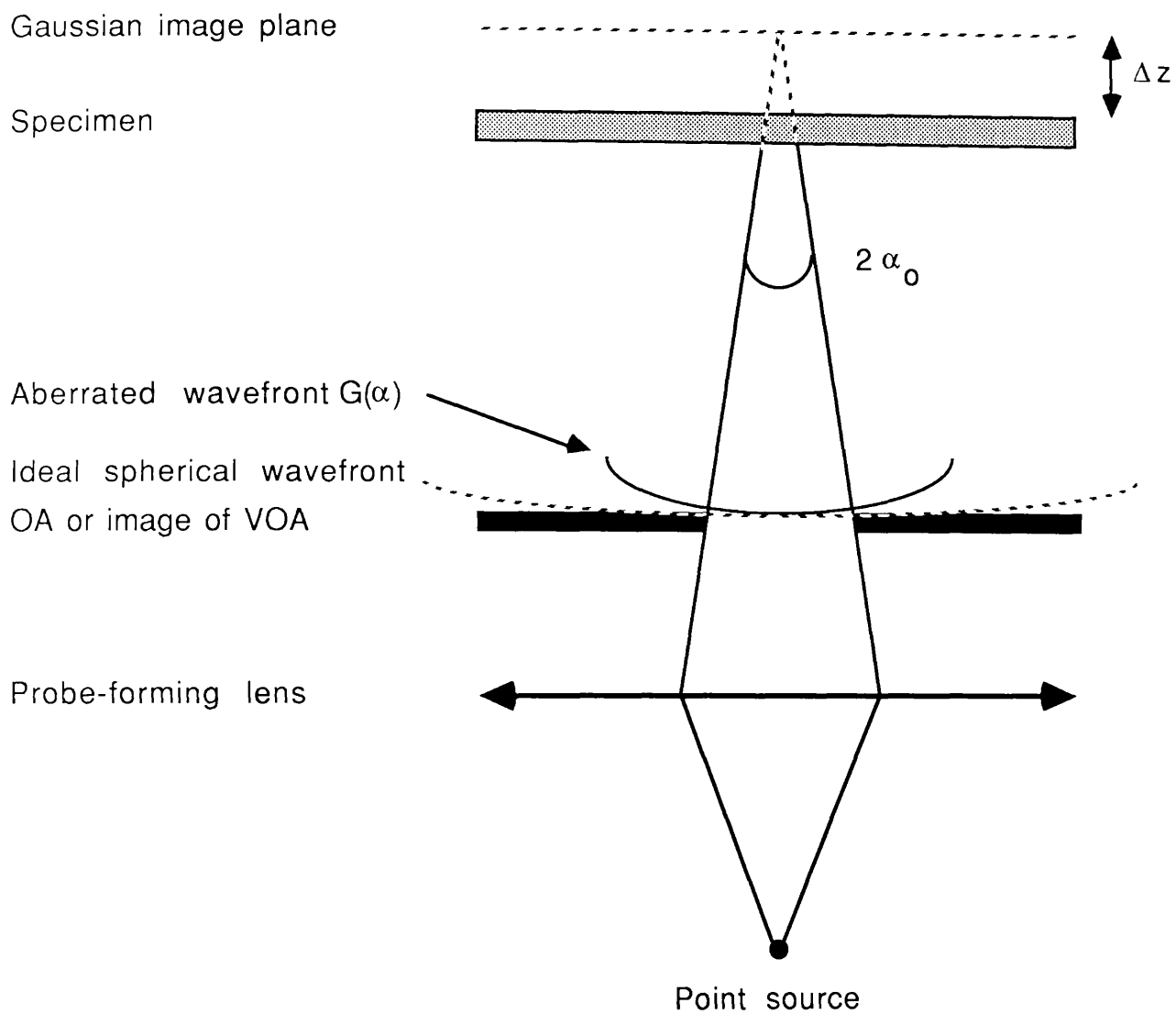


Figure 3.3: Schematic diagram showing the formation of the wavefunction from a monochromatic point source.

Description	Symbol	Value
Probe convergence semi-angle of 50 μm OA	α_o	9.2mrad
Probe convergence semi-angle of 100 μm VOA		11.0mrad
Wavelength of 100keV incident electrons	λ	$3.7 \times 10^{-12} \text{m}$
Characteristic radius of virtual source	r_o (source)	2.5nm
Magnification factor due to operation of C1	M_{C1}	1.45
Magnification factor due to operation of C2	M_{C2}	0.59
Magnification factor due to operation of objective lens (OL)	M_{Obj}	0.03
Characteristic radius of demagnified source using C1 and OL		0.12nm
Characteristic radius of demagnified source using C2 and OL	r_o (probe)	0.07nm
Spherical aberration coefficient of objective lens	C_s	3mm

Table 3.1: Numerical values relevant to electron probe current density calculations in the HB5 STEM

where $A(\underline{\alpha})$ is the pupil function for, in this case, the OA or the VOA and is defined as;

$$A(\underline{\alpha}) = \begin{cases} 1 & \text{if } \alpha < \alpha_0 \\ 0 & \text{if } \alpha \geq \alpha_0 \end{cases} \quad (3.5)$$

and, following Zeitler and Thomson (1970), $W(\underline{\alpha})$ is the phase shift where

$$W(\underline{\alpha}) = \frac{2\pi}{\lambda} \left(C_s \frac{\alpha^4}{4} + \Delta z \frac{\alpha^2}{2} \right) \quad (3.6)$$

λ is the wavelength of the incident electrons. Δz is positive for over-focus of the beam and negative for under-focus. The complex amplitude $\Psi(\underline{x})$ (where \underline{x} can be expressed in polar coordinates (r, ϕ)) falling on the specimen is given by the two-dimensional Fourier transform of $G(\underline{\alpha})$;

$$\psi(\underline{x}) = \int G(\underline{\alpha}) \exp[-(2\pi i/\lambda)(\underline{\alpha} \cdot \underline{x})] d\underline{\alpha} \quad (3.7)$$

Using equations 3.4 to 3.6, this becomes;

$$\psi(r) = \left(\frac{2\pi}{\lambda} \right) \sqrt{\frac{I_0}{\pi \alpha_0^2}} \int_0^{\alpha_0} \exp(iW(\alpha)) J_0(2\pi r \alpha / \lambda) \alpha d\alpha \quad (3.8)$$

I_0 is the primary beam current. $j_{\text{mono}}(r)$ can be easily deduced;

$$j_{\text{mono}}(r) = |\psi(r)|^2 \quad (3.9)$$

As $j_{\text{mono}}(r)$ depends on the defocus length, it is necessary to execute 'J_Dist_Overall' several times for different values of Δz to determine the optimum defocus condition. The radial range over which $j_{\text{mono}}(r)$ can be

estimated depends on the accuracy to which the Bessel function in equation 3.8 is calculated. Functions calculated up to the 50th order are sufficient to estimate $j_{\text{mono}}(r)$ up to radii of 1.2nm while limiting program run time to <15mins. The program does not calculate absolute values of current density but rather its relative distribution and so $j_{\text{mono}}(r)$ is represented in normalised form. Figures 3.4 and 3.5 show two such distributions at optimum defocus conditions for a 100 μm VOA and a 50 μm OA respectively. These distributions are very similar. The reasons for choosing one aperture in favour of the other are given in section 3.2.2.2.

Only coherent contributions to the probe current density distribution have, to this point in the calculations, been considered. The second stage considers the finite size of the electron source. This entails a two-dimensional convolution of the demagnified image of the virtual source with $j_{\text{mono}}(r)$. As mentioned earlier in this section, the size of the demagnified source projected onto the specimen is dependent on the pre-specimen lens configuration. The convolution can be expressed as;

$$j_o(\underline{x}) = j_{\text{mono}}(\underline{x}) * \beta(\underline{x}) \quad (3.10)$$

$\beta(\underline{x})$ is the gaussian shape of the demagnified source at the specimen with characteristic radius $r_o(\text{probe})$ calculated using equation 3.3. \underline{x} can be expressed in polar coordinates (r, ϕ) Expressed fully, equation 3.10 becomes;

$$j_o(\underline{x}) = \int_{r_1=0}^{r_1=\infty} \int_{\phi_1=0}^{\phi_1=2\pi} j_{\text{mono}}(\underline{x}-\underline{x}_1) \beta(\underline{x}_1) r_1 dr_1 d\phi_1 \quad (3.11)$$

$(\underline{x}-\underline{x}_1)=\underline{x}_2$ which can be expressed in polar coordinates (r_2, ϕ_2) . $j_o(\underline{x})$ is radially symmetric (i.e. $j_o(r, \phi)=j_o(r, 0)$ as shown in figure 3.6a), and so when $\phi=0$,

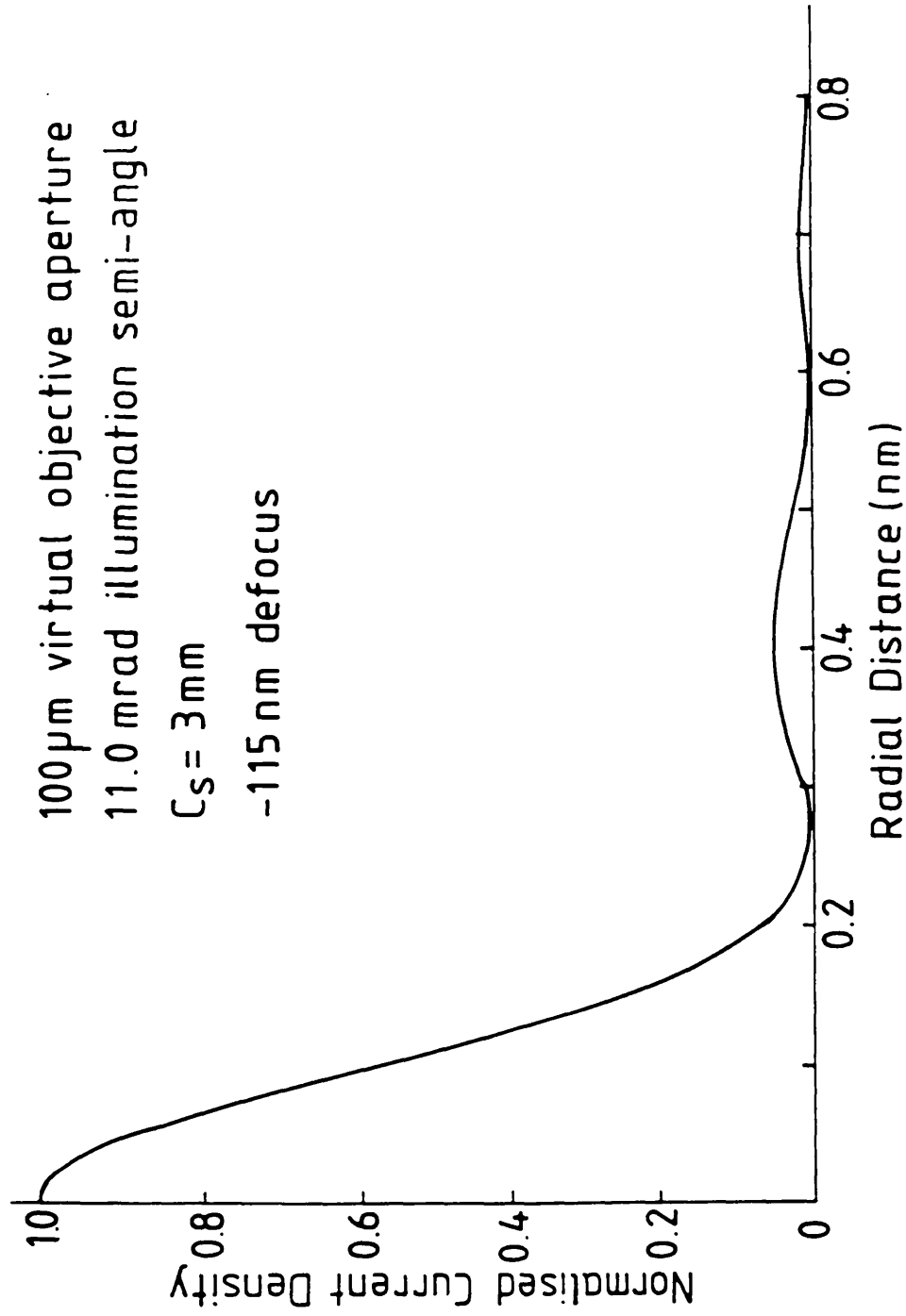


Figure 3.4: Radial current density distribution at the specimen from a monochromatic point source under conditions suitable for EDX microanalysis.

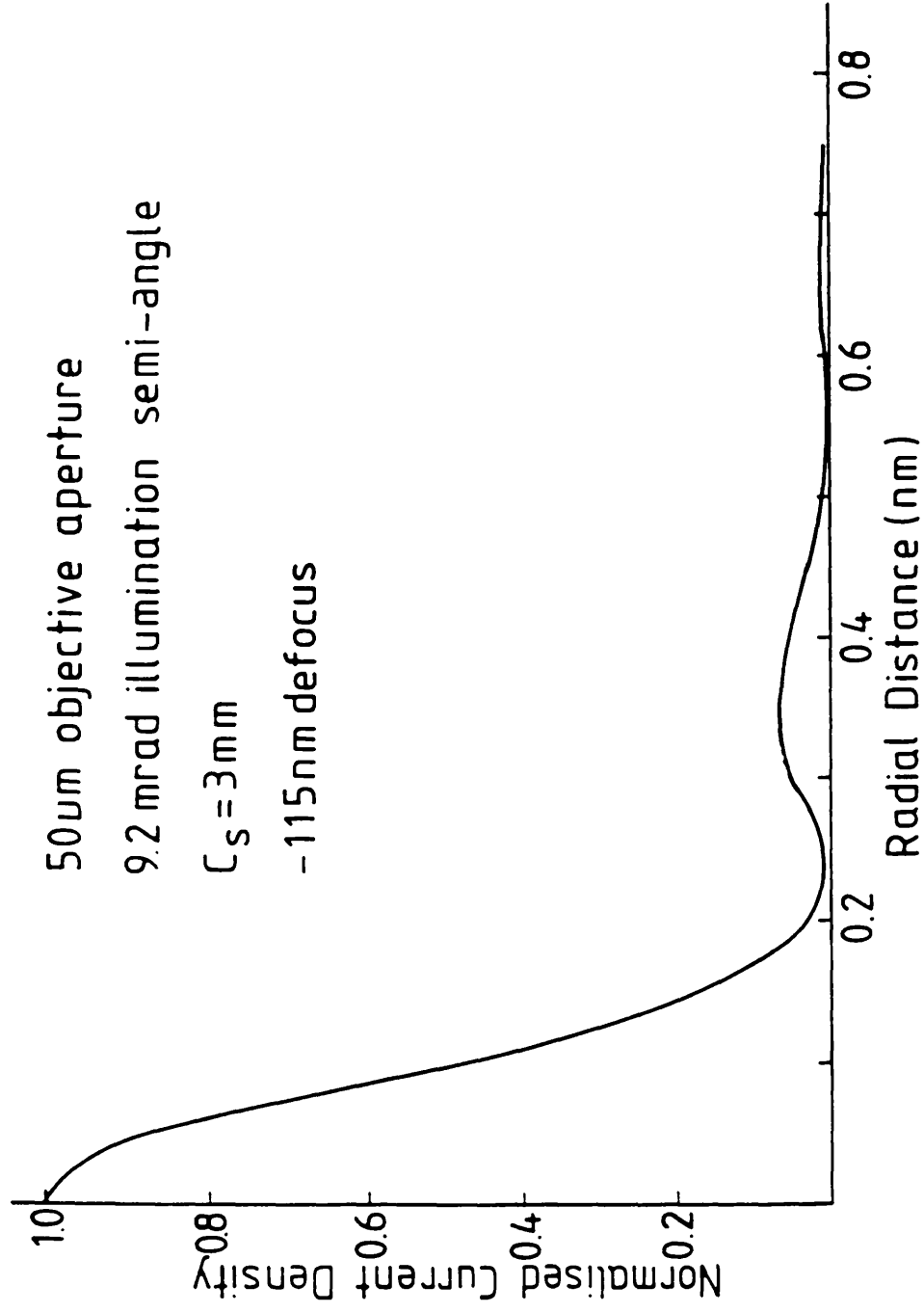


Figure 3.5: Radial current density distribution at the specimen from a monochromatic point source under conditions suitable for high-angle ADFI.

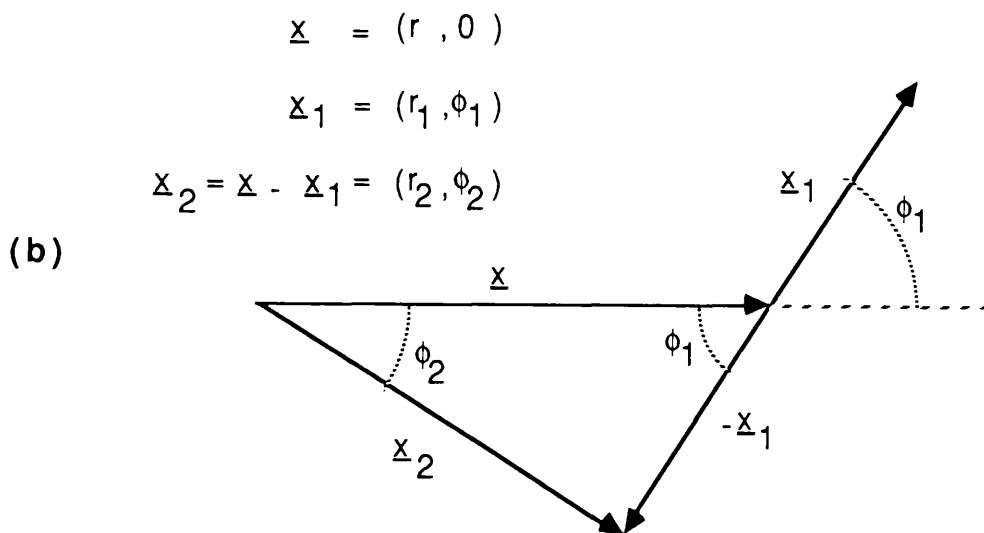
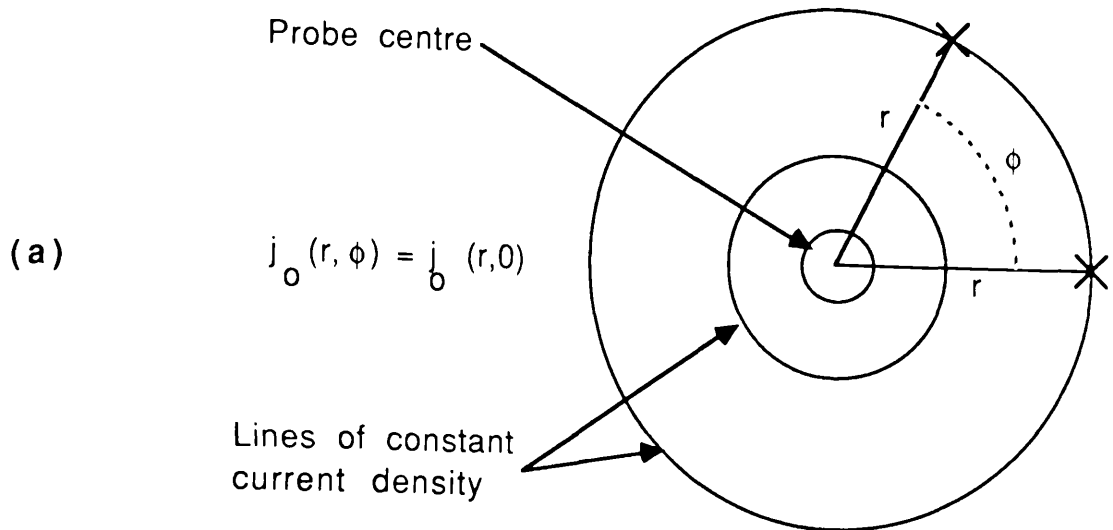


Figure 3.6: (a) Diagram illustrating the radial symmetry of $j_o(r)$
 (b) Vector diagram illustrating the formation of $\underline{x} - \underline{x}_1$
 in equation 3.13.

$$r_2^2 = r^2 + r_1^2 - 2rr_1 \cos(\phi_1) \quad (3.12)$$

(figure 3.6b). $j_{\text{mono}}(x_2)$ is also radially symmetric. Therefore, equation 3.11 reduces to;

$$j_0(r) = \int_{r_1=0}^{r_1=\infty} \int_{\phi_1=0}^{\phi_1=2\pi} j_{\text{mono}}(r_2) \beta(r_1) r_1 dr_1 d\phi_1 \quad (3.13)$$

The form of this equation, for computational purposes is;

$$j_0(r) = K \sum_{m=0}^{M, \Delta m} \sum_{n=0}^{2\pi, \Delta n} j_{\text{mono}}([r^2 + m^2 - 2rm \cos(n)]^{\frac{1}{2}}) \exp\left(\frac{-m^2}{2r_0^2}\right) m \Delta m \Delta n \quad (3.14)$$

where K is a constant, M is the highest value of r to which j_0 is calculated and Δm and Δn are the sampling intervals for radius and angle respectively.

Figures 3.7 and 3.8 both show normalised distributions of $j_0(r)$ calculated by 'J_Dist_Overall' following equation 3.14. The former represents $j_0(r)$ in conditions suitable for EDX microanalysis whereas the latter represents that suitable for high-angle ADFI. Both diagrams show that the effect of incoherent contributions on $j_{\text{mono}}(r)$ is to spread the current density distribution over a wider range of r, and to reduce the effect of high order maxima and minima originally present in $j_{\text{mono}}(r)$.

The work in this thesis is concerned with the variation of composition in a direction perpendicular to the layer interfaces. Assuming that there is little compositional variation in a direction parallel to the layers (y) over a distance equivalent to the probe diameter, the compositional variation is essentially a one dimensional problem. For this reason it is important to calculate the

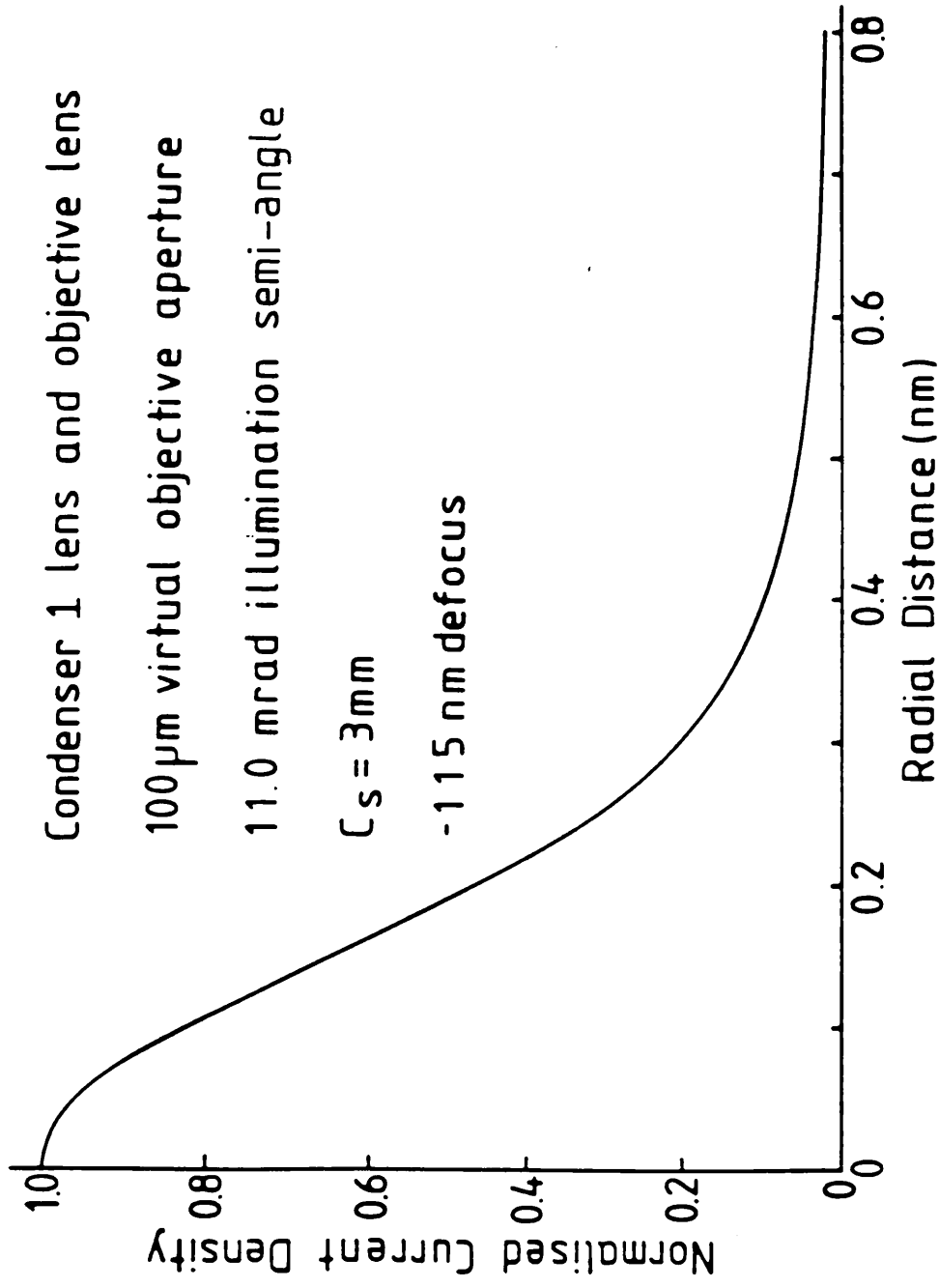


Figure 3.7: Radial current density distribution at the specimen from a monochromatic extended source under conditions suitable for EDX microanalysis.

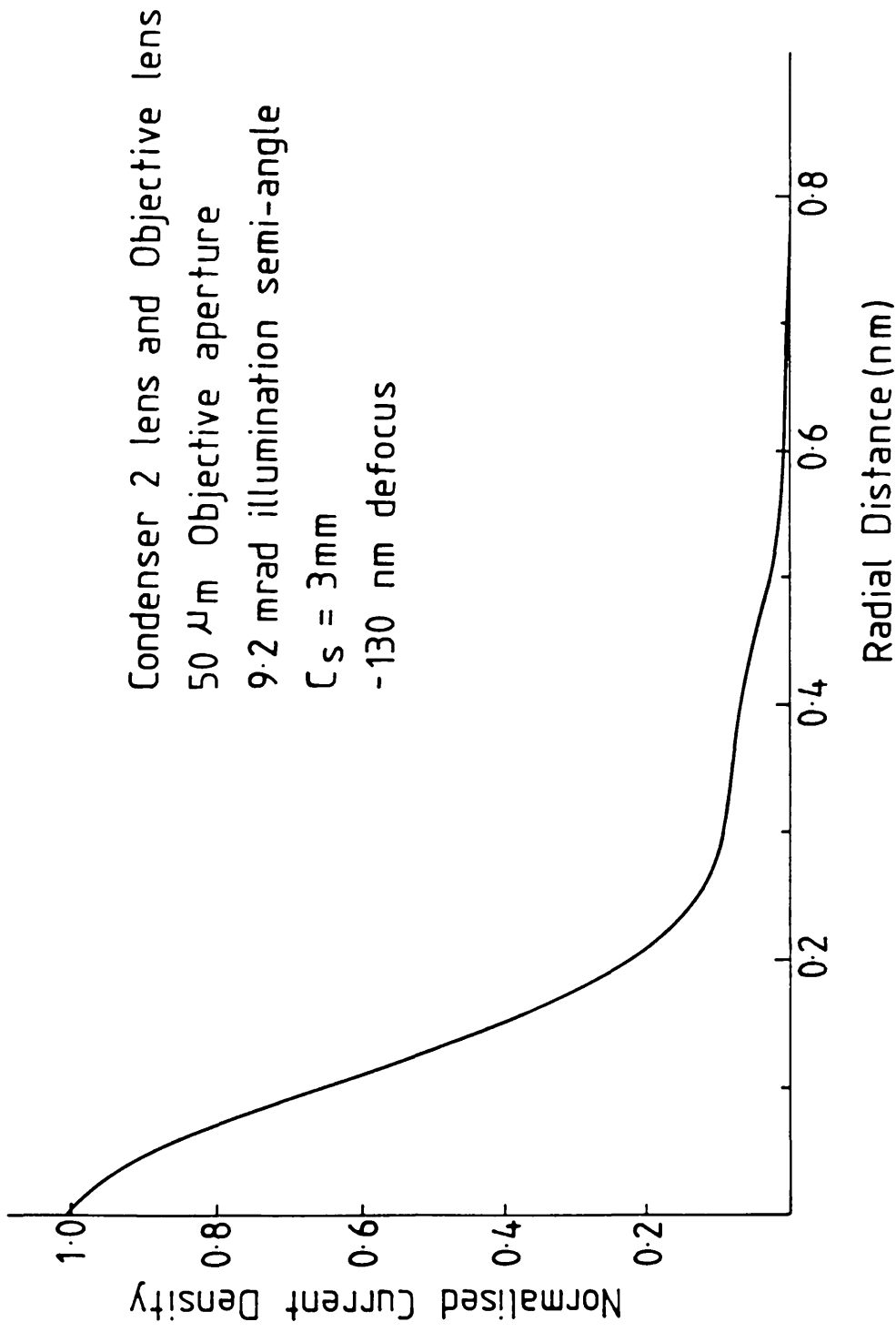


Figure 3.8: Radial current density distribution at the specimen from a monochromatic extended source under conditions suitable for high-angle ADFI.

variation of linear current density $J(x)$ obtained by integrating $j_o(r)$ over y . A schematic diagram illustrating this concept is shown in figure 3.9. The program written to calculate $J(x)$ from $J_o(r)$ is entitled 'J_Dist_Convert' and is listed in appendix A1. Figures 3.10 and 3.11 show the variation of $J(x)$ as a function of distance from the probe centre under the conditions suitable for EDX microanalysis and high-angle ADFI respectively. Comparisons between the fraction of the total current contained within radius R , expressed as;

$$\frac{1}{I_o} \int_0^R j_o(r) 2\pi r dr \quad (3.15)$$

and the fraction of the total current contained between $+X$ and $-X$ of the probe centre, expressed as;

$$\frac{1}{I_o} \int_{-X}^X J(x) dx \quad (3.16)$$

are given in figures 3.12 and 3.13 for EDX microanalysis and high-angle ADFI conditions respectively. These figures highlight the advantages of treating compositional changes as a one dimensional problem and can be used to estimate the percentage of the total probe current contained within a given area. For example, in conditions suitable for EDX microanalysis, 50% and 90% of the total probe current are contained within 0.20 and 0.80nm of the probe centre respectively. For high-angle ADFI, the values are 0.13 and 0.45nm respectively. This information, together with the probe distributions given in figures 3.10 and 3.11 will be used in future chapters in connection with the interpretation of results.

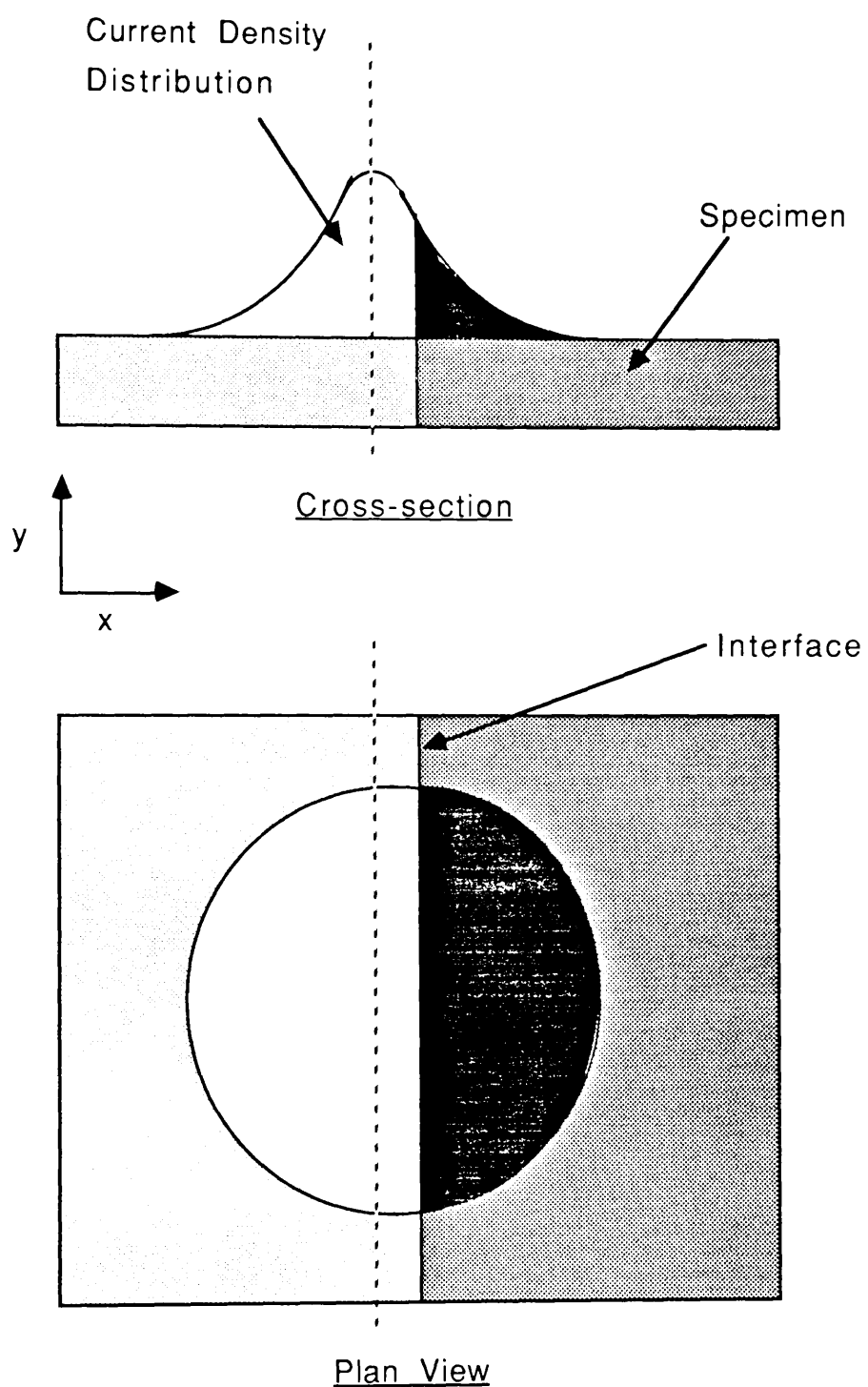


Figure 3.9: Schematic diagram showing the probe area overlapping a boundary.

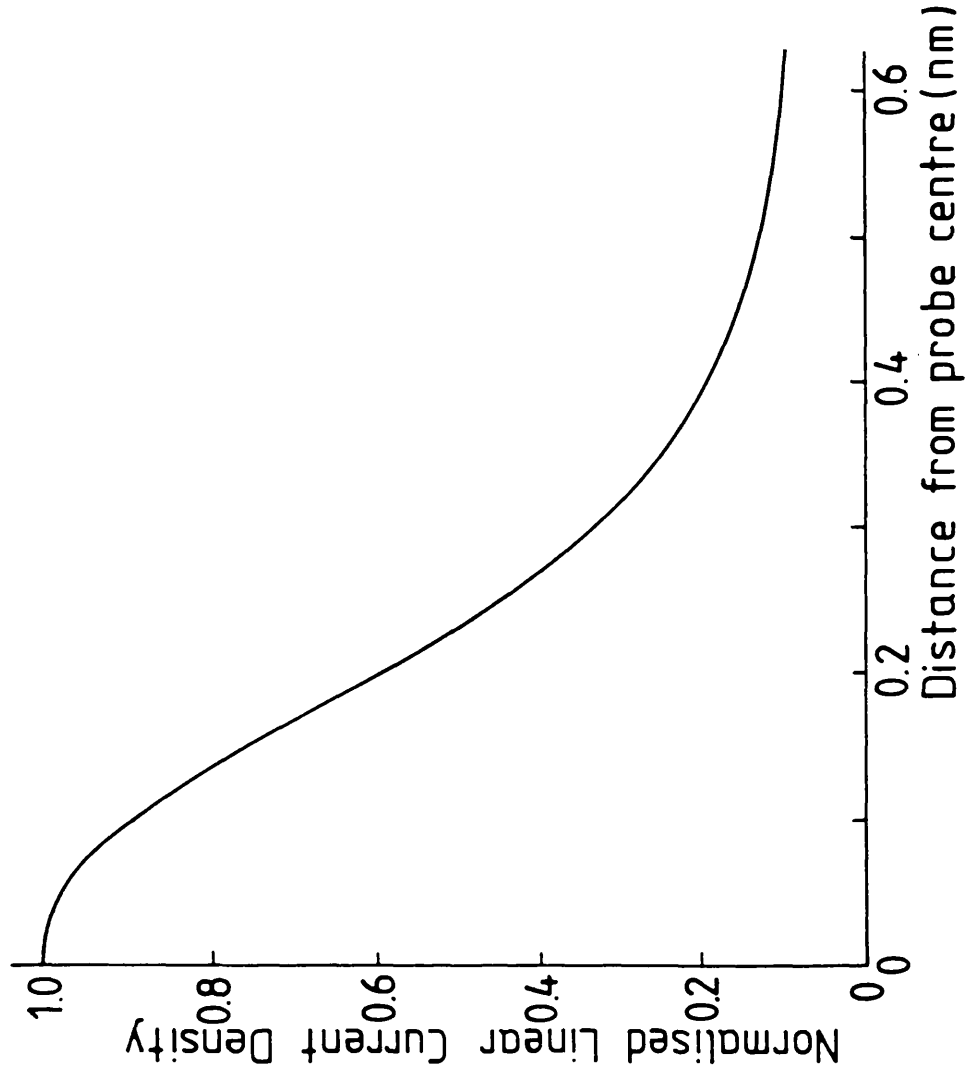


Figure 3.10 Linear current density distribution at the specimen from a monochromatic extended source under conditions suitable for EDX microanalysis.

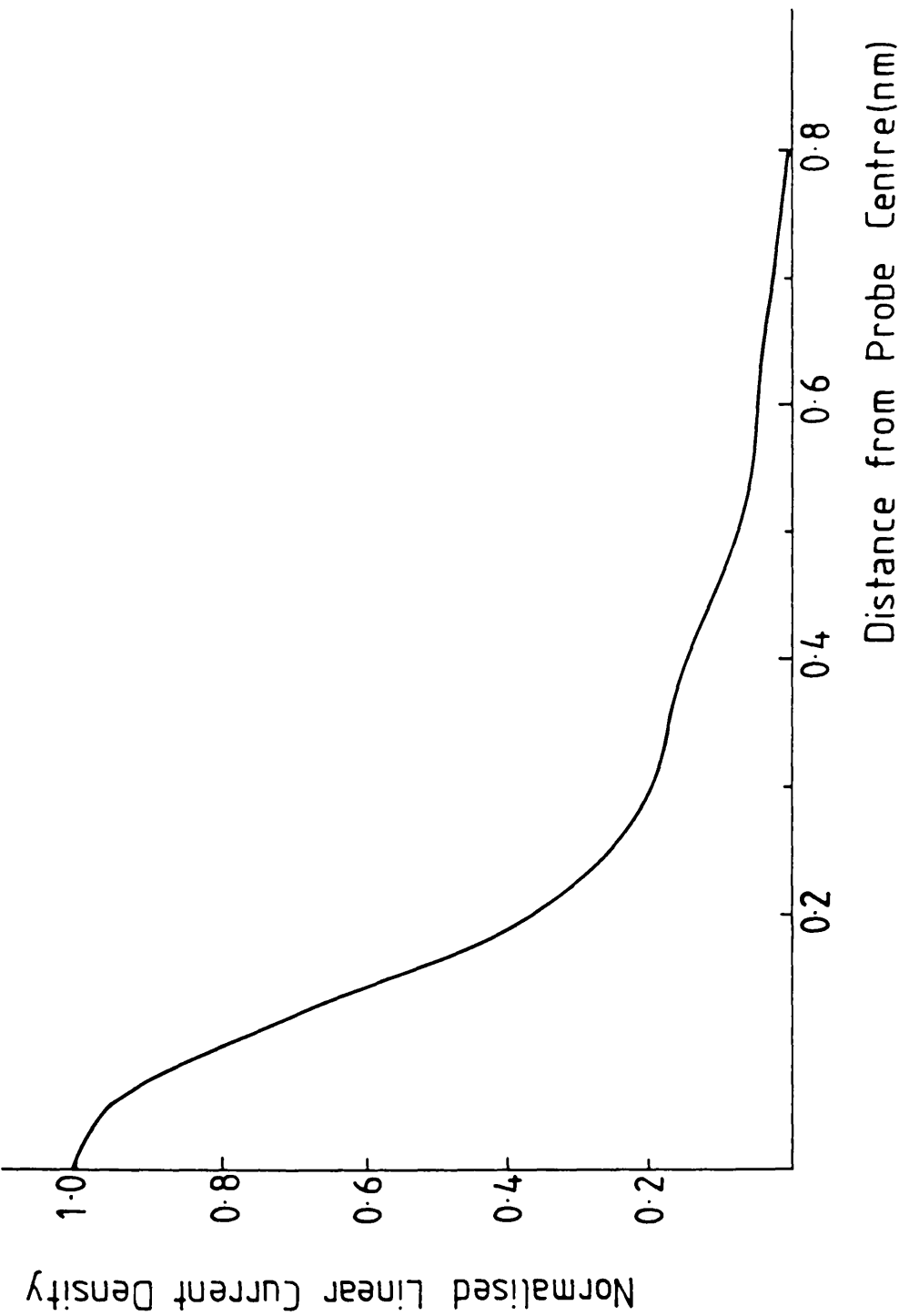


Figure 3.11: Linear current density distribution at the specimen from a monochromatic extended source under conditions suitable for high-angle ADFI.

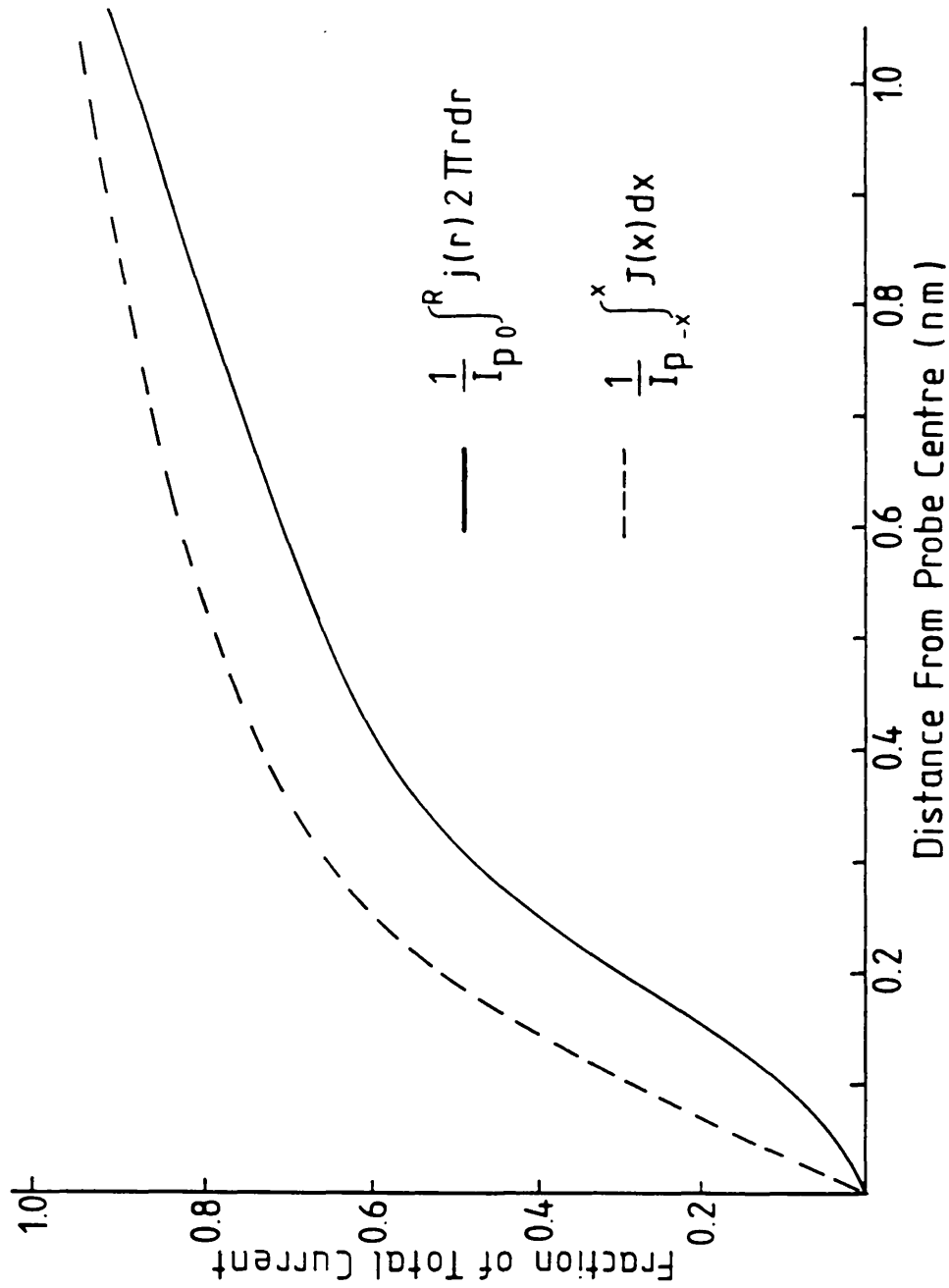


Figure 3.12: Fraction of total probe current contained within distances up to 1nm for radial current density $j_0(r)$ (unbroken line) and linear current density $J(x)$ (broken line) under conditions suitable for EDX microanalysis.

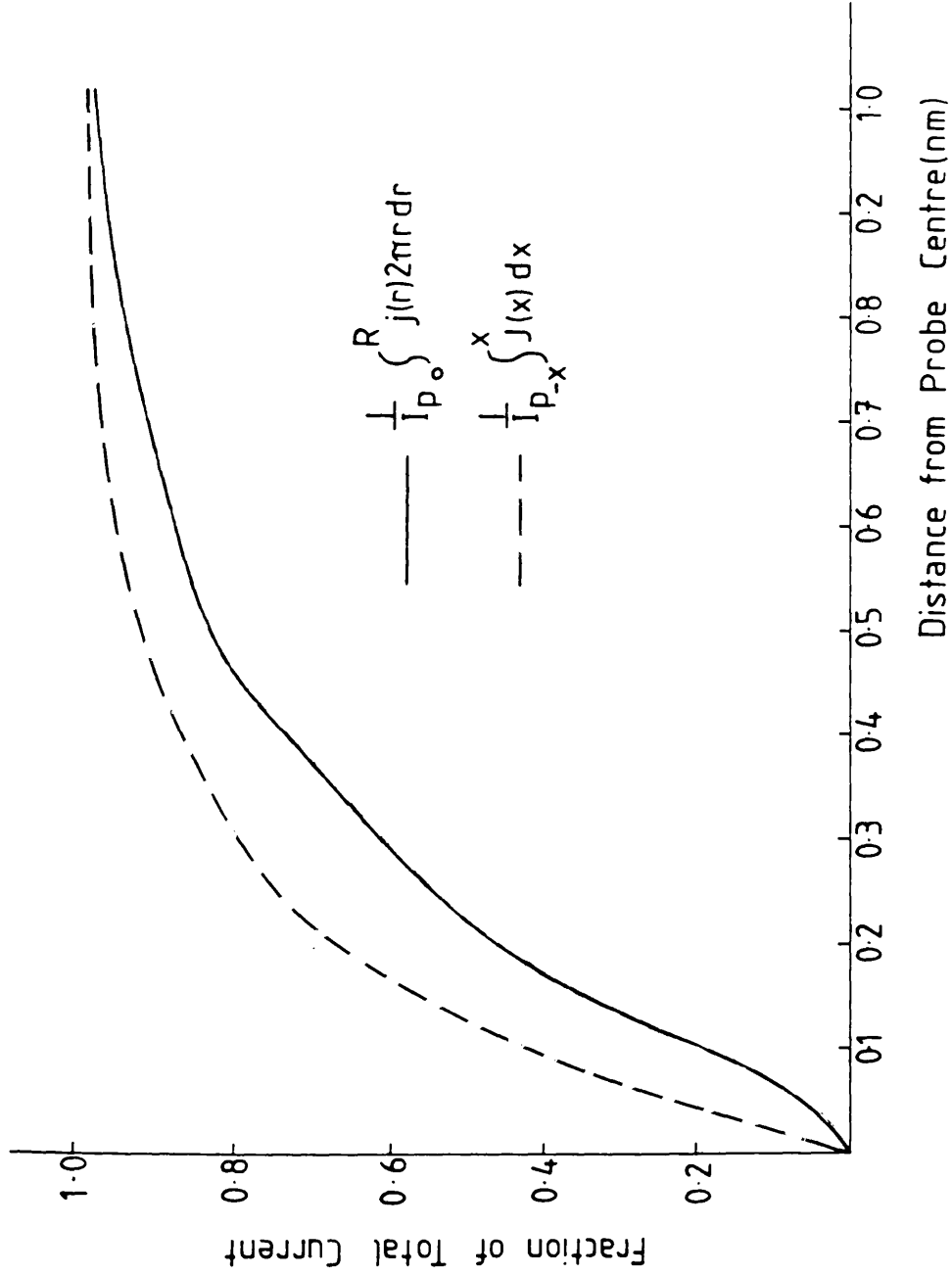


Figure 3.13: Fraction of total probe current contained within distances up to 1 nm for radial current density $j_o(r)$ (unbroken line) and linear current density $J(x)$ (broken line) under conditions suitable for high-angle ADFI.

3.2.3 The Specimen Cartridge

All experiments performed on the HB5 that are described in this thesis were carried out with the specimen held in a $\pm 30^\circ$ double-tilt cartridge with a Be nose-piece manufactured by VG microscopes. The design of the cartridge is such that specimen discs must not possess outer diameters greater than 3mm. The specimen is held in place by means of a small Be circlip and, to ensure a secure fit, the specimen should be no thicker than 150 μ m at any point.

The cartridge is inserted into the microscope via a top-entry loading mechanism, and can be lowered and raised vertically in the objective lens field by the z-lift facility mentioned in section 3.2.2.1. As the cartridge name implies, the specimen can be tilted about both the X and Y axes. This feature enables semiconductor multilayers to be oriented so that the incident beam direction is parallel to the plane of the layers and that the specimen is tilted towards the x-ray detector.

It is necessary for the specimen to attain thermal equilibrium with the interior of the microscope so that specimen drift during the data acquisition period is negligible. Consequently, for all experiments described in this thesis, the cartridge was inserted into the microscope the day before data acquisition.

3.2.4 Post-specimen Lenses

A feature of the modified HB5 STEM is that it is equipped with a series of post-specimen lenses - PSL1, PSL2 and PSL3. This configuration allows the angular distribution of the electrons transmitted through the specimen to be matched to the size and shape of the electron detectors by the choice of a suitable camera length. The lens currents can be controlled manually or by means of a microprocessor unit. Under standard imaging conditions, PSL3 only

3.1 mrad is the collection semi-angle for this configuration.

is used. But for high-angle ADFI, when a low camera length is required to compress the angular distribution of transmitted signal, PSL1 is employed.

3.2.5 Electron Detectors

3.2.5.1 The Bright Field Detector

The bright field detector on the HB5 is a photoelectric detector. Such detectors consist of a scintillator coupled via a light pipe to a photomultiplier tube. The scintillator is positioned so that it collects electrons that have passed through an electron spectrometer. At the spectrometer entrance, a collector aperture (CA) limits the angular range over which the electrons are accepted. In standard bright field image mode, the 500 μ m collector aperture (which, using PSL3, corresponds to a collection angle of 3.1mrad) is used. In the experiments described in this thesis, the detector is used to observe both bright field and (002) dark field images of the multilayer structures. By using two separate grigson coil settings, it is possible to alternate between the two imaging modes. Although not employed here, the spectrometer and bright field detector arrangement can also be used for electron energy loss spectroscopy (EELS); e.g. Craven and Buggy (1984).

3.2.5.2 The Annular Dark Field Detector

The detector used in this project for high-angle ADFI is the annular dark field (ADF) detector. It is a photoelectric detector and is in the form of an annulus designed to detect electrons that are scattered through high angles after interaction with the specimen. Electrons located near the centre of the incident beam pass through the hole in the centre of the annulus to be received by the bright field detector. Although the detector appears annular to incident electrons

in the column, the aluminium coated scintillator screen is in reality an ellipse tilted at an angle of 45° to the incident beam direction, and an aluminium coated glass tube perpendicular to the column reflects the light from the scintillator through a vacuum window onto the photocathode. This complex detector geometry is necessary to produce efficient light coupling to the photocathode which, because of space limitations in the microscope is at 90° to the incident beam direction. The effective inner and outer diameters of the detector are 3.3 and 25mm respectively. The angular range of acceptance of transmitted electrons that these values correspond to depends on the excitation of the post-specimen lenses. As stated in chapter 2, the inner and outer acceptance angles for high-angle ADFI used here are 85 and 200mrad respectively. A detailed description of the technique used to determine these values is given in chapter 4.

3.2.5.3 The Diffraction Screen

The diffraction pattern is observed at a plane below that of the ADF detector. At this position, a retractable fluorescent screen known as the diffraction screen can be inserted. In a similar manner to the ADF detector, the screen has an opening in the centre to allow electrons in the centre of the beam to be transmitted to the bright field detector. The inner and outer diameters of the diffraction screen are 2 and 20mm respectively. The diffraction pattern is normally observed using a low-light level TV camera, and analogue and digital images can be acquired by means of a 35mm camera mounted on the microscope column and a Crystal digital acquisition system respectively. In experiments discussed in this thesis, the diffraction pattern formed on the screen is used to determine specimen orientation and the angular range subtended by the ADF detector.

3.2.6 X-ray Detectors

All EDX microanalysis on the HB5 is carried out using Link Analytical Si(Li) x-ray detectors. These consist of a cooled piece of lithium drifted Si crystal between two thin gold electrodes. A bias of ~500V is placed across the two contacts. X-ray photons entering the crystal ionise the Si atoms, causing the emission of photoelectrons. These then lose energy in the crystal, causing a cascade of electron-hole pairs. The number of such pairs produced are proportional to the initial energy of the photoelectron. The applied bias separates the electrons and holes, and a current pulse proportional to the photon energy is detected at the Au contacts. The pulse is amplified and its height measured. The channel of a multi-channel analyser which represents the corresponding photon energy is then incremented.

Two types of Si(Li) x-ray detector were used in this project; conventional and windowless. The former has a beryllium window of thickness $\sim 8\mu\text{m}$ separating the crystal from the column vacuum. Absorption of photons in this window, however, has the adverse effect of reducing the ability of the crystal to detect photons with an energy below $\sim 3\text{keV}$. For the materials of interest here, this must be taken into consideration when examining the detected signals from the P K transition (2.015keV) and the Al K transition (1.487keV). The windowless detector does not possess such a window (e.g. Goodhew, 1985a), but low energy detection efficiency is still limited by absorption of the photons in the thin Au contact on the entrance surface of the crystal and in the inefficient or 'dead' layer of the Si crystal. As chapter 5 shows, absorption corrections for the windowless detector can be expressed in terms of absorption in an effective Au layer thickness of typically 20nm. The EDX detector is positioned slightly below the specimen plane in the column. The number of photons detected by both

types of detector depends on the solid angle that they subtend at the specimen, and the angle with which they are mounted relative to the horizontal specimen plane. The conventional detector subtends a solid angle of 0.04sr at the specimen and faces it at an angle of 10.5° with respect to the horizontal plane, whereas the values are 0.16sr and 25° for the windowless detector. Consequently, this detector yields a higher count rate than that produced from the conventional type. The multichannel analyser, of a type common to both detectors, has a range of 1024 channels and channel widths can be either 20 or 40eV. All data discussed in this thesis uses the former value thus enabling detection of x-rays up to an energy of 20 keV.

3.3 The Link Analytical AN10000

Initial processing and analysis of experimental data is carried out using a Link Analytical AN10000 system. The system possesses software that can analyse digital images acquired from the electron detectors on the HB5 by a Crystal digital acquisition system. X-ray spectra are acquired using a Si(Li) detector and analysed on the system using the AN10 X-ray Analyser software package. The system is also equipped with the standard peripherals of a VDU, a printer, 1 hard disc that is sub-divided into two directories (DDR and MDR) and floppy disc and tape drives. Fortran programs can be written to supplement existing software and create new analysis routines to suit specific requirements.

The AN10 X-ray Analyser controls acquisition of x-ray spectra from the Si(Li) detector, and stores the result on DDR. Groups of related spectra taken, for example, from different positions across an interface can be stored under the same source filename, helping to simplify the analysis process. The analyser enables up to four spectra to be displayed on the VDU at any one time and also possesses standard processing facilities such as window designation and labelling. Each spectrum is stored as 5 blocks (numbered 0 to 4) of data with

256 words in each block. Block 0 is known as the header block, and contains information about the spectrum such as channel width, count rates, counting time etc.. The remaining blocks store the integer values of the counts recorded in each of the 1024 windows of the multi-channel analyser.

Acquisition of digital images is carried out through the Crystal system using the "Electron Signal Processing" program (ESP). This program enables signals from a detector to be taken from an area of specimen by digitally controlling the position of the electron beam. This enables the acquisition of digital images from both the bright field and ADF detectors. The system can also be linked to the TV camera that monitors the diffraction screen, allowing digital acquisition and processing of diffraction patterns. Images are acquired in arrays of $2^m \times 2^n$ pixels where m and n are integers between 0 and 9. The area of specimen that each pixel represents depends on both the pixel resolution and the magnification of the image. The signal at each pixel can be measured with a precision of either 8 or 16 bits. The recommended dwell time of the beam at each pixel position for the former value is $51\mu\text{s}$ as opposed to $819\mu\text{s}$ for the latter. The higher precision yields more detailed intensity distributions but at the expense of image acquisition time. ESP also possesses the facility to integrate each image over several frames as an aid to increasing statistical accuracy.

All images are stored in a 'buffer' which can be accessed by the image processing program DIGIPAD which is compatible with ESP. Once an image is acquired by ESP, initial processing steps such as contrast enhancement and simple intensity transforms can be implemented in DIGIPAD. In a similar manner to x-ray spectra, groups of images can be stored under a common source filename.

A feature of the AN10000 system of particular relevance to high-angle ADFI is that single lines of pixels from images can be isolated and treated separately by the analysis programs. Furthermore, the memory format of these

profiles is similar to that of x-ray spectra making them available for analysis by techniques included in the x-ray analyser. A description of new analysis programs that have been written for the system that take advantage of these features is given in chapter 4.

3.4 Specimen Preparation

Microanalysis across layer interfaces in compound semiconductor multilayers in the HB5 is only possible if the prepared specimen satisfies the following criteria;

1. As figure 1 indicates, the specimen must be a cross-section; i.e. positioned so that the incident beam direction is parallel to the plane of the layers.
2. The region of interest in the specimen must be transparent to 100keV electrons and located towards the centre of the disc.
3. The specimen must be strong enough to withstand loading and unloading from the specimen cartridge.
4. The outer dimensions of the specimen must conform to the spatial limitations of the cartridge.

A variety of methods can be used to make cross-sectional specimens suitable for both TEM and STEM, some of which are discussed by Goodhew (1985b) and Newcomb et al. (1988). That used in this project, however, was specifically designed to form cross-sections of semiconductor materials. The technique, outlined by Chew and Cullis (1985, 1987) involves ion milling of the material as the final stage of preparation (see also Cullis and Chew, 1986 and Cullis et. al., 1985). It can be described in two stages, namely preparation of the

sample for the milling process, and the milling stage itself. Although the emphasis here is on the preparation of cross-sectional specimens of InGaAs/InP and AlGaAs/GaAs multilayers, the technique can be adapted to make plan-view specimens or prepare cross-sections of materials other than semiconductors.

3.4.1 Pre-milling Preparation

Semiconductor multilayer systems formed by MBE or MOCVD are grown on a wafer of substrate that is usually 2, 3 or 4 inches in diameter. All materials examined here were grown on the (001) face of the substrate, with each wafer possessing a "flat" parallel to the (110) plane. In the first stage of specimen preparation (represented in figure 3.14), small rectangular sections (approximately 10mmx1mm) are cleaved from the wafer using a diamond-tipped scribe. The cuts are made along the crystal planes perpendicular and parallel to the flat, thereby minimising damage to the wafer and avoiding unnecessary loss of material. Areas at the edge of the wafer should be avoided because wafer quality may decrease in this region. The aim of this preparation technique is to enable "edge-on" viewing of these sections and so two such sections are bonded together with the epilayers face to face. This serves to mutually protect each epilayer during the milling process and allows two different material configurations to be examined in one experimental session. The two sections are supported by two small blocks (approximately 10mmx3mmx1mm) of Si to enable easy handling of the materials and to provide sample rigidity for later preparation stages (figure 3.15a). All four pieces are bonded together using 'Devcon 5-minute epoxy' resin. To avoid specimen fracture, the interfaces between each section must be clear of debris and so all sections are cleaned in an ultrasonic bath of acetone for several minutes before the bonding stage. During the bonding process, excess epoxy is removed from

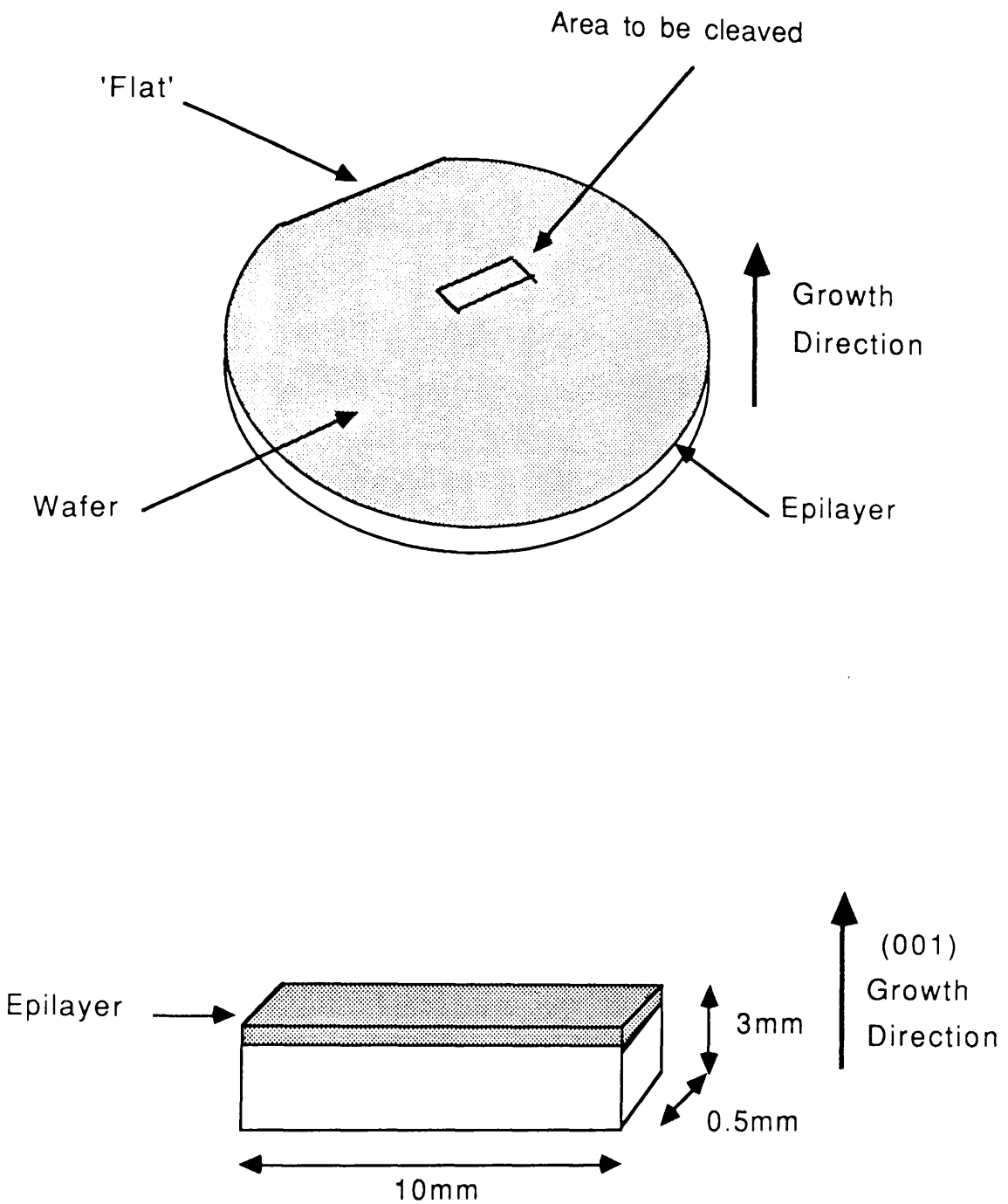


Figure 3.14: Schematic diagram showing a section of wafer suitable for cross-sectional specimen preparation.

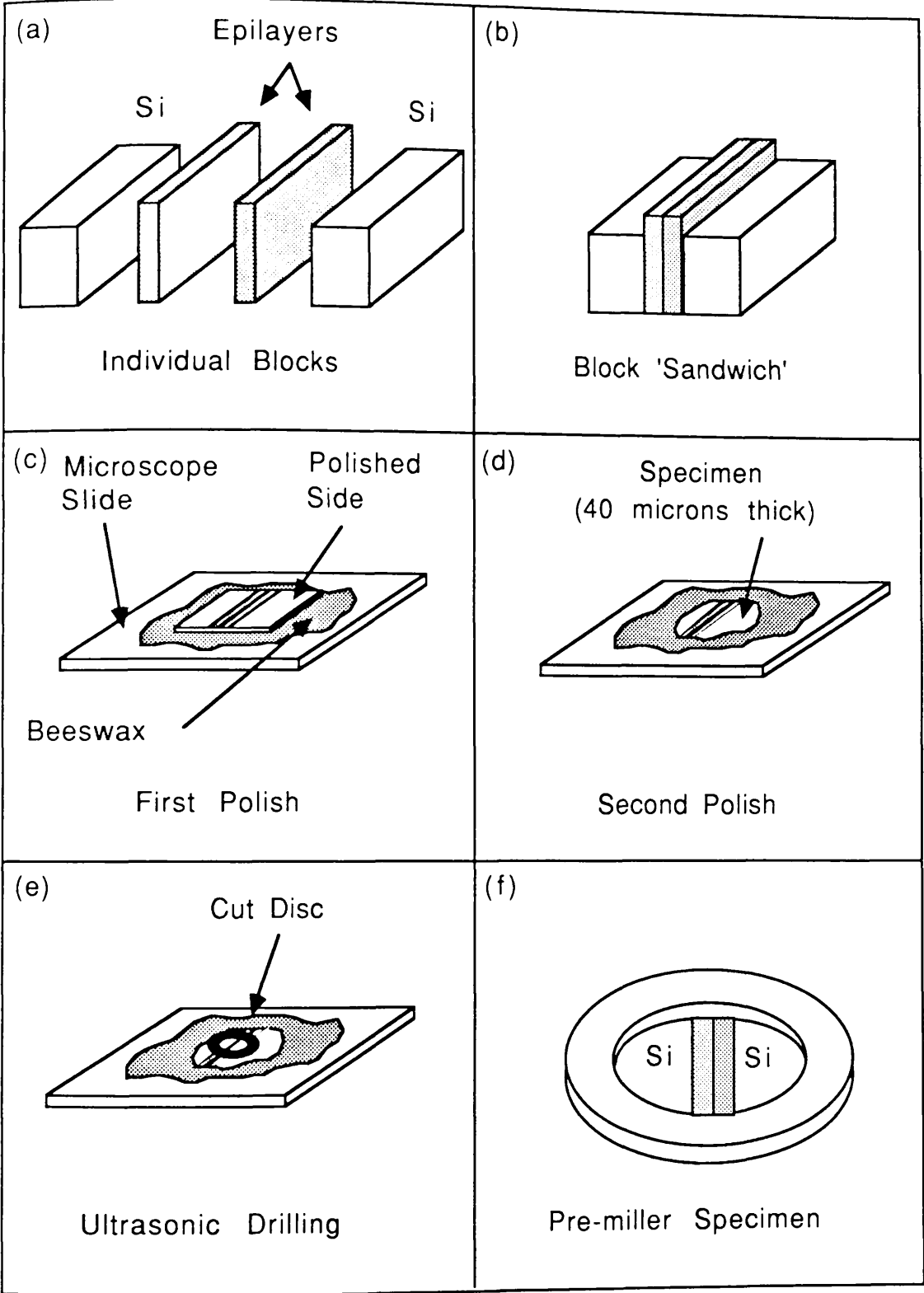


Figure 3.15: Schematic diagram showing six stages of specimen preparation.

the interfaces by gently rubbing the blocks across each other in a lateral direction thereby forcing the epoxy to the edges. A diagram of the final 'sandwich' of blocks is shown in figure 3.15(b). This is held in place by the parallel edges of a standard toolmaker's clamp for ~2hrs so enabling the epoxy to harden.

In the next stage of preparation, the sandwich is held on a section of microscope slide by beeswax, and the exposed side polished to a smooth surface in a hand grinder using 600 grit silicon carbide paper and running water. It is of importance that this side is uniformly flat - this can be verified using a micrometer with an accuracy of $\pm 5\mu\text{m}$. The flattened side is then fine-polished mechanically using $3\mu\text{m}$ water-based diamond paste (figure 3.15c). The partially prepared specimen is then melted off the slide, turned over, and re-attached to a clean slide using new wax. The polishing process is repeated on the second side, thinning the specimen down to between 40 to $50\mu\text{m}$. At this thickness, the block will no longer be rectangular in shape (figure 3.15d). An ultrasonic drill equipped with a drilling tool possessing inner and outer diameters of 2.5 and 3.5mm respectively is employed to cut discs from the sample using 600 grit silicon carbide water-based paste. The interface between the two epilayers must form a line across the diameter of the disc (figure 3.15e). At this stage, the sample is too delicate for manual handling, and does not conform to the requirements of the specimen holder. Consequently, copper washers with inner and outer diameters of 2 and 3mm respectively are hand-thinned to $\sim 70\mu\text{m}$ and subsequently glued on top of the discs using the epoxy resin.

The specimen at this juncture is still attached to the microscope slide, and may possess surface debris that could adversely affect specimen quality during the ion milling process. Therefore, the disc is removed from the slide and cleaned several times in warm organic solvents, namely three times in beakers

of trichloroethylene followed by one in absolute alcohol. The specimen must be dried immediately after this stage on filter paper or velin tissue to avoid the deposition of sediment that again may adversely affect the quality of the finished specimen. A diagram of the specimen fully prepared for ion milling is shown in figure 3.15(f).

3.4.2 Ion Milling

During the final stage of specimen preparation, the specimen is thinned down to 100keV electron transparency by ion milling. Specimens are placed in a sample holder which in turn is placed in a vacuum chamber held at a base pressure of $\sim 10^{-6}$ torr by means of a diffusion pump backed by a rotary pump. The holder is rotated at ~ 1 rev/min about a vertical axis and two beams of ions impinge on opposing faces of the specimen (figure 3.16). Material is removed from the specimen by the beams until a hole is formed in the centre, with the thinnest regions surrounding the hole. The angle of incidence of the beams can be varied and the value chosen depends on the specimen geometry required and the degree to which the specimen is susceptible to ion damage. The beams of ions are formed by pumping small amounts of gas through needle valves into the ion sources which, due to the shape of the anode, form a saddle field when a potential difference of between 4 and 10kV is applied between the anode and the outer casing of the source which acts as the cathode. At either end of the source is a small hole ~ 1 mm in diameter which limits the size of the ion beam. The source configuration is such that an ion beam leaving the back of the source is identical to that impinging on the specimen. An electrically isolated metal plate placed in the path of the rear beam monitors the ion current at the specimen.

The materials discussed in this thesis are milled by beams of Ar^+ and I^+

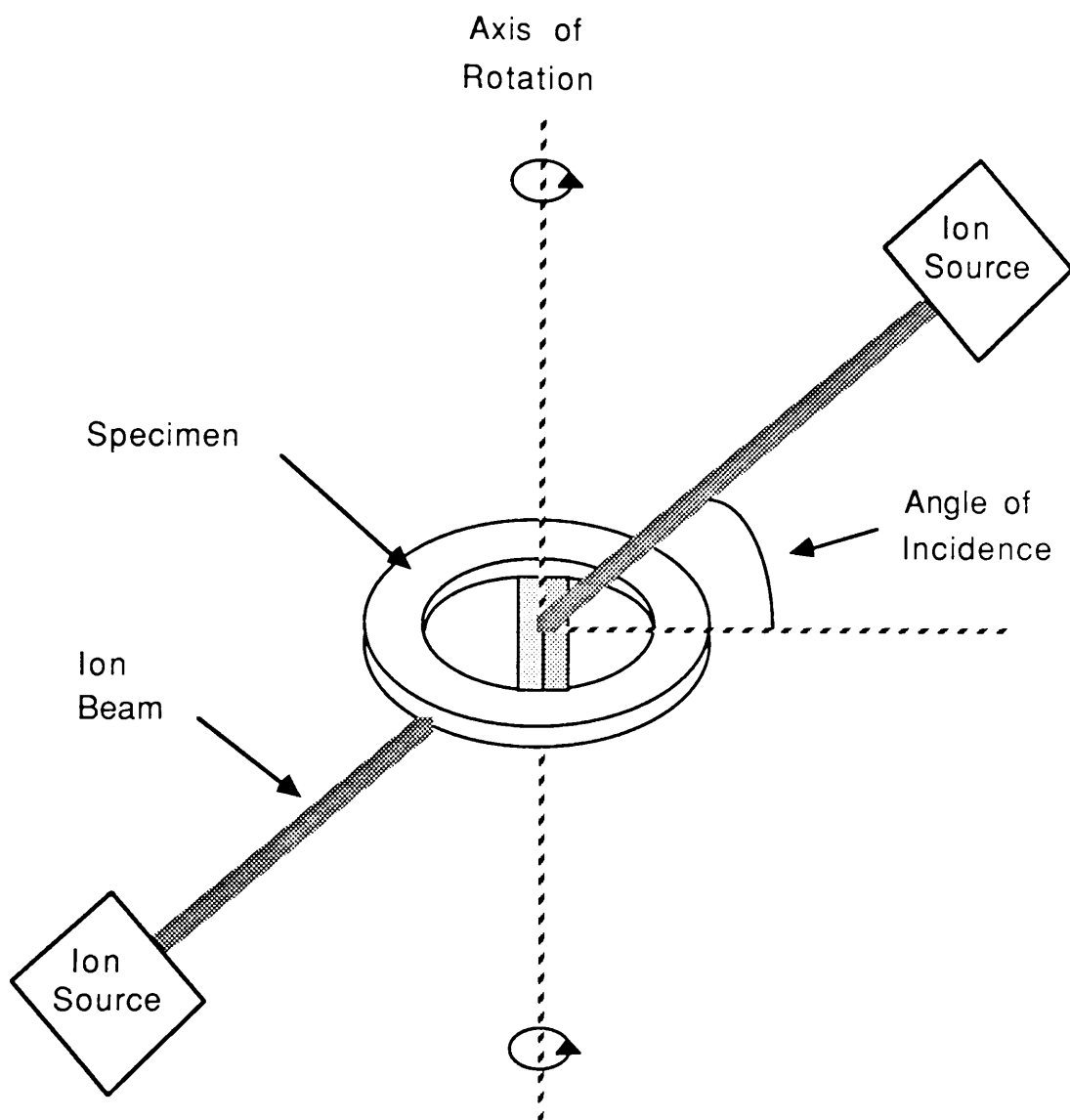


Figure 3.16: Schematic diagram showing the ion beam thinning configuration for a cross-sectional specimen

ions. The former is used to prepare specimens of AlGaAs/GaAs multilayers by feeding Ar gas into the system from a compressed gas cylinder. Ar⁺ ions, however, are unsuitable for the preparation of InGaAs/InP multilayers for two reasons; Firstly, elemental disproportionation in InP causes the formation of metallic In droplets on the specimen surface. Secondly, an artifact of the thinning process is that it forms an amorphous layer on the specimen surface. If the material is thinned using the heavier ionic species, I⁺, the first named effect is not observed and the second, although not completely removed, is considerably reduced. I vapour was supplied to the sources through a glass/PTFE tap from an ampoule containing I crystals. This was originally developed by Chew and Cullis (1984). A block diagram of a milling system common to that used at both Glasgow and RSRE is shown in figure 3.17.

Beam-induced structure in the specimen can also be limited if both the beam angle of incidence is kept to a minimum (ideally <12°), and the specimen is cooled during the milling process. The former precaution is possible if the specimen is held between two, thin, flat Ta discs, enabling incidence angles of ~10°. The specimen is cooled by pumping liquid N₂ through a tube in a small block that is in contact with the specimen holder.

Both AlGaAs/GaAs and InGaAs/InP multilayer specimens were milled using 6keV ions at beam currents of ~20μA per gun during normal operation. For AlGaAs/GaAs (using Ar⁺ ions), this corresponds to a milling rate of ~10μm per hour as opposed to ~20μm per hour for InGaAs/InP using I⁺ ions. Final milling for both materials was carried out at reduced beam energies of ~3keV and reduced currents of ~10μA per gun. This was done to minimise the effects of damage on the finished specimen surface.

A disadvantage of cross-sectional specimens is that the area of interest for microanalysis is very small and, with this preparation technique, only two such areas exist on any one specimen. To maximise the probability of finding an area of specimen suitable for microanalysis in the microscope, the angle of incidence

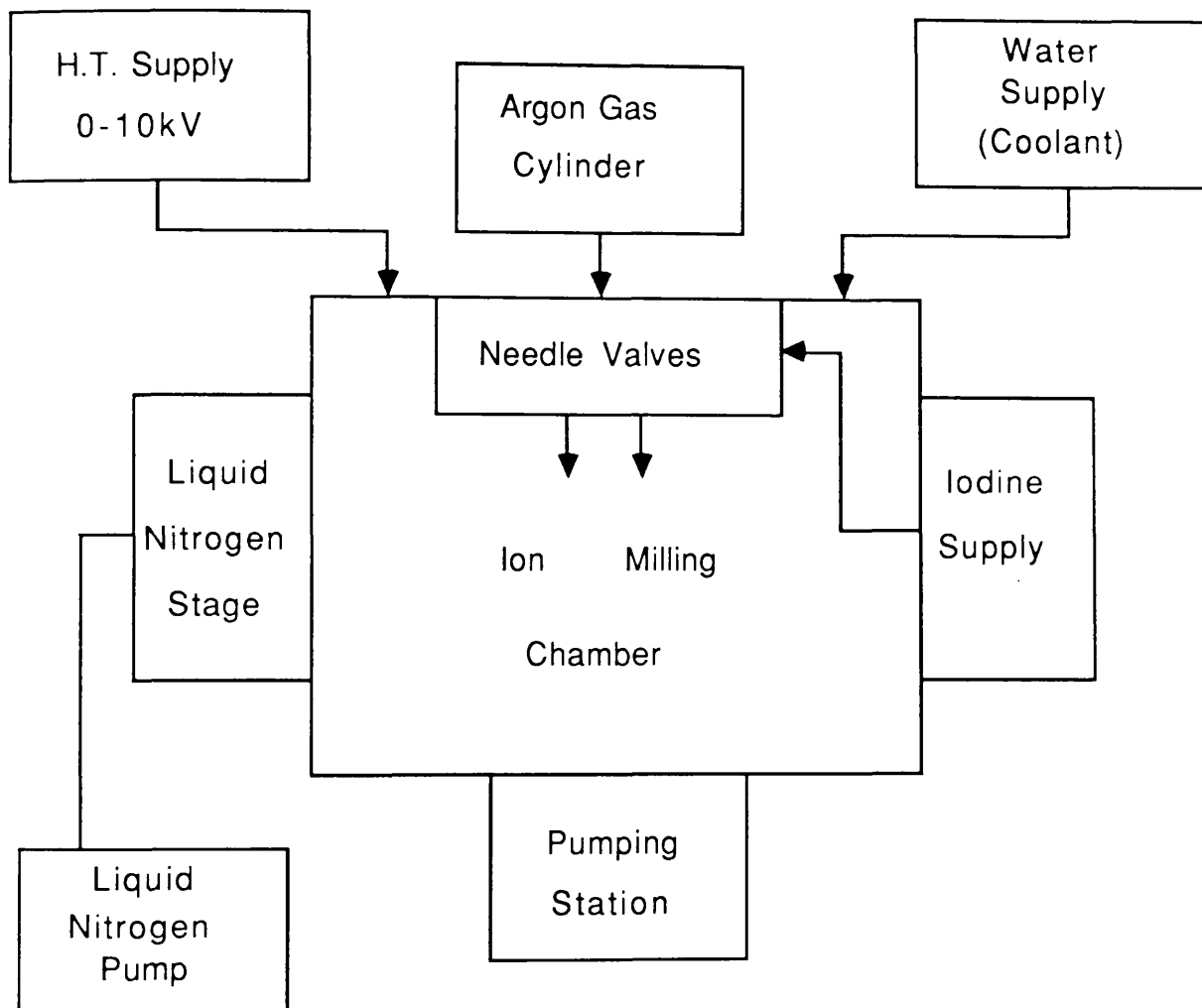


Figure 3.17: Block diagram of the ion milling system common to both Glasgow and RSRE

of the beam is increased to $\sim 14^\circ$ during the final stage of thinning. At this angle, the ion beams mill the semiconductor in preference to the epoxy resin. Consequently, small needles develop at either side of the hole where the two epilayers are bonded together. As figure 3.18 shows, this has the effect of increasing the area of epilayer surrounding the hole, and has the added advantage of isolating the epilayer from much of the substrate.

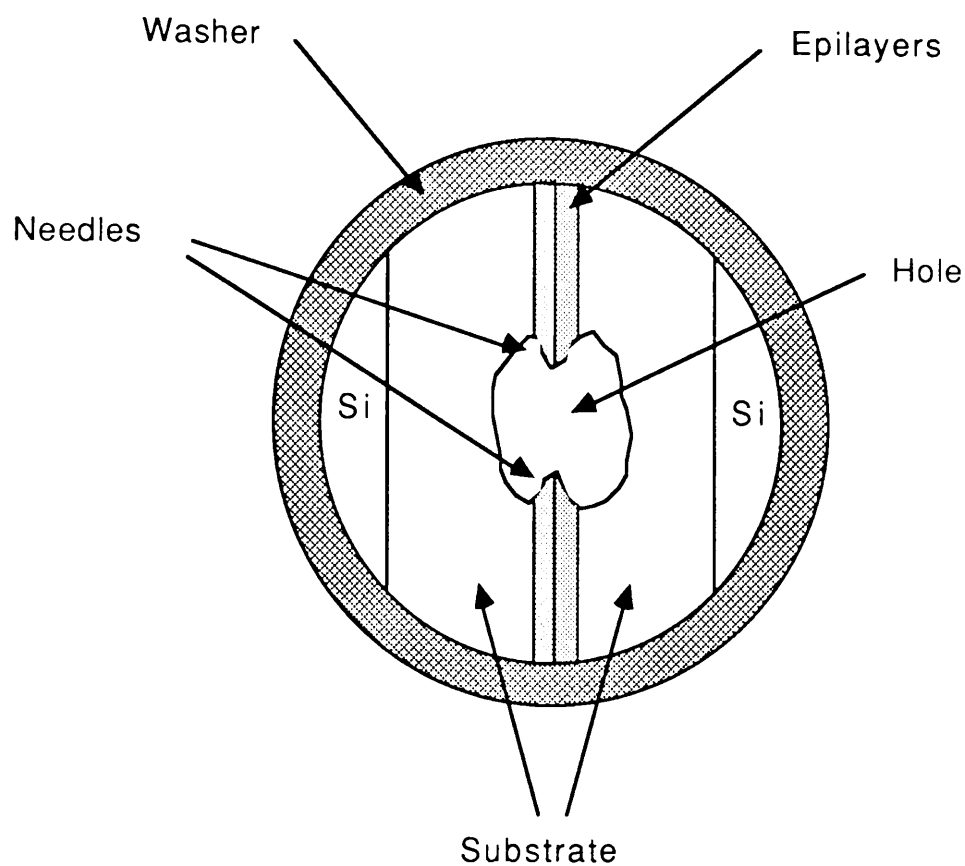


Figure 3.18: Plan view of a cross-sectional specimen suitable for EDX microanalysis.

Chapter 4

Considerations for imaging techniques that reveal layer contrast.

4.1 Introduction

As has already been stressed earlier in this thesis, the incident beam direction in the microscope must be exactly parallel to the plane of the specimen layers to enable microanalysis across interfaces with as high a spatial resolution as possible. It is also important that each interface is clearly observable in the microscope so that the probe can be placed at known distances from a layer boundary. Both conditions can be met if the materials are imaged using an (002) dark field imaging technique (Petroff, 1977) that is described in section 4.2. However, it is shown in this section that quantitative analysis of compound semiconductor multilayers using this technique is very difficult.

The post-specimen lens arrangement and ADF detector geometry in the modified HB5 STEM discussed in chapter 3 are ideally suited to another imaging technique that reveals layer contrast related to specimen composition, namely annular dark field imaging (ADFI). Pennycook (1986) showed that, provided suitable values of inner and outer ADF detector acceptance angles θ_1 and θ_2 are used, the variation of the mean atomic number \bar{Z} across the material can be determined. The theoretical basis of high-angle ADFI is discussed in the section on image formation from high-angle elastically scattered electrons in chapter 2. Section 4.3 establishes suitable experimental conditions in the microscope for high-angle ADFI. This technique is an incoherent imaging technique (e.g. Cowley, 1976) and so the detected ADF intensity $f(\text{ADF})$ across

a line scanned parallel to the direction of material growth can be expressed as a convolution between the linear probe current density distribution $J(x)$ calculated in chapter 3 and a function $f(\bar{Z})$ that is directly related to the change in \bar{Z} across the specimen;

$$f(\text{ADF}) = J(x) * f(\bar{Z}) \quad (4.1)$$

Section 4.4 gives a description of the simple analytical techniques that are applied to high-angle ADF images to estimate $f(\bar{Z})$.

4.2 Structure Factor Contrast

Petroff (1977) demonstrated that conventional images of $\text{Al}_x\text{Ga}_{1-x}\text{As}/\text{GaAs}$ taken under two beam conditions, where only the beam diffracted along the (002) plane is allowed through the objective aperture, reveal layer contrast related to the structure factor $F_{(002)}$ of each layer. This technique is known as (002) dark field imaging. In general;

$$F_{(hkl)} = \sum_{\text{unit cell}} f_a(2\theta_B) e^{-2\pi i(hx_a + ky_a + lz_a)} \quad (4.2)$$

where $f_a(2\theta_B)$ is the atomic scattering factor of the a^{th} atom at Bragg angle θ_B and x_a , y_a and z_a are the coordinates of the atom within the unit cell. For (002) dark field imaging, $\theta_B = \theta_{(002)}$ where,

$$\theta_{(002)} = \frac{\lambda}{2d_{(002)}} = \frac{\lambda}{a} \quad (4.3)$$

λ is the wavelength of the incident electrons, $d_{(002)}$ is the spacing between (002) planes and a is the lattice parameter of the material. $\theta_{(002)}$ is 6.5 and 6.3mrad for GaAs and InP respectively. The values of f_a for 100 keV incident electrons scattered through an angle $2\theta_B \simeq 12\text{mrad}$ are given in table 4.1 for all elements of interest in this thesis. A comprehensive listing of f_a values is given by Doyle and Turner (1967). The kinematical diffraction intensity $I_{KIN}(X)$ from an (002) dark field image of material X is a function of $F_{(002)}$;

$$I_{KIN}(X) \propto F_{(002)} \bar{F}_{(002)} \quad (4.4)$$

The coordinates of atoms within a unit cell of GaAs are $(0,0,0)$, $(0, \frac{1}{2}, \frac{1}{2})$, $(\frac{1}{2}, 0, \frac{1}{2})$ and $(\frac{1}{2}, \frac{1}{2}, 0)$ for Ga and $(\frac{1}{4}, \frac{1}{4}, \frac{1}{4})$, $(\frac{3}{4}, \frac{3}{4}, \frac{1}{4})$, $(\frac{1}{4}, \frac{3}{4}, \frac{3}{4})$ and $(\frac{3}{4}, \frac{1}{4}, \frac{3}{4})$ for As (figure 4.1). The structure factor for this cell is;

$$F_{(002)} = 4(f_{Ga} - f_{As}) \quad (4.5)$$

$f_{Ga} \simeq f_{As}$ and so $F_{(002)}$ is very small. However, in $Al_xGa_{1-x}As$, where the atoms occupying the Ga sites are assumed to be either Ga or Al, the structure factor is;

$$F_{(002)} = 4[xf_{Al} + (1-x)f_{Ga} - f_{As}] \simeq 4x(f_{Al} - f_{Ga}) \quad (4.6)$$

and so $I_{KIN}(Al_xGa_{1-x}As)$ is greater than $I_{KIN}(GaAs)$. The above argument can be extended to the $In_xGa_{1-x}As/InP$ multilayer system which possesses a similar structure where $F_{(002)}$ is always greater for InP than $In_xGa_{1-x}As$ thus enabling layer contrast. The numerical values of $F_{(002)}$ for InP, GaAs and their lattice-matched alloys are given in table 4.2. Using this information, the ratio of $I_{KIN}(InP)$ to $I_{KIN}(In_xGa_{1-x}As)$ at the lattice match value of $x=0.53$, for example, is predicted to be $\sim 20:1$.

Element	$f(2\theta)_a$ (Å)
Al	3.741
P	4.289
Ga	5.365
As	5.970
In	8.138

Table 4.1: List of relativistically corrected atomic scattering factors f_a of several elements for 100keV electrons scattered through angle 2θ of ~12mrad.

Material	$F_{(002)}$ (Å)
GaAs	2.42
$\text{Ga}_{0.3}\text{Al}_{0.7}\text{As}$	4.37
InP	15.40
$\text{In}_{0.53}\text{Ga}_{0.47}\text{As}$	3.46

Table 4.2: Numerical values of structure factor $F_{(002)}$ for materials that are relevant to this thesis.

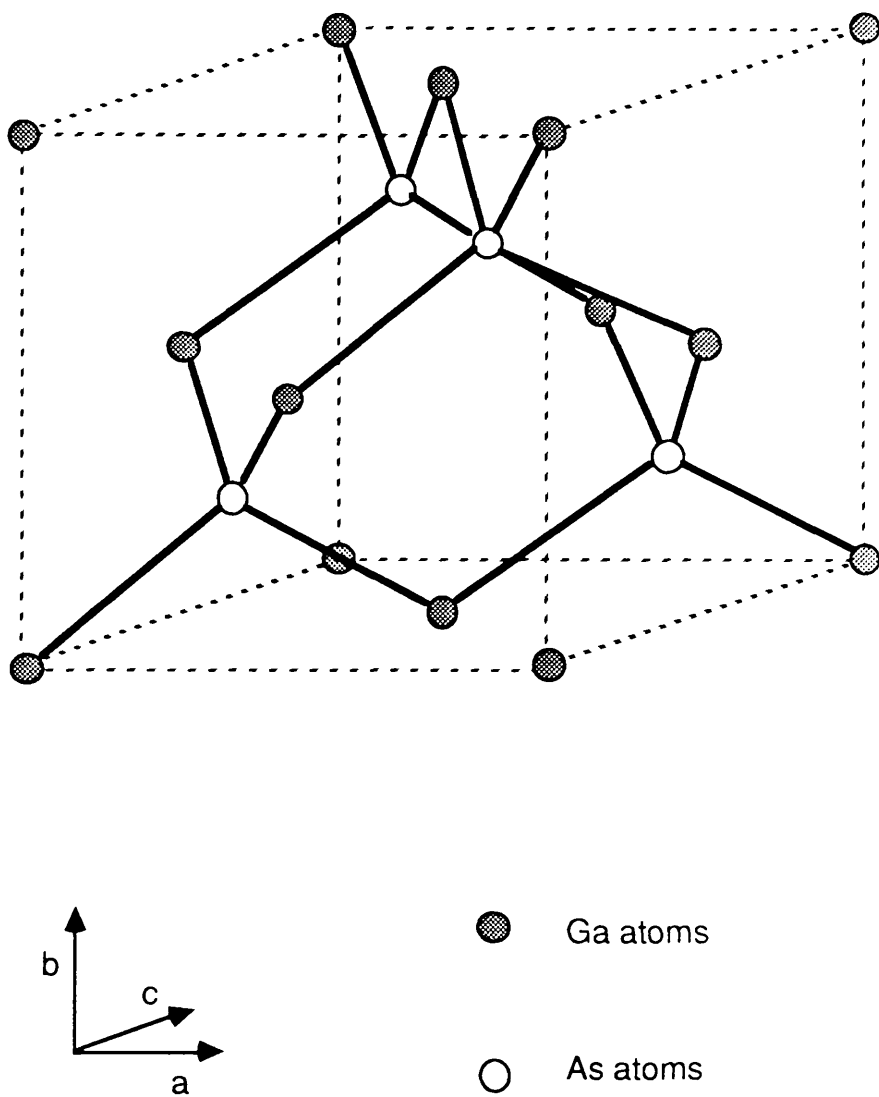


Figure 4.1: The crystal structure of one unit cell of GaAs

$\beta_0 = 1.6\text{mrad}$ when PSL3 only is used.

Figure 4.2 is a schematic diagram which illustrates the experimental conditions required to form (002) dark field images. The diagram shows that to collect signals from the (002) reflection only, the following condition must be satisfied;

$$\alpha_o + \beta_o < 2\theta_B \quad (4.7)$$

where α_o is the illumination semi-angle and β_o is the collection semi-angle. This condition is satisfied for both multilayer systems of interest by using the 25 μ m OA ($\alpha_o = 4.0$ mrad) and the 250 μ m collector aperture ($\beta_o = 1.6$ mrad). Figure 4.3 shows an (002) dark field image of an InGaAs/InP multilayer that was acquired in the HB5 using this aperture configuration. In the image, the interfaces are well defined and the InGaAs layers are darker than the InP layers as suggested by theory. However, Loretto (1987) observed that the relative intensities between layers of different compositions can vary according to both the local thickness and the contribution made by inelastically scattered electrons. This is demonstrated in figure 4.3 where there is a decrease in layer contrast to the left of the image. The latter named effect occurs because plasmon scattering can be more intense for one material in a multilayer system than another (e.g. Boothroyd and Stobbs, 1988). These unequal contributions can be filtered out by energy-filtered imaging, but the intensity contributions due to changes in specimen thickness remain. Although (002) dark field imaging is well suited for the location and orientation of interfaces in the microscope, the image demonstrates that quantitative analysis of structure factor contrast can be very complicated. This project looks towards high-angle ADFI as a means of obtaining such information.

4.3 Attainment of suitable experimental conditions for high-angle ADFI

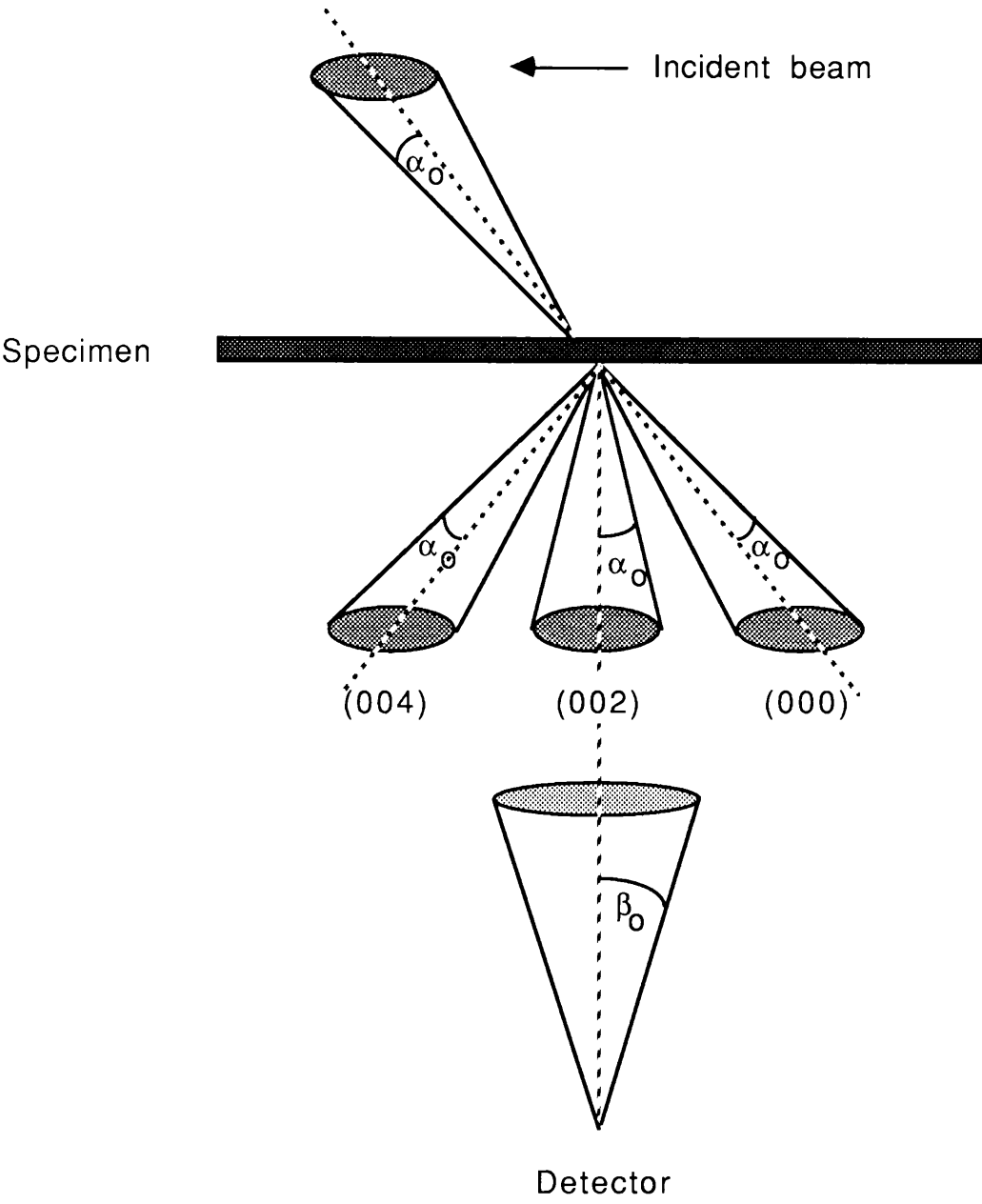


Figure 4.2: Schematic diagram showing idealised conditions required to enable (002) dark field imaging.

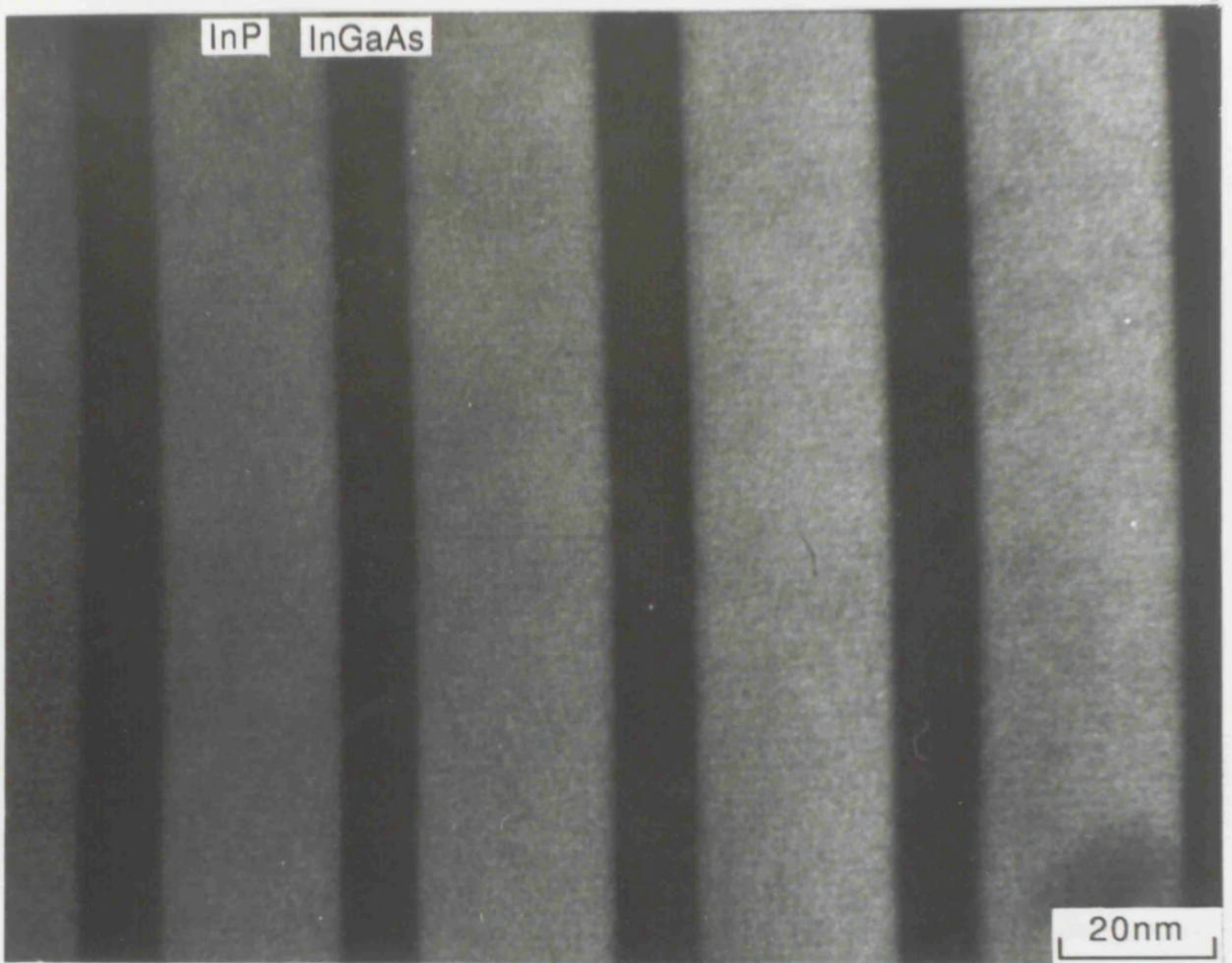


Figure 4.3: (002) dark field image of an InGaAs/InP multilayer.

A full investigation into elemental concentrations across semiconductor multilayers by high-angle ADFI can only be implemented if suitable values of θ_1 and θ_2 are determined. Provided strong electron channeling directions are avoided (Pennycook, 1986), θ_1 must be sufficiently high as to enable the acquisition of \bar{Z} -contrast images that are independent of exact specimen orientation. Suitable experimental conditions were found by examining a specimen at varying PSL excitations and specimen tilt angles. The test specimen was an InGaAs/InP multilayer grown by MOCVD on an InP substrate. It consisted of 10nm InGaAs layers grown between 20nm buffer layers of InP.

Chapter 3 stated that the angular compression of transmitted electrons at the ADF detector is controlled using the PSLs. For all high-angle ADFI discussed in this thesis, PSL1 only is used. A low excitation of this lens corresponds to a higher value of camera length (CL) than that for high excitations. The values of θ_1 and θ_2 to which each CL corresponds is determined by calibrating a Kikuchi diffraction pattern formed at the diffraction screen. For the PSL excitation used here, the spatial distribution of diffraction features is assumed to be the same on the ADF detector as that on the diffraction screen. At each value of CL, the specimen was tilted $\sim 22^\circ$ away from the [110] pole along the (004) Kikuchi line and, with the probe positioned at a thin area of substrate, a diffraction pattern was recorded. Patterns can be recorded from the diffraction screen by using either a 35mm camera or the 'Crystal' digital acquisition system described in chapter 3. The latter was preferred as this enables access to simple image processing programs that are available in the software package 'DIGIPAD'. Figure 4.4 shows two patterns acquired using 'Crystal' at PSL1 settings of (a) -4 (coarse control), 4.39 (fine control) and (b) -5 (coarse), 4.39 (fine), corresponding to CLs of 70 and 35mm respectively. The apparent distortion parallel to the y-axis in each pattern is

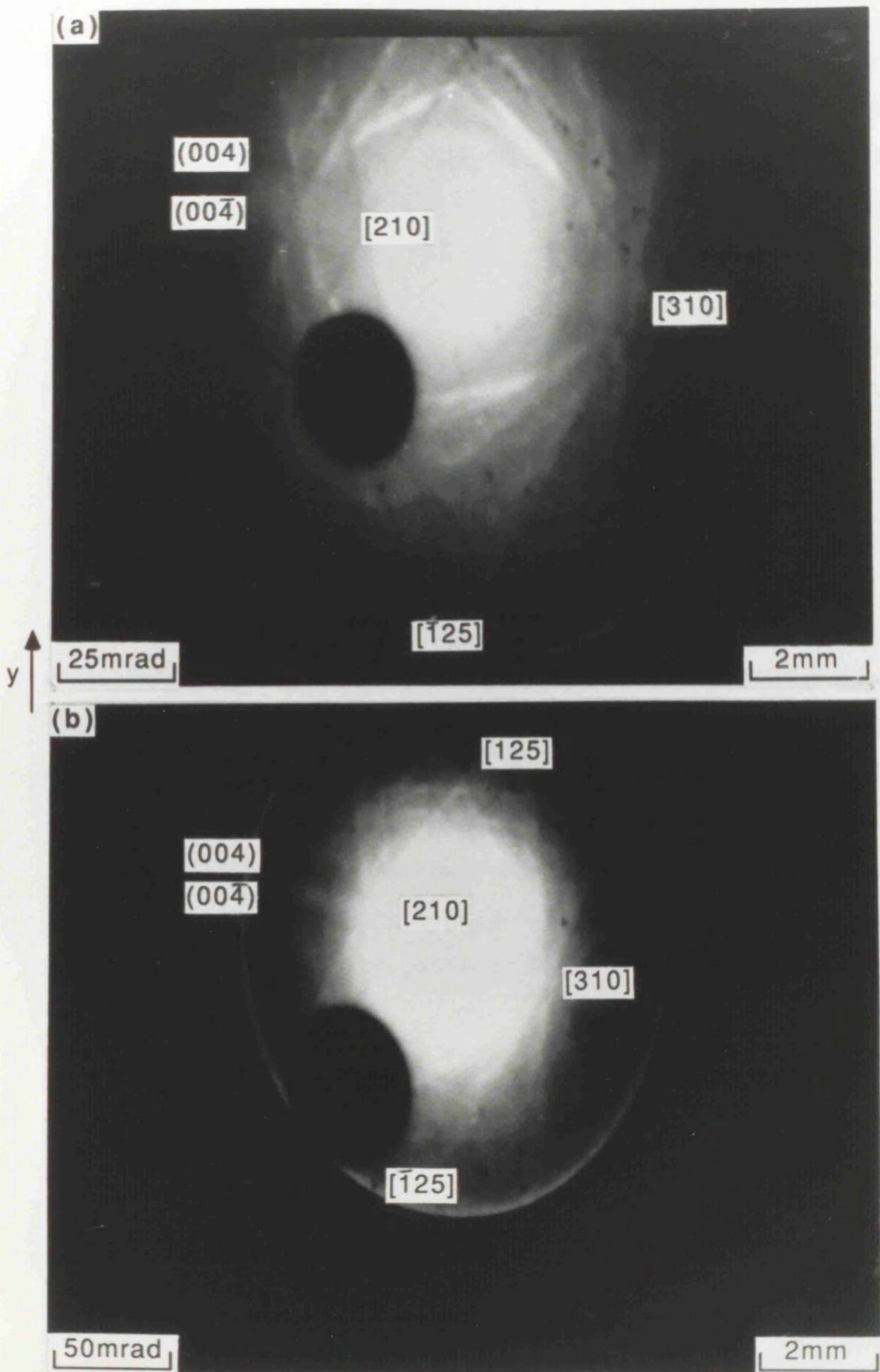


Figure 4.4: Digitally acquired Kikuchi diffraction patterns taken at an (a) high and (b) low CL from an area of InP.

entirely attributable to the acquisition and display software of the analysis system. All calculations on the spatial distribution of features on each pattern take this effect into consideration. Marked on the patterns in figure 4.4 are the [210], [310], [125] and $\bar{[125]}$ poles and the (004) and (00 $\bar{4}$) Kikuchi lines. Buggy (1985) observed that for low CLs in the HB5, diffraction patterns can be subject to radial distortion. Figure 4.5 shows a graph plotting position on the diffraction screen as a function of the angle through which electrons have been scattered from the incident beam direction for both values of CL. The graph shows that, to a good first approximation, the spatial distribution of poles in both diffraction patterns is linear. This is substantiated by observing that the distance between the (004) and (00 $\bar{4}$) Kikuchi lines in figure 4.4 remains constant across each pattern. The outer limit of angular acceptance in both patterns is clearly defined. This is because the angular range over which scattered electrons are detected in the HB5 is limited by a lens bore and, as a result, θ_2 is limited to 200mrad for both low and high CLs. Another feature clearly visible in each image is a dark disc. This is the diffraction screen aperture which has a known diameter (d_{diff}) of ~2mm, and is used to evaluate the CL. Using the information provided by the diffraction patterns, the acceptance semi-angle of the aperture (θ_{diff}) at the high CL is 27mrad, whereas at the low CL, θ_{diff} =52mrad. The diameter (d_{ADF}) of the aperture in the ADF detector is also known (d_{ADF} =3.3mm) and so θ_1 can be easily determined;

$$\theta_1 = \theta_{\text{diff}} \frac{d_{\text{ADF}}}{d_{\text{diff}}} \quad (4.8)$$

Using equation 4.8, θ_1 is 45mrad for the high CL and 85mrad for the low CL.

For this experiment only, ADF images were recorded using a Toltec digital acquisition system. Figure 4.6(a) shows a typical 256x256 pixel ADF image of an InGaAs layer. An intensity profile showing the average intensity fluctuation

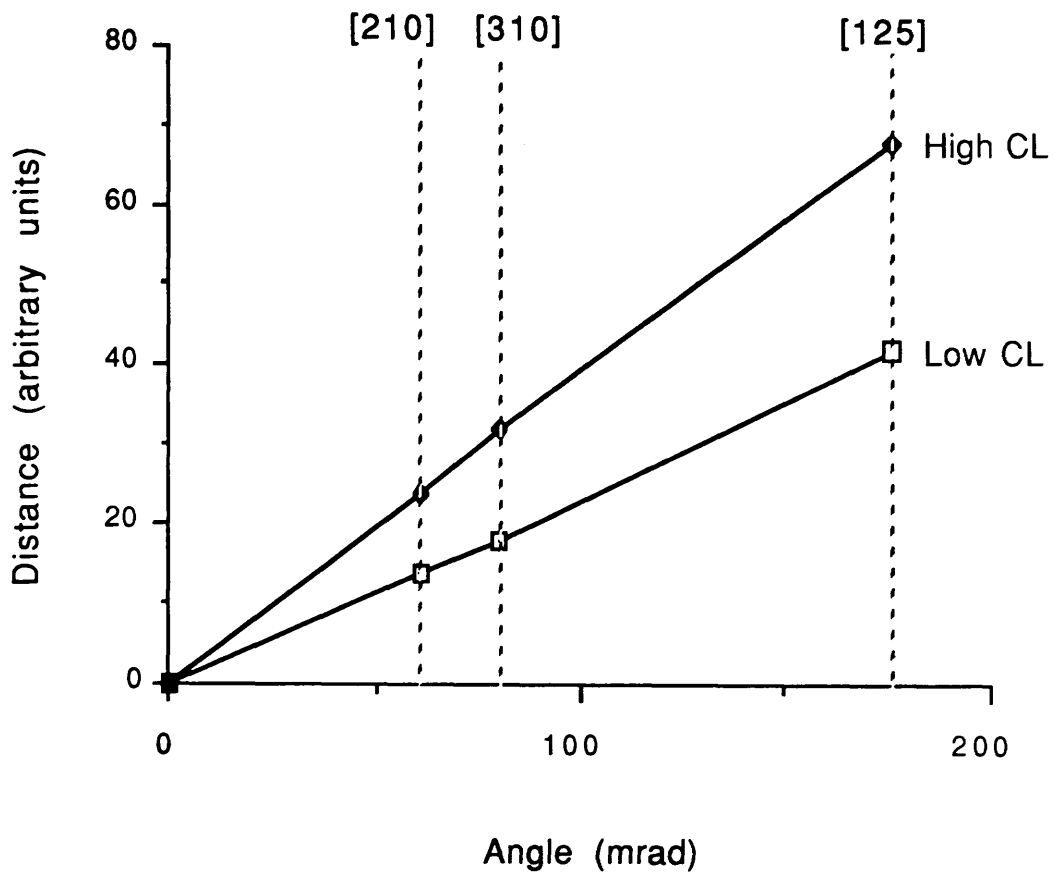


Figure 4.5 Plot of distance against angle for the diffraction patterns shown in figure 4.4

Growth direction →

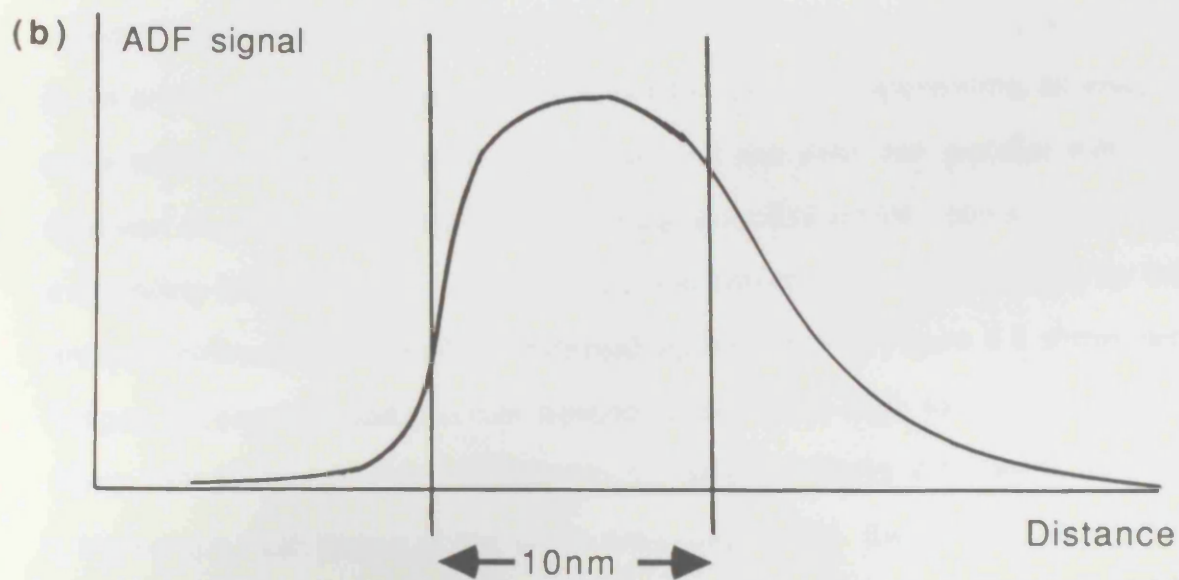
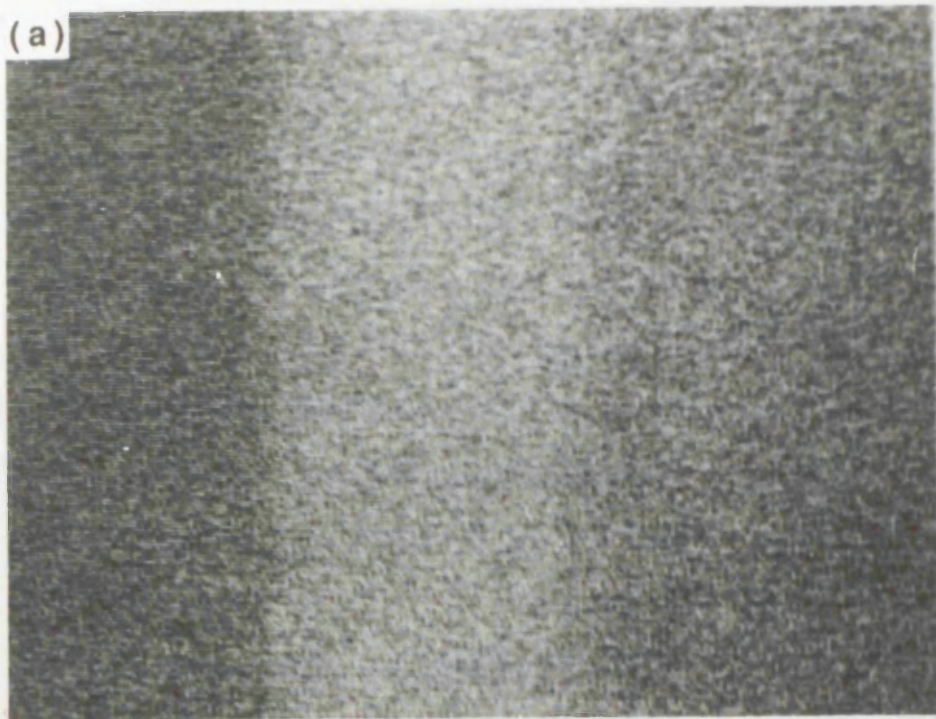


Figure 4.6: (a) High-angle ADF image of a 10nm InGaAs layer

(b) ADF intensity variation from (a)

across the image is given in figure 4.6(b). Figure 4.7 shows four such profiles obtained for low and high values of CL and at specimen tilts of $\sim 16^\circ$ and 28° away from the [110] pole along the (004) kikuchi band. At the high CL, although layer contrast is evident, both profiles vary significantly with specimen tilt - this is in accord with the observations made by Pennycook (loc. cit.). However, at the low CL, the profiles show an asymmetrical distribution consistent with differences in interface composition. A full description of the investigation into this system by both high-angle ADFI and EDX microanalysis is given in chapter 7. The lens excitations giving $\theta_1=85\text{mrad}$ and $\theta_2=200\text{mrad}$ were used for all high-angle ADFI experiments discussed in future chapters.

4.4 Acquisition and analysis of high-angle ADF images

All digitally acquired images discussed in the remainder of this thesis were recorded and analysed using the Link Systems AN10000 described in chapter 3. To enable direct comparison of results from different experiments, all images were recorded with the scan rotated so that the lines ran parallel with the direction of growth. Each horizontal line contains 512 pixels - corresponding to a sampling interval of 0.13nm per pixel - and can be treated individually by the analysis software as a profile of detected signal intensity. Figure 4.8 shows two images recorded in the manner described. An (002) dark field image of two 10nm AlGaAs layers grown between buffer layers of GaAs is shown in (a), with a high-angle ADF image of the same area given in (b). Each image consists of 64 lines of 512 pixels, with the intensity at each pixel measured to 8-bit precision over a dwell time of $51\mu\text{s}$ per pixel.

To enable meaningful interpretation of results, high-angle ADF images must undergo an analysis procedure that reduces signal noise effects and takes into consideration variations in specimen thickness and the probe linear current

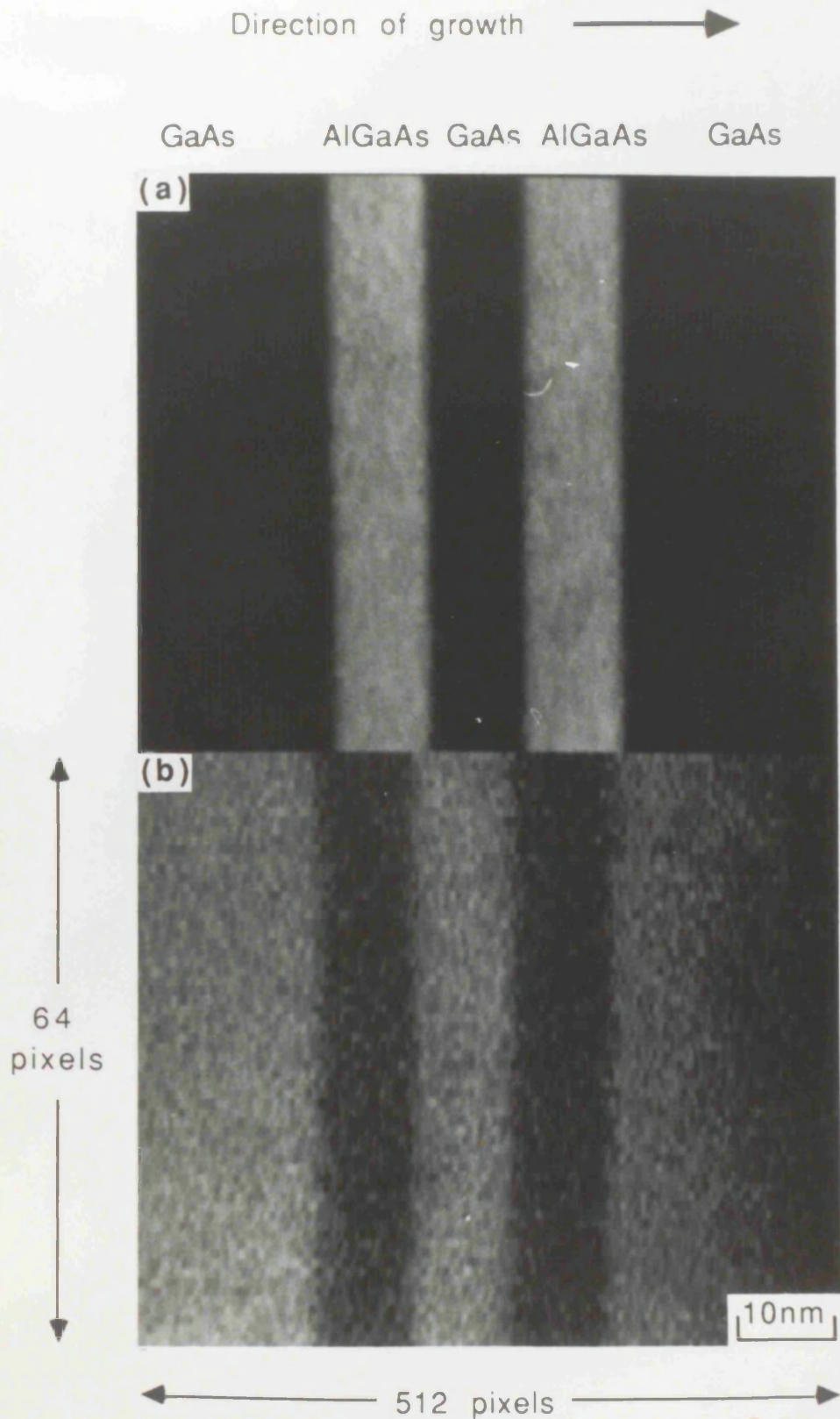


Figure 4.8: (a) (002) digital image of an AlGaAs/GaAs multilayer
(b) Digital high-angle ADF image from of the same area

density distribution $J(x)$. Using the image in figure 4.8(b), the remainder of this section addresses these problems with the aid of simple processing techniques that can be quickly and easily applied to all high-angle ADFI data. All analysis programs referred to in this section were written in Fortran77 for the AN10000 system and are listed in appendix A2.

4.4.1 Profile noise reduction

Figure 4.9 shows three single line profiles taken from the image in figure 4.8(b). Whilst they show similar features, the amount of noise present precludes their direct comparison. Averaging over all 64 lines in the image reduces this effect (figure 4.10b), but this in turn reduces edge acuity at layer interfaces when small variations in well thickness are present. A suitable compromise was found by taking an average over m consecutive line profiles (where $m=10$ in figure 4.10c). The noise present in the averaged profile is further reduced by means of a median filter. An n -point median filter is a one-dimensional filter which replaces the value associated with each pixel with the median value of the n pixels around it. This has the effect of reducing noise whilst preserving information on abrupt changes in signal intensity. Figure 4.11 shows an (a) 3-point, (b) 7-point and (c) 11-point filter applied to the profile in figure 4.10(c) using program 'MEDFIL'. The diagram shows that filters of increasing sampling width reduce noise effects but retain edge definition. Consequently, an 11-point filter is applied to all profiles at this stage of analysis.

4.4.2 Thickness corrections

The evaluation of high-angle ADF cross-sections in chapter 2 showed that the detected signal intensity is a function of specimen thickness t . Ideally, t

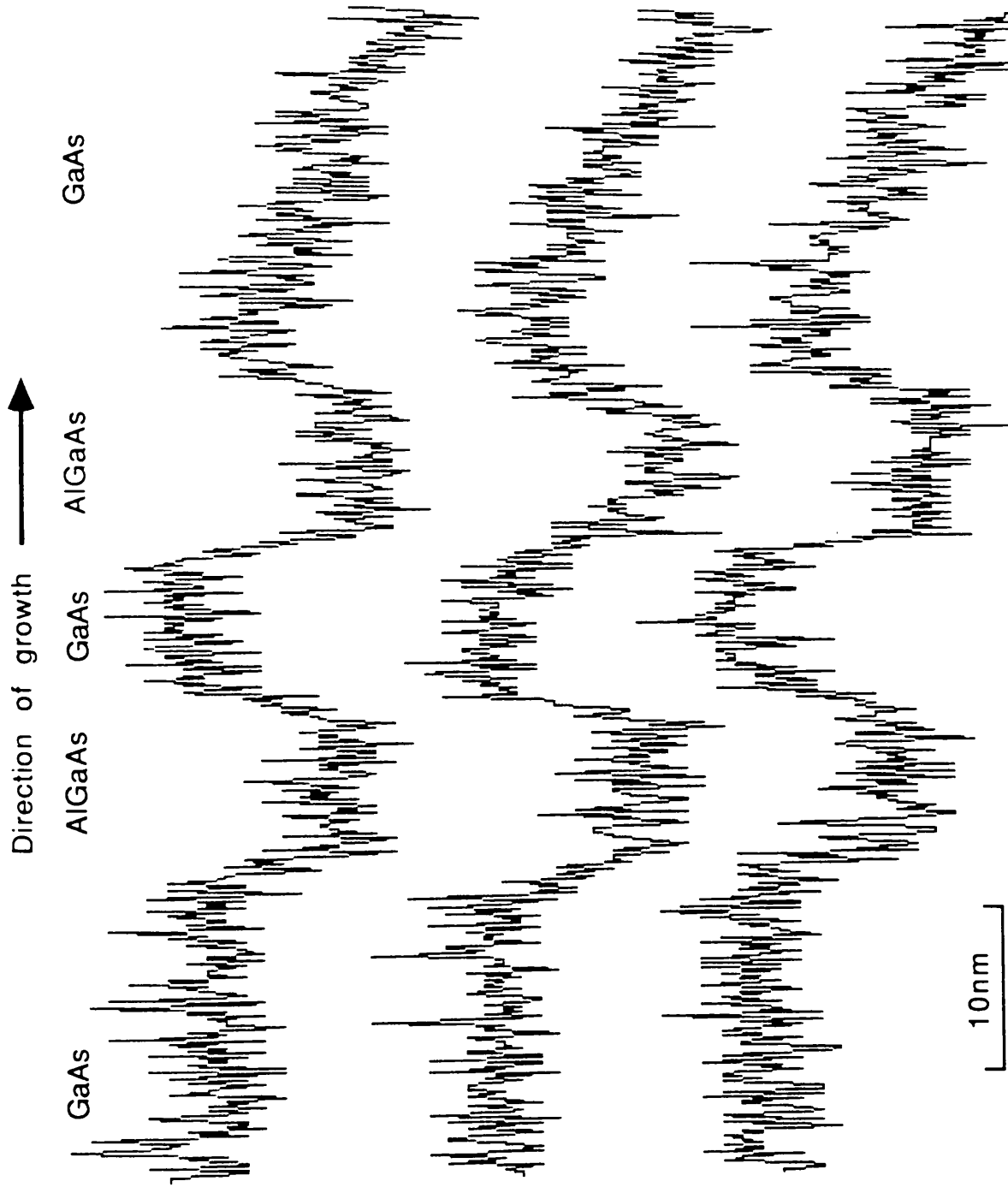


Figure 4.9: 3 single line profiles taken from figure 4.8(b)

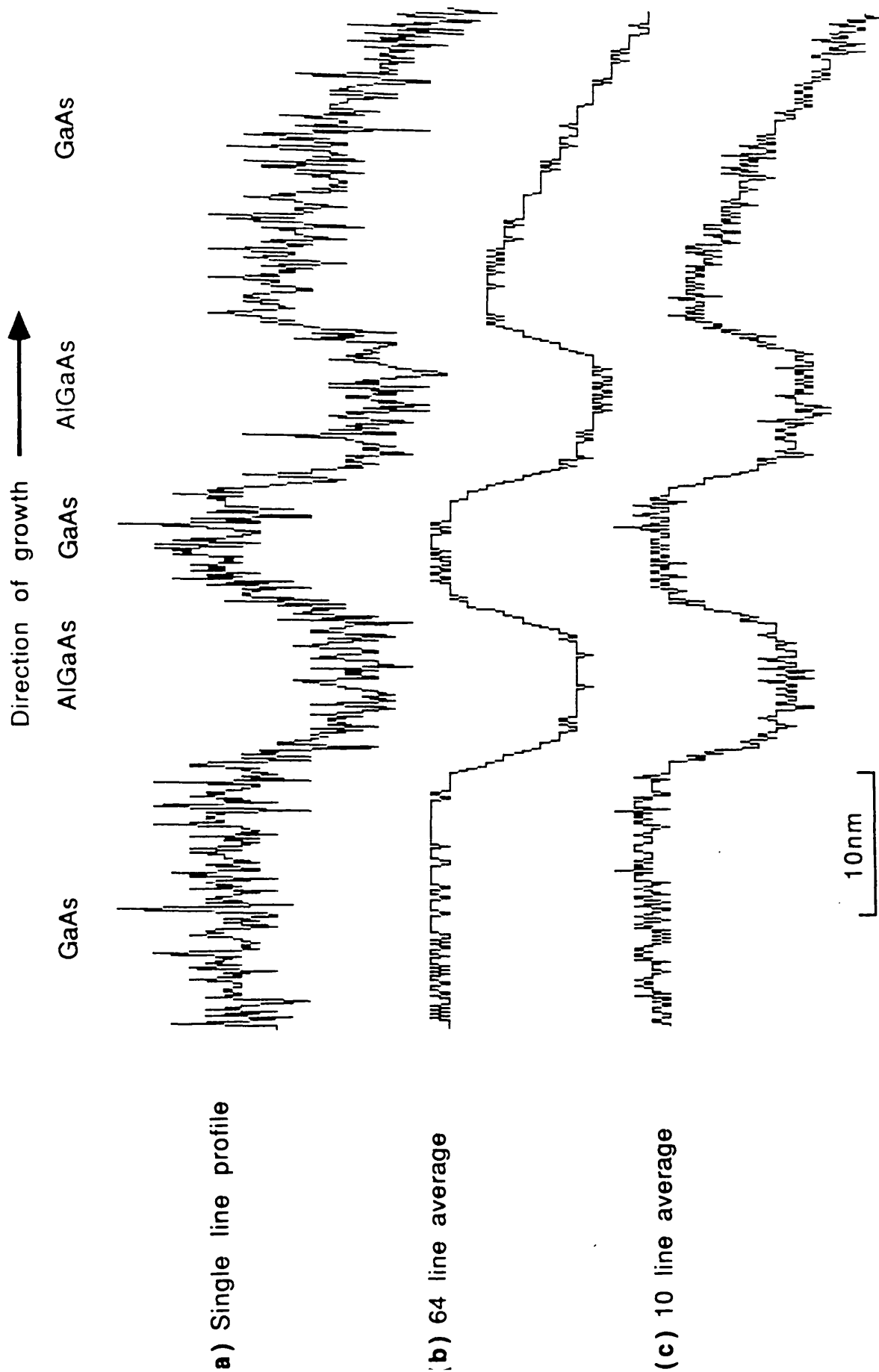


Figure 4.10: Comparison of single and averaged line profiles

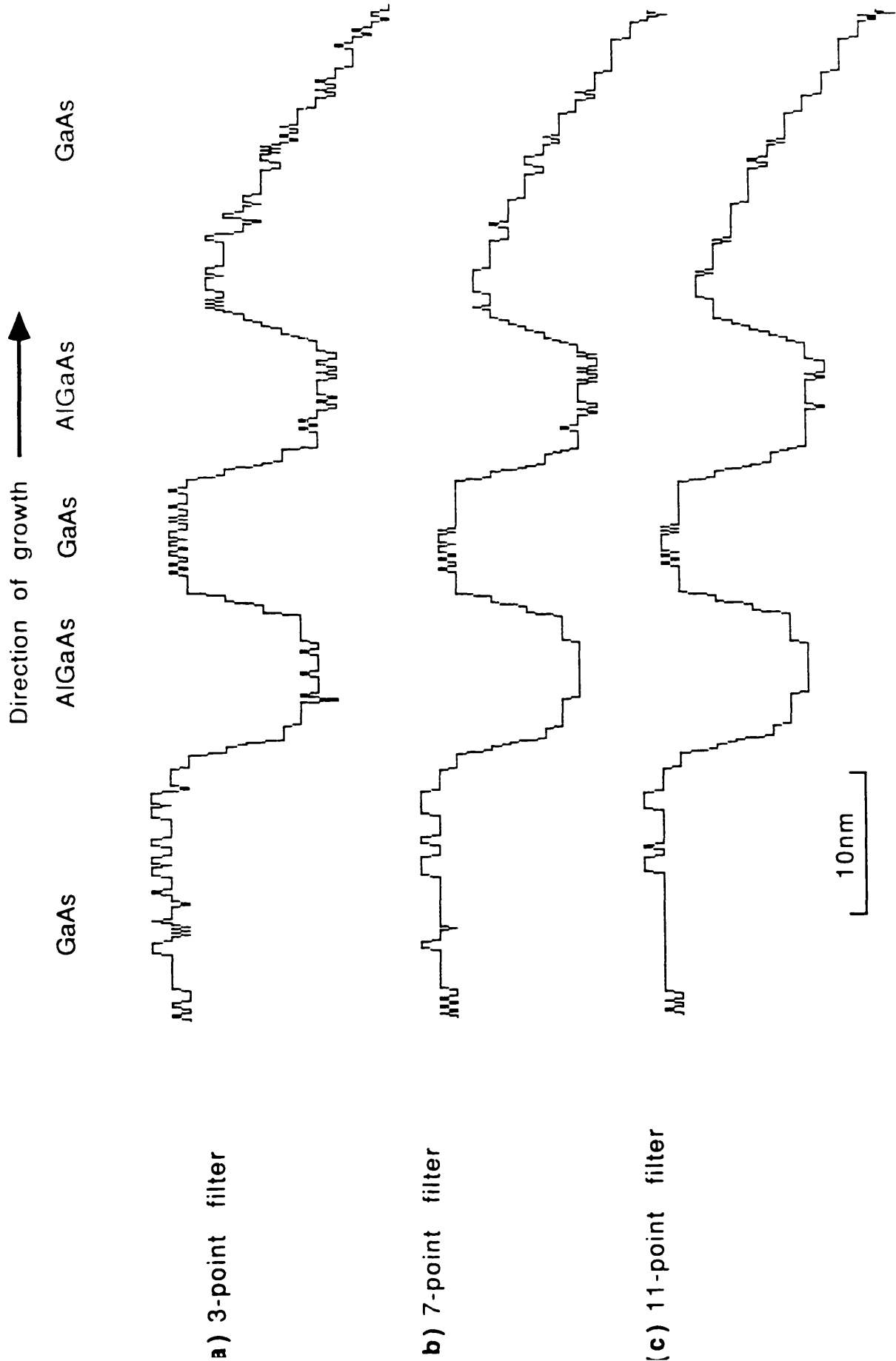


Figure 4.11: Comparison of median filters

should be constant over the area scanned by the probe. However it is not always possible to find such regions in specimens formed by ion milling techniques, and so a t-correction step is sometimes necessary as in the example discussed here. Following Guest (1961), the correction method fits a cubic polynomial to the intensity distribution attributable to changes in specimen thickness. By choosing N pixels in regions of constant concentration in the buffer layers, away from the quantum wells, the intensity Int_i at the i th pixel can be expressed in terms of the pixel number l_i (where $1 \leq l \leq 512$),

$$Int_i = a + bl_i + cl_i^2 + dl_i^3 \quad (4.9)$$

The parameters a, b, c and d can be obtained by solving the simultaneous equations;

$$\begin{aligned} aN + b\sum_i^N l_i + c\sum_i^N l_i^2 + d\sum_i^N l_i^3 &= \sum_i^N Int_i \\ a\sum_i^N l_i + b\sum_i^N l_i^2 + c\sum_i^N l_i^3 + d\sum_i^N l_i^4 &= \sum_i^N l_i Int_i \\ a\sum_i^N l_i^2 + b\sum_i^N l_i^3 + c\sum_i^N l_i^4 + d\sum_i^N l_i^5 &= \sum_i^N l_i^2 Int_i \\ a\sum_i^N l_i^3 + b\sum_i^N l_i^4 + c\sum_i^N l_i^5 + d\sum_i^N l_i^6 &= \sum_i^N l_i^3 Int_i \end{aligned} \quad (4.10)$$

These equations are solved using a matrix inversion routine included in cubic fitting program 'CUBFIT'. Figure 4.12(b) shows an intensity distribution calculated in this manner that was designed to fit the processed experimental profile in figure 4.12(a). The regions of (a) that were chosen to calculate (b) are marked by a W on the diagram. Dividing (a) by (b) results in a t-corrected

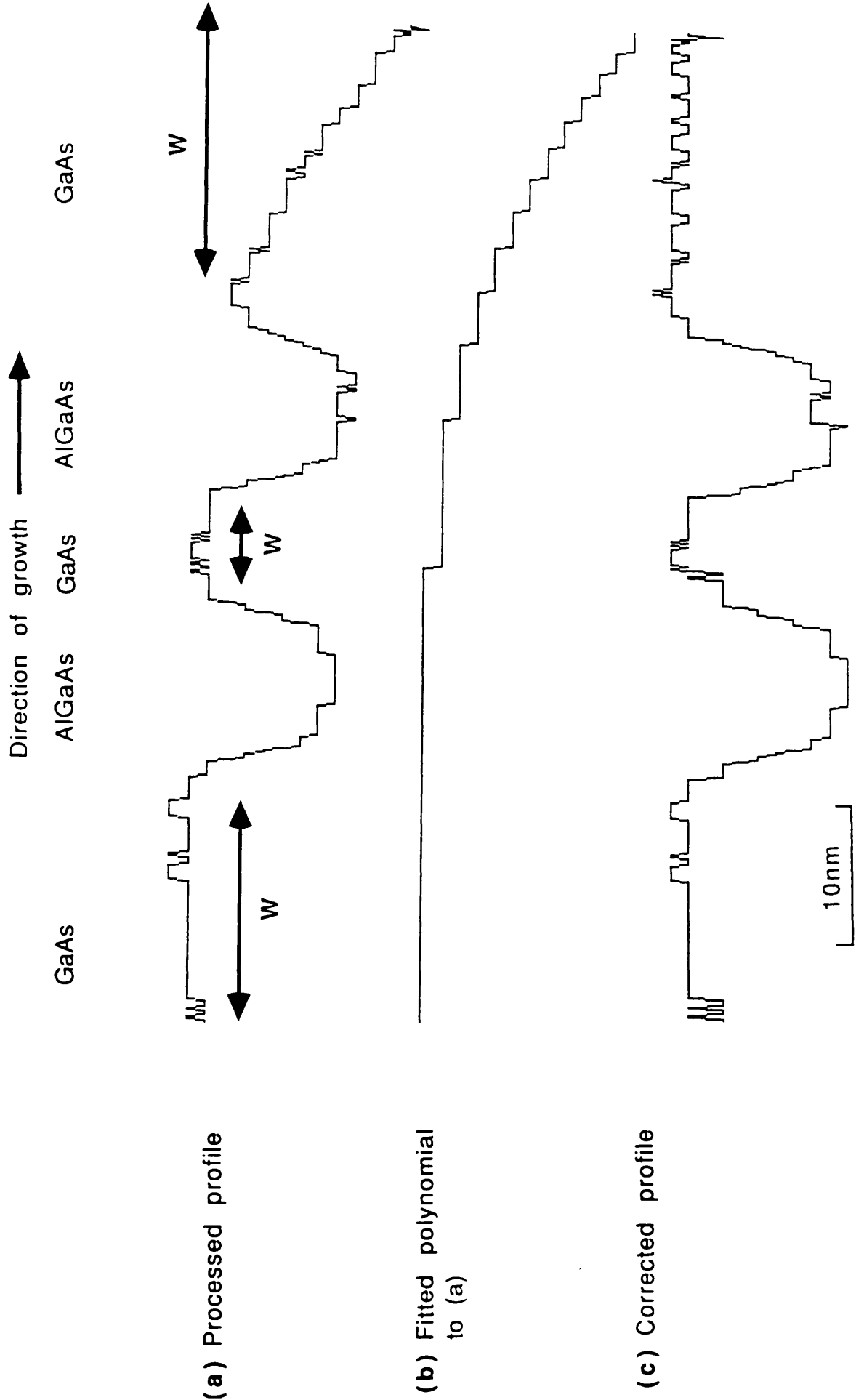


Figure 4.12: Thickness correction steps applied to a processed profile

intensity distribution in which the signal intensity from the buffer material remains constant (figure 4.12c). Figure 4.12 shows that the t-correction steps have the adverse effect of exaggerating the noise present in the original profile, and so this technique should only be applied if necessary.

4.4.3 Simulation of intensity profiles

Equation (4.1) shows that the detected intensity from high-angle elastically scattered electrons can be expressed as a one-dimensional convolution of $J(x)$ with an intensity variation related directly to \bar{Z} in the specimen. The problem of estimating $f(\bar{Z})$ can be approached in two ways; either by performing a Fourier transform on the processed profile or by convoluting $J(x)$ with simulations of $f(\bar{Z})$. Despite the steps taken to reduce signal noise, the amount of noise still present in the processed profile prohibits meaningful interpretation of results using the former method, and so the latter is preferred. Figure 4.13 shows the linear distribution of current in the probe used to form the image in figure 4.8(b). The diagram is represented in histogram form and has a sampling interval equivalent to the pixel length. A processed intensity profile across one AlGaAs well is shown in figure 4.14(a). That in (b) is a model of $f(\bar{Z})$ possessing a linear variation of \bar{Z} over 1nm (~ 1.8 unit cell dimensions) at each interface. The result of the one-dimensional convolution between this model and $J(x)$ using program 'CONVO' is shown in figure 4.14(c). As figure 4.15 shows, this profile gives the closest agreement between theoretical simulation and processed experimental profile. Models possessing more abrupt interfaces under-estimate the transition width whereas the width is over-estimated when less abrupt interfaces are used. It should be noted, however, that a transition width of 1.5nm (~ 2.6 unit cell dimensions) does give closer agreement with experiment than that of 0.5nm (~ 0.9 unit cell dimensions). A full discussion of the relevance of these results to studies of the MBE grown AlGaAs/GaAs system is given in chapter 6.

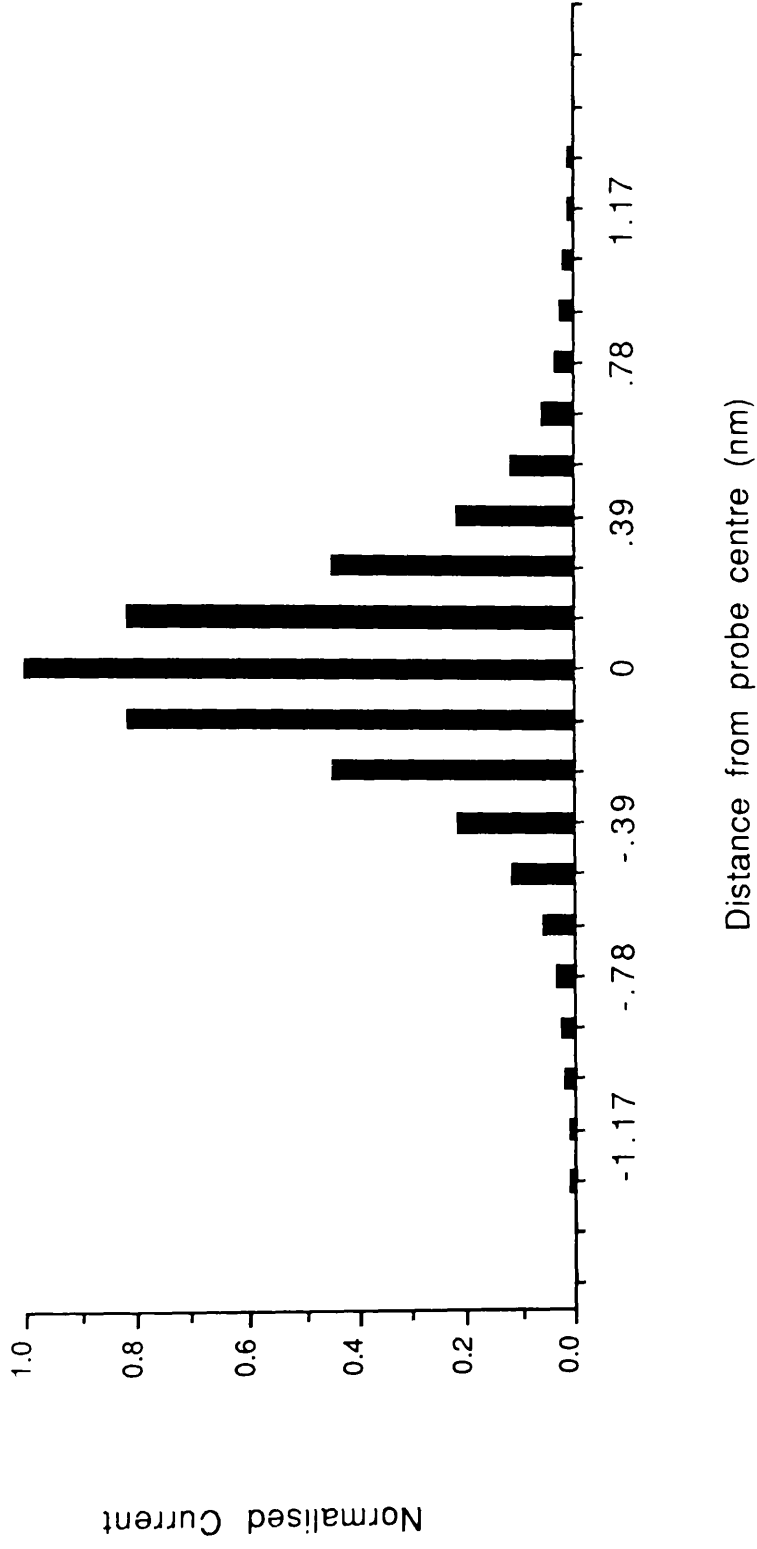


Figure 4.13: Histogram showing the distribution of current in the probe using a sampling interval of .13nm

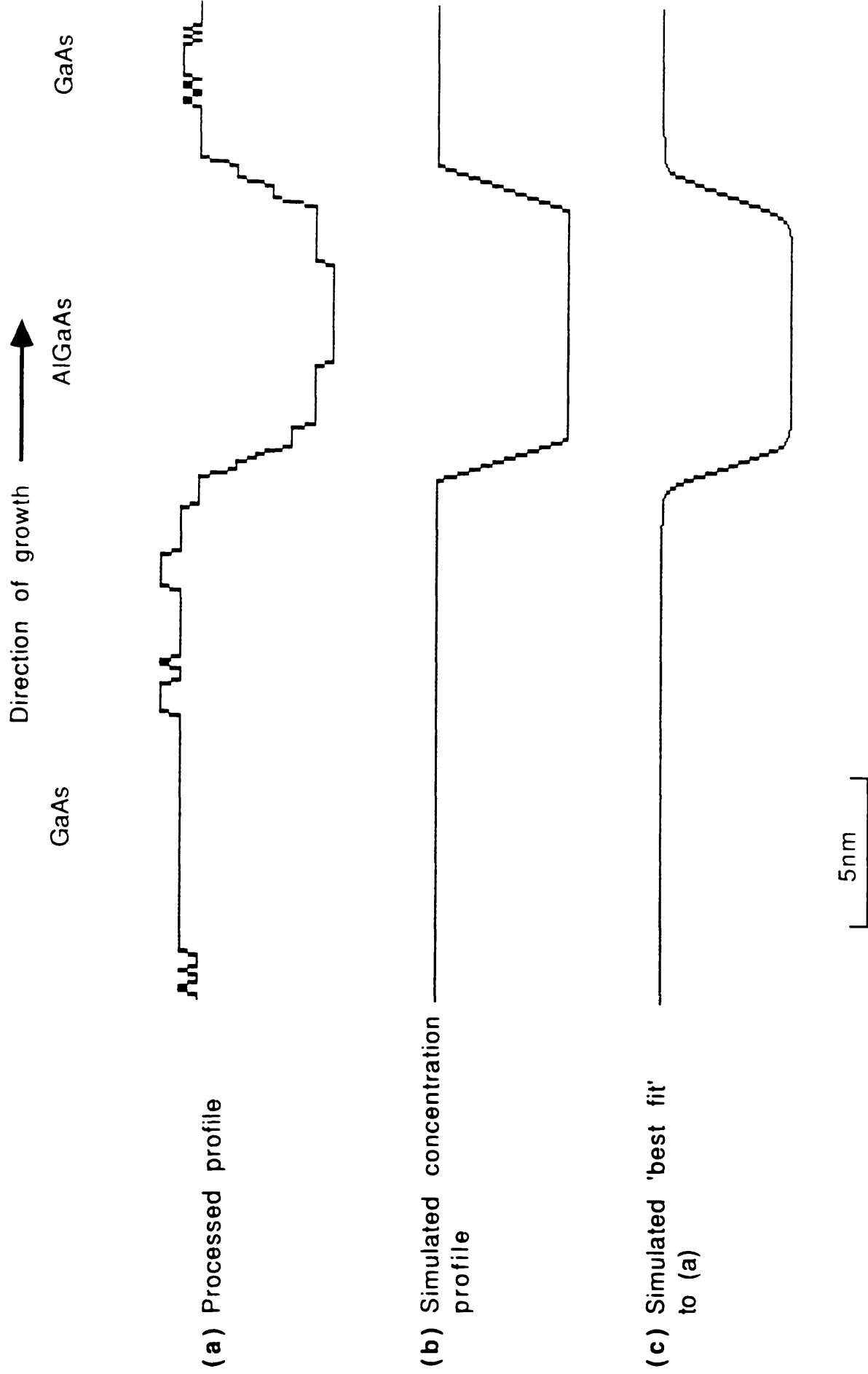


Figure 4.14: Comparison of a processed profile with simulated line profiles

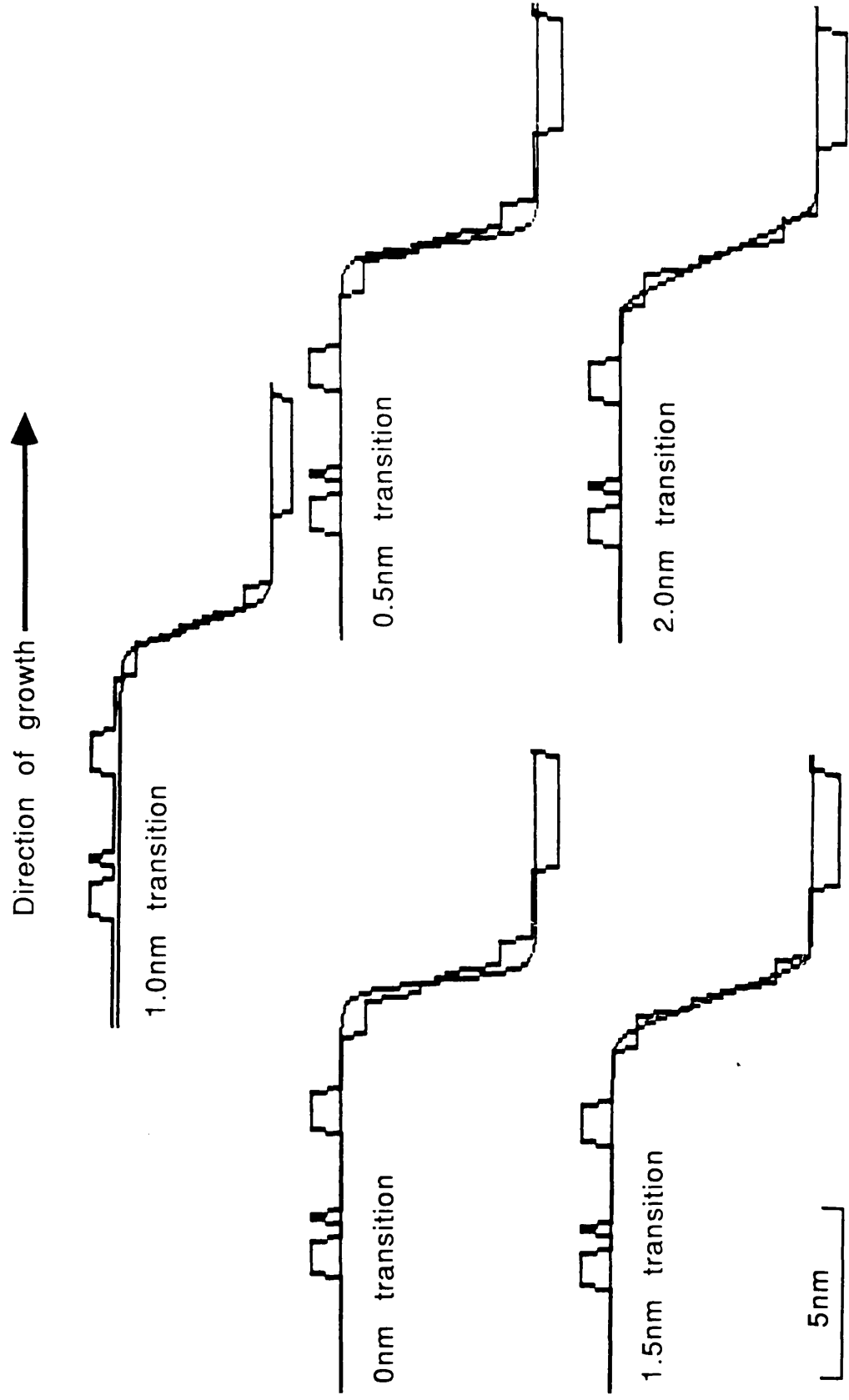


Figure 4.15: Comparison between an experimentally acquired profile and simulated profiles calculated from a range of transition widths.

Chapter 5

Considerations for EDX microanalysis.

5.1 Introduction

A major advantage of EDX microanalysis is that elemental concentrations can be measured directly without recourse to information provided by other analytical techniques. The aim of experiments using EDX microanalysis in this thesis is to measure the way in which relative concentrations change as a function of position across layers and interfaces in a direction parallel to that of material growth in AlGaAs/GaAs and InP/InGaAs systems. Figure 5.1 shows the format in which such information is displayed.

This chapter is concerned with various aspects of EDX microanalysis that must be addressed to extract as much information as possible from experimental data. Section 5.2 discusses the way in which the resolution-limiting factors of specimen thickness and beam spreading should be balanced to optimise the spatial resolution of the technique. Having established this criterion, section 5.3 describes the Monte Carlo program used to quantify the effects of beam broadening in the specimen as a function of specimen thickness. The following section extends the scope of the program to simulate experimental conditions and to estimate the way in which detected signal profiles vary according to the abruptness of the interfaces.

Preferential absorption of characteristic x-ray signals before detection can seriously affect the measured concentration from the volume of specimen excited. Sections 5.5 and 5.6 discuss two aspects of absorption, namely self-absorption in the specimen and absorption in the EDX detector. Section 5.7 describes the methods used to determine film thicknesses experimentally whilst

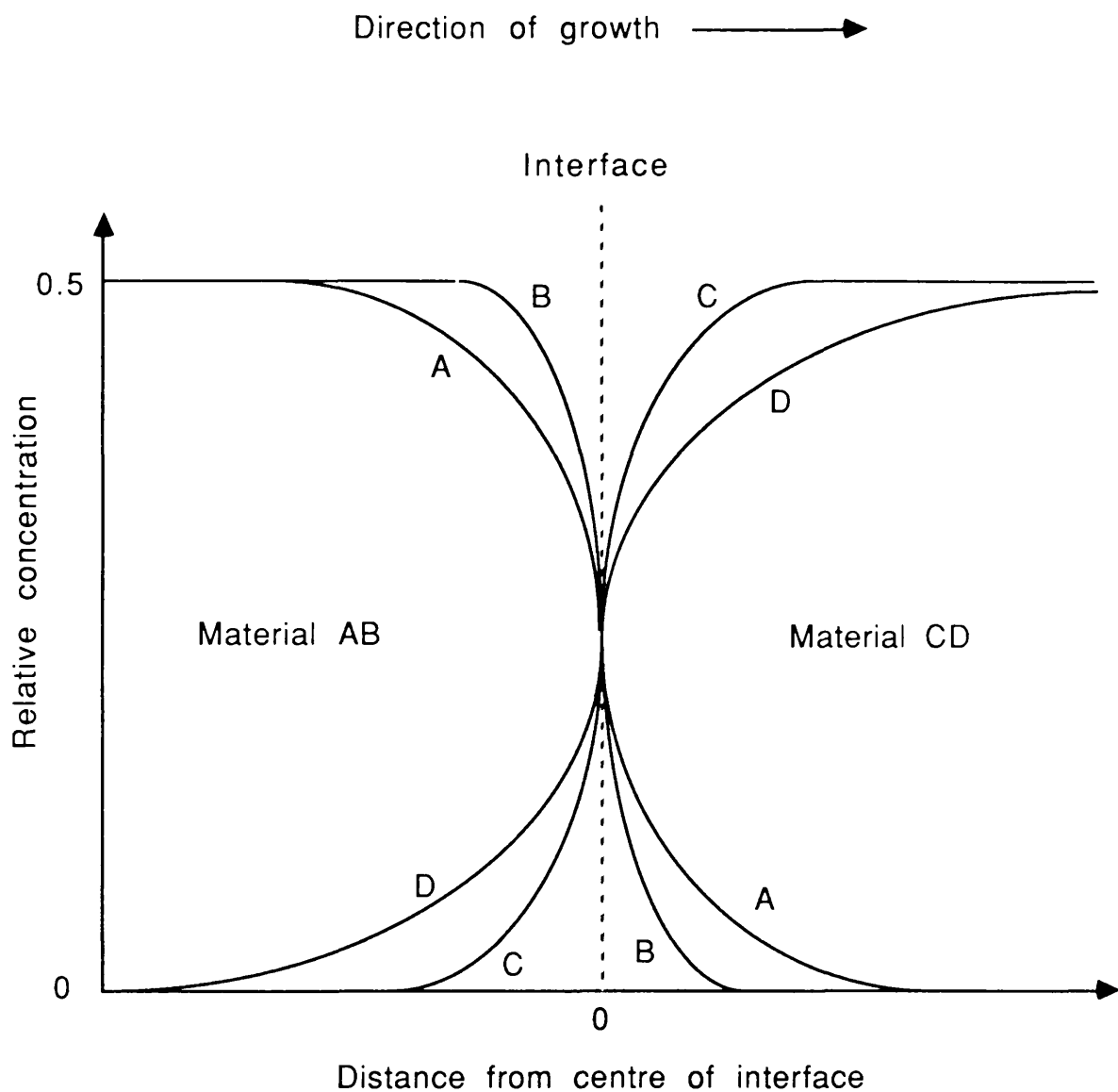


Figure 5.1: Graph showing the format used to map the changes in relative concentrations of elements across a layer boundary.

the final section gives an overview of the experimental procedure involved in a typical EDX experiment.

5.2 Factors affecting spatial resolution

The principal factors that govern the spatial resolution of EDX microanalysis are the radial current density distribution in the probe and the effect of elastic scattering within the specimen. Section 3.2 showed that the former is to a great extent under the control of the experimenter, although a high probe current is desirable to obtain adequate statistics in the characteristic x-ray peaks without unduly lengthening the time over which spectra are acquired. Control over the effect of elastic scattering is through selection of the thickness of specimen to be analysed, as this parameter is crucial in determining the extent of beam broadening.

When deciding the optimum value of specimen thickness, the main consideration relates to the fact that the number of x-rays generated (N) is proportional to the product of the total beam current (I_p) and specimen thickness (t);

$$N \propto I_p t \quad (5.1)$$

Thus, if t assumes too small a value, acquisition times for the attainment of adequate statistical significance again become unacceptably long. The optimum procedure then appears to be one in which the probe size and elastic scattering effects make comparable contributions to the spatial resolution.

5.3 Determination of suitable specimen thicknesses for EDX microanalysis using Monte Carlo simulations

To gain insight into how the spatial resolution of EDX microanalysis and specimen thickness are linked, it should be recalled that elastic scattering depends on the energy of the incident electron (E), the density of the material under investigation (ρ), the specimen thickness and the direction in which the electrons are propagating with respect to the lattice of the crystalline specimen. Glas (1986) showed that providing the electron beam is not travelling close to a prominent zone axis, the last named effect can, to a first approximation, be ignored. Under such an assumption, this section uses a simple single-scattering Monte Carlo program which follows a procedure described by Kyser (1979) and more recently by Joy (1988) to estimate suitable values of t for EDX microanalysis. The program, entitled 'Monty' is written in QL Super-Basic for use on a Sinclair QL minicomputer, and is listed in full in appendix A3.

The program computes the path of an electron through a single-element material (atomic number Z) by describing its trajectory as a series of elastic scattering events. This process is carried out for typically 2000 electrons to give statistically adequate information. A schematic diagram showing the coordinate system used in 'Monty' and the effect of beam spreading in the specimen is given in figure 5.2(a). In the course of each trajectory calculation, the effect of inelastic scattering is taken into consideration by assuming that the electron loses energy as a function of distance travelled through the specimen. Calculations for each electron terminate when it either exits the specimen or when its energy has fallen below a pre-determined minimum. At each scattering event (such as that represented in figure 5.2(b), the electron is deflected through an angle ϕ with respect to the incident direction and through azimuthal angle ψ with respect to the base of the cone. The distance travelled between events, or path length, is assigned the variable 'st' in the program. 'Monty' firstly calculates the screened Rutherford elastic scattering cross-section σ_E for an incident electron with energy E ;

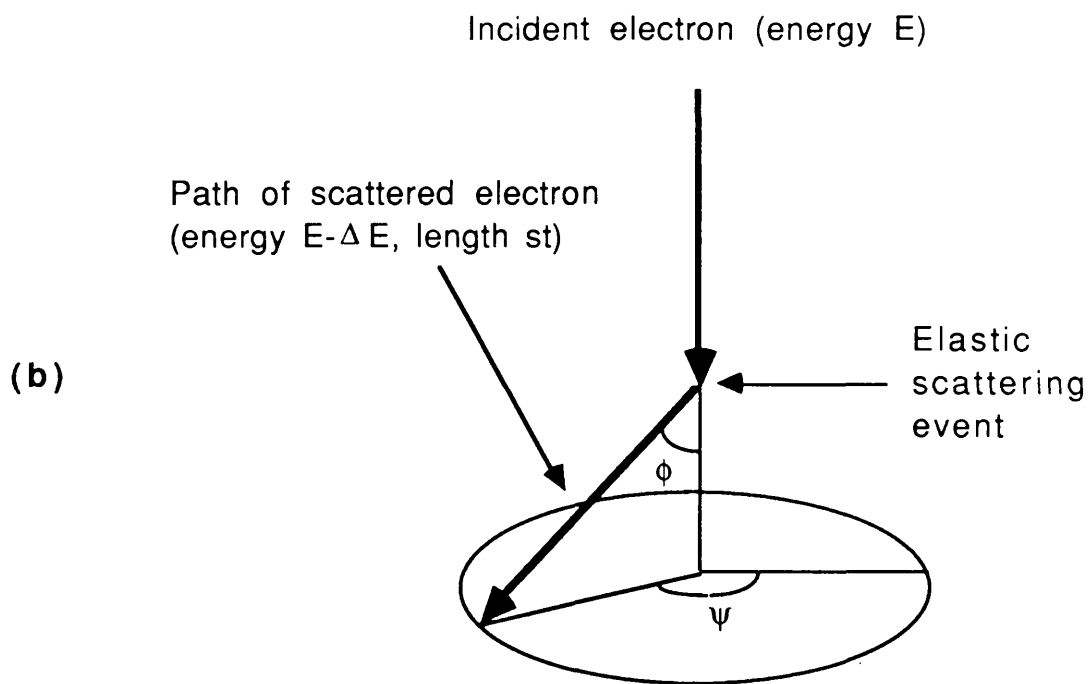
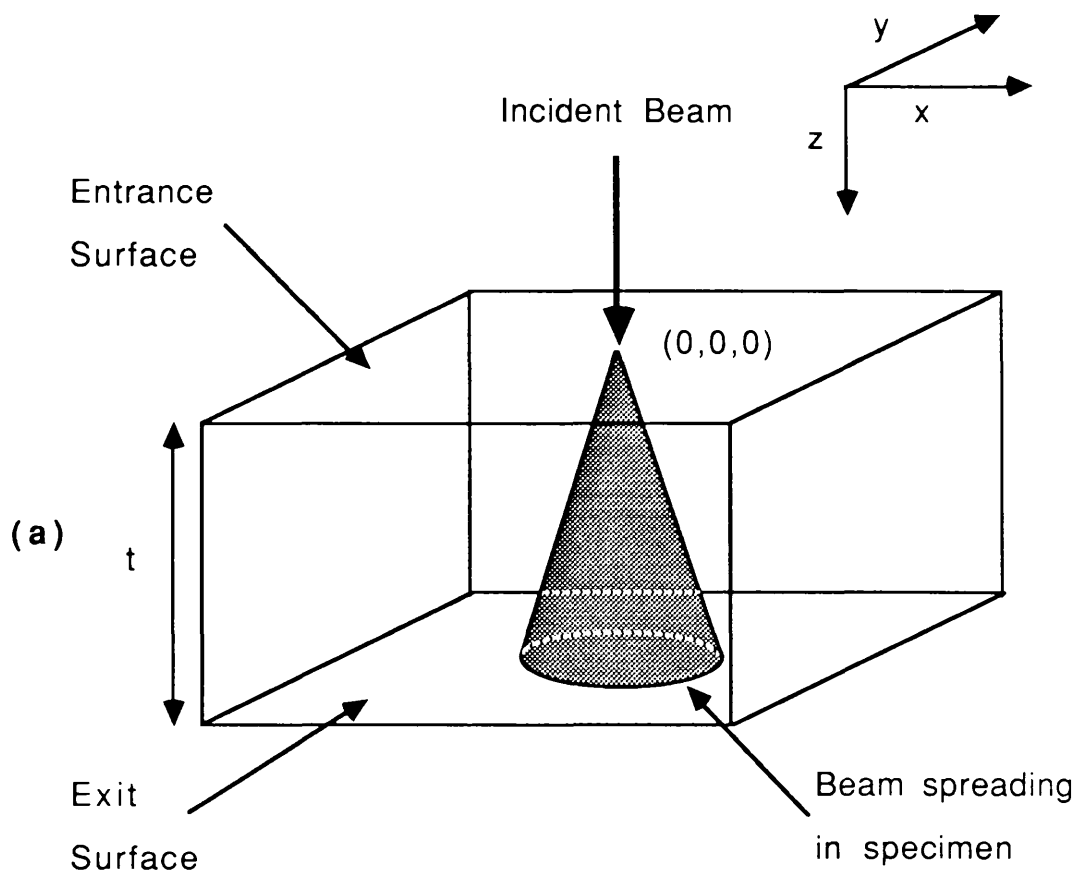


Figure 5.2: Coordinate system used for Monte Carlo simulations.

$$\sigma_E = 5.21 \times 10^{-21} \frac{Z^2}{E^2} \frac{4\pi}{\gamma(1+\gamma)} \left(\frac{E+511}{E+1022} \right)^2 \quad (\text{cm}^2) \quad (5.2)$$

where E is expressed in keV. γ is the charge screening factor which is defined as (Bishop, 1976);

$$\gamma = 3.4 \times 10^{-3} \frac{Z^{0.67}}{E} \quad (5.3)$$

Once σ_E and γ have been evaluated, the mean free path λ_P of an electron with energy E in the material is calculated using the relation;

$$\lambda_P = \frac{A}{N_A \rho \sigma_E} \cdot 10^7 \quad (\text{nm}) \quad (5.4)$$

where A is the atomic weight of the material in gm/mole and N_A is Avogadro's number. At each scattering event, angle ϕ is defined as;

$$\phi = \cos^{-1} \left(1 - \frac{2\gamma \cdot \text{RND}}{(1+\gamma \cdot \text{RND})} \right) \quad (5.5)$$

RND is a Super-Basic command that generates a random number between 0 and 1. Azimuthal angle ψ is not related to γ , and can be assigned any value between 0 and 2π with equal probability and so;

$$\psi = 2\pi \cdot \text{RND} \quad (5.6)$$

Each separate path length is related to λ_P using the following equation;

$$st = -\lambda_p \ln(RND) \quad (5.7)$$

As stated in the program outline, rather than calculating individual inelastic scattering events, the electron is assumed to lose energy continuously as it travels through the material. The rate of energy loss $-(dE/ds)$ is calculated using the Bethe relation (Bethe, 1930), where;

$$\frac{dE}{ds} = -78500 \frac{\rho Z}{AE} \ln\left(\frac{1.166E}{J}\right) \quad (\text{keV/cm}) \quad (5.8)$$

J is the mean ionisation potential in keV of the material which represents the rate of energy transfer due to all possible inelastic events and can be calculated analytically using the expression (Berger and Selzer, 1964);

$$J = \left[9.76Z + \frac{58.5}{Z^{0.19}} \right] \cdot 10^{-3} \quad (\text{keV}) \quad (5.9)$$

The amount of energy lost by an electron between successive collisions is $-\Delta E$, where;

$$\Delta E = st \left(\frac{dE}{ds} \right) \quad (5.10)$$

After each single path calculation, λ_p is re-evaluated to take into consideration the drop in electron energy. Equation 5.8 is invalid when E becomes less than J and so in 'Monty', J defines the lower limit of allowed electron energy. In film thicknesses of interest here (typically $\leq 50\text{nm}$), incident electrons lose only a small percentage of their initial energy in the specimen and so the lower energy limit is rarely reached.

Figure 5.3 shows a 2-dimensional projection in the x - z plane from a 2000

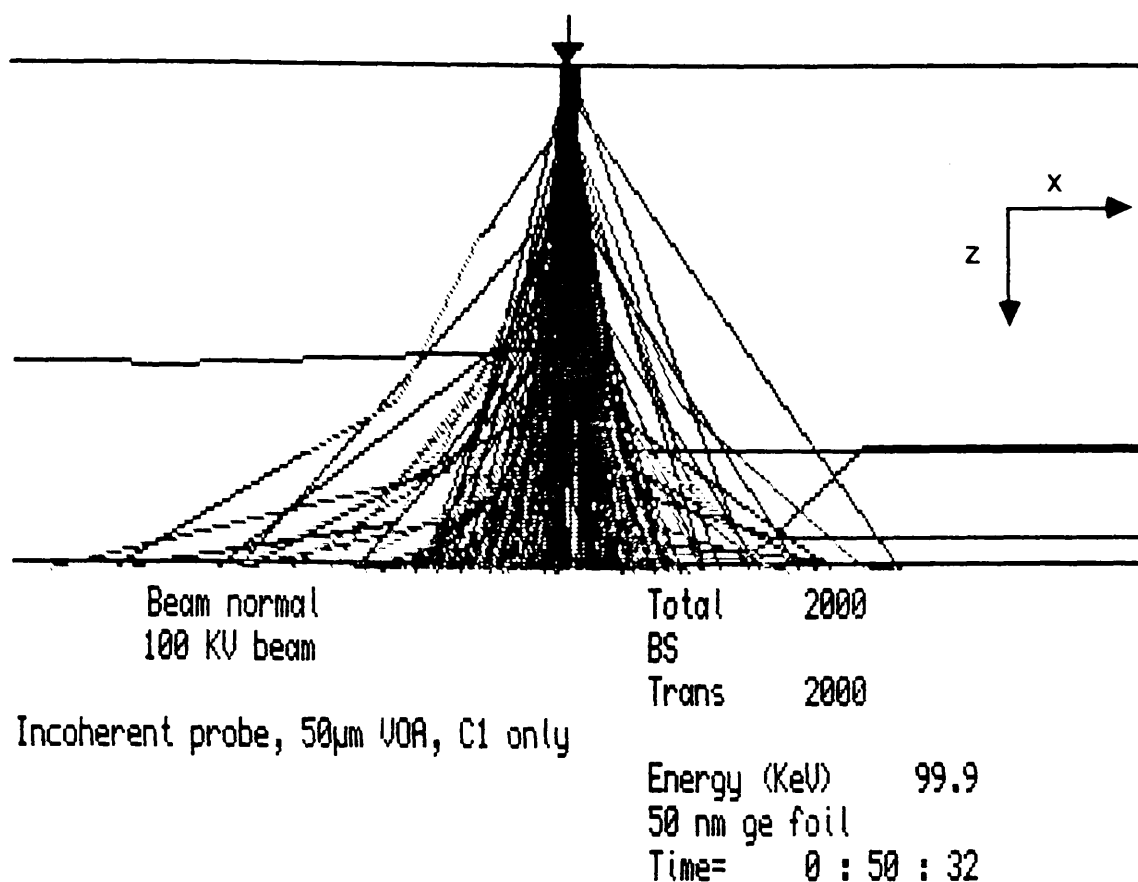


Figure 5.3: 2-dimensional projection of electron trajectories in the x-z plane from a Monte Carlo simulation run on a Sinclair QL minicomputer.

electron trajectory simulation using 'Monty'. Such a display gives an indication of the degree of beam spreading in the specimen. Of much greater use to the experimenter, however, is the numerical output from the simulations. A major advantage of the program is that it can be adapted to give information on specific problems related to beam spreading. Of interest in this section, for example, is the radial distribution of electrons at the exit surface as a function of specimen thickness. The specimen used for all simulations described here is a Ge ($Z=32$) film. Table 5.1 lists all the values of parameters relevant to the simulations.

In order to determine suitable values of t for EDX microanalysis, the extent to which beam spreading is affected by t only is considered by executing 'Monty' for values between 0 and 50nm with a δ -function probe incident at the origin. Figure 5.4 shows, in histogram form with a sampling interval of 0.2nm, the radial distribution of transmitted electrons in the material from simulations in Ge films possessing thicknesses of 10, 30 and 50nm. Using these data, the radial values within which 50% and 90% of the total transmitted signal is detected can be deduced easily. A graph plotting these values as a function of t is given in figure 5.5. In agreement with the single scattering expression of Reed and co-workers (1977), the graph shows that generation of x-rays distant from the probe becomes increasingly serious as t increases. Comparison of figure 5.5 with the information on the radial probe current density distribution given in figure 3.12 suggests that for the resolution of EDX microanalysis to be influenced equally by the instrument and the specimen, sample thicknesses of ~45nm would be an ideal choice under the experimental conditions used here. However, as it is rarely possible to choose precise values experimentally, values of t in the range 30 to 80nm were used for the experiments described in this thesis.

Description	Symbol	Value
Atomic Weight	A	72.6
Atomic Number	Z	32
Density	ρ	5.35gcm^{-3}
Mean Ionisation Potential	J	0.34keV
Elastic Scattering Cross-section	σ_E	$5.72 \times 10^{18} \text{ cm}^2$
Mean Free Path	λ	$3.9 \times 10^{-6} \text{ cm}$
Charge Screening Factor	γ	3.47×10^{-4}
Rate of Energy Loss	dE/ds	$10.8 \times 10^3 \text{ keVcm}^{-1}$

Table 5.1: Numerical values of parameters relevant to Monte Carlo simulations in a Ge foil with 100keV electrons incident.

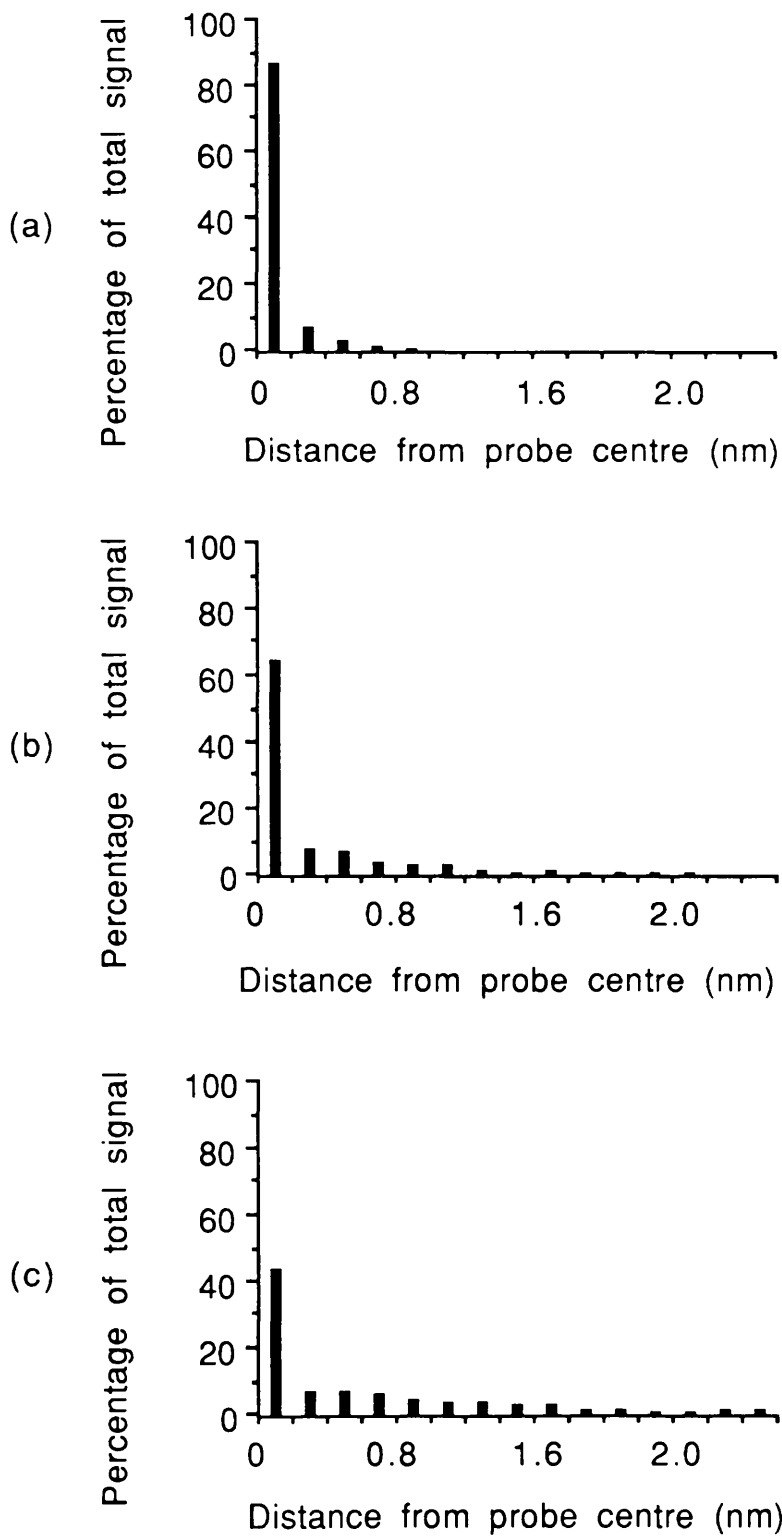


Figure 5.4: Graphs showing the radial distribution of transmitted electrons from Monte Carlo simulations in an (a) 10nm, (b) 30nm and (c) 50nm Ge foil using a δ -function incident probe.

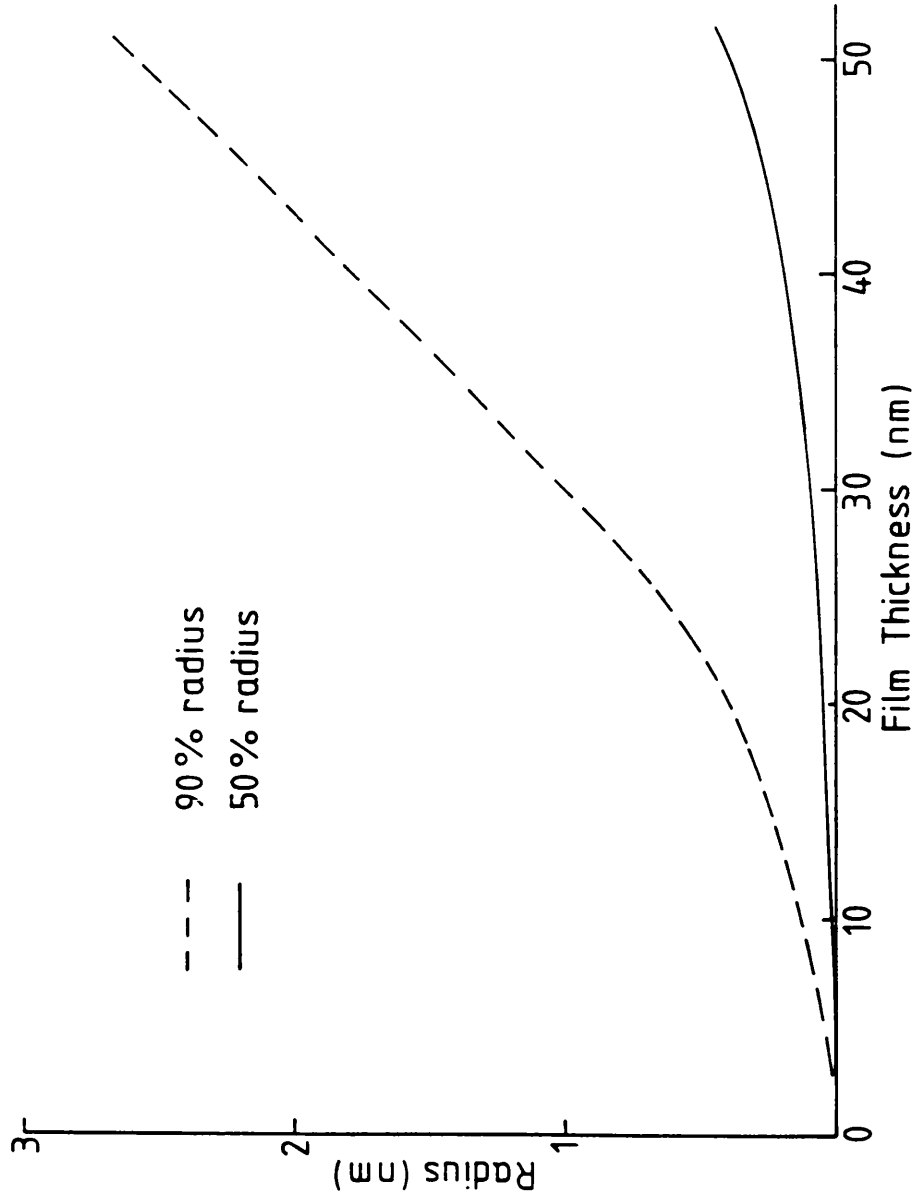


Figure 5.5: Variation of radii containing 50% and 90% of generated x-rays as a function of film thickness estimated from Monte Carlo simulations.

5.4 Simulation of detected signal profiles

Additional subroutines can be included in the Monte Carlo program to predict the way in which the detected signal from an elemental species changes as a function of probe position across an interface. To this point in the chapter, simulations have only been concerned with a δ -function probe incident on the specimen. Here, 'Monty' is adapted so that the probe is defined by the radial current density distribution $j(r)$ used in this thesis for all EDX microanalysis. A full description of the steps taken to calculate $j(r)$ is given in chapter 3. Figure 5.6 shows $j(r)$ in histogram form, with each bar corresponding to the percentage of total probe current contained within an annulus of width 0.05nm. The data from this graph is used as the probability distribution function that determines the radial component of the initial coordinates of each trajectory simulation. As the probe is radially symmetric, the angular component of the initial coordinates can have any value between 0 and 2π , and can be calculated in the same manner as that shown in equation 5.6.

Estimation of detected signals using data taken solely from the exit surface of the specimen in 'Monty' would not give a true reflection of the distribution of x-ray signal emanating from the specimen, and would serve to over-estimate the degree of signal spreading. This is because a high percentage of electrons travel some distance into the specimen before the first scattering event takes place. The theoretical model used here assumes that an x-ray can be generated with equal probability at any point on the path along which the electron travels. If, in the course of a completed simulation, the total length travelled by all the electrons in the specimen is L , and l_n is that travelled in the n^{th} section, then the detected signal from the n^{th} section, s_n (as a fraction of the maximum possible), that is attributable to elemental species Y can be

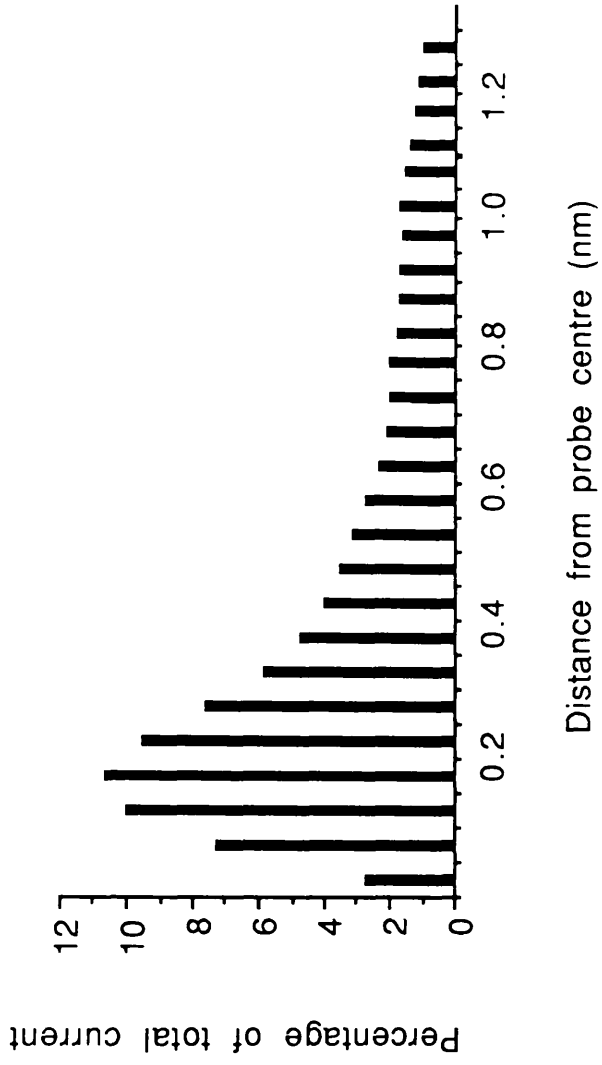


Figure 5.6: Current density distribution in radial histogram form for probe suitable for EDX microanalysis.

expressed as;

$$s_n = \frac{l_n}{L} c_n \quad (5.11)$$

where c_n is the concentration of Y (as a fraction of the maximum possible) in the n^{th} volume element. Provided that elemental concentrations in the specimen do not vary significantly in the y-direction, analysis of signals as a function of probe position across an interface can be treated as a one-dimensional problem and so, as figure 5.7 illustrates, this model is applied to 'Monty' by dividing the specimen into a series of sections possessing a width 0.2nm along the x-axis, infinite length along the y-axis and height t . In the course of each separate path calculation, 'Monty' records both the total path length travelled and that travelled through each section. At the end of a full simulation, the path length data is displayed in histogram form, showing the distribution of l_n/L as a function of distance from the probe centre along the x-axis. This distribution is denoted as $P(x)$. Figure 5.8 shows $P(x)$ taken from 2000 electron simulations in 10, 30 and 50nm Ge films using the incident probe radial current distribution illustrated in figure 5.6.

In a manner similar to the ADF profile simulation technique described in chapter 4, an estimate of the detected signal, $S(x)$, as a function of position at points across an interface from elemental species Y can be expressed as a one-dimensional convolution between $P(x)$ and profile $C(x)$ related to the actual change in concentration of Y along a direction perpendicular to the interface;

$$S(x) = P(x) * C(x) \quad (5.12)$$

Therefore, if the probe is positioned at the i^{th} section, the signal s_i from that point is;

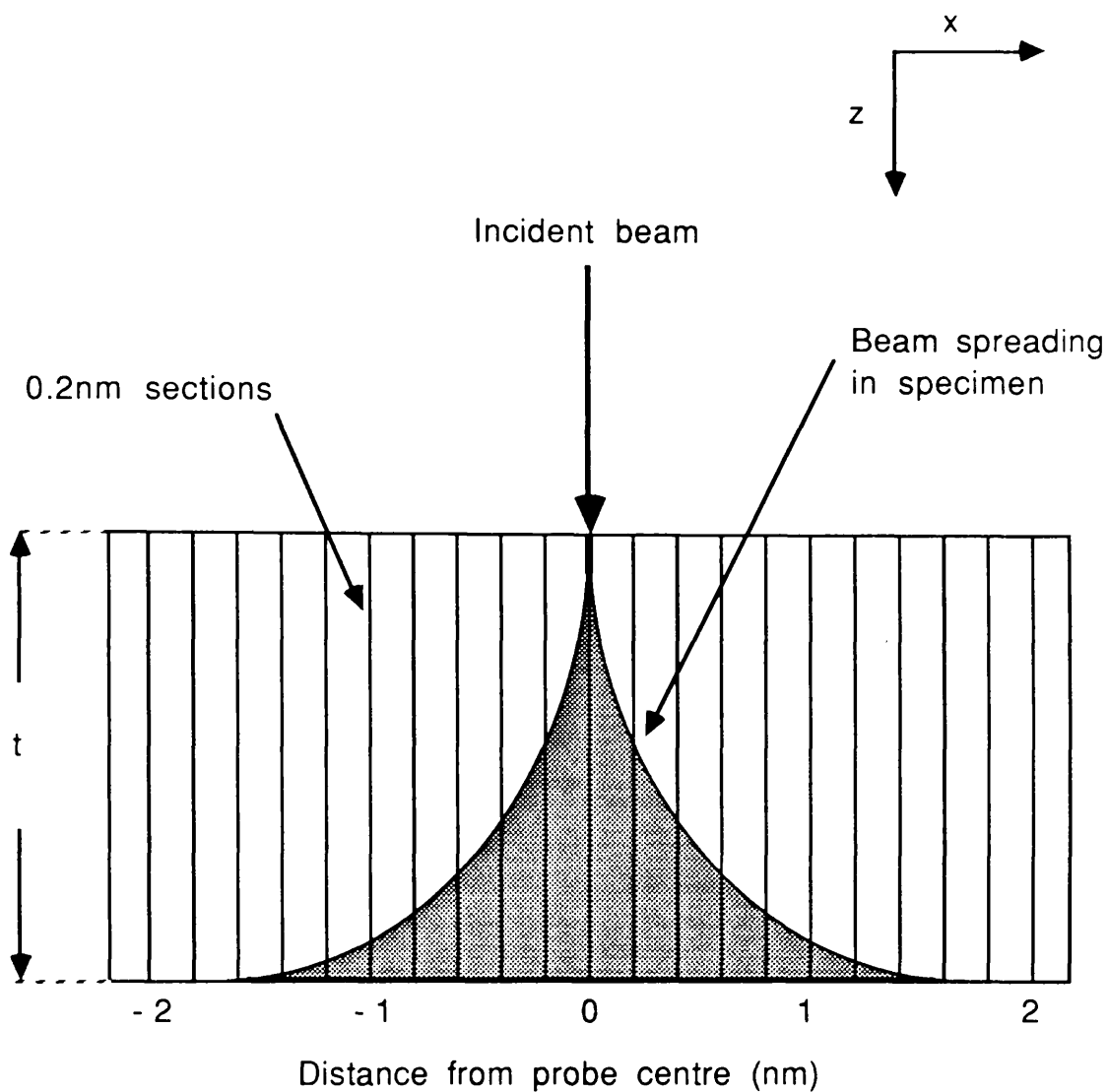


Figure 5.7: Schematic diagram illustrating the system used to estimate the path length distribution of electron trajectories in Monte Carlo simulations.

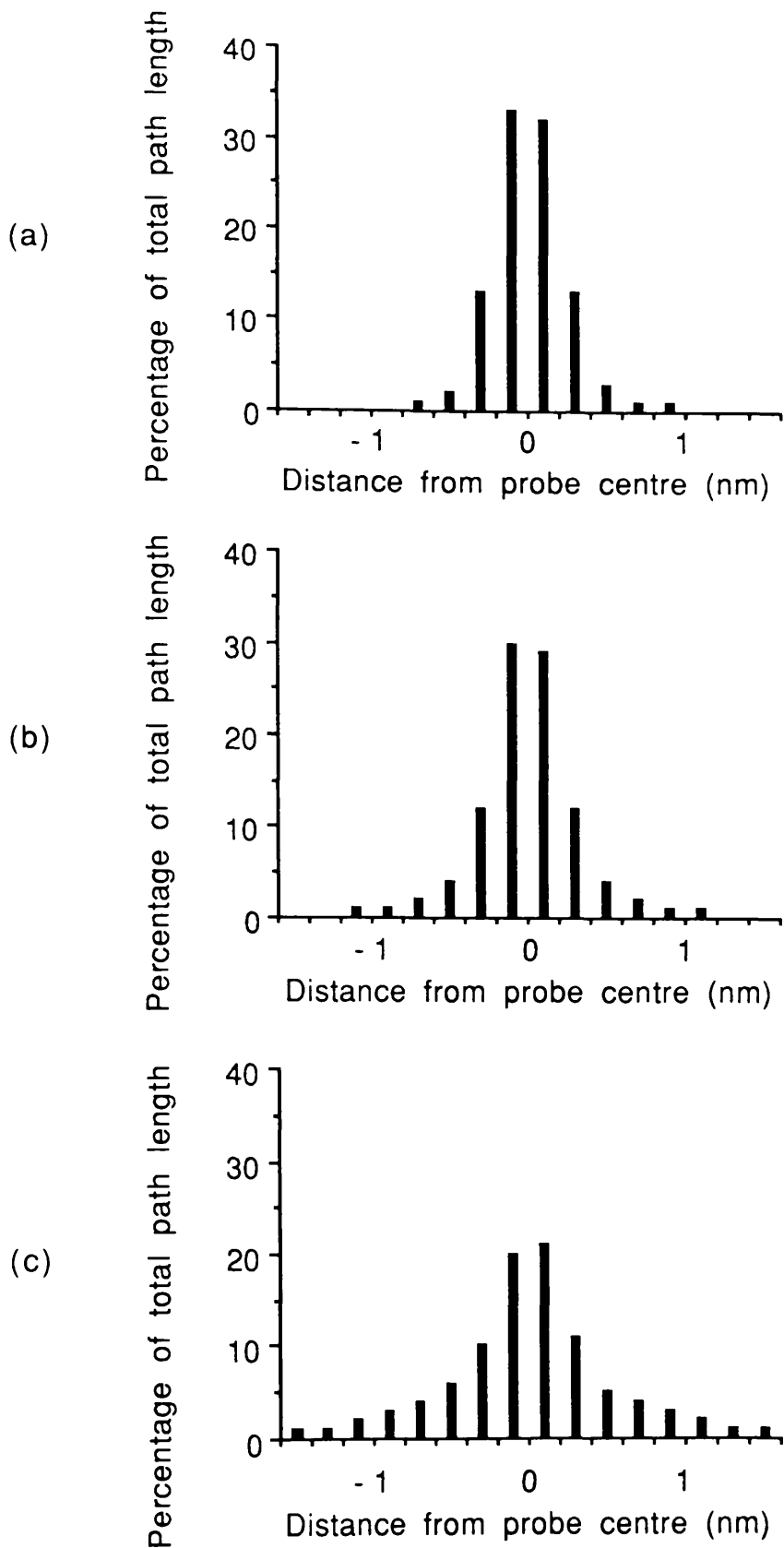


Figure 5.8: Graphs showing the distribution of trajectory path lengths in film thicknesses of (a) 10, (b) 30 and (c) 50nm using Monte Carlo simulations.

$$S_i = \frac{1}{L} \sum_{m=-\frac{Q}{2}}^{\frac{Q}{2}} I_m c_{i+m} \quad (5.13)$$

where $P(x)$ is spread over Q sections. Using the path length data from the 50nm Ge film, figure 5.9 shows $S(x)$ calculated for four interfaces of varying degrees of abruptness. In future chapters, these results will be used in comparison with experimental data as an aid to the interpretation of results.

5.5 Self-absorption of characteristic x-rays

Having established a suitable range of t for EDX microanalysis that balances the constraints of probe size and beam spreading, the effects of self-absorption of characteristic x-rays of interest in the specimen becomes an important consideration. In the AlGaAs/GaAs system, this applies to the Al K characteristic x-ray (1.487 keV) which is particularly susceptible to absorption by Ga and As. In the InGaAs/InP system, Ga and As may also contribute significantly to the self-absorption of the P K characteristic x-ray (2.015 keV).

The method used to estimate the effects of self-absorption is illustrated in figure 5.10. The model assumes that, as the electron beam passes through the specimen, x-rays can be generated from any section ds positioned a distance s into the specimen. The distance in the specimen in a direct line between ds and the detector through which generated photons must pass is known as the absorption path length and is denoted by d_{abs} . At the exit surface, where $s=s_{max}$, d_{abs} has maximum value $d_{abs}(max)$ where;

$$d_{abs}(max) = t \csc(\xi) \quad (5.14)$$

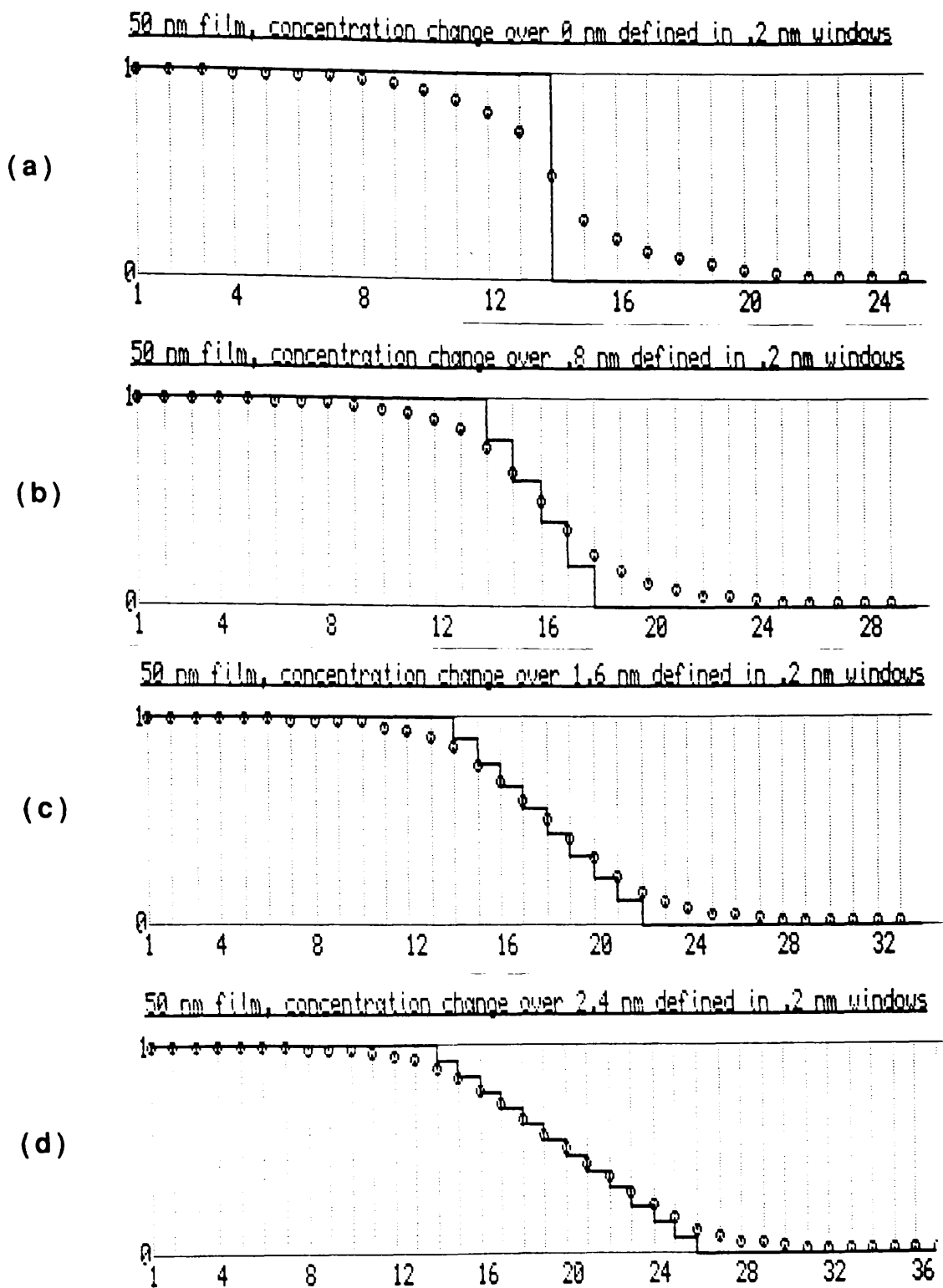


Figure 5.9: Estimates of the detected signal as a function of probe position from an (a) an abrupt interface and from interfaces with concentration distributions spread over (b) 0.8, (c) 1.6 and (d) 2.4nm.

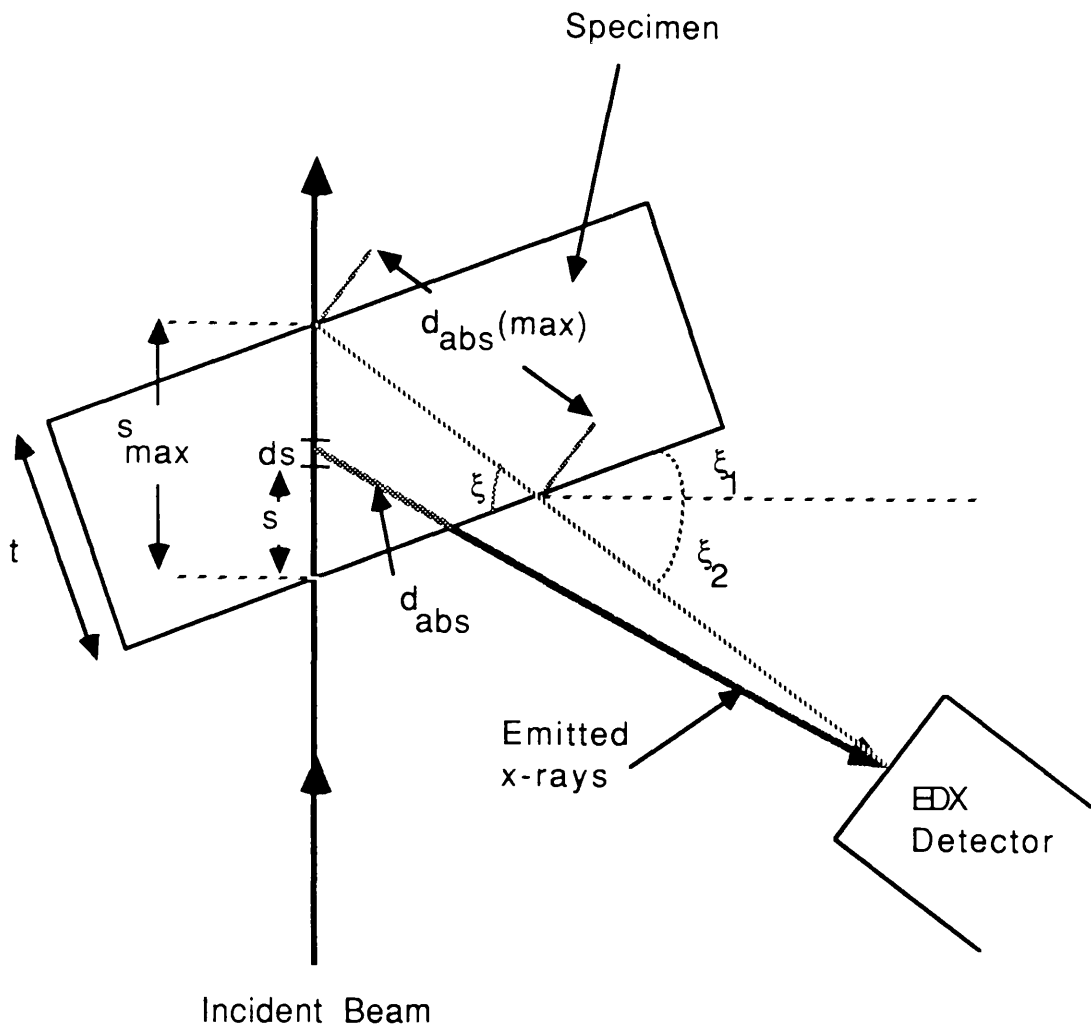


Figure 5.10: Illustration of method used to calculate the effects of self-absorption in the specimen.

ξ is the sum of two angles;

$$\xi = \xi_1 + \xi_2 \quad (5.15)$$

ξ_1 is the angle through which the specimen is tilted towards the detector and has a value of 22° for all experiments discussed in this thesis. ξ_2 is the angle subtended by the detector relative to the horizontal plane. Using the values of ξ_2 given in chapter 3, ξ is 32.5° for experiments using the conventional detector and 47° for those using the windowless detector. The x-ray signal intensity at the detector from ds , $I_{OA}(ds)$, is expressed as;

$$I_{OA}(ds) = I_{OI} \frac{ds}{s_{max}} \exp \left[- \left(\frac{\mu}{\rho} \right) \rho d_{abs} \right] \quad (5.16)$$

where I_{OI} is the total generated x-ray intensity and (μ/ρ) is the mass absorption coefficient for the characteristic x-ray energy of interest in the specimen. Integration of equation 5.16 gives the total detected intensity I_{OA} ;

$$\begin{aligned} I_{OA} &= \int_0^{s_{max}} I_{OA}(ds) ds \\ &= \frac{I_{OI}}{s_{max}} \int_0^{s_{max}} \exp \left[- \left(\frac{\mu}{\rho} \right) \rho d_{abs} \right] ds \end{aligned} \quad (5.17)$$

Using equation 5.14, the ratio of the detected intensity to that generated can be calculated;

$$\frac{I_{OA}}{I_{OI}} = \frac{\left[1 - \exp \left[- \left(\frac{\mu}{\rho} \right) \rho t \csc(\xi) \right] \right]}{\left(\frac{\mu}{\rho} \right) \rho t \csc(\xi)} \quad (5.18)$$

Using the mass absorption coefficients calculated by Heinrich (1987), table 5.2 lists the values of (μ/ρ) for the absorption of the P K characteristic photon in InP and $\text{In}_{0.53}\text{Ga}_{0.47}\text{As}$ and that of the Al K characteristic photon in GaAs and $\text{Al}_{0.3}\text{Ga}_{0.7}\text{As}$. Also listed are the densities of InP, GaAs and their lattice-matched alloys. The final column of table 5.2 gives the values of I_{OA}/I_{OI} for $t=45\text{nm}$ for all relevant combinations of characteristic signal, specimen type and detector used in this thesis. As would be expected, the results show that there is greater absorption at lower values of ξ . The results also indicate that there is a significant amount of absorption ($\sim 10\%$) of the Al K characteristic signal in the AlGaAs/GaAs system. Therefore, interpretation of EDX data acquired from this system must take self-absorption into consideration at all times. In the InGaAs/InP system, absorption of the P K characteristic signal is significant only in the presence of a high concentration of Ga and As. The highest absorption correction that must be made is when analysing the P K signal from a region of InGaAs using the conventional detector.

5.6 Low energy detector efficiencies

The ability of the Li-doped Si crystal in the EDX detectors used in this project to detect photons with an energy below $\sim 3\text{keV}$ is affected by the absorption of photons in the Au contact at the crystal surface, the inefficient or 'dead' layer of Si and, in the case of the conventional detector, in the Be

Photon Energy (keV)	Absorbing Material	Density (gcm^{-3})	$(\mu/\rho) \text{ (cm}^2\text{g}^{-1}\text{)}$	I_{OA}/I_{OA} Conventional Windowless ($\xi = 32.5^\circ$) ($\xi = 47^\circ$)	
PK 2.015	InP	4.787	1316	0.97	0.98
	$\text{In}_{0.53}\text{Ga}_{0.47}\text{As}$	5.526	2440	0.95	0.96
Al K_α 1.487	GaAs	5.316	5461	0.89	0.92
	$\text{Al}_{0.3}\text{Ga}_{0.7}\text{As}$	4.870	5415	0.90	0.93

Table 5.2: Parameters relevant to the absorption of characteristic x-rays of interest in materials used in this project.

window. The characteristic x-rays of interest to this thesis that have energies in this region are the P K (2.015keV) and the Al K (1.487keV) transitions. This section estimates the detector efficiency ϵ for both characteristic signals in the conventional and windowless detectors. It should be noted that the values of ϵ discussed here are theoretical predictions and that, if possible, reliance should be placed on experimental data. The values of parameters that are relevant to this discussion are listed in table 5.3.

In a conventional detector, absorption of photons in the Be window is by far the most significant effect, and it is convenient to describe $\epsilon_{\text{conventional}}$ in terms of an effective Be window thickness, τ_{Be} . That found suitable for the detector used here is 8.3 μm . At low energies, $\epsilon_{\text{conventional}}$ is expressed as;

$$\epsilon_{\text{conventional}} = \exp \left[- \left(\frac{\mu}{\rho} \right)_{\text{Be}} \rho_{\text{Be}} \tau_{\text{Be}} \right] \quad (5.19)$$

where ρ_{Be} is the density of Be. $(\mu/\rho)_{\text{Be}}$ is the mass absorption coefficient for the photon energy of interest in Be and is evaluated following Heinrich (1987). Equation 5.19, when evaluated for photons with energies corresponding to that of the P K and Al K characteristic x-rays gives values of $\epsilon_{\text{conventional}}$ of 0.90 and 0.75 respectively to within an accuracy of $\leq 2\%$ (Chapman et. al., 1983) and so the analysis of experimental results must take the fall-off of $\epsilon_{\text{conventional}}$ into consideration. As future chapters will show, this is achieved by including $\epsilon_{\text{conventional}}$ directly in the calculations used to determine the relative elemental concentrations from x-ray spectra.

In the windowless detector, absorption occurs only in the Au contact and the Si 'dead' layer. A result of this is that $\epsilon_{\text{windowless}}$ begins to fall below unity at lower energies than $\epsilon_{\text{conventional}}$. $\epsilon_{\text{windowless}}$ can be expressed in terms of an effective Au contact thickness, τ_{Au} ;

Detector Type	Principal absorbing material	Density (gcm^{-3})	τ	(μ/ρ) for P K x-ray ($\text{cm}^2 \text{g}^{-1}$)	(μ/ρ) for Al K x-ray ($\text{cm}^2 \text{g}^{-1}$)	ϵ for P K x-ray	ϵ for Al K x-ray
Conventional	Be	1.82	8.3 μm	71.9	188.9	0.90	0.75
Windowless	Au	19.32	20nm	1192	2301	0.995	0.991

Table 5.3: Parameters relevant to the calculation of low energy detection efficiencies for characteristic x-rays of interest to this thesis

$$\epsilon_{\text{windowless}} = \exp \left[- \left(\frac{\mu}{\rho} \right)_{\text{Au}} \rho_{\text{Au}} \tau_{\text{Au}} \right] \quad (5.20)$$

Paterson (1989) estimated τ_{Au} using several methods. Although this results in values of τ_{Au} ranging from 11 to 28nm, a value of $\tau_{\text{Au}}=20\text{nm}$ gives $\epsilon_{\text{windowless}}$ values of 0.995 and 0.991 for photons with energies corresponding to those of the P K and Al K characteristic x-rays respectively and so the effect of absorption of the characteristic signals of interest in the windowless detector is negligible.

5.7 Experimental determination of film thickness

The experimental method used in this thesis in the initial determination of specimen thickness follows a convergent beam electron diffraction (CBED) technique described by Kelly et. al. (1975). This technique is most suited to measuring film thicknesses that are greater than those suitable for microanalysis. Equation 5.1 shows, however, that estimates of the value of t in specimen regions of interest can be made by simply comparing x-ray count rates with those recorded from the area examined by the CBED technique. This procedure is followed for all values of film thickness quoted in this thesis. The values of parameters used in the following discussion of the CBED technique that are relevant to the materials of interest in this project are listed in table 5.4.

The CBED technique is based on a two-beam dynamic theory that relates the minima in intensity oscillations in the CBED patterns to specimen thickness using the following equation (McGillavry, 1940);

Element	$f(2\theta_{004})$ (Å)
In	4.081
Ga	2.606
As	2.760
P	1.629
Al	0.582

Material	Lattice Constant (nm)	V_C (m ³)	$F_{(004)}$ (nm)	$\xi_{(004)}$ (nm)
GaAs	0.565	1.8×10^{-28}	2.15	71.2
Al _{0.3} Ga _{0.7} As	0.565	1.8×10^{-28}	1.90	80.3
InP	0.587	2.02×10^{-28}	2.28	75.1
In _{0.53} Ga _{0.47} As	0.587	2.02×10^{-28}	2.46	69.7

Table 5.4: Parameters relevant to the measurement of film thicknesses by the CBED technique.

$$\left(v_i^2 + \frac{1}{\xi_{(hkl)}^2} \right) = n_i^2 \quad (5.21)$$

where v_i is the deviation of the i^{th} minimum from the exact Bragg position, $\xi_{(hkl)}$ is the extinction distance for a Bragg reflection from the (hkl) plane and n_i is an integer. For a film that has a thickness between $m\xi_{(hkl)}$ and $(m+1)\xi_{(hkl)}$, $n_i = m+1$. $\xi_{(hkl)}$ is expressed as;

$$\xi_{(hkl)} = \frac{\pi V_c \cos(2\theta_{(hkl)})}{\lambda F_{(hkl)}} \quad (5.22)$$

V_c is the volume of a unit cell of the material, $\theta_{(hkl)}$ is the Bragg angle for a reflection from the (hkl) plane and $F_{(hkl)}$ is the structure factor as defined in section 4.2. v_i is expressed as;

$$v_i = \frac{\lambda}{d_{(hkl)}^2} \left(\frac{\Delta\theta_i}{2\theta_{(hkl)}} \right) \quad (5.23)$$

$d_{(hkl)}$ is the separation between the (hkl) planes and $\Delta\theta_i$ is the angle between the exact Bragg position of the diffracted beam and the centre of the i^{th} minimum. In order to reduce the effects of multiple scattering, low order reflections (where, for example, $d_{(hkl)} > 0.15\text{nm}$) should be avoided. Conversely, high order reflections ($d_{(hkl)} < 0.05\text{nm}$) should also be avoided because diffracted intensities are very low and hence difficult to observe without recourse to image processing. The reflection used in this project for both the AlGaAs/GaAs and InGaAs/InP systems that conforms to the above constraints is along the (004) plane. $F_{(004)}$ can be expressed in terms of the relativistically

corrected atomic scattering factors $f(2\theta_{(004)})$ of each elemental species in the material of interest for example, in InP;

$$F_{(004)} = 4[f_{\text{In}} + f_{\text{P}}] \quad (5.24)$$

In $\text{In}_x\text{Ga}_{1-x}\text{As}$, $F_{(004)}$ is expressed as;

$$F_{(004)} = 4[xf_{\text{In}} + (1-x)f_{\text{Ga}} + f_{\text{As}}] \quad (5.25)$$

Evaluation of $F_{(004)}$ for GaAs and $\text{Al}_x\text{Ga}_{1-x}\text{As}$ is carried out in a similar manner. Using the information on structure factors, $\xi_{(004)}$ is evaluated for all the materials of interest (table 5.4). Film thicknesses are found experimentally by moving the convergent probe across the specimen from $t=0$. As t increases, the number of minima converging the centre of the disc are counted until the parameter $\Delta\theta_1/2\theta_{(004)}$ can be easily measured from the diffraction pattern. Figure 5.11 shows such a pattern that clearly shows the (000) and (004) discs and the intensity oscillations in the (004) reflection. $\Delta\theta_1$ and $2\theta_{(004)}$ are clearly marked on the figure.

As stated previously, having determined the local thickness in one region of a specimen for a particular material/detector configuration, subsequent thickness measurements for the same configuration need only be related to the number of counts recorded in a particular characteristic x-ray peak. For example, using a windowless detector, ~7000 counts are recorded in the Ga K_α characteristic peak from an acquisition time of 10s in a 50nm thick GaAs film.

5.8 Experimental procedure

This chapter has discussed several aspects related to EDX microanalysis of

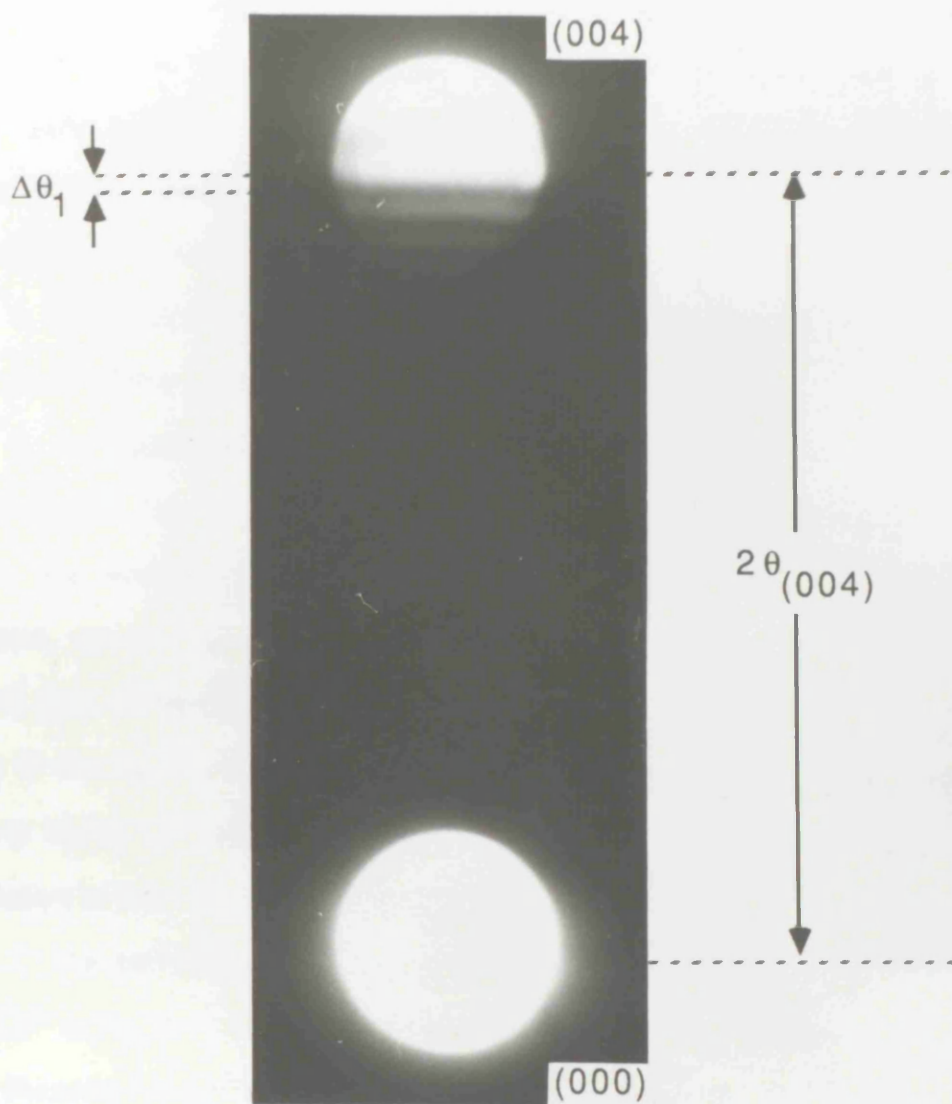


Figure 5.11: CBED pattern showing the (000) and (004) Bragg reflections that are used to determine foil thickness

semiconductor multilayer systems that must be taken into consideration in an experimental situation.

The first step of a typical experiment is to locate and orient the multilayers. Location of the layers can be achieved quickly by monitoring the ADF signal. This is because, even at standard PSL excitations, there is sufficient elastically scattered signal to provide contrast between both InGaAs and InP, and AlGaAs and GaAs layers. The specimen is then tilted $\sim 22^\circ$ along the (004) Kikuchi line to a position midway between the [210] and [310] poles. The reasons for choosing such an orientation are as follows;

1. The specimen is oriented so that the incident beam direction is parallel to the plane of the layers.

2. As described previously, the Monte Carlo analyses are based on the assumption that electron channeling effects are negligible if prominent zone axes are avoided (Glas, 1986). Although 22° tilt suits the purposes of this project, as long as poles are avoided, the precise angular distance from the [110] pole along the (004) line is unimportant. Glas (loc. cit.) notes that this is due to the fact that electron channeling effects are generally very small when using highly convergent illumination thus leading to a correspondingly small variation in the x-ray emission as a function of specimen orientation.

3. The self-absorption of x-rays increases significantly at low tilt angles and so 22° is found to be a suitable choice of tilt that reduces such effects without significantly increasing the effective thickness of the specimen.

At this stage, specimen thicknesses are determined using the procedure described in section 5.7.

The pre-specimen optical configuration in the microscope used for EDX microanalysis that defines the probe current density distribution at the specimen was described in detail in chapter 3. With the microscope carefully aligned in this configuration, acquisition of x-ray spectra from positions across layer interfaces can begin. The aim of the experiment is to acquire enough

information so that measured concentration distributions across layers and interfaces such as that in figure 5.1 can be produced. With this in mind, figure 5.12 shows a schematic diagram showing the positions at which spectra are acquired in the course of a typical experiment. The distance between each acquisition point is determined by the aims of the experiment and the rate at which concentrations change as a function of distance - this can be estimated quickly by acquiring a high-angle ADF image of the relevant area. Figure 5.13 shows an x-ray spectrum from an EDX experiment of the type described. In this case, the spectrum was taken from a position close to an interface between InGaAs and InP using a conventional detector. The characteristic peaks that are used to determine the relative concentrations are clearly labelled. An advantage of the AN10000 acquisition system (described in chapter 3) is that the acquisition software enables groups of such spectra to be treated as one data file thereby simplifying the analysis procedure.

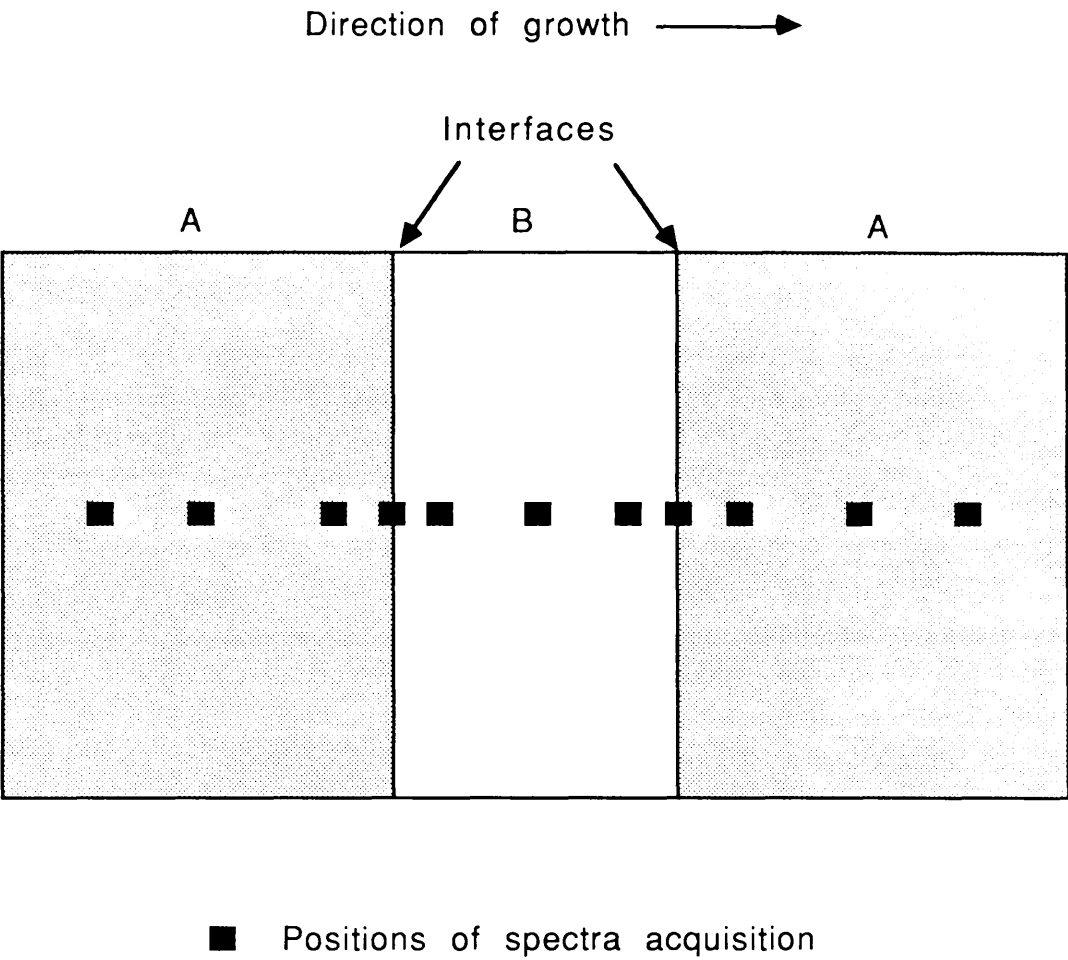


Figure 5.12: Schematic diagram showing the positions at which x-ray spectra are acquired during the course of a typical experiment.

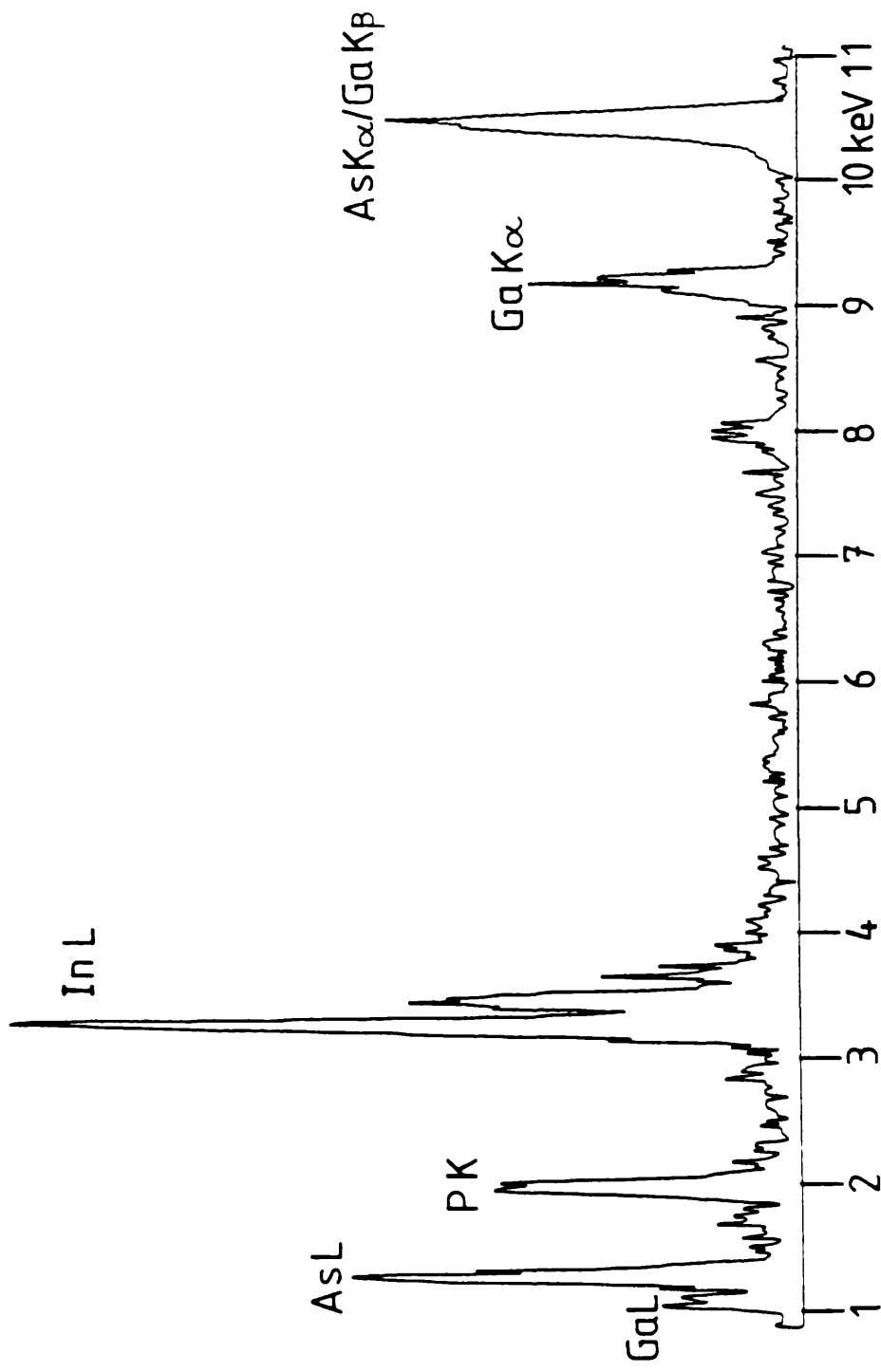


Figure 5.13: Typical x-ray spectrum from a position close to an interface in an InGaAs/InP multilayer system.

Chapter 6

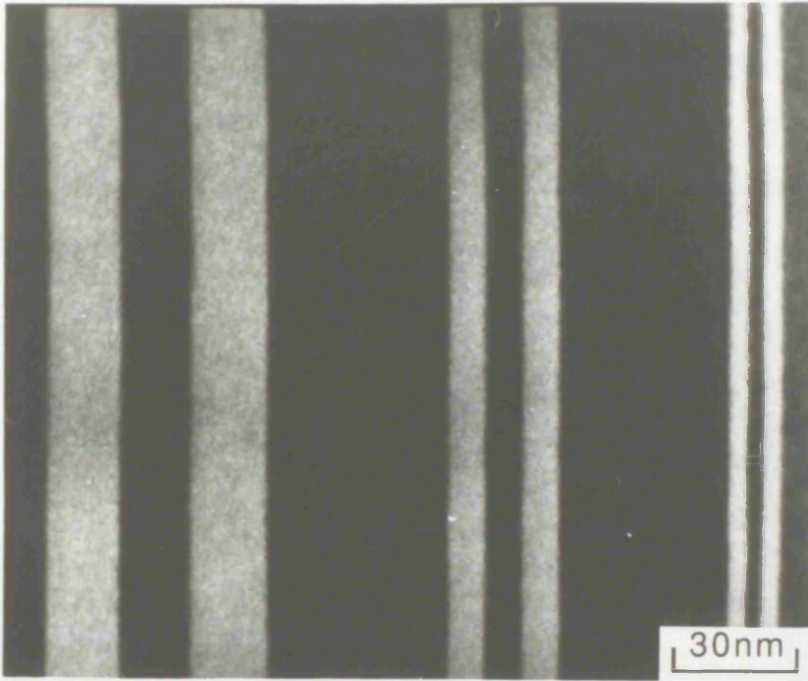
Analysis of the AlGaAs/GaAs system grown by MBE.

6.1 Introduction

Growth of the lattice matched AlGaAs/GaAs multilayer system by MBE is an established technique that can produce layer interfaces of a very high quality. Such a system is therefore ideally suited for use as a test specimen in experiments that compare the abilities of high-angle ADFI and EDX microanalysis for the determination of elemental concentrations across multilayers with high spatial resolution. The specimen used here comprised three pairs of AlGaAs layers whose widths are 20, 10 and 5nm. A digital (002) dark field image of the specimen is given in figure 6.1.

The chapter begins by discussing high-angle ADFI analyses of the specimen and assesses both the spatial resolution of the technique and the accuracy with which \bar{Z} in the material can be measured using image contrast information and a knowledge of the elastic scattering cross sections. This is followed by a section which describes a series of EDX microanalysis experiments that were performed on the test specimen. The section begins by describing the method used to calculate elemental compositions in the AlGaAs/GaAs system from x-ray spectra. Using results calculated by this method, conclusions are drawn on the way in which spatial resolution of the technique is affected by beam broadening in the specimen. Taking beam spreading effects into consideration, the compositions of the specimen are measured at the layer centres. In section 6.4, high-angle ADFI and EDX microanalysis are directly compared and conclusions are drawn on the way in which data amassed by the two techniques can be used to best effect.

Direction of growth \longrightarrow



Light bands: AlGaAs

Dark bands: GaAs

Figure 6.1: (002) dark field image of an AlGaAs/GaAs multilayer consisting 20nm, 10nm and 5nm AlGaAs wells.

6.2 High-angle ADFI

To enable as full an understanding as possible of results from an investigation into the variation of \bar{Z} across multilayers using high-angle ADFI, it is important to establish experimentally the spatial resolution of the technique and the confidence with which the relative values of \bar{Z} between layers of different composition can be determined from image contrast information and a knowledge of the elastic scattering cross-sections. This section addresses both considerations by applying the image analysis technique discussed in chapter 4 to high-angle ADF images of the AlGaAs/GaAs test specimen shown in figure 6.1.

6.2.1 Determination of the spatial resolution

Figure 6.2 shows high-angle ADF intensity profiles taken from digital images of (a) the 20nm, (b) the 10nm and (c) the 5nm AlGaAs wells that were grown in the test specimen. Each profile is the average of 10 consecutive linescans and has had the level of noise reduced by means of an 11-point median filter. No correction for the variation in thickness across the specimen has been made. The figure clearly shows that there is a considerable decrease in high-angle ADF signal intensity over the area examined by the images, particularly in profile (c). This is attributable to a non-uniformity in specimen thickness that is a feature of cross-sectional specimens made by the technique described in chapter 3. An important feature, however, is that although t varies significantly over the area of interest, the distance over which the detected signal intensity changes at interfaces (denoted here as the detected transition width) varies only slightly when the three profiles are compared. This suggests

that the effect of beam broadening in the specimen is not as significant for high-angle ADFI as it is for EDX microanalysis. An explanation for this is that signals generated a long way from where the probe is centred are not collected by the ADF detector at all. Whilst it is desirable to use as thin a region of specimen as possible for high-angle ADF analyses, the value of film thickness is not the overriding criterion. Chapter 4 showed that corrections made to profiles to account for changes in t tend to exaggerate noise effects and so it is also of importance to select a region of specimen in which there is only a small variation in thickness. Using these arguments, the interfaces found most suitable for the determination of the spatial resolution are those between the left hand 10nm AlGaAs well in figure 6.2(b) and the GaAs layers.

Figure 6.3 shows three separate intensity profiles (denoted A, B and C) that were taken from a high-angle ADF image of the AlGaAs well of interest. Each profile is an average of 8 consecutive linescans, and the level of noise has been reduced by means of an 11-point median filter. As for all high-angle ADF images discussed in this thesis, each pixel corresponds to a sampling interval of 0.13nm in a direction perpendicular to the plane of the layers. No variations in local film thickness were observed and so thickness correction steps were not necessary. The profiles in figure 6.4 (denoted D, E and F) were processed in the same way as those in figure 6.3, but were taken from an image acquired at a different location along the AlGaAs well. The discussion on profile analysis given in chapter 4 used, as an example, profiles taken from a third high-angle ADF image of the well of interest. These profiles, together with those in figures 6.3 and 6.4 show that the variation in detected signal across the well is symmetric and so profile analysis will concentrate on a single transition type, namely the GaAs to AlGaAs transition.

The method used to estimate the variation in \bar{Z} in a direction perpendicular to the plane of the layers, $f(\bar{Z})$, from a high-angle ADF intensity profile is described in chapter 4 and involves the convolution of the linear probe current

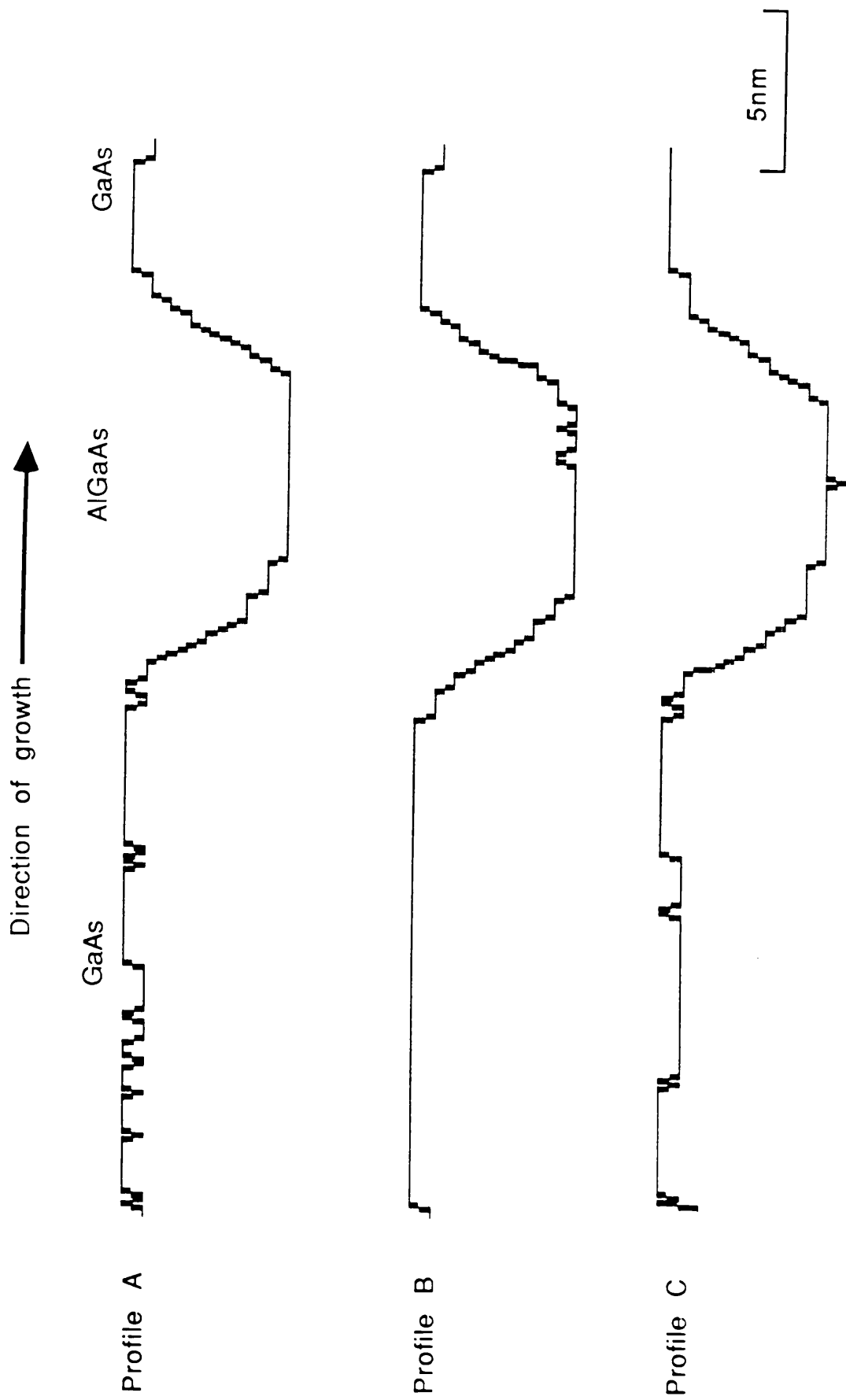


Figure 6.3: 3 processed profiles taken from a high-angle ADF image of the specimen shown in figure 6.1.

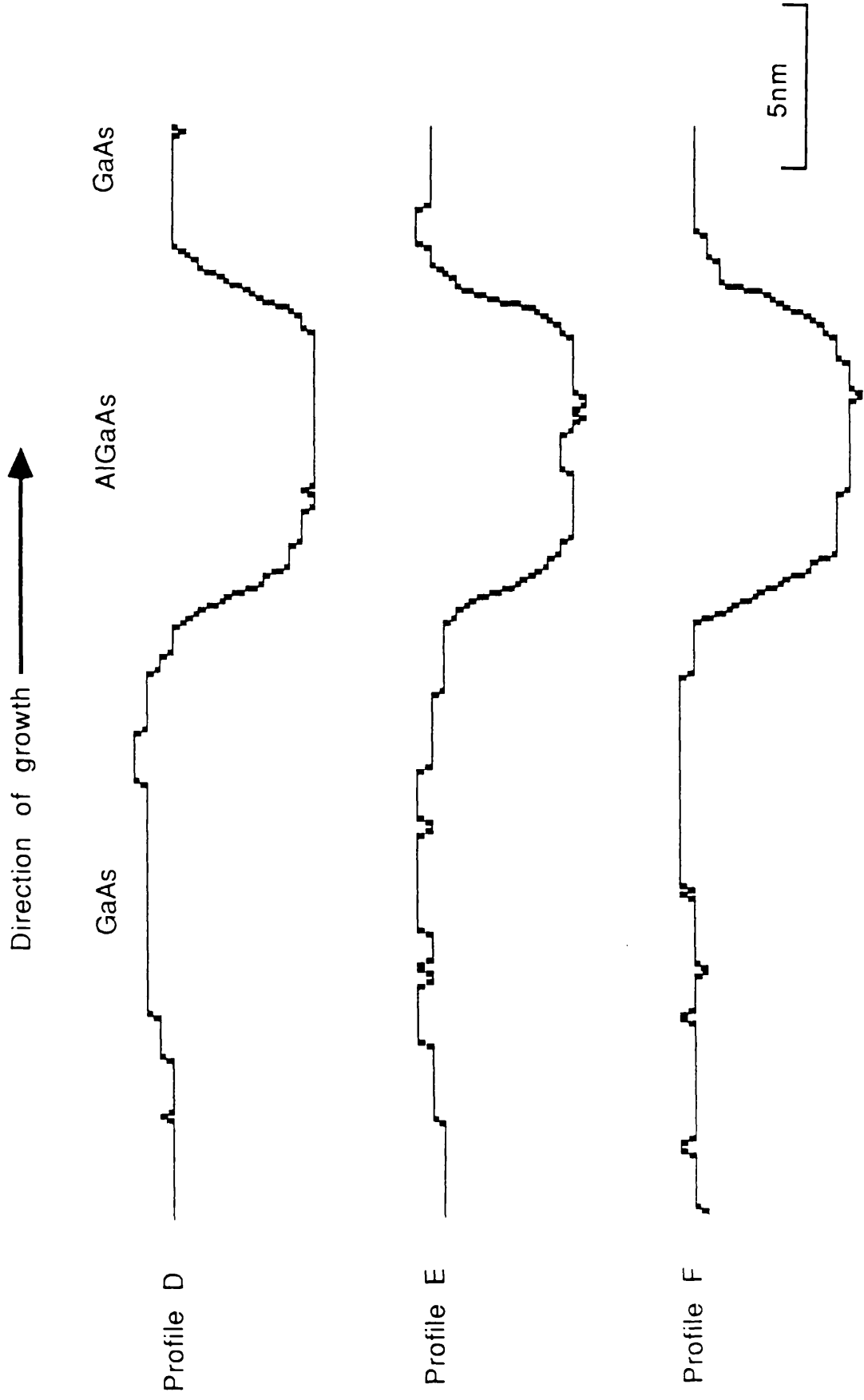


Figure 6.4: 3 processed profiles taken from a high-angle ADF image of a different area of the same specimen analysed in figure 6.3.

density distribution $J(x)$ with simulations of $f(\bar{Z})$ that possess linearly varying interface transition widths of different sizes to find the 'best fit' to the experimental profile. The discussion in chapter 4 demonstrated that the best fit to the experimental profiles was found using an interface transition spanning 1nm, although that spanning 1.5nm also gave reasonable agreement. Transition widths of 0 and 0.5nm underestimated the detected profile, whereas that of 2nm gave an overestimate. However, figures 6.5 and 6.6 demonstrate that, in general, the best fit to profiles A to F was obtained using an interface transition of 2.5nm (~4.4 unit cell dimensions). Transition widths of 0.5nm (~0.9 unit cell dimensions) and 1.5nm (~2.6 unit cell dimensions) were, as figures 6.7 and 6.8 show, found to underestimate the signal variation detected experimentally, although the 1.5nm transition does give a better agreement with profile D, E and F than A, B and C. Figures 6.9 and 6.10 show that transition widths of 3.5nm (~6.2 unit cell dimensions) and 4.5nm (~8 unit cell dimensions) give an overestimate of the detected profile in all cases.

The results show that clear differences in the quality of fit between simulated profile and experiment can be observed if the theoretical transition width is varied by $\pm 1\text{nm}$. Under optimum experimental conditions, simulated transition widths of 1nm gave good agreement with experiment, which suggests that the interfaces are of a high quality. However, such conditions, possibly attributable to some instability in the position of the probe at the specimen caused by the introduction of noise from external sources, are not easily achieved and calculated transition widths of 2.5nm generally give agreement with experiment. If the spatial resolution of the technique is defined as the distance from an abrupt interface at which the measured \bar{Z} profile begins to change (equivalent to one half of the best fit transition width) then, from the data discussed in this section, the spatial resolution is no worse than 1.25nm. For examination of both the AlGaAs/GaAs and InGaAs/InP systems, a technique

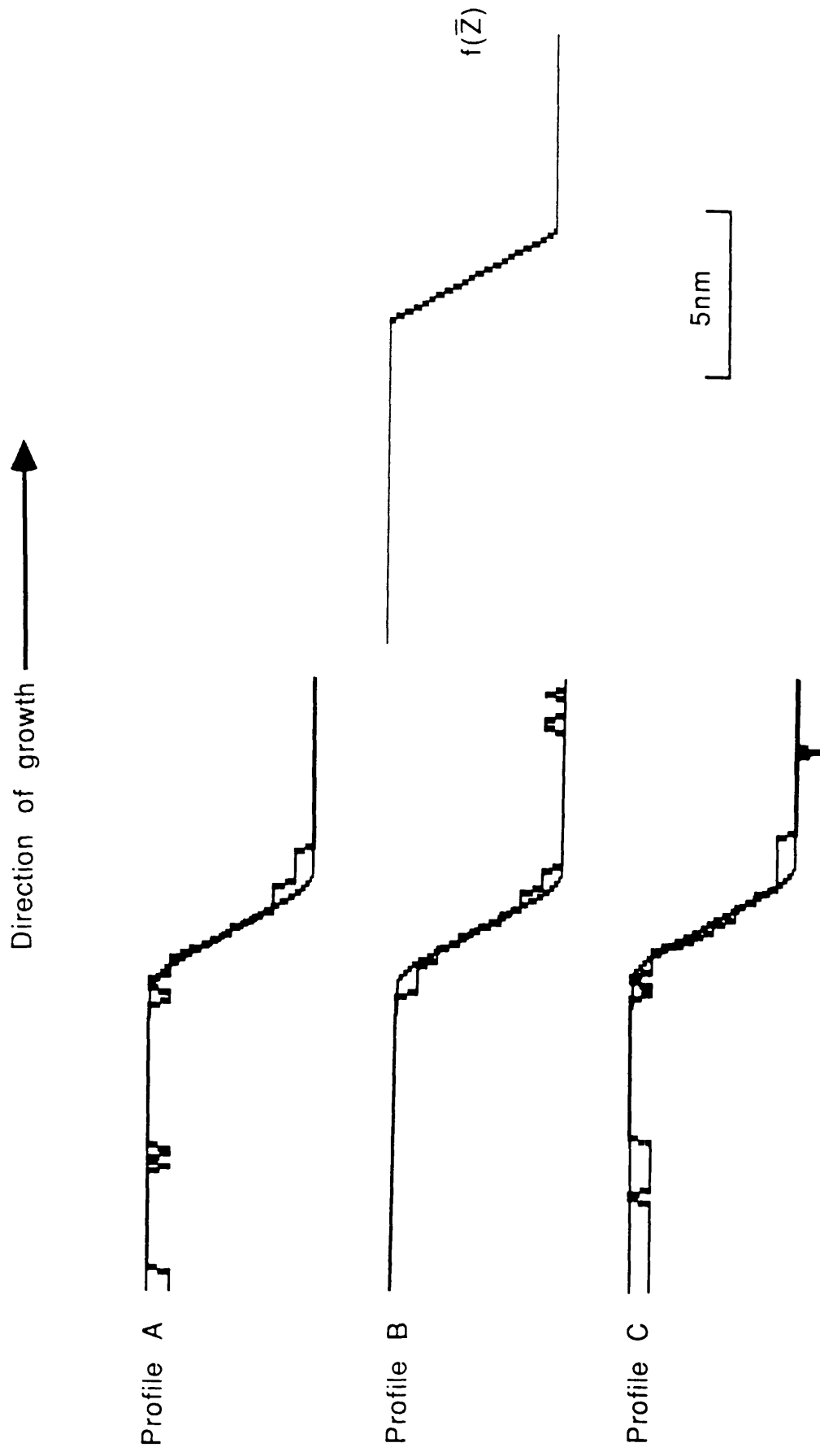


Figure 6.5: Comparison between interfaces from profiles A, B and C with a simulated profile calculated from a transition width of 2.5nm.

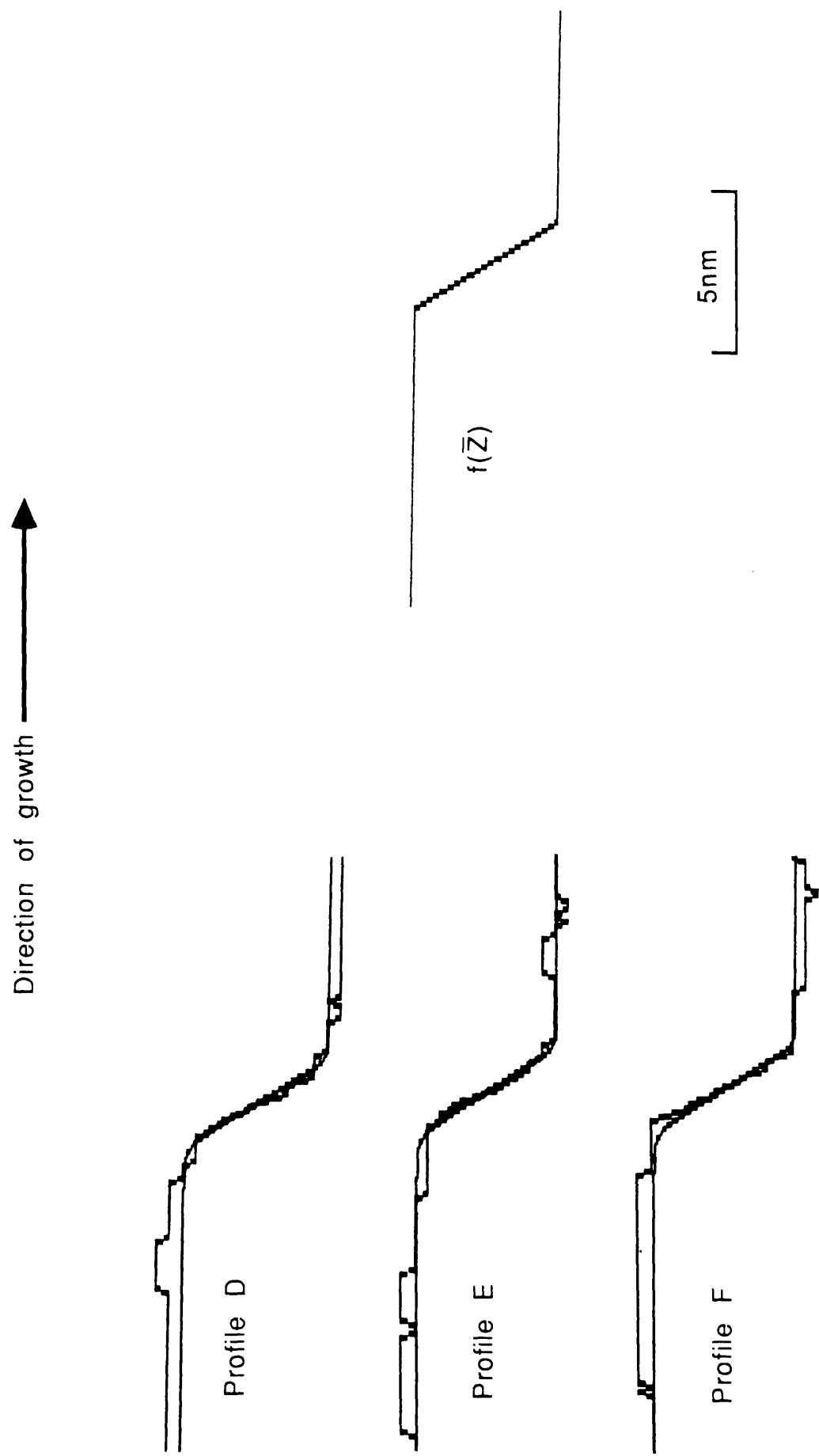


Figure 6.6: Comparison between interfaces from profiles D, E and F with a simulated profile calculated from a transition width of 2.5nm.

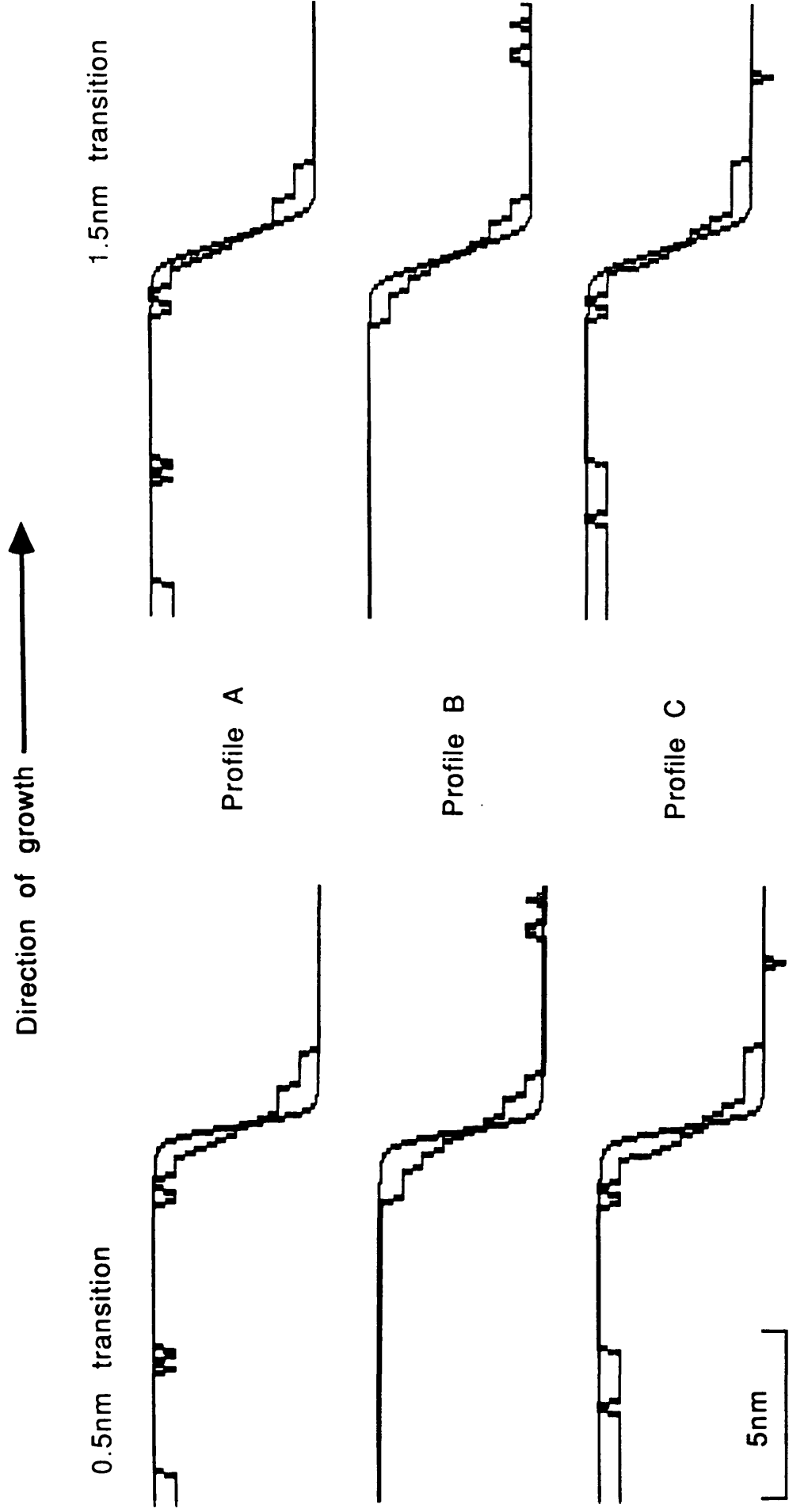


Figure 6.7: Comparison between interfaces from profiles A, B and C with simulated profiles calculated from transition widths of 0.5nm and 1.5nm.

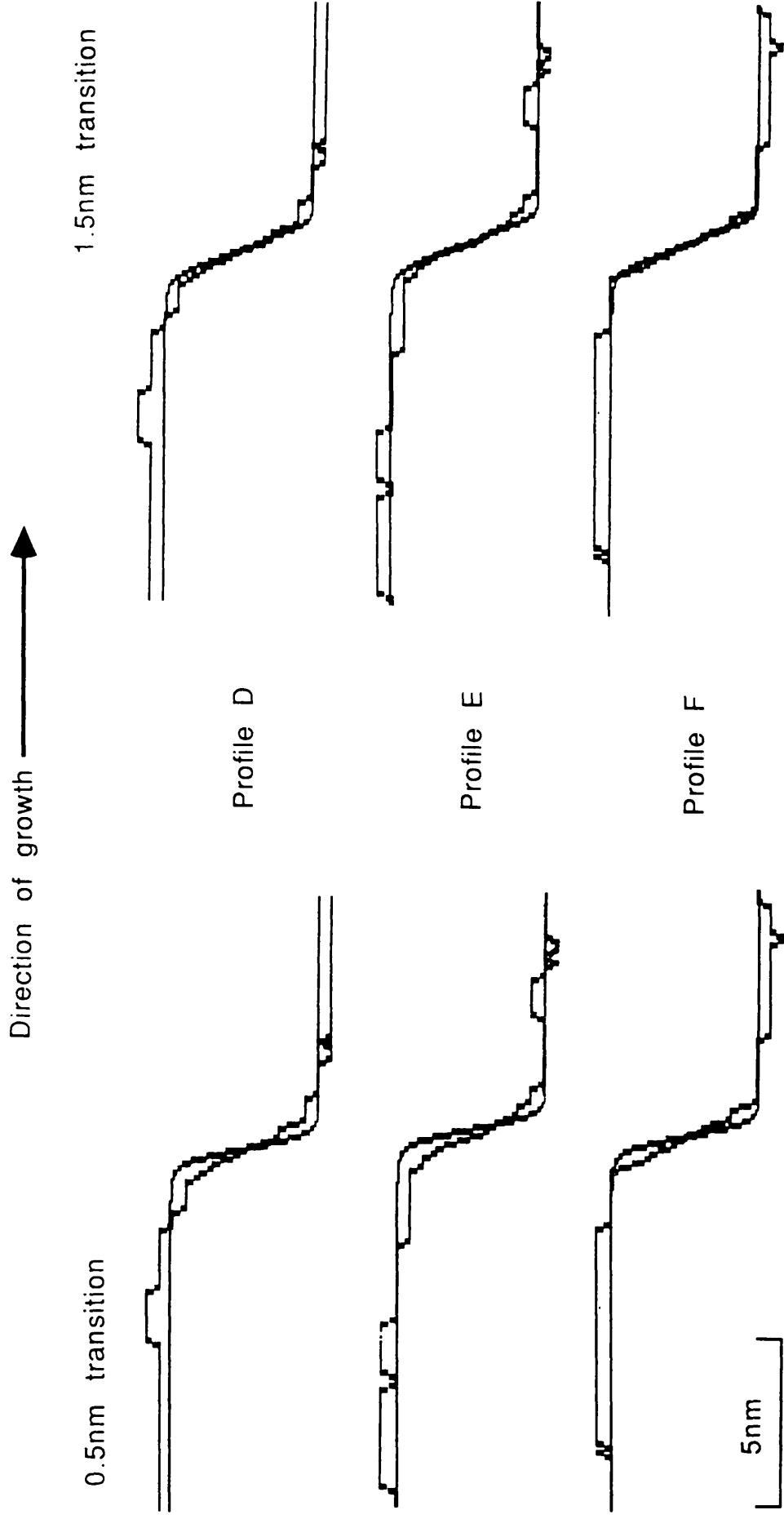


Figure 6.8: Comparison between interfaces from profiles D, E and F with simulated profiles calculated from transition widths of 0.5nm and 1.5nm.

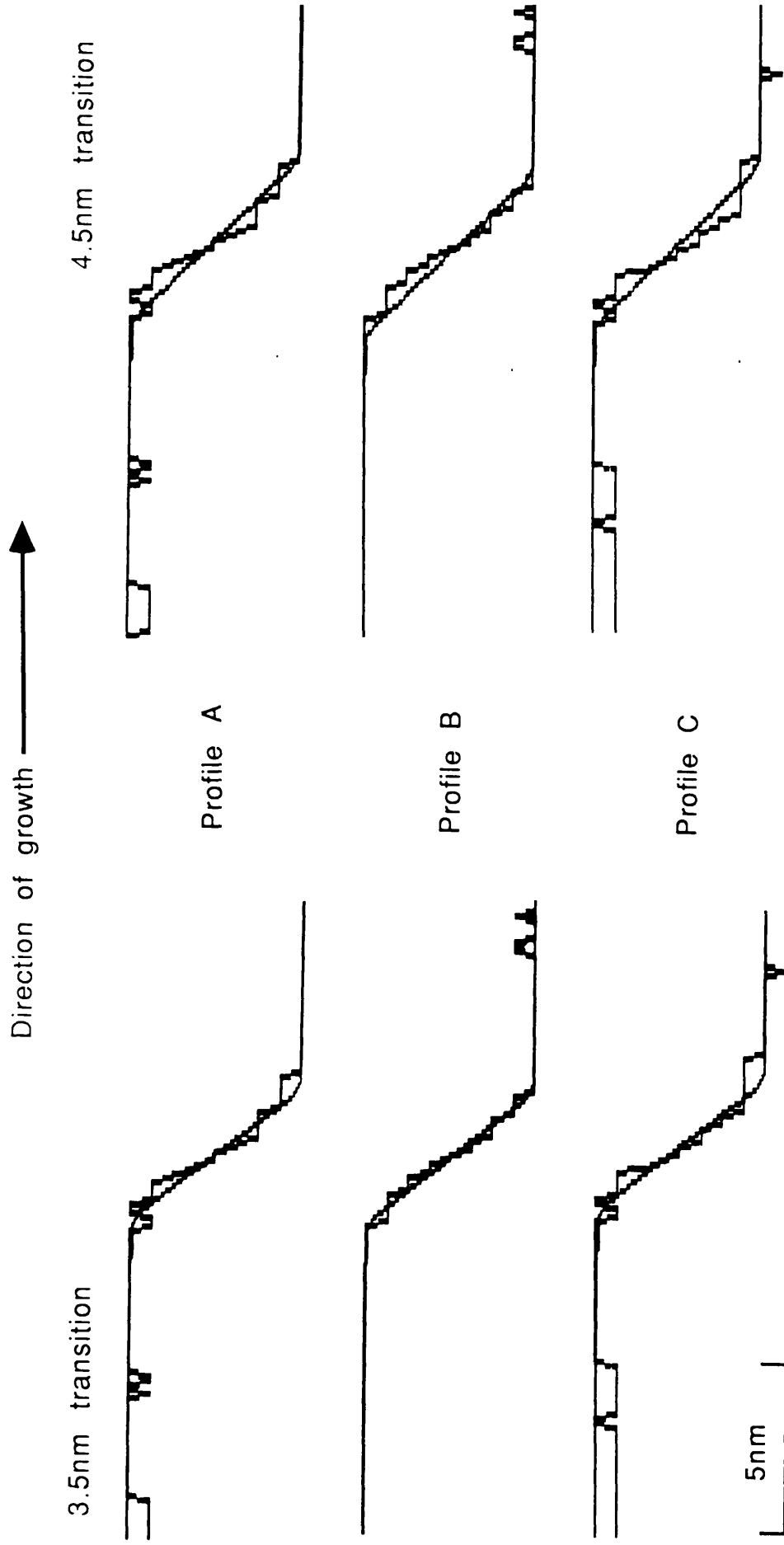


Figure 6.9: Comparison between interfaces from profiles A, B and C with simulated profiles calculated from transition widths of 3.5nm and 4.5nm.

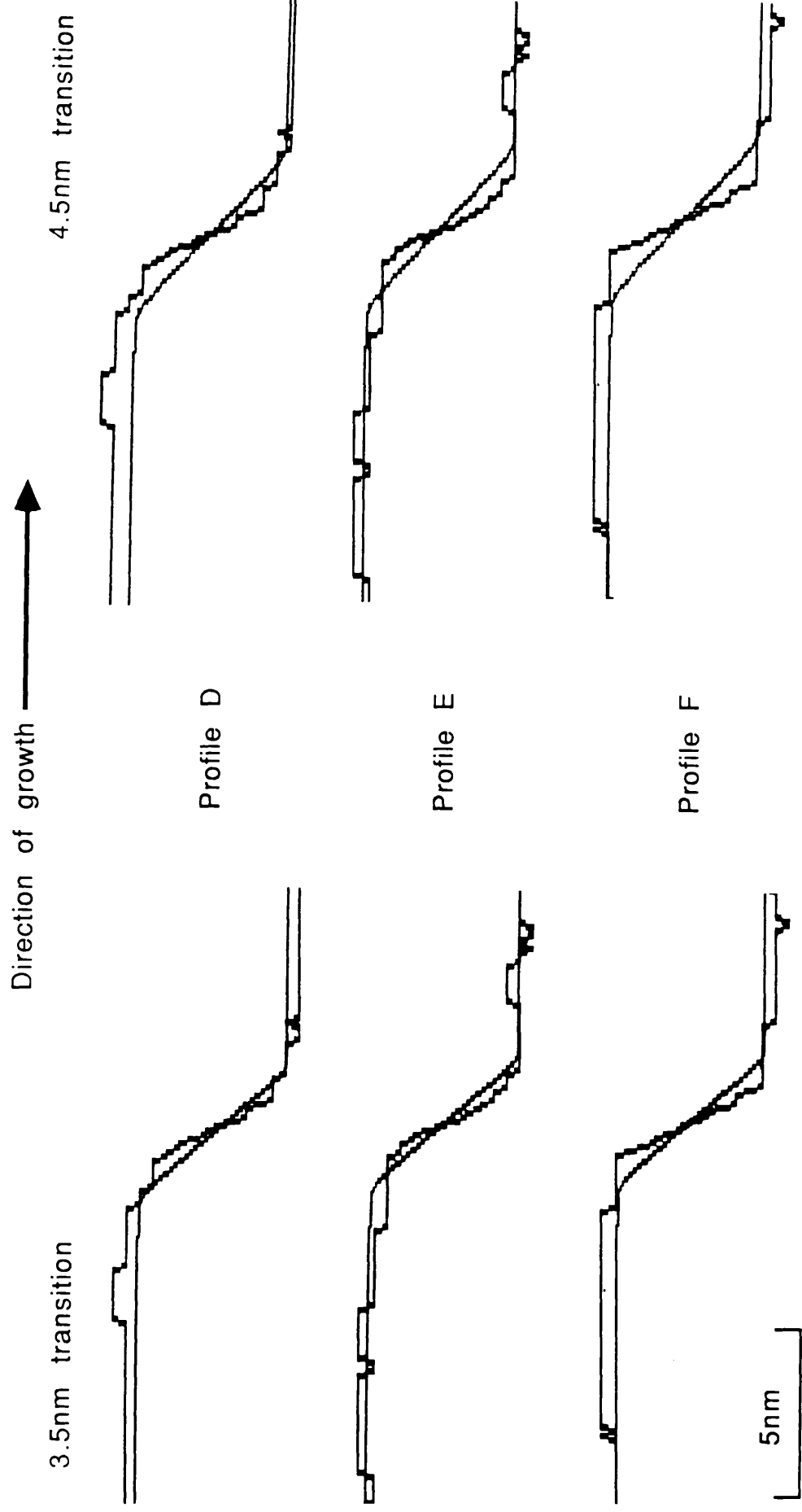


Figure 6.10: Comparison between interfaces from profiles D, E and F with simulated profiles calculated from transition widths of 3.5nm and 4.5nm.

It should be noted that all dark current measurements were made retrospectively, and not on the day of the original experiment.

with such a demonstrated resolution can provide much useful information.

6.2.2 Quantitative analysis of layer contrast

The discussions on the variation of high-angle ADF signal as a function of probe position across multilayers has, to this point, been primarily concerned with the spatial variation of image intensity rather than the contrast detected between signals recorded from each layer. The signal intensity from high-angle ADF images is generally very low and all image contrast observed to this point has been electronically enhanced. In order to measure the level of high-angle ADF contrast between layers of AlGaAs and GaAs without contrast enhancement, an image of the 10nm layers in the test specimen was recorded under the same conditions as described in section 6.2.1 but with zero black level.

In this discussion, the values of transition widths are not the prime consideration and so an average was taken of all 64 linescans in the image. The resulting intensity distribution is that shown uppermost in figure 6.11. In this figure, the y-axis represents the average number of counts recorded in each pixel, the values of which are 114 in regions of GaAs and 111 in AlGaAs, corresponding to a very low level of image contrast. An important consideration, however, is that in each image acquired from the HB5 there is a contribution to the detected intensity in each pixel that is attributable to a level of 'dark current'. This is effectively a constant background signal with an intensity that is determined by the gain of the signal amplifier during the acquisition of each image. The dark current contribution is measured by acquiring an image at the same level of monitor signal gain as before but with the field emission gun switched off. For the profile discussed here, the dark current level is (on average) 46 counts per pixel as shown in figure 6.11. When the dark current contribution is subtracted from the original profile, the average intensity in the

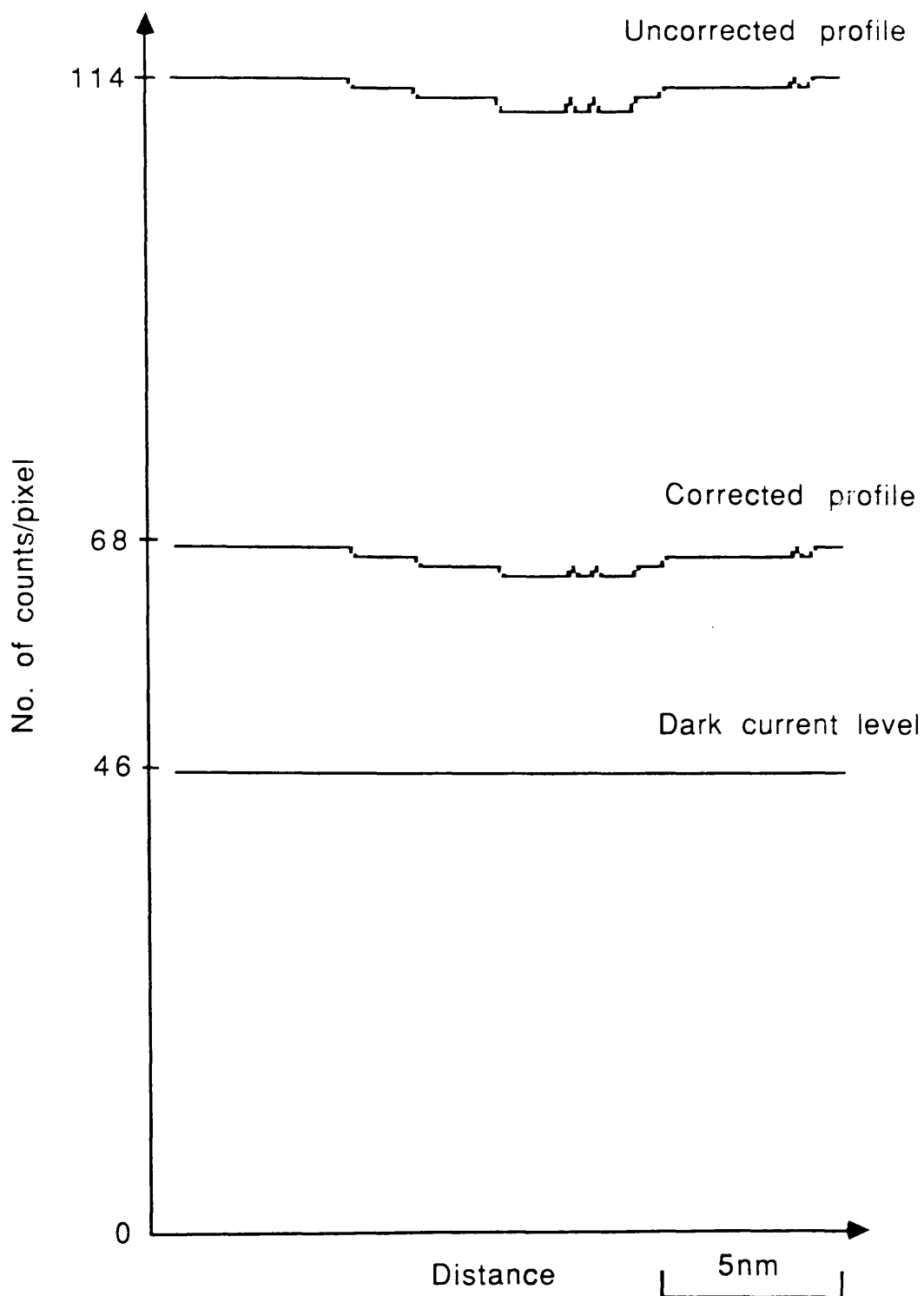


Figure 6.11: Dark current corrections for an absolute intensity profile of a 10nm AlGaAs layer, showing the layer contrast level that is revealed when no black level is applied.

AlGaAs and GaAs layers becomes 68 and 65 counts per pixel respectively. This corresponds to a level of contrast, C (defined in equation 2.1), of 0.05. Table 6.1 shows that the dark current corrected value still is lower than those predicted for the $\text{Al}_{0.3}\text{Ga}_{0.7}\text{As}/\text{GaAs}$ system using the theoretical models for the elastic scattering cross-section described in chapter 2. A value for C of 0.05 using, for example, the Fleischmann cross section (which gives the closest agreement between experiment and theory) is equivalent to the contrast predicted between, say, $\text{Al}_{0.13}\text{Ga}_{0.87}\text{As}$ and GaAs. It should be noted, however, that the same value of C is possible from a high-angle ADF image of alternate layers of $\text{Al}_x\text{Ga}_{1-x}\text{As}$ possessing different, non-zero values of 'x'. A more direct analytical technique is therefore required to check the validity of the contrast predictions and to measure the elemental concentrations in each layer.

6.3 EDX microanalysis

EDX microanalysis is a direct analytical technique in that it can be used to measure elemental concentrations in a specimen without recourse to other methods. In this section, the technique is employed to examine the test specimen that was analysed using high-angle ADFI in the previous section. The aims of the experiments described here are to form 'maps' of elemental concentration as a function of probe position across the AlGaAs/GaAs system (as outlined in chapter 5) and to measure the composition in the layer centres.

The section begins by describing the analysis method used to determine composition from spectra, with particular emphasis given to the problems that are associated with analysis of the Al, Ga and As characteristic signals. This is followed by a discussion of results from series of spectra that were acquired from the test specimen.

All spectra examined in this section were acquired using a windowless EDX detector. Under the experimental conditions discussed in chapter 5, spectral

Approach used	Contrast
Experimental (with dark current)	0.03
Experimental (without dark current)	0.05
Born	0.12
Moliere	0.11
Fleischmann	0.11
\bar{Z}^2	0.16
$\bar{Z}^{4/3}$	0.11

Table 6.1: Comparison between experimentally measured contrast from an AlGaAs/GaAs multilayer system with that predicted for an Al_{0.3}Ga_{0.7}As/GaAs system using several theoretical approaches.

acquisition times of 10s were found to yield sufficient statistical significance in the characteristic x-ray peaks of interest (typically between 5000 and 10000 counts in the Ga K_{α} peak in a spectrum acquired in a region of GaAs).

6.3.1 Analysis of spectra

The most convenient way to express elemental compositions in an $Al_xGa_{1-x}As$ /GaAs system is in terms of partial atomic fractions p_{Al} and p_{Ga} , where p_{Al} is the ratio of the number of atoms of Al (n_{Al}) to that of As (n_{As});

$$p_{Al} = \frac{n_{Al}}{n_{As}} \quad (6.1)$$

p_{Ga} is expressed in a similar manner. In a layer of $Al_xGa_{1-x}As$, p_{Al} and p_{Ga} have values x and $(1-x)$ respectively. The analysis technique that is used to determine the values of p_{Al} and p_{Ga} from x-ray spectra is a two stage procedure: Firstly, the numbers of detected characteristic x-rays of each element are evaluated and, secondly, the ratios of these counts are converted into the relevant partial atomic fractions. A program, written in Super Basic for use on a Sinclair QL minicomputer and entitled 'AlGaAs_Analyse' that can perform all numerical calculations involved in the analysis procedure (including error calculations) on series of spectra is given in appendix A4.

A typical spectrum obtained from a region of AlGaAs in the specimen under investigation is shown in figure 6.12. The first stage of analysis is to calculate the number of detected counts in each relevant characteristic x-ray peak which, in this discussion, are the Al K, Ga K_{α} and As K_{α} peaks. Analysis involves the separation of the uninformative bremsstrahlung background from the spectrum to isolate the characteristic x-ray peaks of interest. For the spectral acquisition

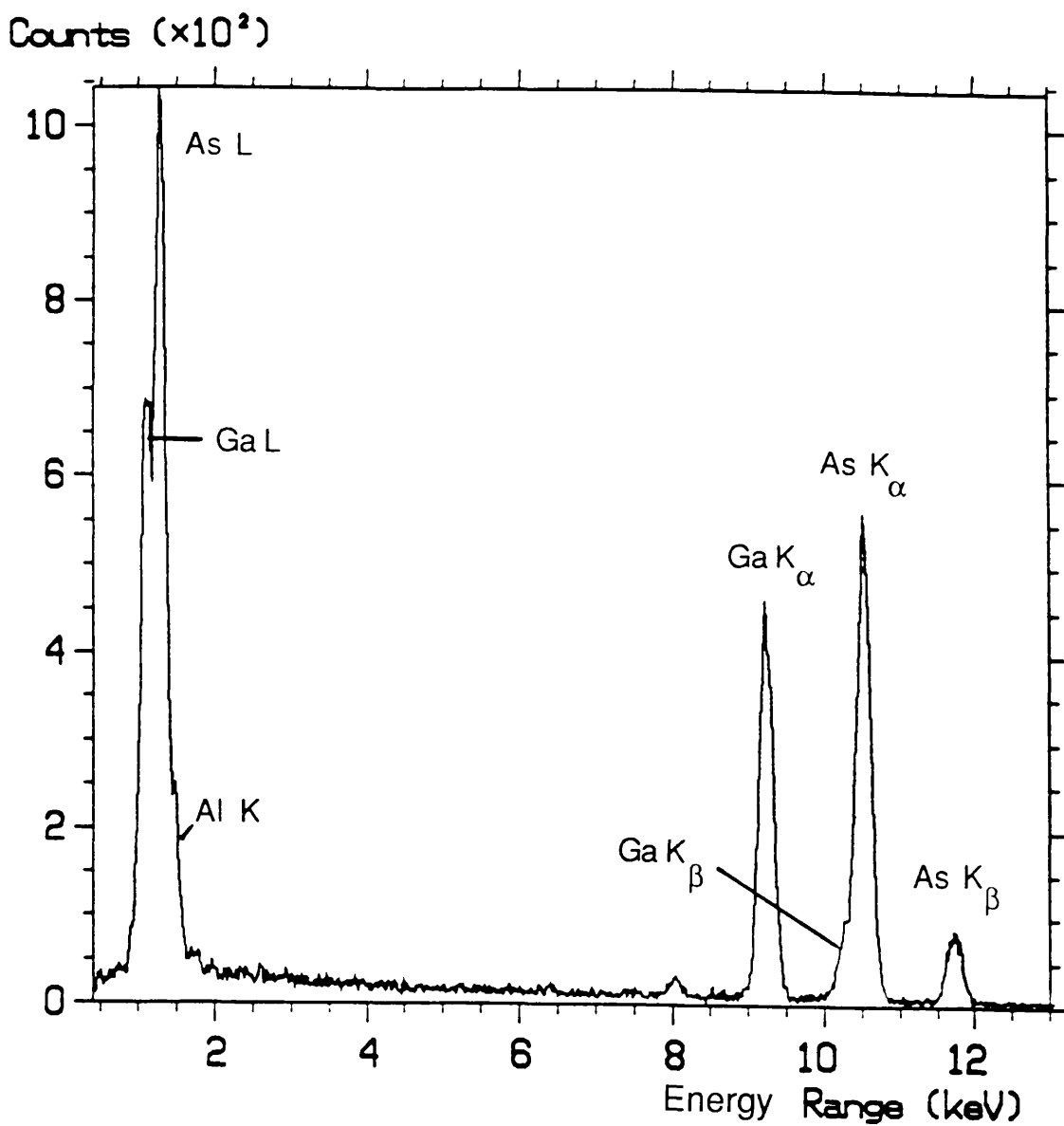


Figure 6.12: Typical x-ray spectrum acquired from a region of AlGaAs

times used here, the background in the energy region of the Ga K_{α} and As K_{α} peaks is small and its energy variation slow, and so signal separation can be achieved by linear interpolation of the background on either side of the individual peaks, as illustrated schematically in figure 6.13. Figure 6.14 shows, however, that extraction of the As K_{α} signal is complicated by an overlap with the Ga K_{β} peak. This difficulty is resolved by subtracting the number of Ga K_{β} counts, calculated from the measured Ga K_{α} signal and a knowledge of the partitioning of the characteristic photons between the K_{α} and the K_{β} lines for Ga (Scofield, 1974) from the total counts in the combined peak. The partition function, s_K , is defined in chapter 2 and has a value of 0.873 for Ga. Figure 6.15 compares a spectrum acquired from an area of AlGaAs (broken line) with that acquired from GaAs (unbroken line). The graph illustrates the problems associated with the extraction of the Al K characteristic signal in that there is a significant overlap of the Al K peak by the As L peak and a smaller overlap with the Si K peak. Si is incorporated into the specimen in small quantities as a result of the specimen preparation technique used. The method used here to estimate the number of detected Al K counts is to firstly subtract the background by linear interpolation from just below the Ga L peak to just above the Si K peak and, secondly, to record the number of counts in the upper energy half of the peak. By doubling this value, an estimate of the detected Al K signal is obtained. However, it should be noted that the number of counts recorded is likely to include a signal that is attributable to As and, to a lesser extent, Si.

The second stage of analysis relates the number of detected counts (N) in each characteristic x-ray peak and the number of atoms (n) in the volume irradiated by the beam to give p_{Al} and p_{Ga} , where;

$$p_{Al} = \frac{n_{Al}}{n_{As}} = K_{AlAs} \frac{N_{Al}}{N_{As}} \quad (6.2)$$

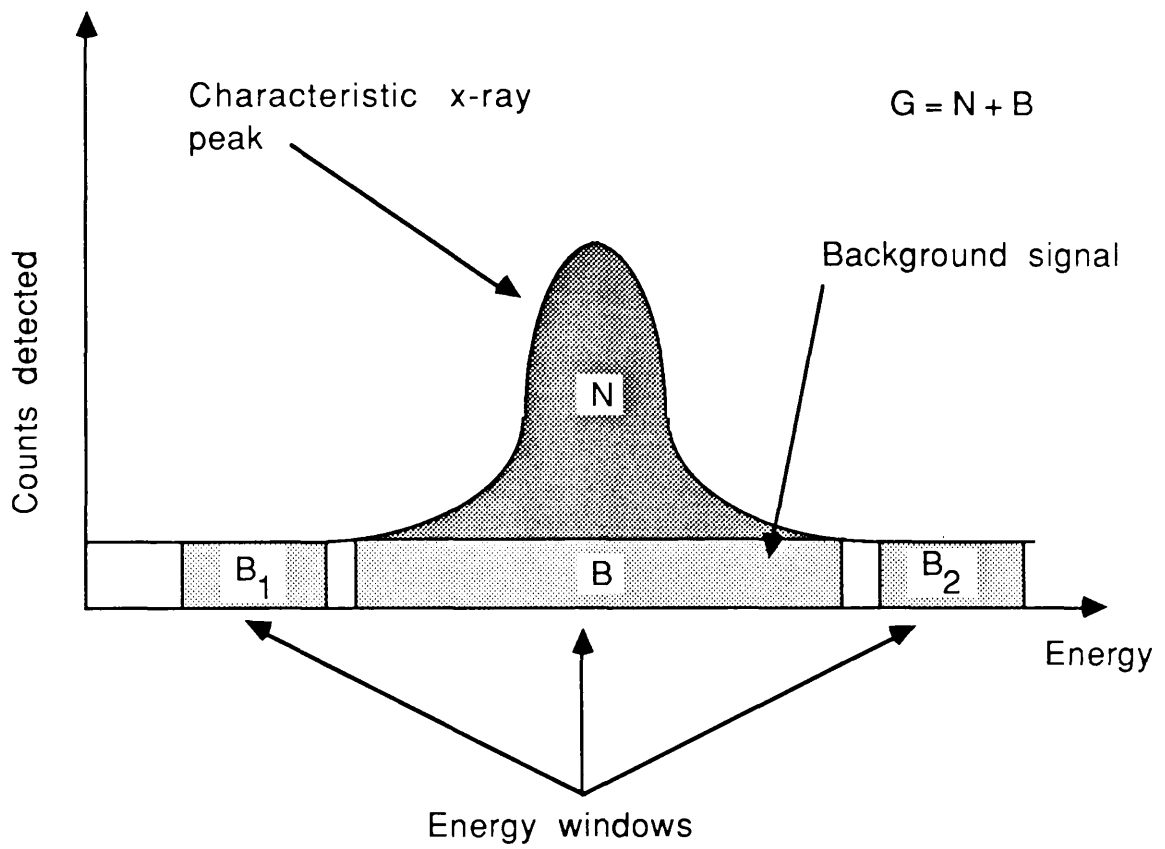


Figure 6.13: Schematic diagram illustrating the way in which the background x-ray signal is separated from the characteristic x-ray signal.

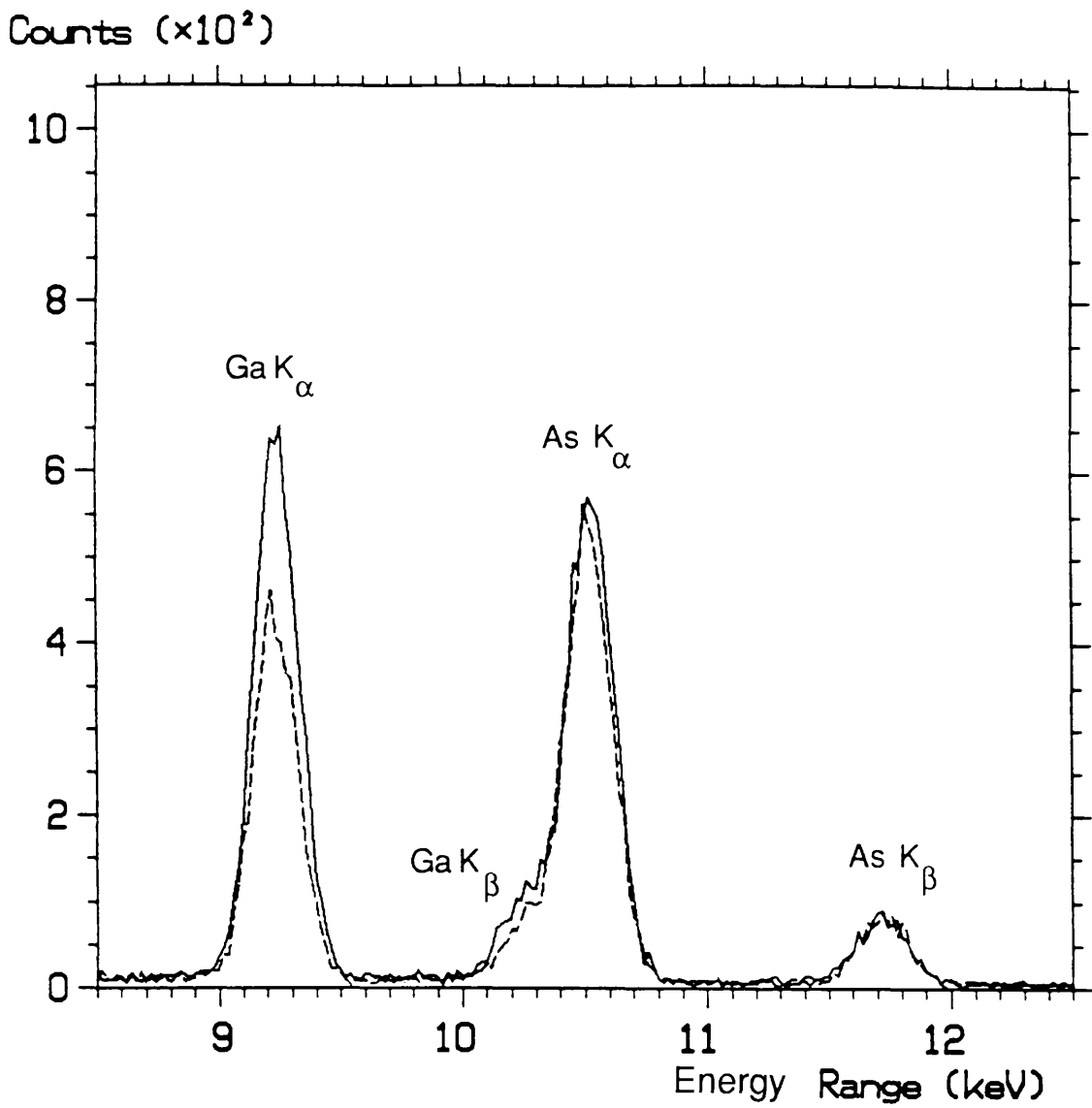


Figure 6.14: Comparison of an x-ray spectrum acquired in a region of GaAs (continuous line) with that acquired in a region of AlGaAs, showing the overlap that occurs between the Ga K_β and As K_α peaks.

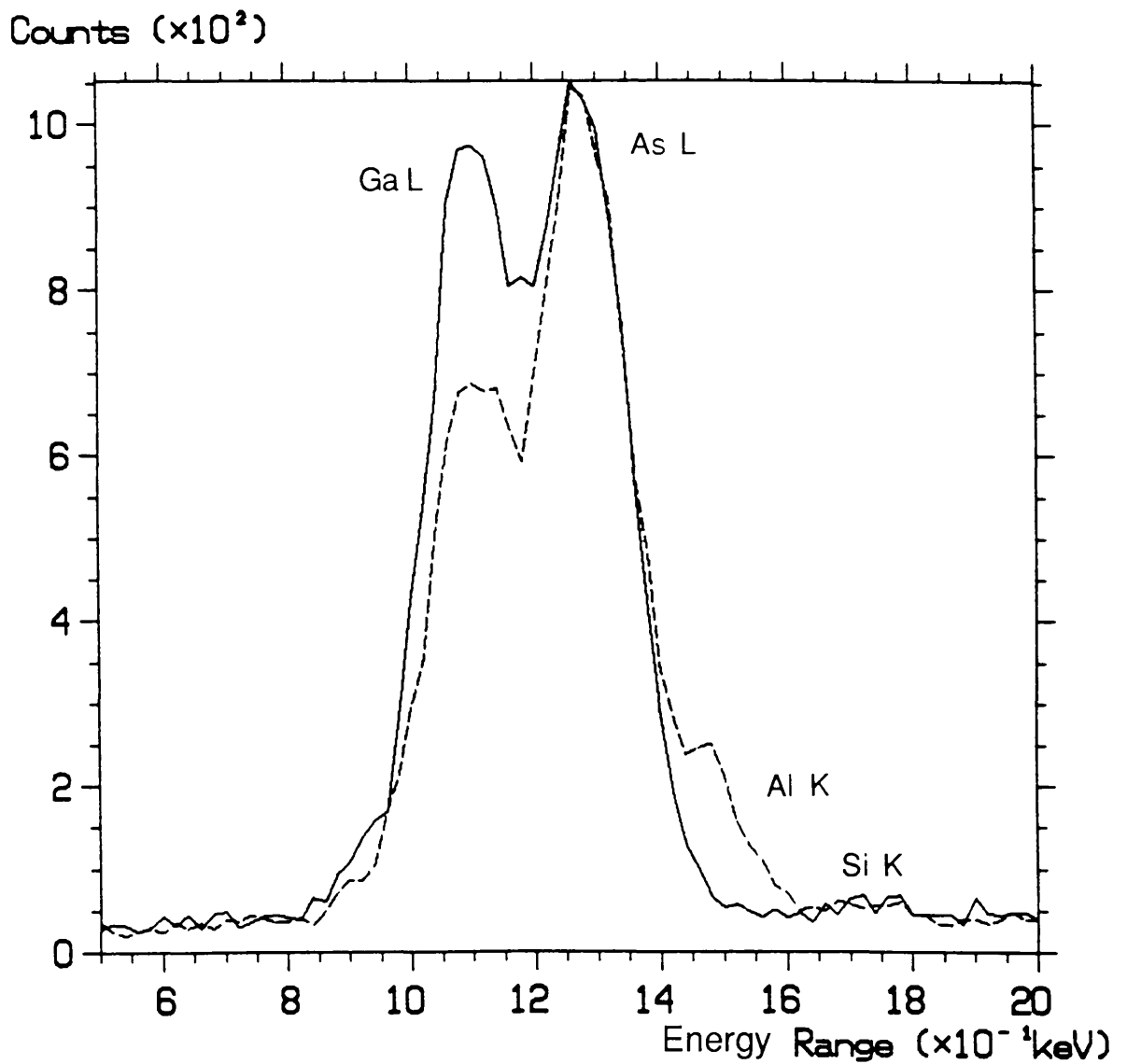


Figure 6.15: Comparison of an x-ray spectrum acquired in a region of GaAs (continuous line) with that acquired in a region of AlGaAs, showing the overlap that occurs between the As L and Al K peaks.

and;

$$p_{\text{Ga}} = \frac{n_{\text{Ga}}}{n_{\text{As}}} = K_{\text{GaAs}} \frac{N_{\text{Ga}}}{N_{\text{As}}} \quad (6.3)$$

The K-factors K_{AlAs} and K_{GaAs} relate the relative efficiency of production and detection of characteristic signals. For analyses using the windowless detector, K_{AlAs} is expressed in the form;

$$K_{\text{AlAs}} = \frac{\sigma_c(\text{As})\epsilon_{\text{windowless}}(\text{As})}{\sigma_c(\text{Al})\epsilon_{\text{windowless}}(\text{Al})} \quad (6.4)$$

where σ_c is the cross section for the production of K_α characteristic photons and $\epsilon_{\text{windowless}}$ is the detection efficiency of the windowless EDX detector at the relevant photon energy. The values of $\epsilon_{\text{windowless}}$ for the elements of interest here are given in table 5.3. Using the expression for σ_c that is given in equation 2.24, K_{AlAs} can be expressed as;

$$K_{\text{AlAs}} = \frac{s_K(\text{As})\omega_K(\text{As})}{I_K(\text{As})} \ln \left[\frac{0.89E_0}{I_K(\text{As})} \right] \frac{I_K(\text{Al})}{s_K(\text{Al})\omega_K(\text{Al}) \ln \left[\frac{0.89E_0}{I_K(\text{Al})} \right]} \frac{\epsilon_{\text{As}}}{\epsilon_{\text{Al}}} \quad (6.5)$$

where E_0 is the energy of the incident electrons. The values of s_K , fluorescence yield ω_K and ionisation energy I_K for each element of interest are given in table 2.4. K_{GaAs} is calculated using an expression similar to that in equation 6.5. The values of K_{AlAs} and K_{GaAs} used for analyses described in this section are 0.88 and 0.90 respectively.

K-factors can be determined either by the method described above or experimentally through the use of standards of known composition. For the

experiments described here, no AIAs standard was available to measure K_{AIAs} experimentally and so calculations of p_{AI} rely solely on the theoretical value. K_{GaAs} , however, can be determined experimentally by acquiring spectra from the GaAs substrate on which the epilayers of the test specimen are grown. Longer spectral acquisition times were used to reduce statistical uncertainties. The measured value of K_{GaAs} agreed with the theoretical value to within 1%, and so $K_{\text{GaAs}} = 0.90$ is used to determine p_{Ga} in this section.

The errors in the extracted characteristic signals are essentially governed by Poisson statistics of the gross and nett counts in the energy ranges or 'windows' of interest. If, as figure 6.13 illustrates, G denotes the number of gross counts in a window and B is the number of counts calculated to be background signal;

$$B = f(B_1 + B_2) \quad (6.6)$$

B_1 and B_2 are the number of counts in the selected background windows (as illustrated in figure 6.13) and f is the ratio of the number of channels in the characteristic peak window to those in the background windows. The number of characteristic x-ray counts, N , is defined by;

$$N = G - B \quad (6.7)$$

and the error associated with N , δN , is expressed as;

$$\delta N^2 = \delta G^2 + \delta B^2 \quad (6.8)$$

and using Poisson statistics, $\delta G^2 = G$ and δB^2 is defined as;

$$\delta B^2 = f^2(B_1 + B_2) \quad (6.9)$$

If there are sufficient characteristic counts in a peak, i.e. if $B \ll G$, then;

$$\delta N^2 \simeq G \quad (6.10)$$

Equation 6.10 applies to the calculation of errors in the Ga K_α and As K_α peaks for all spectra discussed here, but not for the Al K peak as the Al concentration is very low in relation to the other elements and so equation 6.8 applies. The errors associated with the partial atomic fractions can now be calculated;

$$\begin{aligned} \left(\frac{\delta p_{Ga}}{p_{Ga}} \right)^2 &= \left(\frac{\delta N_{Ga}}{N_{Ga}} \right)^2 + \left(\frac{\delta N_{As}}{N_{As}} \right)^2 \\ &\simeq \frac{G_{Ga}}{N_{Ga}^2} + \frac{G_{As}}{N_{As}^2} \end{aligned} \quad (6.11)$$

and;

$$\begin{aligned} \left(\frac{\delta p_{Al}}{p_{Al}} \right)^2 &= \left(\frac{\delta N_{Al}}{N_{Al}} \right)^2 + \left(\frac{\delta N_{As}}{N_{As}} \right)^2 \\ &= \frac{G_{Al} + f^2(B_1 + B_2)}{N_{Al}^2} + \frac{G_{As}}{N_{As}^2} \end{aligned} \quad (6.12)$$

In the following discussion on experimental results, reference will also be made to partial atomic fraction p_{Al+Ga} where;

$$p_{Al+Ga} = p_{Al} + p_{Ga} \quad (6.13)$$

The error associated with $p_{\text{Al+Ga}}$ can be easily evaluated;

$$\delta p_{\text{Al+Ga}}^2 = \delta p_{\text{Al}}^2 + \delta p_{\text{Ga}}^2 \quad (6.14)$$

The errors discussed above apply to individual measurements of partial atomic fractions, and are used in graphs that map their variation as a function of probe position across the layers. In the following discussion it is sometimes convenient to express partial atomic fractions as an average taken from several spectra. In this case the associated error is the adjusted error, Δ , which relates to the statistical spread of measurements. For an individual measurement M , there is approximately a 65% probability that (Barford,1967);

$$\bar{M} - \Delta < M < \bar{M} + \Delta \quad (6.15)$$

where \bar{M} is the mean value of the measurements of M .

6.3.2 Results

The results discussed here were taken from four separate EDX experiments carried out across the AlGaAs layers following the experimental procedure described in chapter 5. The experiments can be categorised into two sets, namely type 'A' comprising 27 spectra which were acquired across the two 10nm AlGaAs wells, and type 'B' comprising 21 spectra which were acquired across the two 5nm AlGaAs wells. The 20nm wells were not used for microanalysis because the high values of film thickness (>100nm) and consequent beam broadening in the regions of interest precluded meaningful quantitative analysis. A schematic diagram showing the positions at which spectra were acquired in both series A and B is given in figure 6.16. The first

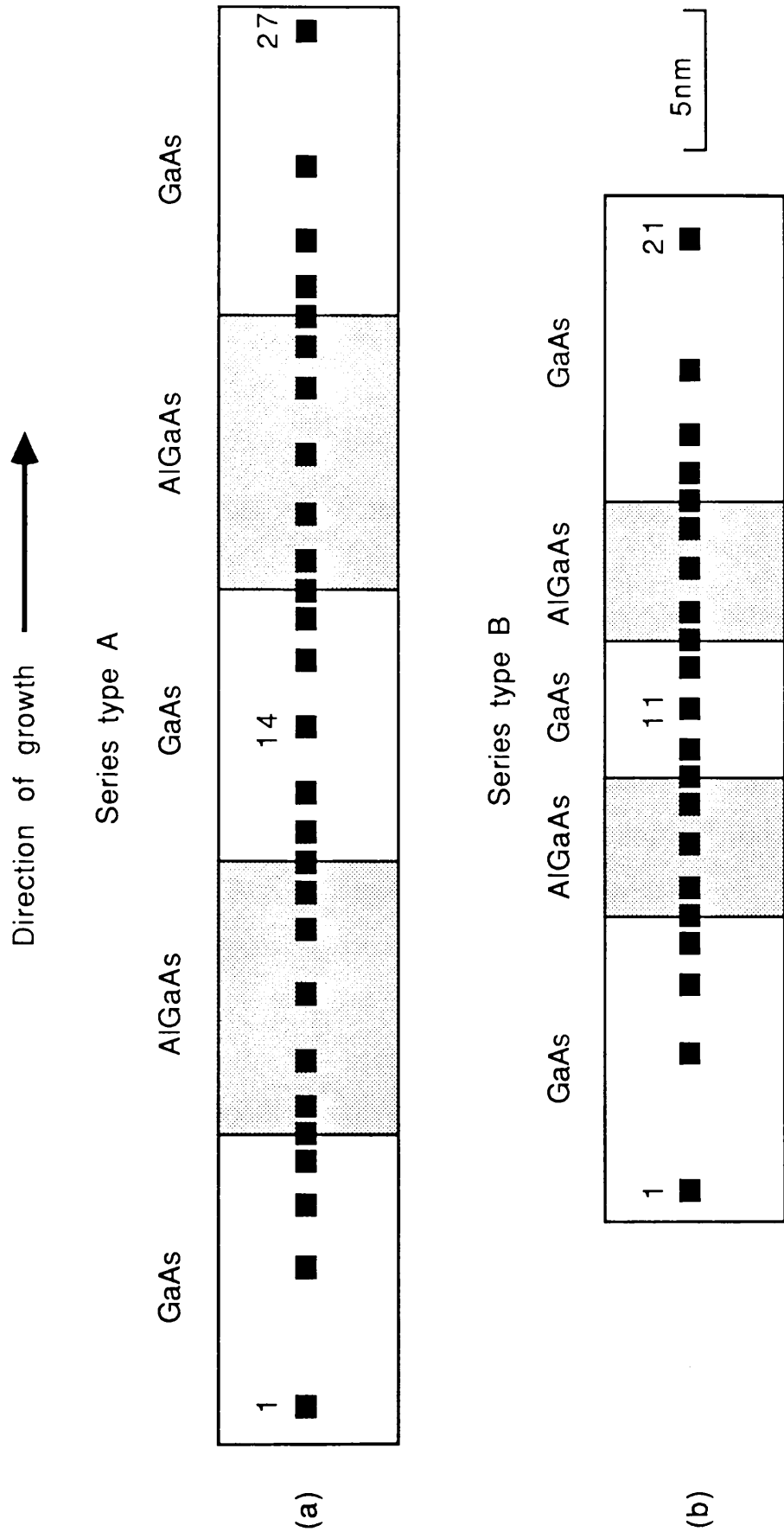


Figure 6.16: Schematic diagram showing the positions at which x-ray spectra are acquired from the (a) 10nm and (b) 5nm AlGaAs layers of the specimen shown in figure 6.1.

and last spectra in each series were acquired at a distance of 10nm away from the nearest AlGaAs layer, and the smallest distance that separates two successive spectra is 1nm at layer interfaces. Each series type was acquired at two separate locations in the same specimen. Following the analysis procedure described in section 6.3.1, the partial atomic ratios of interest were calculated for each spectrum. The results from series A are plotted in figure 6.17 and those from series B are given in figure 6.18. Using these results, a table listing the average values of partial atomic fractions from several groups of spectra is given in table 6.2.

6.3.2.1 Determination of specimen concentrations

Much useful information on both the microanalysis technique and the test specimen is revealed in figures 6.17 and 6.18. Before a full discussion of results can begin, it is important to establish the most suitable method by which specimen concentrations can be measured from the available data. In the course of the spectrum analysis procedure, no correction was made for the self absorption of the Al K characteristic signal in the specimen. Absorption effects are clearly illustrated in figures 6.17 and 6.18 by the marked decrease in $p_{\text{Ga+Al}}$ below unity in the AlGaAs layers. Table 6.2 shows that the average value of p_{Al} from the four spectra acquired in the centre of the 10nm AlGaAs wells is 0.238 and that of $p_{\text{Al+Ga}}$ is 0.941. The number of counts detected in the As K_{α} peak indicated that the specimen is ~60nm thick in this region and so application of the self absorption model described in chapter 5 for $t=60\text{nm}$ predicts that ~11% of the Al K signal will be absorbed before detection. The value of $p_{\text{Al+Ga}}$ in the AlGaAs layers when corrected for self absorption is therefore ~0.96 compared with a value of ~1 in the layers of GaAs. This result suggests that the theoretical value of K_{AlAs} that is used to determine p_{Al} is not

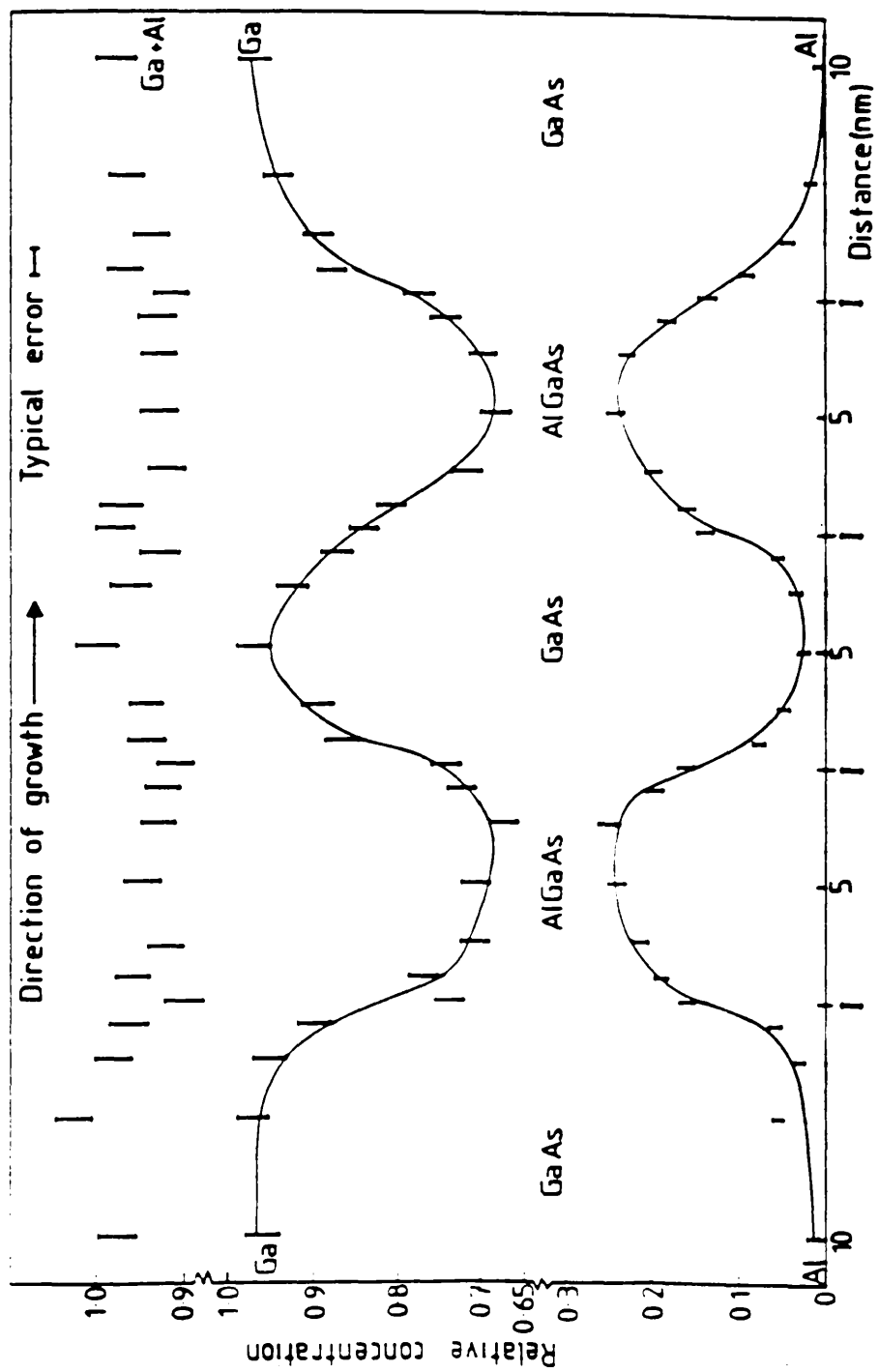


Figure 6.17(a): Graph showing the variation of partial atomic fractions across two 10nm AlGaAs layers calculated from EDX data.

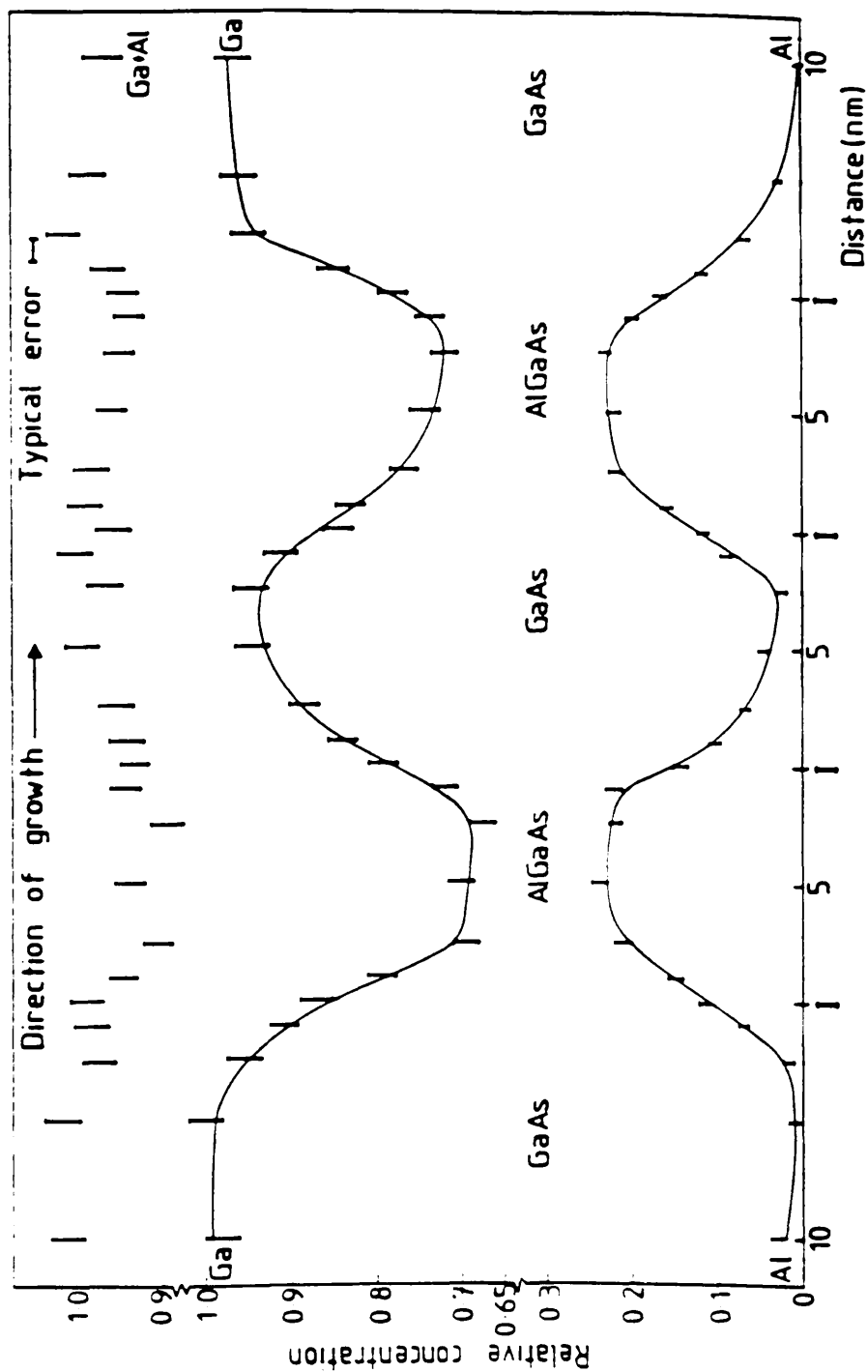


Figure 6.17(b): Graph showing the variation of partial atomic fractions across two 10nm AlGaAs layers in a different region of specimen from that in (a) and calculated from EDX data.

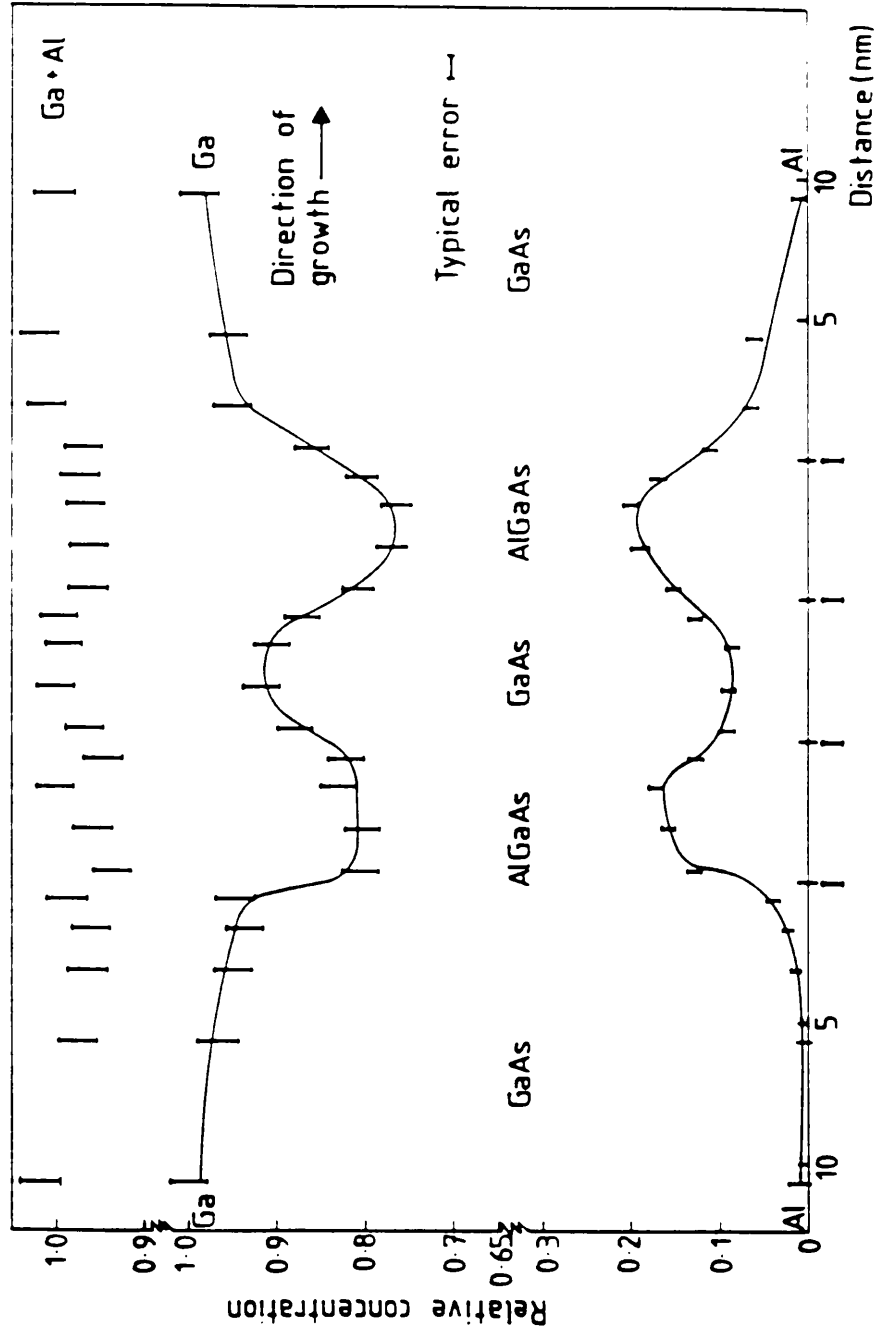


Figure 6.18(a): Graph showing the variation of partial atomic fractions across two 5nm AlGaAs layers calculated from EDX data.

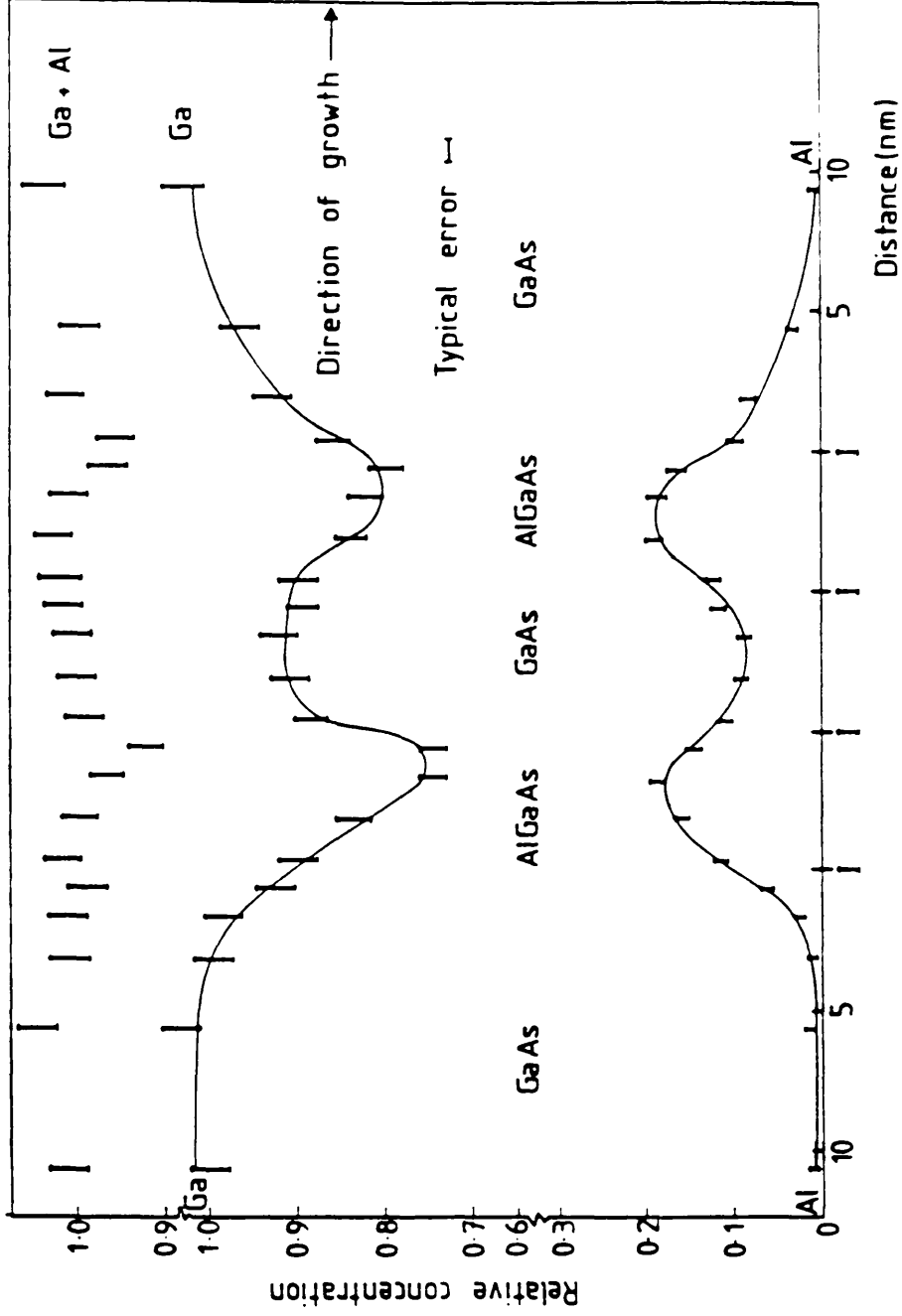


Figure 6.18(b): Graph showing the variation of partial atomic fractions across two 5nm AlGaAs layers in a different region of specimen from that in (a) and calculated from EDX data.

Areas of spectrum acquisition	p_{Al}	p_{Ga}	p_{Al+Ga}	Concentration (using p_{Ga})
10nm AlGaAs layers (4 spectra)	0.238±0.003	0.702±0.007	0.941±0.005	Al Ga As 0.30 0.70
10nm AlGaAs layers (12 spectra)	0.227±0.005	0.707±0.005	0.933±0.007	Al Ga As 0.29 0.71
10nm GaAs layer (2 spectra)	0.037±0.010	0.982±0.012	1.009±0.003	Al Ga As 0.02 0.98
10nm GaAs layer (6 spectra)	0.041±0.007	0.927±0.013	0.968±0.009	Al Ga As 0.07 0.93
GaAs buffer layers	0.018±0.008	1.003±0.016	1.020±0.014	Ga As 1.0 1.0

Table 6.2: List of the partial atomic fractions and compositions measured from groups of spectra acquired at different regions of the AlGaAs/GaAs test specimen.

ideally suited to the experimental configuration used, and/or the method used to extract the Al K signal is not sufficiently accurate to enable quantitative analysis. As a result of the good agreement between experiment and theory, greater confidence can be placed in the value of K_{GaAs} used in the calculations. Table 6.2 shows that the mean value of p_{Ga} calculated from several spectra acquired in the GaAs buffer layers is 1.003, suggesting that there is a 1:1 Ga:As ratio in these regions. In addition, figure 6.14 shows that whilst the As signal is the same magnitude in spectra acquired from regions of GaAs (continuous line) and AlGaAs (broken line) of approximately the same thickness, the Ga signal is noticeably reduced in AlGaAs. As would be expected from a crystal of high quality, these results are consistent with there being either an Al or a Ga atom in one sublattice site and an As atom in the other. Consequently, specimen compositions need only be deduced from the measured values of p_{Ga} and so all the compositions quoted in the right hand column of table 6.2 are calculated from the corresponding value of p_{Ga} . The errors suggest that 0.02 should be regarded as the upper limit of the uncertainty with which the value of x in $\text{Al}_x\text{Ga}_{1-x}\text{As}$ is measured. It should be stressed that although p_{Ga} only is used to determine composition, the variation of p_{Al} as a function of probe position across the layers nevertheless provides important information on, for example, the extent of beam spreading in the specimen.

6.3.2.2 Beam broadening effects

A feature of figures 6.17 and 6.18 is that, although the trends in compositional variation across the multilayer system can be readily observed, the degree to which signals are spread across the interface are considerable. An example of this is the apparently high Al content measured in the centre of the middle GaAs layer of each figure. High-angle ADFI analyses of the system revealed that the transition width of compositions at interfaces is no greater than

2.5nm. This suggests that the spatial variations of composition apparent in the figures can be ascribed more to beam broadening than to a broad concentration gradient. The non-uniformity in t in the region of the 5nm AlGaAs wells together with the small dimension of the wells in relation to the average value of t (~50nm) precludes direct comparison between the experimental data from series B with the Monte Carlo simulations described in chapter 5. However, a comparison of the left hand GaAs to AlGaAs transition in series A with the simulated signal variations in figure 5.9 shows that, close to the interface, there is reasonable agreement between simulation and experiment. Although no exact estimate of the transition width can be made, this result is consistent with the high-angle ADF observations on the abruptness of the interface transitions. The Monte Carlo simulations do, however, underestimate the effect of signal 'tailing' at distances greater than 2nm from the position where the probe is centered. Determination of compositions in the centre of the layers must take tailing effects into consideration and so such measurements rely on the information that is available from the experimental data recorded.

6.3.2.3 Layer centre composition measurements

The mean values of p_{Ga} and p_{Al} from the 4 spectra that were acquired from the centres of the 10nm AlGaAs wells and from the 2 spectra taken from the centre of the 10nm GaAs buffer layer that separate the two AlGaAs wells are listed in table 6.2. Also given in the table are the average values of p_{Ga} and p_{Al} in the same wells, but calculated from the central spectra plus those acquired 2.5nm from the interfaces. Analysis of these values, together with observation of figure 6.17 shows that, in general, the detected values of p_{Ga} and p_{Al} change more rapidly across the centre of the GaAs layer than the AlGaAs layers. This can be explained by considering the contribution to the total detected signal that

is attributable to beam broadening across interfaces into neighbouring layers. In order to measure layer centre compositions accurately, tailing effects must be quantified.

When the probe is positioned at the centre of the 10nm GaAs layer in which the actual value of p_{Ga} is denoted as p_1 , but that detected is p_1' , then the difference between p_1 and p_1' can be attributed to a fraction, u , of the total detected signal originating from the neighbouring AlGaAs layers which possess a value of p_{Ga} of p_2 . p_1' can be expressed as;

$$p_1' = (1-u)p_1 + up_2 \quad (6.16)$$

When the probe is positioned at the centre of an AlGaAs layer, the detected value of p_{Ga} , p_2' can be expressed as;

$$p_2' = (1-u)p_2 + up_1 \quad (6.17)$$

It should be noted that because the system discussed here comprises layers that are 10nm wide, these calculations are based on the assumption that the signal detected from distances >10nm into neighbouring layers is negligible. Table 6.2 shows that the values of p_1' and p_2' are 0.982 and 0.702 respectively. If p_1 can be measured experimentally without recourse to tailing considerations, then p_2 can be found by solving the quadratic equation;

$$p_2^2 + p_2(p_1 - p_1' - p_2') + p_1(p_1' - p_1) = 0 \quad (6.18)$$

with this information, u can be deduced;

$$u = \frac{p_1' - p_1}{p_2 - p_1} \quad (6.19)$$

This can be achieved by observing that the high-angle ADF signal level from the 10nm GaAs well is similar to that from the wider GaAs buffer layers that separate each pair of wells, suggesting that the composition is similar in both. Table 6.2 shows that the value of p_{Al} in the buffer layers is finite but small. As discussed in section 6.3.1, this signal can be ascribed to the presence of As and, to a lesser extent, Si. This is substantiated by observing that the mean value of p_{Ga} in these regions is 1.003. The buffer layers are ~40nm wide and so tailing effects are negligible. Using $p_1=1$ and taking the positive root of equation 6.18 yields values of p_2 and u of 0.71 and 0.06 respectively. This means that there is a tailing contribution of ~6% from neighbouring layers, but that this effects the measured concentrations in the GaAs layer more than in the AlGaAs layers. In summary, these analyses have measured the compositions in the centre of the AlGaAs and GaAs layers as being $Al_{0.29}Ga_{0.71}As$ and $Ga_{1.0}As_{1.0}$ respectively, with an error of ± 0.02 associated with each value of x .

6.4 Comparison of high-angle ADFI with EDX microanalysis

The results discussed in this chapter provide important information on the relative merits of high-angle ADFI and EDX microanalysis when applied to semiconductor multilayers, and the way in which each can be employed to yield the most information from a specimen.

In terms of experimental procedure, high-angle ADFI is useful in that data acquisition and processing can be carried out quickly and easily, so enabling simple analyses to be performed in the course of an experimental run on the microscope. This allows subsequent experiments to be 'targeted' to yield information on specific features of interest. An example of this is that the positions at which x-ray spectra are acquired across the layers are determined

from the variations in \bar{Z} indicated by the high-angle ADF images.

The resolution attainable by high-angle ADFI was found to be no worse than 1.25nm. This is superior to EDX microanalysis for two reasons. Firstly, chapter 2 showed that the cross-section for high-angle elastic scattering is several orders of magnitude greater than for x-ray generation and so it is possible to use a smaller probe containing less current. Secondly, the results discussed in this chapter have shown that beam broadening effects are less severe because signals generated a long way from where the probe is centered are not collected. A possible factor that may limit the spatial resolution of high-angle ADFI, other than those inherent to the technique, may be instabilities associated with the position of the probe caused by external interference.

Application of EDX microanalysis to the test specimen showed that the compositions in the AlGaAs and GaAs layers were measured to be $\text{Al}_{0.29}\text{Ga}_{0.71}\text{As}$ and $\text{Ga}_{1.0}\text{As}_{1.0}$ respectively with an error associated with each value of x of ± 0.02 . Using the elastic scattering cross-section models to predict high-angle ADF image contrast, these compositions give rise to a considerably higher value of C than that observed. In addition, there is little agreement between the models as to the level of contrast expected. This suggests that in an attempt to provide a simple analytical expression for the elastic scattering cross-section, the models discussed are not sufficiently accurate to enable quantitative analysis by high-angle ADFI. Consequently, although the way in which \bar{Z} varies across a specimen can be determined with high spatial resolution from high-angle ADF images, information on the variation in concentration of particular elemental species and on the compositions at layer centres requires guidance from EDX microanalysis.

In conclusion, a combination of the high spatial resolution of high-angle ADFI together with the quantitative information that is available using EDX microanalysis can be used to yield much information on composition variations across multilayer systems.

Chapter 7

Analysis of the InGaAs/InP system grown by MOCVD at atmospheric pressure.

7.1 Introduction

A number of material growth techniques, such as solid source MBE, gas source MBE, chemical beam epitaxy (CBE) and low pressure MOCVD have been employed to grow InGaAs/InP multilayer structures (e.g. Claxton et. al., 1987, Panish et. al., 1986; Tsang and Schubert, 1986 and Razeghi et. al., 1986). The specimens investigated in this chapter, however, were all grown by MOCVD at atmospheric pressure. This technique has a number of practical advantages in terms of ease of equipment construction and operation compared to other techniques which are carried out at low pressure or under high vacuum. The multilayer systems of interest were grown on (001) InP substrates from arsine, phosphine, trimethylindium (TMI) and trimethylgallium (TMG) at atmospheric pressure in a MOCVD reaction chamber using hydrogen as the carrier gas (Bass et. al., 1987). All layers of InGaAs were grown with the intention of being lattice matched to the InP buffer layers. Optical (Skolnick et. al., 1987) and electrical (Kane et. al., 1987) measurements have shown that the materials, when compared to those grown by other techniques, are of the highest quality. TEM studies by Chew et. al. (1987) revealed that although the structures are atomically perfect, topographical imperfections in the form of non-planar interfaces were observed and appeared to be confined to the InGaAs to InP growth transitions. To enable the optimisation of the growth technique and consequently improve material quality, quantitative information with high spatial resolution on the way in which the concentrations of elemental species vary

across the system is highly desirable. With this aim in mind, this chapter discusses the use of high-angle ADFI and EDX microanalysis to investigate the material of interest.

7.2 High-angle ADFI

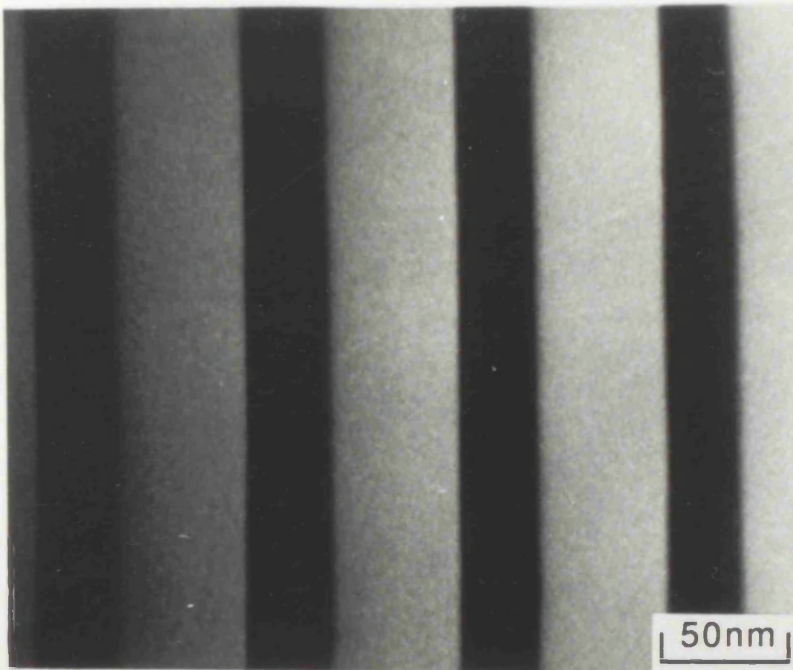
All high-angle ADFI studies discussed in this section were carried out using a multilayer system comprising 32 InGaAs layers, each 30nm in width, grown between 50nm InP buffer layers. An (002) dark field image of several of the layers is shown in figure 7.1.

7.2.1 Intensity profile analysis

Figure 7.2 shows three separate intensity profiles (denoted A, B and C) that were taken from a high-angle ADF image of a single InGaAs layer. Each profile is an average of 8 consecutive linescans, and the level of noise in each has been reduced by means of an eleven point median filter. Each pixel corresponds to a sampling interval of 0.13nm in a direction parallel to that of material growth. No thickness correction was applied to the profiles, as only small variations in t over the areas of interest were observed. The profiles in figure 7.3 (denoted D, E and F) were processed in the same way as those in figure 7.2, but were taken from an image acquired from a different region of the same specimen.

All the profiles in figures 7.2 and 7.3 possess similar features, the most striking of which is a marked asymmetry whereby the interface for growth proceeding from InP to InGaAs (type 1 interface) is much more abrupt than that from growth proceeding from InGaAs to InP (type 2 interface). Following the technique described in chapter 4, simulated intensity profiles of both interface

Direction of growth



Light bands: InP

Dark bands: InGaAs

Figure 7.1: Digital (002) dark field image of an area of InGaAs/InP multilayer grown by MOCVD at atmospheric pressure. The system comprised 32 InGaAs layers, each 30nm in width.

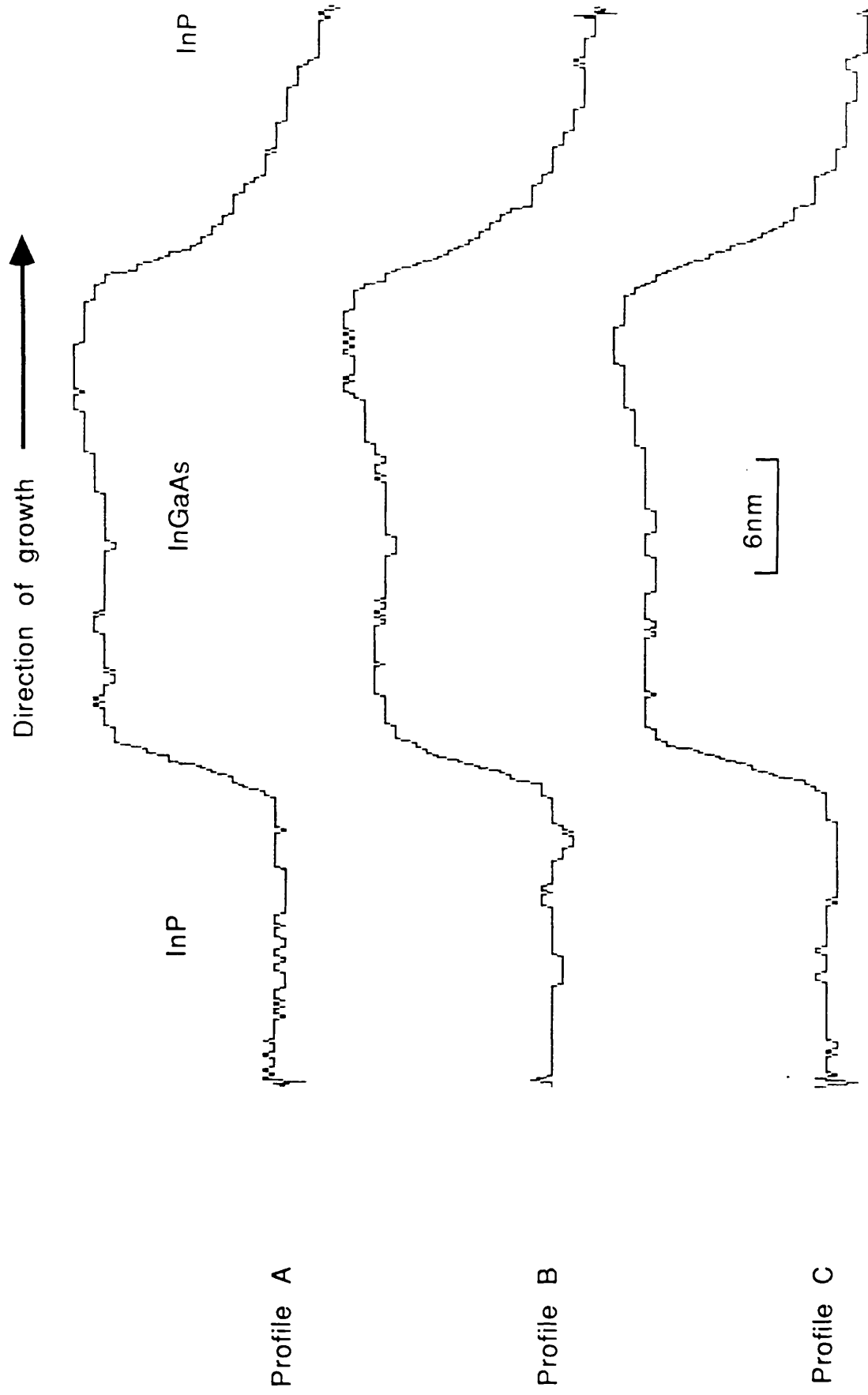


Figure 7.2: 3 processed profiles taken from a high-angle ADF image of the specimen shown in figure 7.1

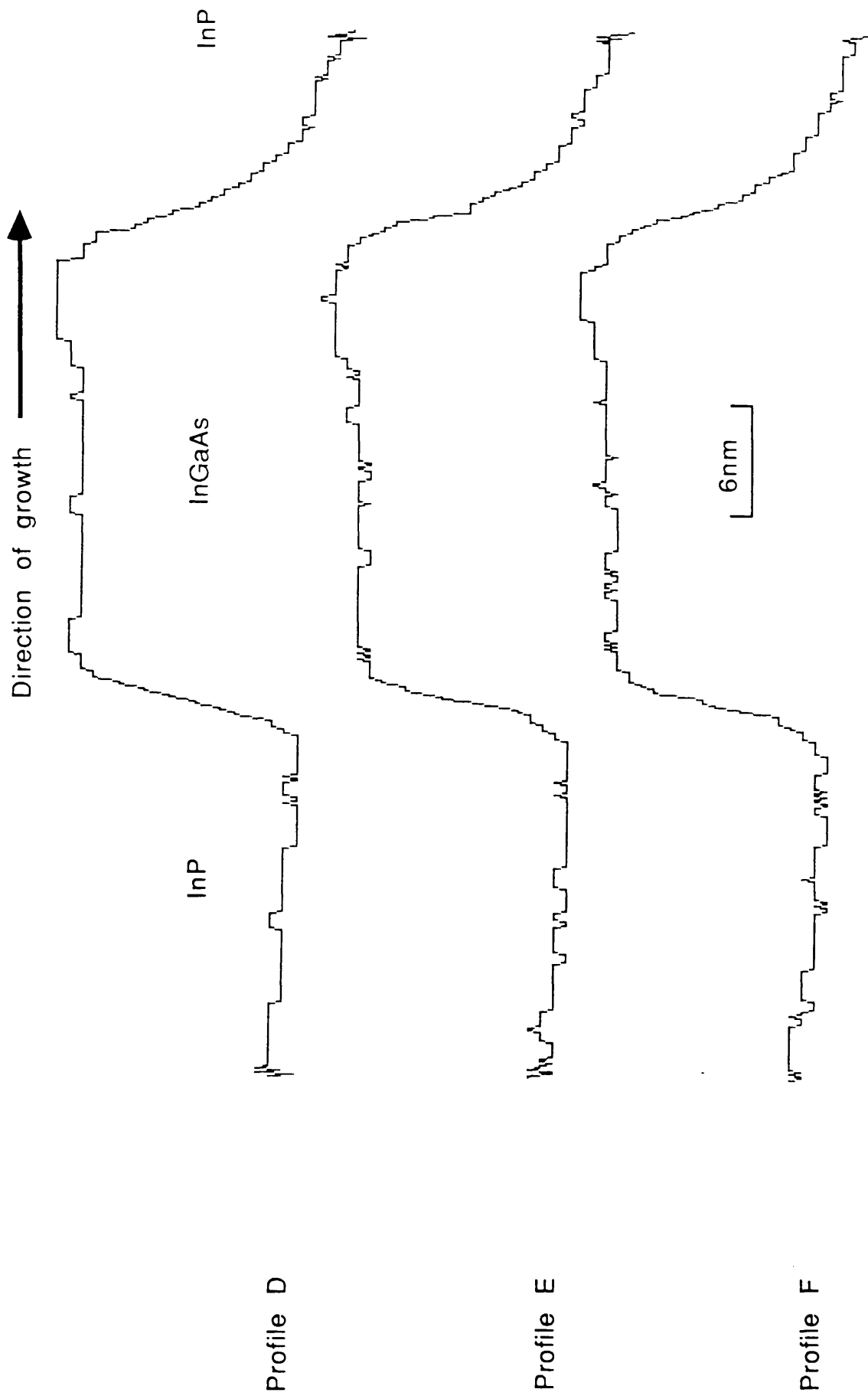


Figure 7.3: 3 processed profiles taken from a high-angle ADF image of a different area of the same specimen analysed in figure 7.2

types were calculated by performing convolutions of $J(x)$ with models of $f(\bar{Z})$ that possessed concentration changes which varied linearly across a range of transition widths.

Figures 7.4 and 7.5 demonstrate that the 'best fit' to the detected profile across the type 1 interface was obtained using an interface transition spanning 3nm (~ 5.3 unit cell dimensions). Figure 7.6 and 7.7 show that transition widths of 1nm and 2nm whilst fitting small parts of the experimentally acquired profiles, generally underestimate the signal variation detected. Transition widths of 4nm and 5nm (shown in figures 7.8 and 7.9) overestimate the detected signal variation in all cases. The quality of fit in figures 7.4 and 7.5, with perhaps the exception of profile E is very high.

All profiles taken from high-angle ADF images of the system of interest indicate that, in addition to the difference in transition widths between the two interface types, the detected signals from the type 2 interfaces are complicated by a slight increase in intensity from the InGaAs layer that spans a distance of ~ 7 nm (12 unit cell dimensions) before the transition to InP. Although no linearly varying simulation can fully account for all the features detected from the type 2 interface, figures 7.10 to 7.13 show that some simulated profiles do agree closely with selected regions of the experimental profiles: Figures 7.10 and 7.11 compare simulated intensity profiles calculated using linear transitions over 5nm (~ 9 unit cells) and 8nm (~ 13 unit cells) with profiles A to F, whereas figures 7.12 and 7.13 show similar comparisons with simulated profiles that were calculated from transitions spanning 10.5nm (~ 18 unit cells) and 13nm (~ 22 unit cells).

Quantitative high-angle ADF analysis of the system of interest was carried out following the method described in chapter 6.2.2. The profile shown in figure 7.14 is an average over all 128 linescans of an image acquired with zero offset and zero black level. Dark current contributions have been subtracted from the profile. The apparent broadening of the interface transition in this profile in

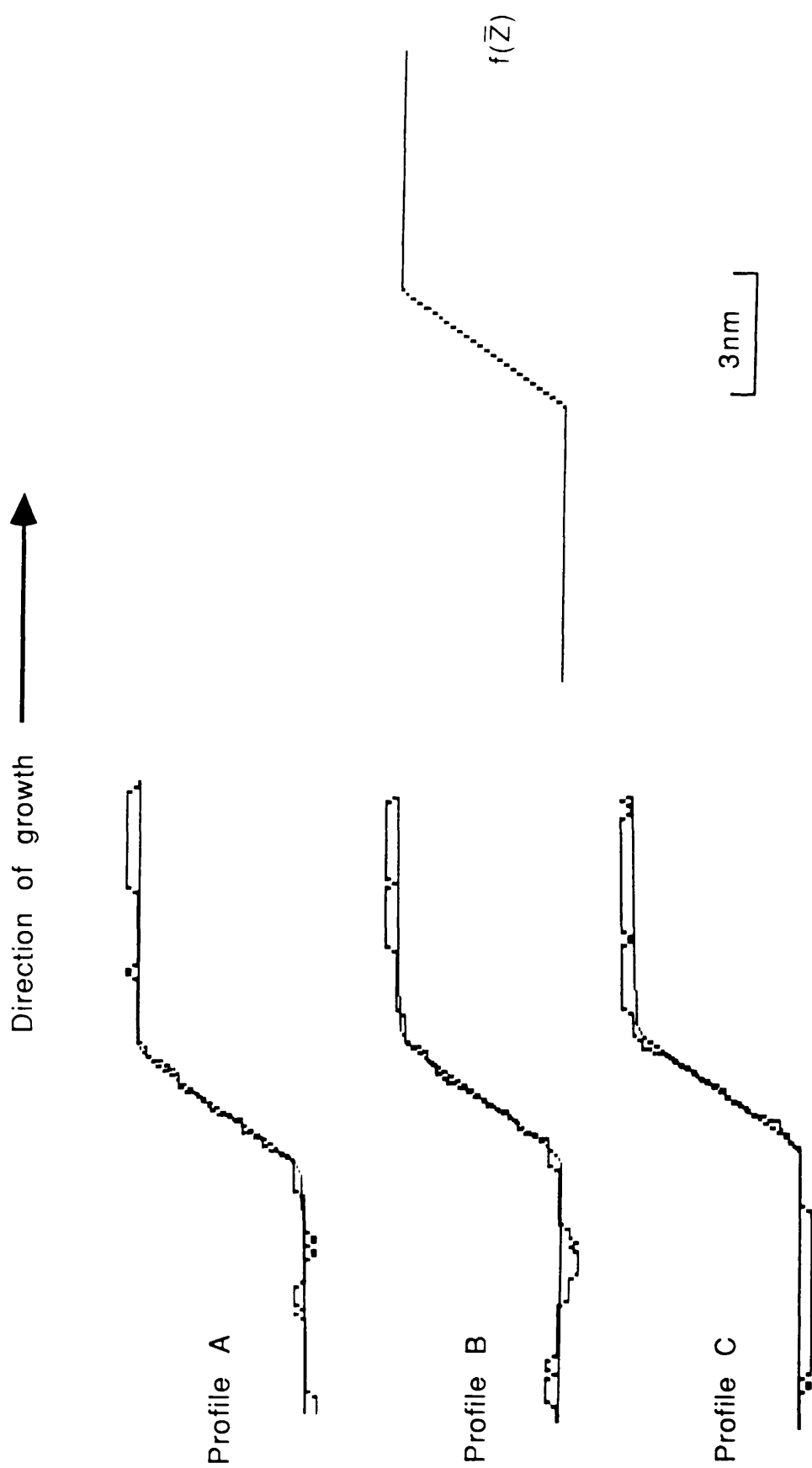

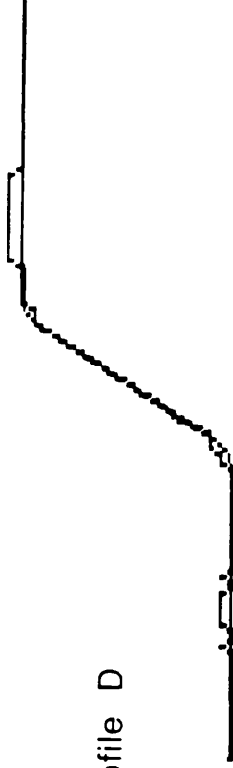


Figure 7.4: Comparison between the type 1 interfaces of profiles A, B and C with a simulated profile calculated from a transition width of 3nm

Direction of growth 

Profile D



Profile E



Profile F



$f(\bar{Z})$



3nm

Figure 7.5: Comparison between the type 1 interfaces of profiles D, E and F with a simulated profile calculated from a transition width of 3nm

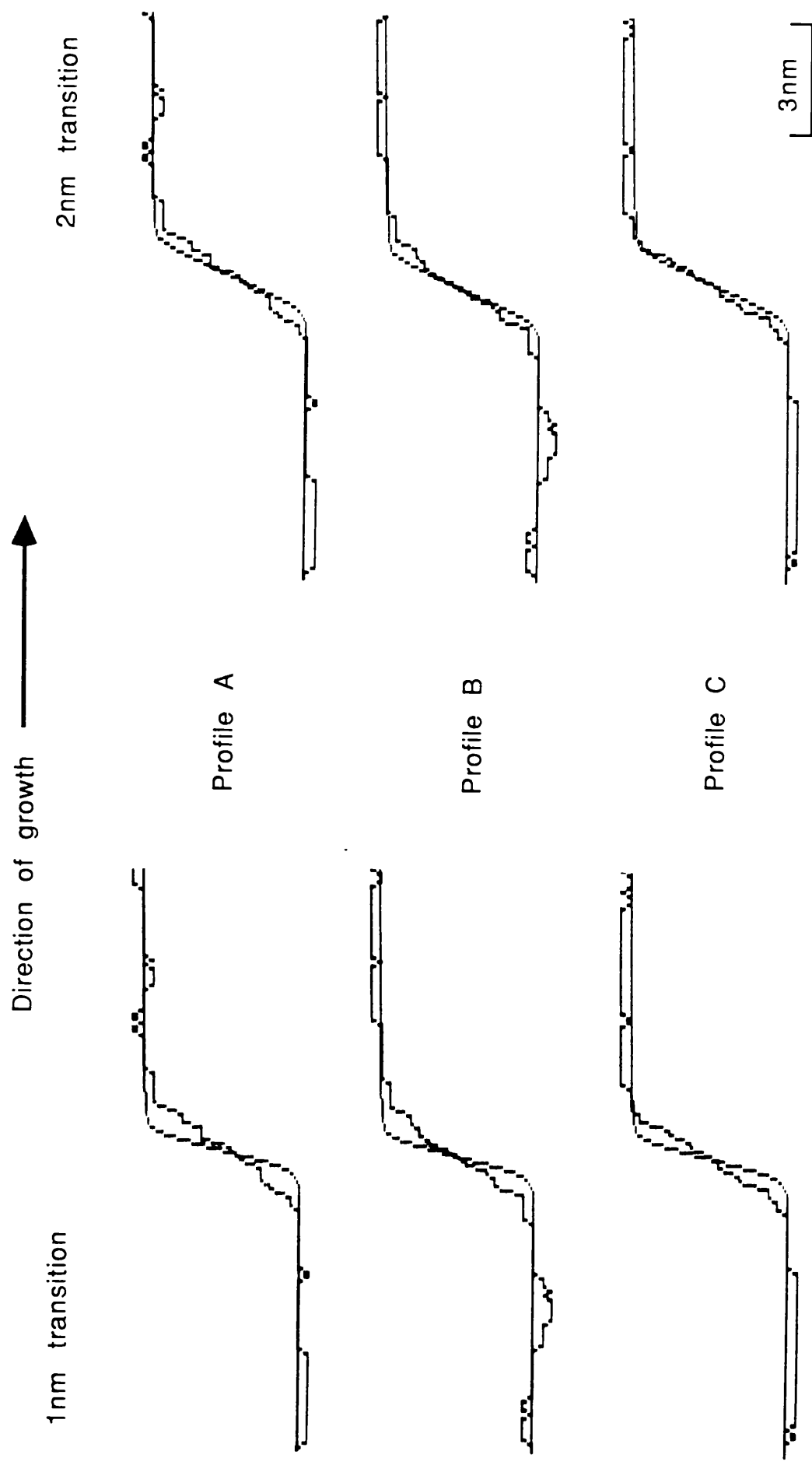


Figure 7.6: Comparison between the type 1 interfaces of profiles A, B and C with simulated profiles calculated from transition widths of 1nm and 2nm

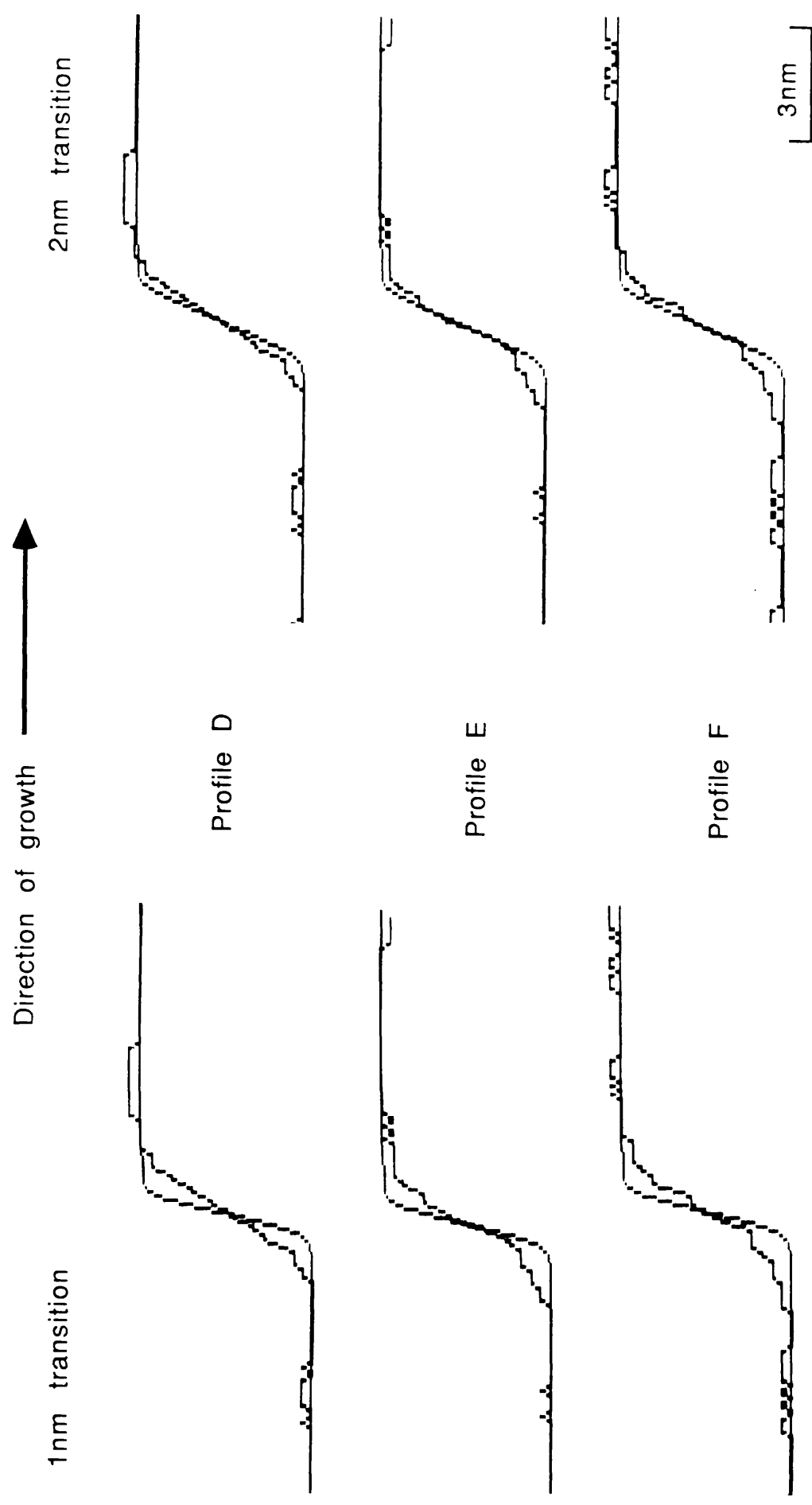


Figure 7.7: Comparison between the type 1 interfaces of profiles D, E and F with simulated profiles calculated from transition widths of 1nm and 2nm

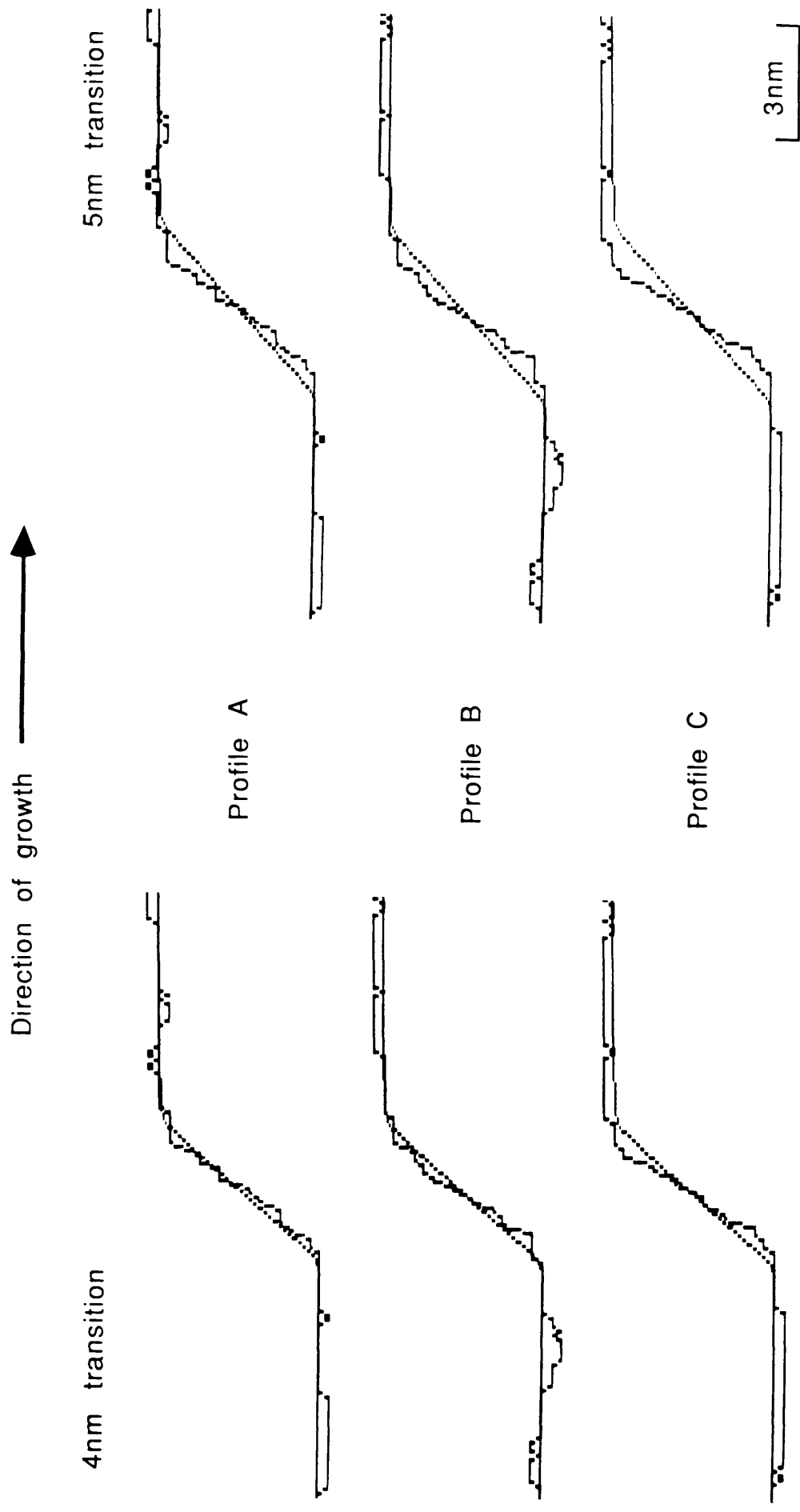


Figure 7.8: Comparison between the type 1 interfaces of profiles A, B and C with simulated profiles calculated from transition widths of 4nm and 5nm

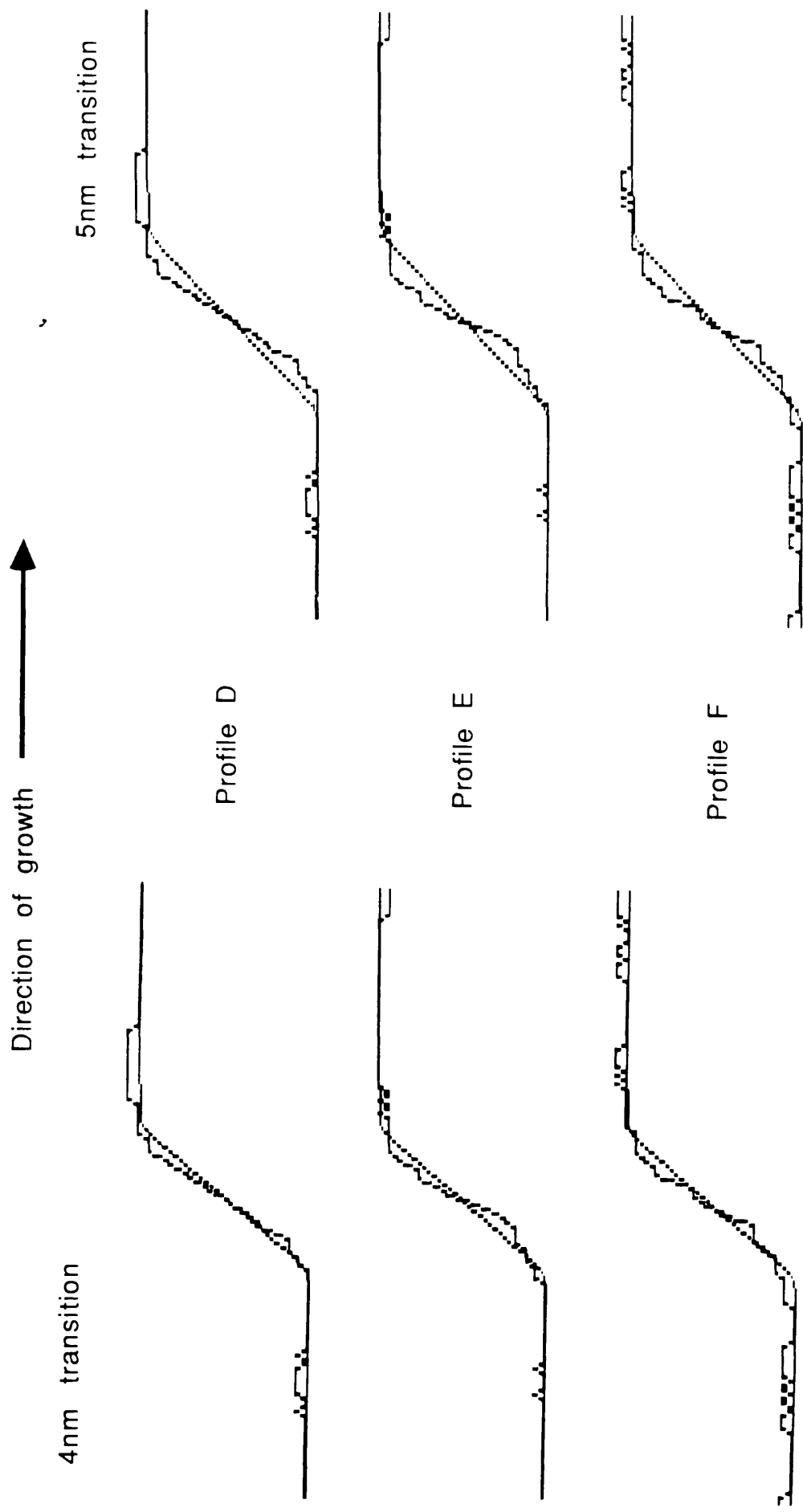


Figure 7.9: Comparison between the type 1 interfaces of profiles D, E and F with simulated profiles calculated from transition widths of 4nm and 5nm

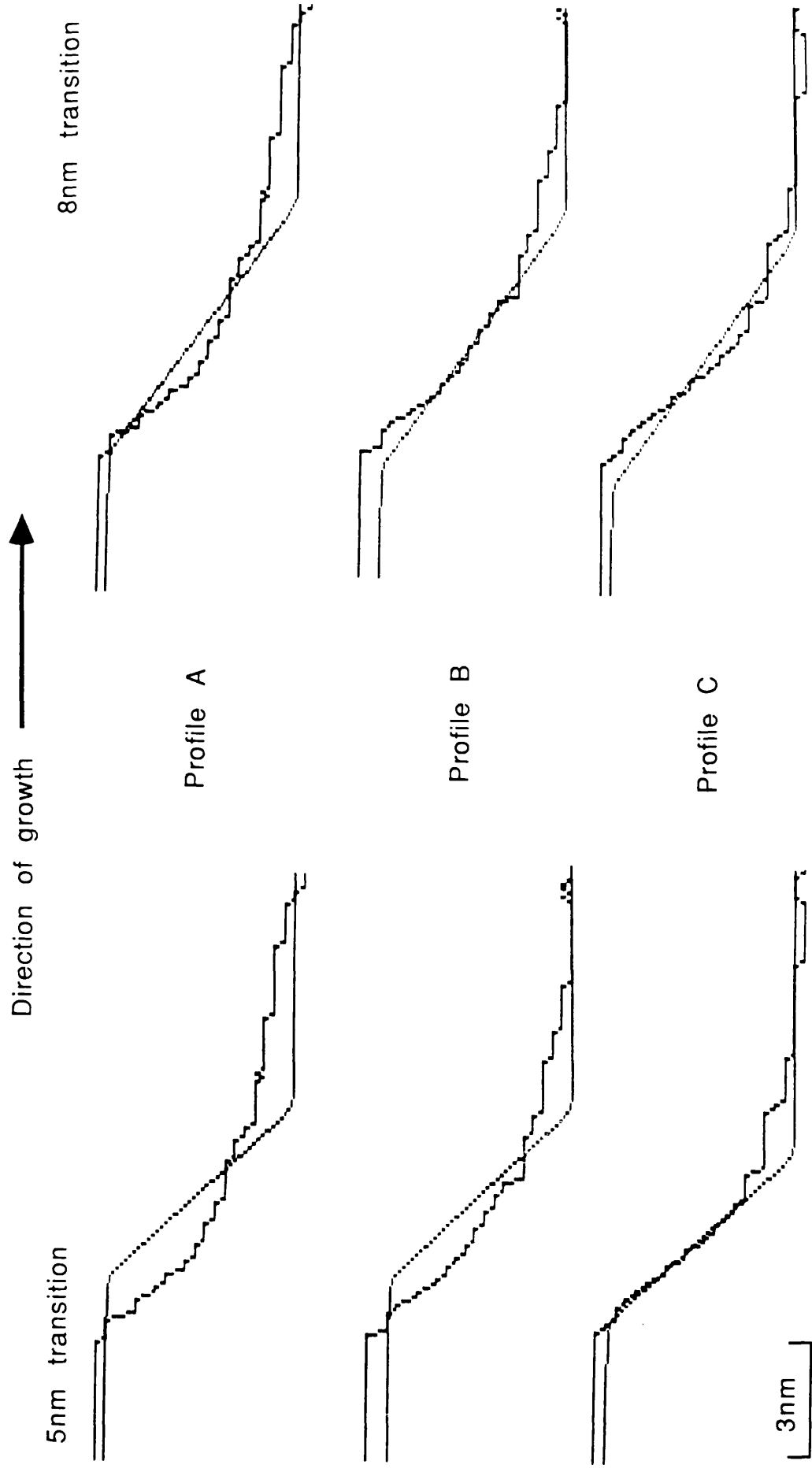


Figure 7.10: Comparison between the type 2 interfaces of profiles A, B and C with simulated profiles calculated from transition widths of 5nm and 8nm

Direction of growth →

5nm transition

8nm transition

Profile D

Profile E

Profile F

3nm

Figure 7.11: Comparison between the type 2 interfaces of profiles D, E and F with simulated profiles calculated from transition widths of 5nm and 8nm

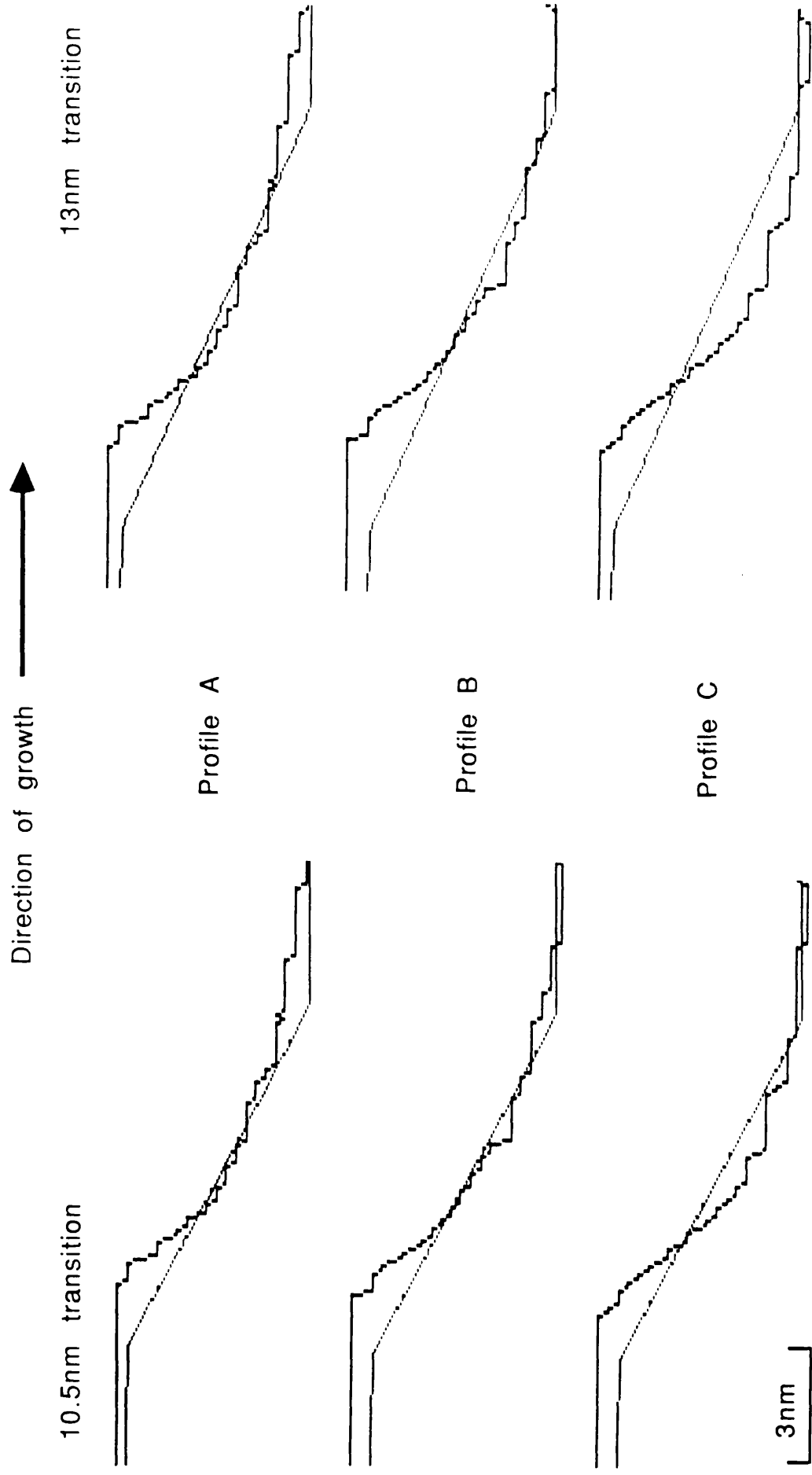


Figure 7.12: Comparison between the type 2 interfaces of profiles A, B and C with simulated profiles calculated from transition widths of 10.5nm and 13nm

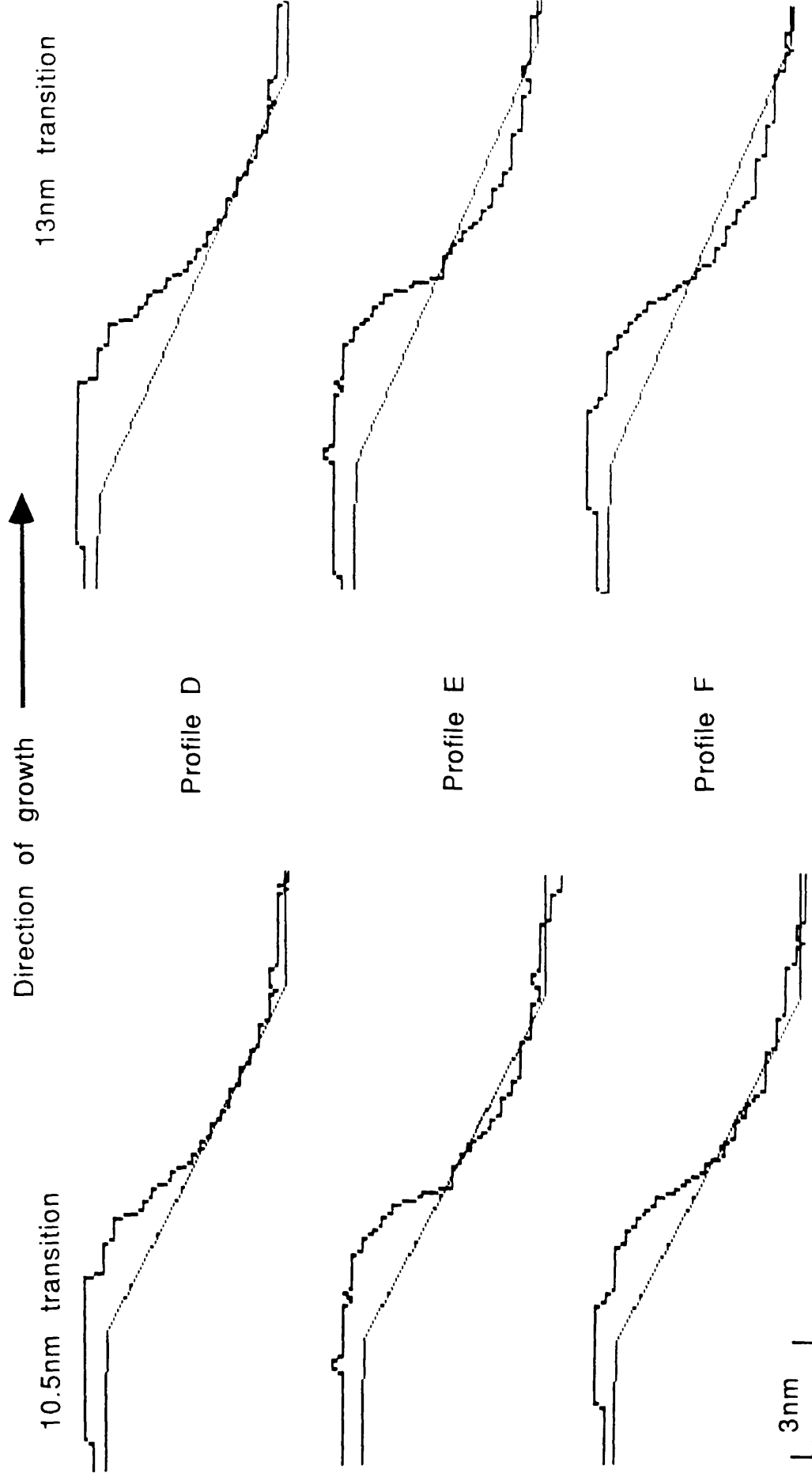


Figure 7.13: Comparison between the type 2 interfaces of profiles D, E and F with simulated profiles calculated from transition widths of 10.5nm and 13nm

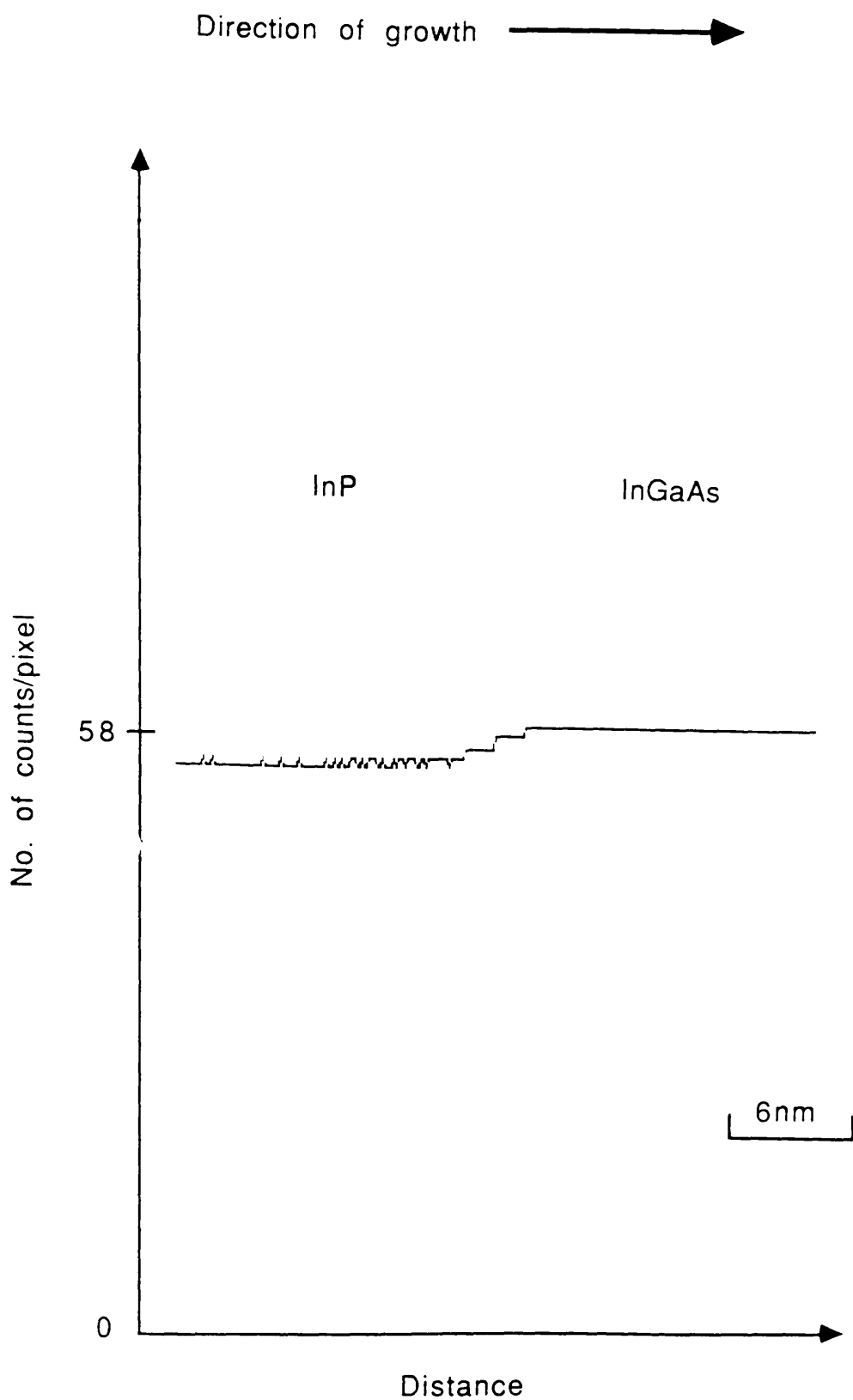


Figure 7.14: Contrast detected between layers of InGaAs and InP from an image acquired with zero offset and zero black level. Dark current contributions have been taken into consideration.

relation to those shown in figures 7.2 and 7.3 is a result of the large number of linescans sampled. The level of contrast (C) detected between the centre of the InP and InGaAs layers was found to be 0.07.

7.2.2 Discussion

A number of preliminary observations can be made from the high-angle ADF data. The results show that the detected intensity distribution across the multilayer exhibits a strong dependence on the direction of material growth. In particular, the type 2 transition (spanning approximately 20 unit cell dimensions) is much less abrupt than those of type 1 (~5 unit cell dimensions). This suggests that the observations of Chew et. al. (1987) may be associated with graded changes in composition across the type 2 boundary that are a result of the growth conditions employed. Such concentration transitions, however, imply that there may also be variations in lattice parameter as a function of position across the interface which can in turn lead to the presence of strain in these regions. As was discussed in chapter 2, Treacy et. al. (1988) observed that strain may lead to an increase in detected high-angle ADF intensity. It is likely, therefore, that the detected signal variations can be attributed to both changes in \bar{Z} and the presence of strain. This may account for the slight increase in detected signal from the InGaAs layer before the interface. The relative magnitude of each effect cannot, however, be quantified easily.

Quantitative high-angle ADF analysis of the InGaAs/InP system revealed that the contrast, C, measured between the layers was 0.07. This value is compared in table 7.1 with those predicted in chapter 2 for an $\text{In}_{0.53}\text{Ga}_{0.47}\text{As}/\text{InP}$ lattice matched system using several elastic scattering models. As in the case of the AlGaAs/GaAs system discussed in the previous chapter, the detected contrast is considerably lower than that predicted.

Approach used	Contrast
Experimental (without dark current)	0.07
Born	0.09
Moliere	0.20
Fleischmann	0.12
Z^2	0.24
$Z^{4/3}$	0.17

Table 7.1: Comparison between theoretical high-angle ADF contrast values in an $\text{In}_{0.53}\text{Ga}_{0.47}\text{As}/\text{InP}$ system with that measured experimentally from an InGaAs/InP multilayer system grown by MOCVD at atmospheric pressure.

Furthermore, there is a considerable variation in the value of C predicted from different models. Using the Born cross-section (which gives the closest agreement between experiment and theory), 0.07 contrast corresponds to that predicted between layers of $\text{In}_{0.48}\text{Ga}_{0.52}\text{As}$ and InP . It should be noted that in a complex system such as that examined here, there is a great number of possible compositions that can lead to the level of contrast detected and so further comment on the merits of high-angle ADFI as a direct quantitative analytical technique is not possible without direct compositional information.

7.3 EDX microanalysis

This section describes EDX microanalysis investigations carried out on InGaAs/InP multilayers that were grown by MOCVD at atmospheric pressure. The experimental procedure and analysis techniques employed here are similar to those established in the previous chapter, although particular emphasis is now given to the problems involved in the analysis of specimens in which the relative concentrations of four elemental species can vary. The aim of the experiments described here is to supplement the data recorded using high-angle ADFI with quantitative information on the way in which the concentrations of specific elemental species vary across the systems as a function of material growth and on the material compositions in the centre of the layers.

Each series of x-ray spectra discussed in this section was acquired using either a windowless or conventional EDX detector. It was found that when the former was employed, acquisition times of 10s were sufficient to provide characteristic x-ray peaks with adequate statistical significance (typically ~8000 counts in the In L peak in a spectrum acquired from a 50nm thick region of InP) whereas times of 30s were found suitable when acquiring spectra using the conventional detector.

7.3.1 Analysis of spectra

The analysis procedure described here was carried out on series of spectra using the program 'InGaAs_Analyse' which was written in Super Basic for use on a Sinclair QL minicomputer. The program is listed in full in appendix A4.

Elemental concentrations in the InGaAs/InP multilayers were measured by calculating the number of characteristic counts detected in the P K, In L, Ga K $_{\alpha}$ and As K $_{\alpha}$ peaks. The method by which the number of Ga K $_{\alpha}$ and As K $_{\alpha}$ counts were evaluated is described in detail in chapter 6. Figure 7.15 shows a comparison between a spectrum acquired from a region of InP (continuous line) with that acquired from an area containing Ga and As (broken line) in the energy range of the P K peak. The figure shows that, provided care is taken to avoid the Si K peak (Si is incorporated in the specimen in small quantities as a result of the specimen preparation technique used), extraction of the P K characteristic signal from the bremsstrahlung background can be achieved by linear interpolation from just above the As L peak to the high energy side of the P K peak. Minor complications, however, exist for the In L peak which, as figure 7.16 illustrates, consists of a number of lines and extends over a range of ~1.2keV. The latter part of this range overlaps with the I L peaks and it was not unusual to find small quantities of I, which was used in the thinning process, incorporated in the specimen. To ensure that no I counts were included in the signal ascribed to In, it was necessary to use a window smaller than the full In peak width and thus sum only the counts falling in the restricted energy region where no overlap occurred. The window used for all analyses described here extended over an energy region from 3.12 to 3.78 keV.

A departure from the analysis process described in chapter 6 is that at this stage of the procedure, corrections were considered for the self-absorption of generated x-rays in the specimen and the generation of additional x-rays by

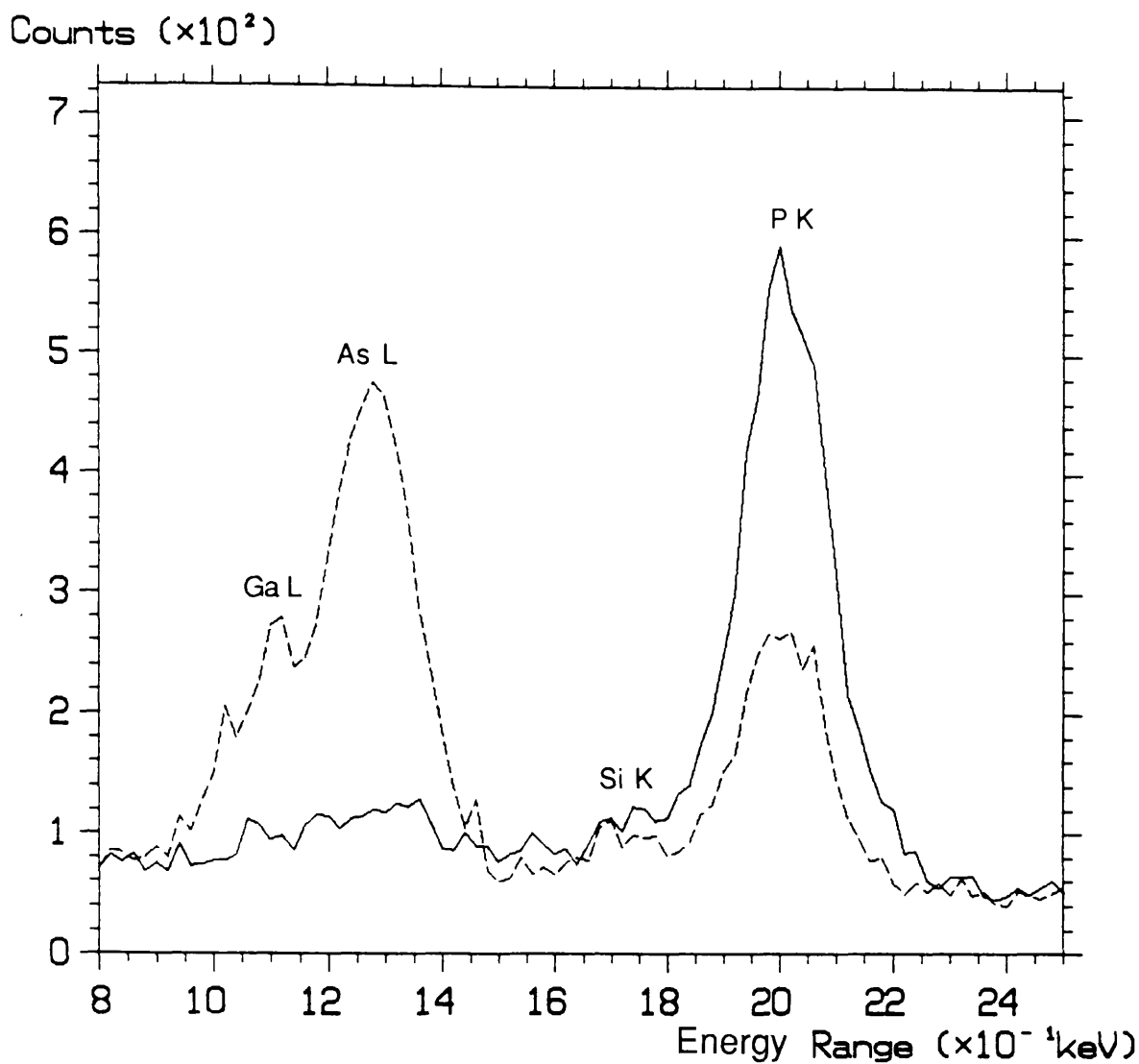


Figure 7.15: Comparison of an x-ray spectrum acquired in a region of InP (continuous line) with that acquired in a region containing Ga and As (broken line) in the energy range of the P K peak.

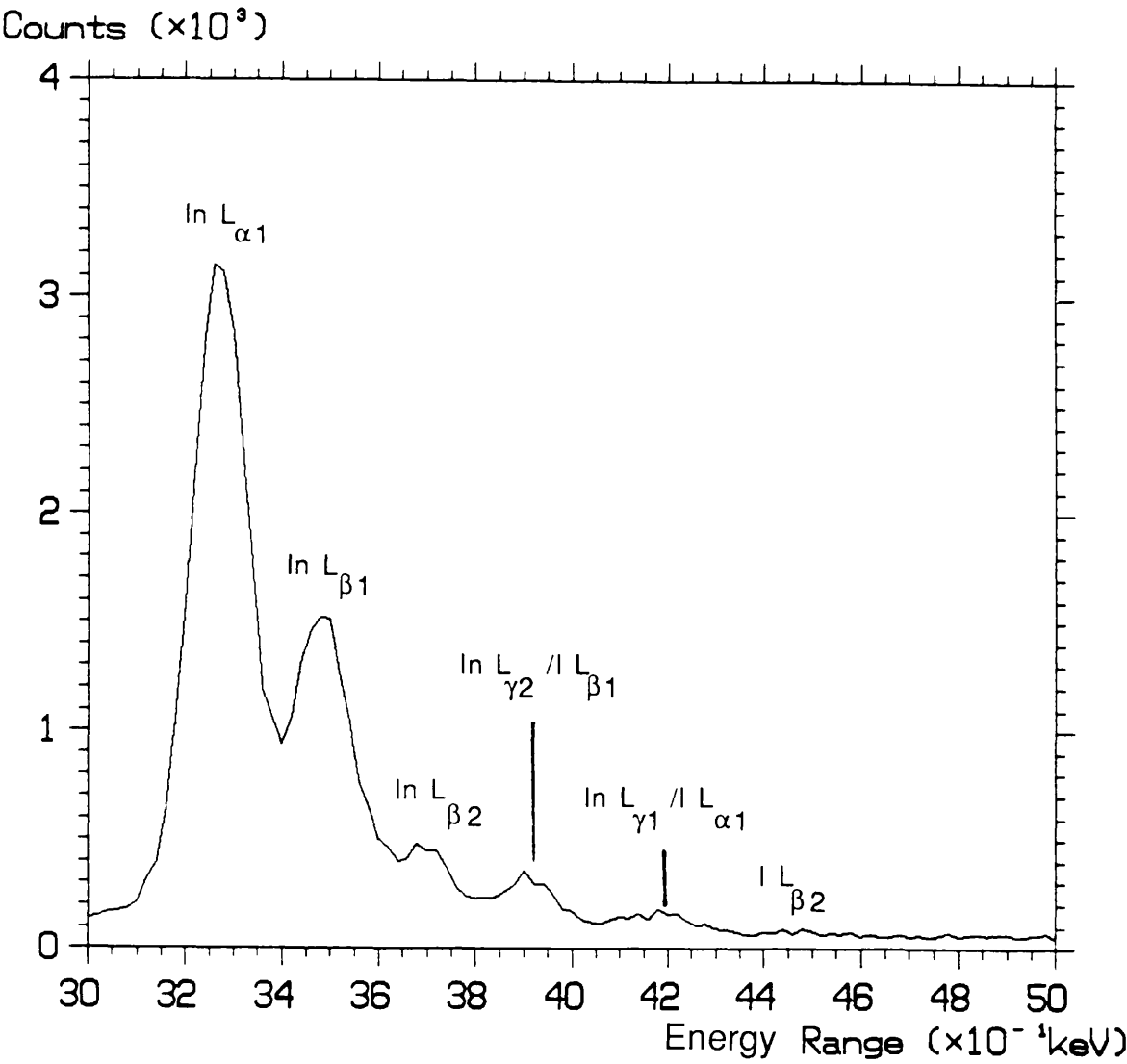


Figure 7.16: X-ray spectrum showing the overlap that occurs between the In L and I L lines

fluorescence. The latter was negligible for specimens with thicknesses in the range used in this project while, as chapter 5 showed, the former was significant only in the cases where P was present along with a high concentration of As and Ga. A spectrum acquired from such a region is shown by the broken line in figure 7.15. It was found that suitable corrections could be made by multiplying the number of P characteristic counts measured from spectra acquired in regions of InGaAs by an absorption factor, 'Pabs'. The numerical value of this factor varied slightly from series to series, depending on the local film thickness, but remained constant over each individual series analysed. The maximum value of 'Pabs' used corresponded to 5% absorption of the P signal. This is in general agreement with the calculations described in chapter 5.

In a manner similar to that described in chapter 6, the second stage of analysis relates the number of detected counts (N_i) in each characteristic peak to the number of atoms (n_i) in the volume irradiated by the beam to yield elemental concentrations. For the InGaAs/InP system, the most convenient way to express such concentrations is in terms of the atomic fractions (f_i) for each of the elements in the material;

$$f_i = \frac{n_i}{\sum_j n_j} = \frac{N_i}{\left(N_i + \sum_{j \neq i} K_{ji} N_j \right)} \tag{7.1}$$

where j and i take values between 1 and 4. The K_{ji} values relate the relative efficiency of production and detection of the characteristic signals and are defined in equation 6.4. All K-factors are related by a chain rule defined by;

$$K_{ji} = K_{jk} K_{ki} \tag{7.2}$$

From equation 7.2 it is apparent that only three K-values need be determined either experimentally, through the use of standards of known composition or from a knowledge of the individual factors in equation 6.4. Here both approaches were used. For experiments using the windowless detector, K_{GaAs} , K_{GaP} and K_{InP} were determined experimentally from x-ray analyses of pure GaAs, GaP and InP specimens using standard experimental conditions but with longer acquisition times to reduce statistical uncertainties. The values obtained for the measured K-factors and those deduced using equation 7.2 are listed in table 7.2. The values of K_{GaAs} and K_{GaP} calculated using equation 6.5 are 0.901 and 1.036 respectively, which is in close agreement with the experimental values. For experiments using the conventional detector, K_{GaAs} and K_{InP} were determined experimentally, the values obtained being 0.90 and 0.44 respectively. The former value is again in close agreement with that calculated from theory. Greater difficulties, however, were encountered in deriving a reliable value relating In or P to Ga or As as no suitable standard was available at the time when the conventional detector was in use. Consequently, reliance had to be placed on theoretical calculations. The value used for K_{AsP} was 0.79 and was selected on the basis of the extensive theoretical calculations of Rez (1984). This value was chosen because of the close agreement between predictions based on this theory and experimental measurements made on Al (Steele, 1987), whose atomic number is close to that of P. A full list of the K-factors used for analyses employing the conventional EDX detector is given in table 7.2. The table shows that there is a significant difference between the windowless and conventional detectors over the K-values relating In and P to Ga and As. The values are consistent with the conventional detector being less efficient at low energies than predicted in chapter 5 using a Be window effective thickness of $8.3\mu\text{m}$. This may be attributable to the accumulation of contamination on the surface of the Be window. It should be noted, however, that the results discussed in this chapter are self-consistent to a high degree, irrespective of

K-value	Detector used	Elements					
		InGa	InP	InAs	GaAs	GaP	AsP
	Conventional	0.63	<u>0.44</u>	0.56	<u>0.90</u>	0.71	0.79
	Windowless	0.49	<u>0.49</u>	0.44	<u>0.90</u>	<u>1.00</u>	1.11

Table 7.2: K-factors used in the analysis of InGaAs/InP systems using both windowless and conventional EDX detectors. Those values determined experimentally are underlined.

detector type employed, and so confidence can be placed in both sets of K-factors used.

As in chapter 6, the error (δf) associated with each atomic fraction measurement is governed by Poisson statistics of the gross and nett counts in the peaks of interest. In this case, the most convenient method to calculate δf is to express equation 7.1 in terms of numerator U and denominator V;

$$f_i = \frac{U_i}{V_i} \quad (7.3)$$

and so;

$$\left(\frac{\delta f_i}{f_i} \right)^2 = \left(\frac{\delta U}{U} \right)^2 + \left(\frac{\delta V}{V} \right)^2 \quad (7.4)$$

δV can be calculated from the expression;

$$\begin{aligned} \delta V^2 &= \delta N_i^2 + \sum_{j \neq i} K_{ji}^2 \delta N_j^2 \\ &\simeq N_i + \sum_{j \neq i} K_{ji}^2 N_j \end{aligned} \quad (7.5)$$

this approximation is based on the assumption that the numbers of characteristic counts in the peaks of interest is much greater than those attributable to the background. Using the same approximation;

$$\delta U_i^2 \simeq N_i \quad (7.6)$$

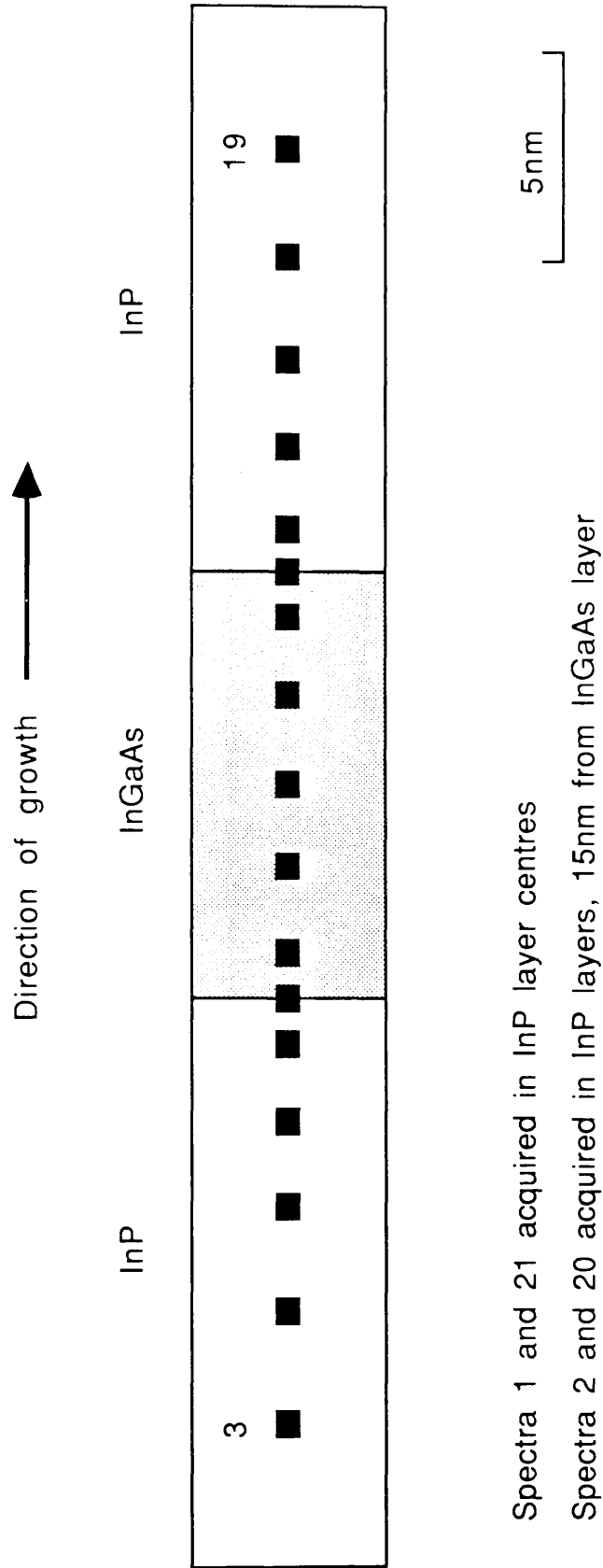
The errors associated with the mean values of atomic fractions at layer centres

that are quoted in the following section were calculated following the procedure described in section 6.3.1.

7.3.2 Results

Initial investigations using EDX microanalysis were carried out using two multilayer systems (denoted here as specimens 1 and 2). Specimen 1 comprised 50 InGaAs layers, each 10nm in width, that were grown between 50nm buffer layers of InP. Specimen 2 was a more complicated structure in that it comprised one 15nm InGaAs well followed by three 10nm InGaAs wells, with each well separated by 5nm InP buffer layers. The positions at which x-ray spectra were acquired across individual layers in specimens 1 and 2 are given in figures 7.17 and 7.18 respectively. Each series acquired from specimen 1 comprised 21 spectra, whereas 29 spectra comprised each series carried out across specimen 2. In general, steps of 1nm were used when recording spectra in the vicinity of the interfaces, where the composition changed rapidly, while steps of 10nm were employed near the centres of the broad InP layers. Using the analysis procedure described in the previous section, figures 7.19 and 7.20 show plots of the variations in atomic fraction of each element calculated from several series of spectra acquired across specimens 1 and 2 respectively. Due to the complicated nature of elemental distributions across specimen 2, the results in figure 7.20 are separated into plots of the variation of f_{In} and f_{Ga} , and f_{As} and f_{P} .

All the results shown in figures 7.19 and 7.20 exhibit the same feature revealed by high-angle ADFI, namely the marked dependence of interface abruptness on the direction of growth. This is firm evidence for significant elemental redistribution in the vicinity of the type 2 interfaces. Examination of the results in figure 7.19 clearly shows that beyond type 2 interfaces in the



Spectra 1 and 21 acquired in InP layer centres

Spectra 2 and 20 acquired in InP layers, 15nm from InGaAs layer

Figure 7.17: Schematic diagram showing the positions at which x-ray spectra were acquired from MOCVD grown InGaAs/InP specimen type 1.

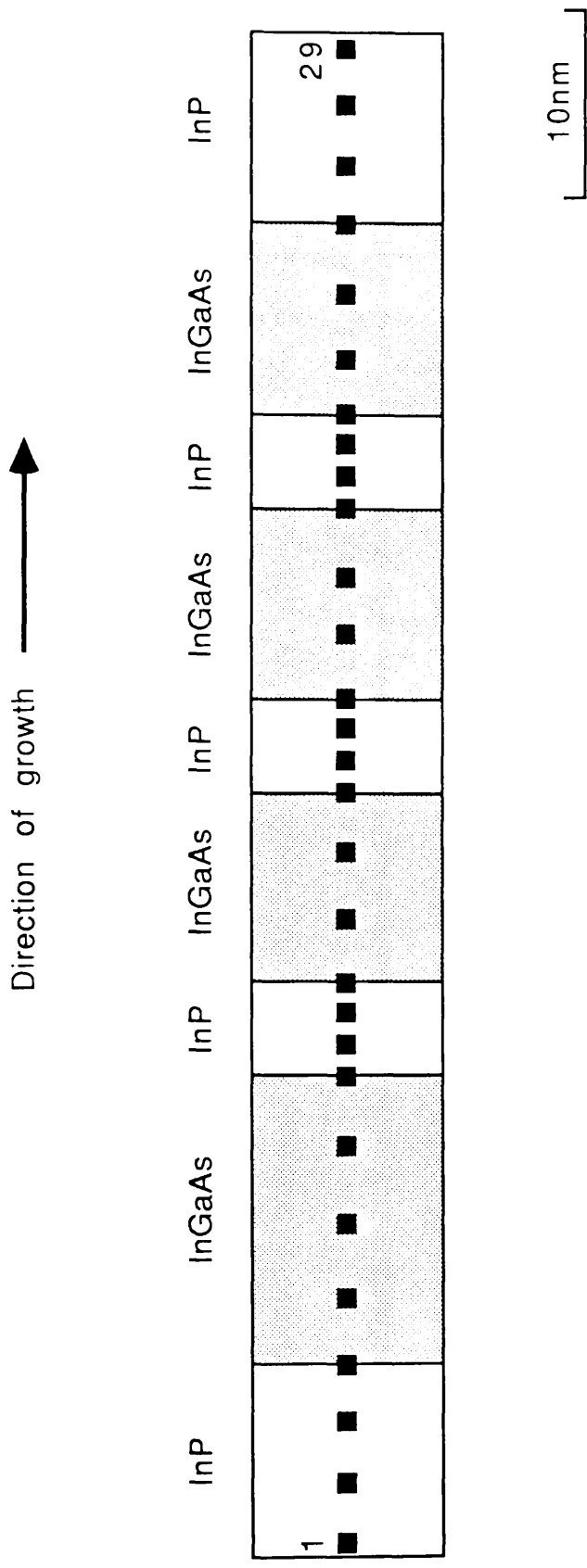


Figure 7.18: Schematic diagram showing the positions at which x-ray spectra were acquired from MOCVD grown InGaAs/InP specimen type 2.

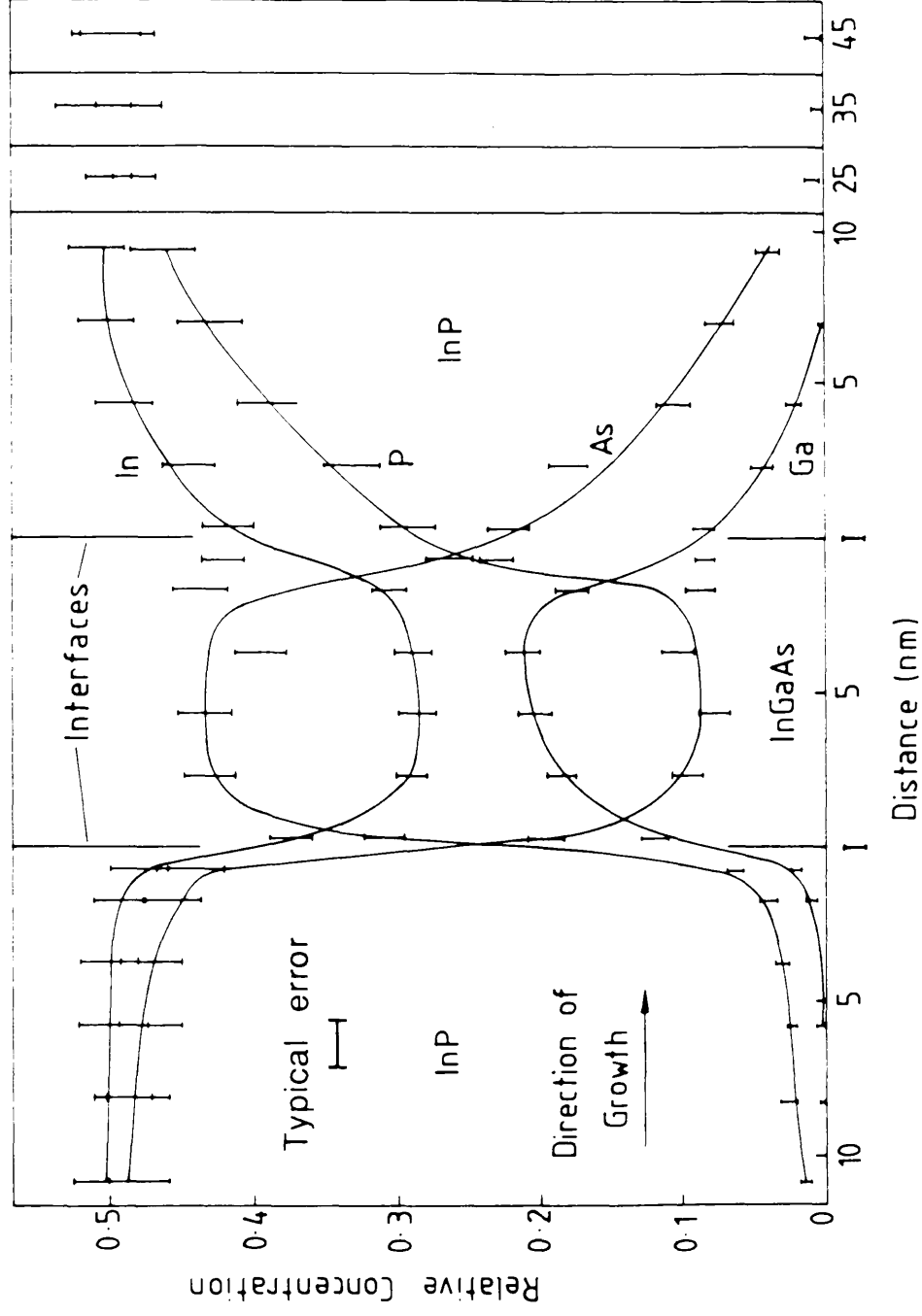


Figure 7.19(a): Graph showing the variation of atomic fractions across an InGaAs layer in specimen 1 calculated from EDX data

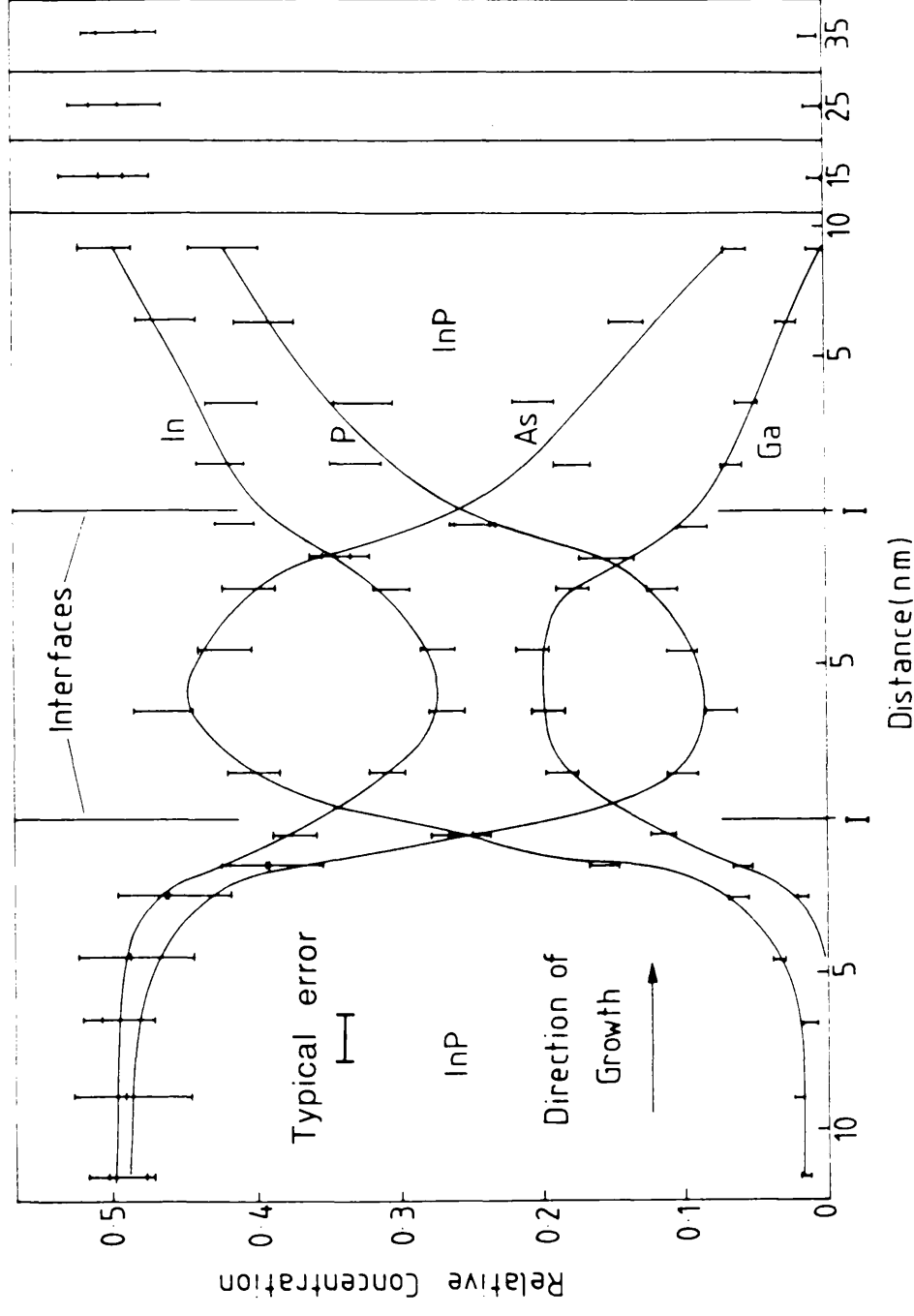


Figure 7.19(b): Graph showing the variation of atomic fractions across an InGaAs layer in specimen 1 in a different region from that in (a) and calculated from EDX data

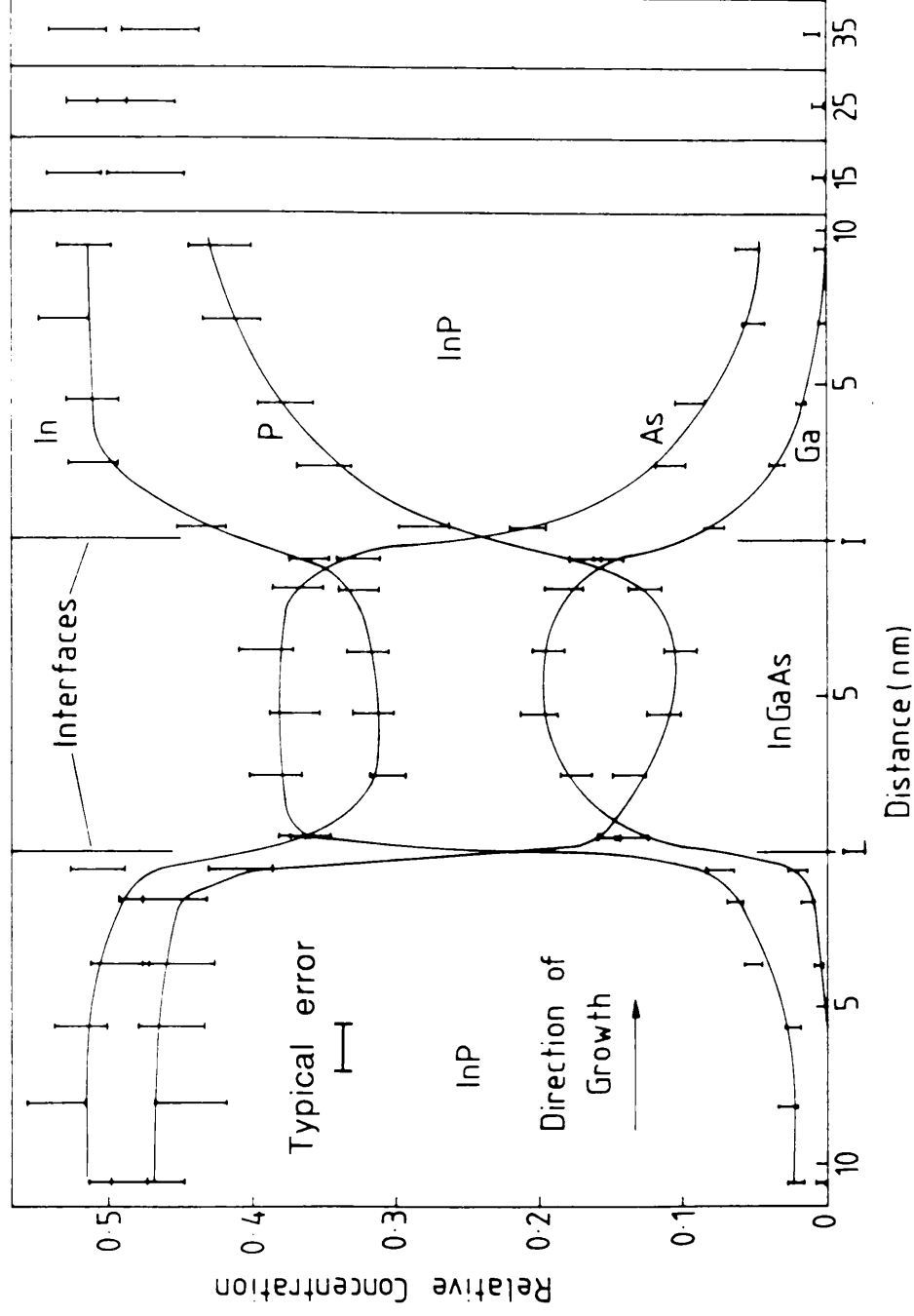


Figure 7.19(c): Graph showing the variation of atomic fractions across an InGaAs layer in specimen 1 in a different region from that in (a) and (b) and calculated from EDX data

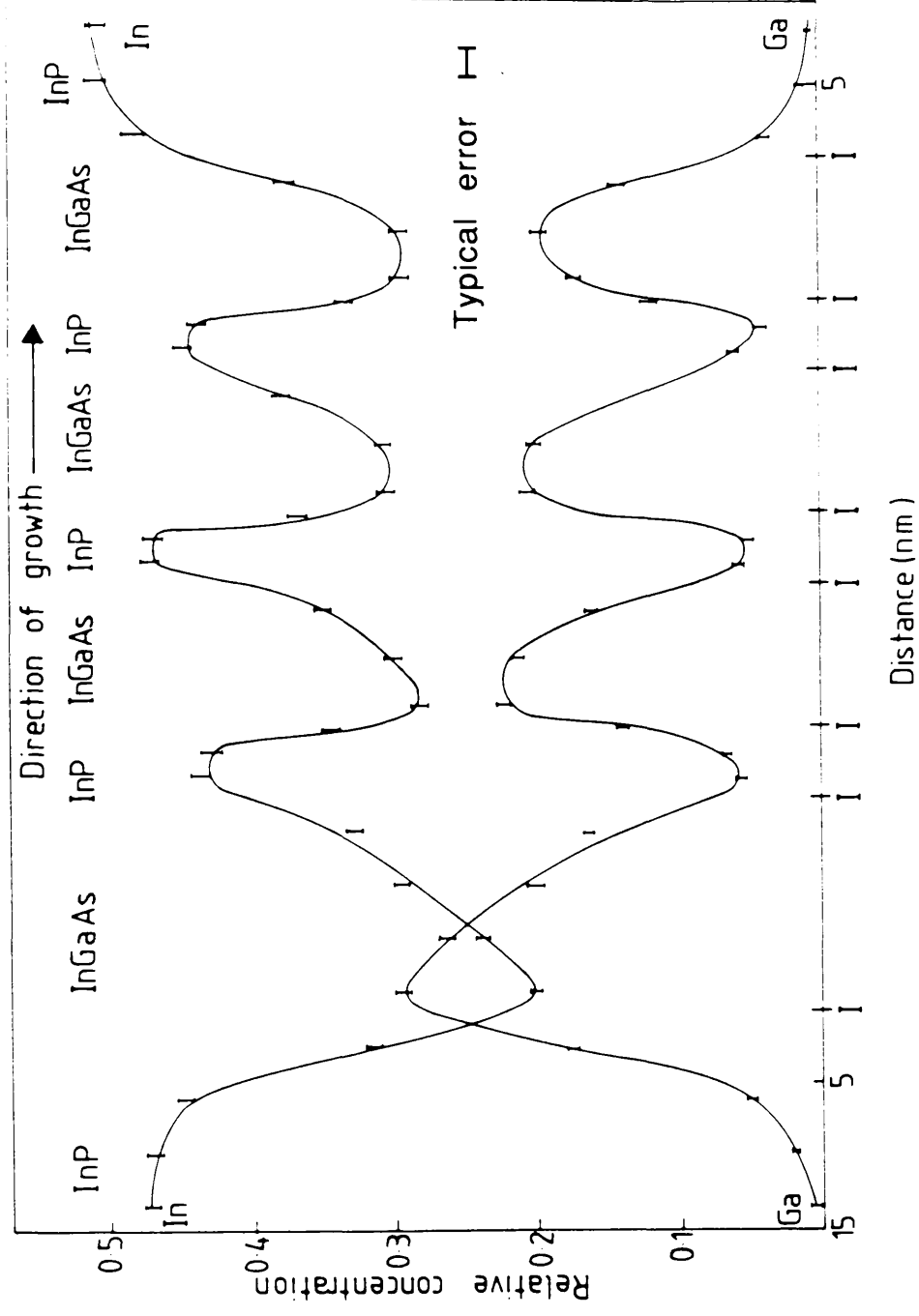


Figure 7.20(a): Graph showing the variation of the atomic fractions for In and Ga across an InGaAs layer in specimen 2 calculated from EDX data

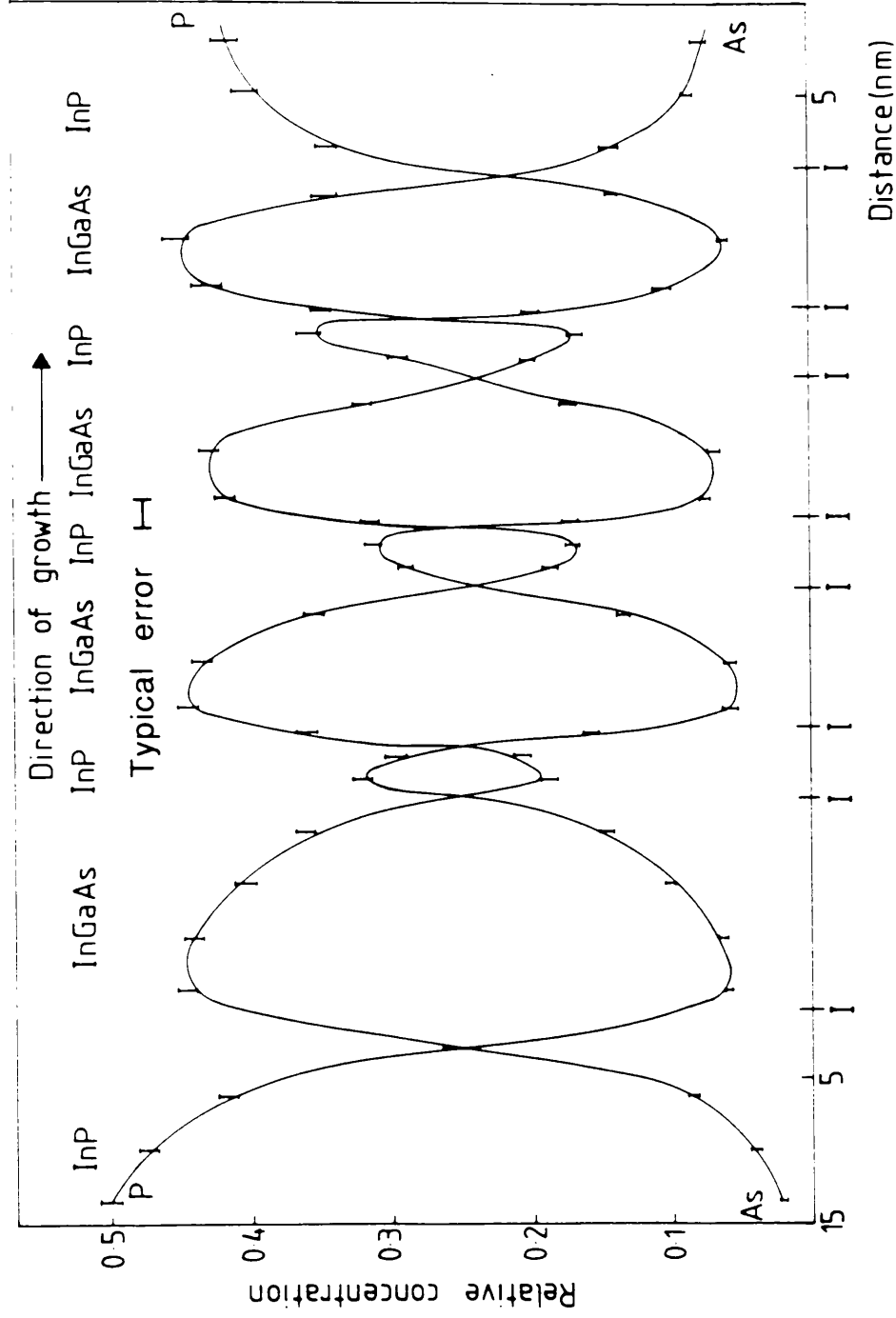


Figure 7.20(b): Graph showing the variation of the atomic fractions for As and P across an InGaAs layer in specimen 2 in the same region as that in (a) and calculated from EDX data

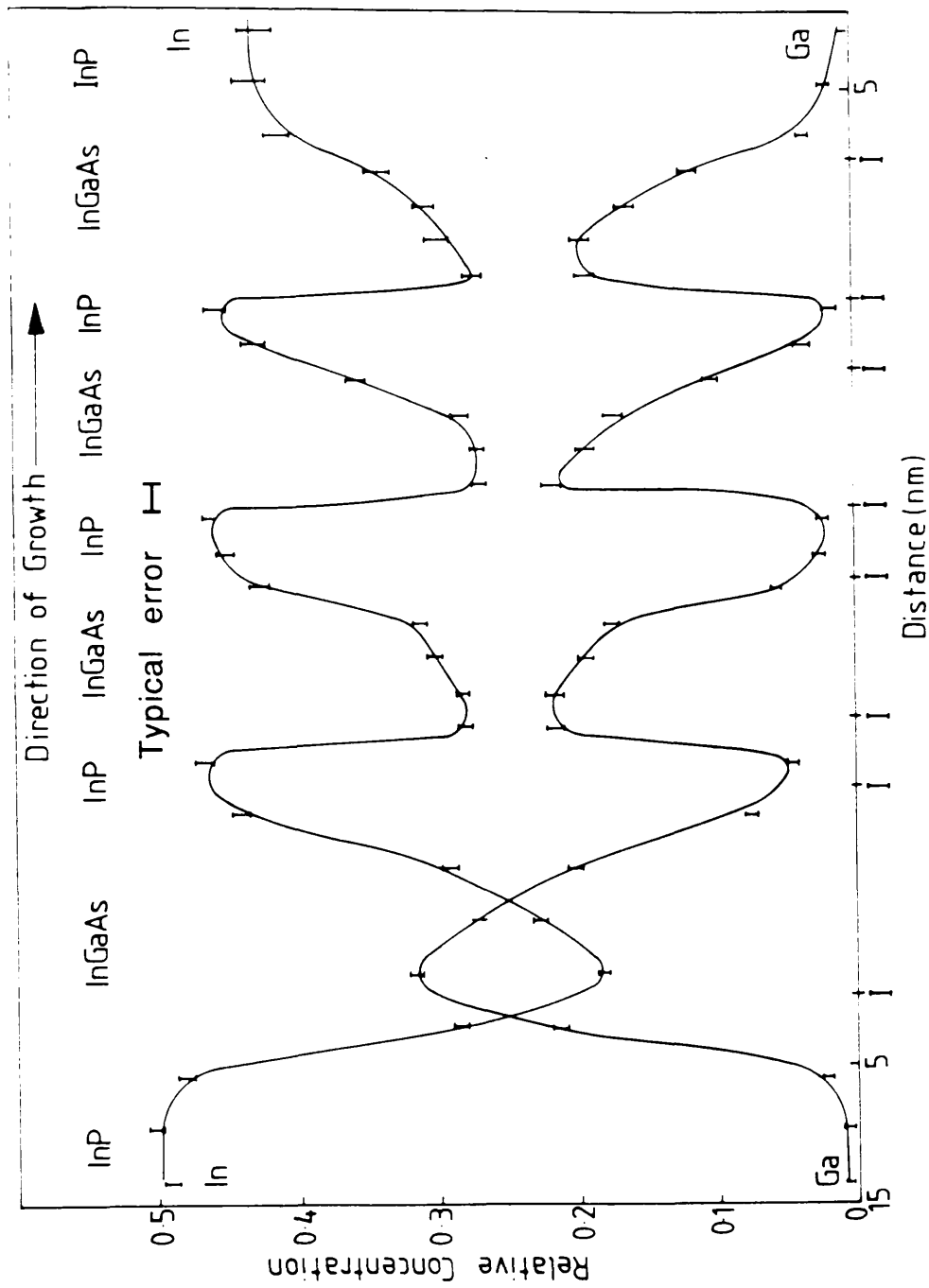


Figure 7.20(c): Graph showing the variation of the atomic fractions for In and Ga across an InGaAs layer in specimen 2 in a different region as that in (a) and (b) and calculated from EDX data

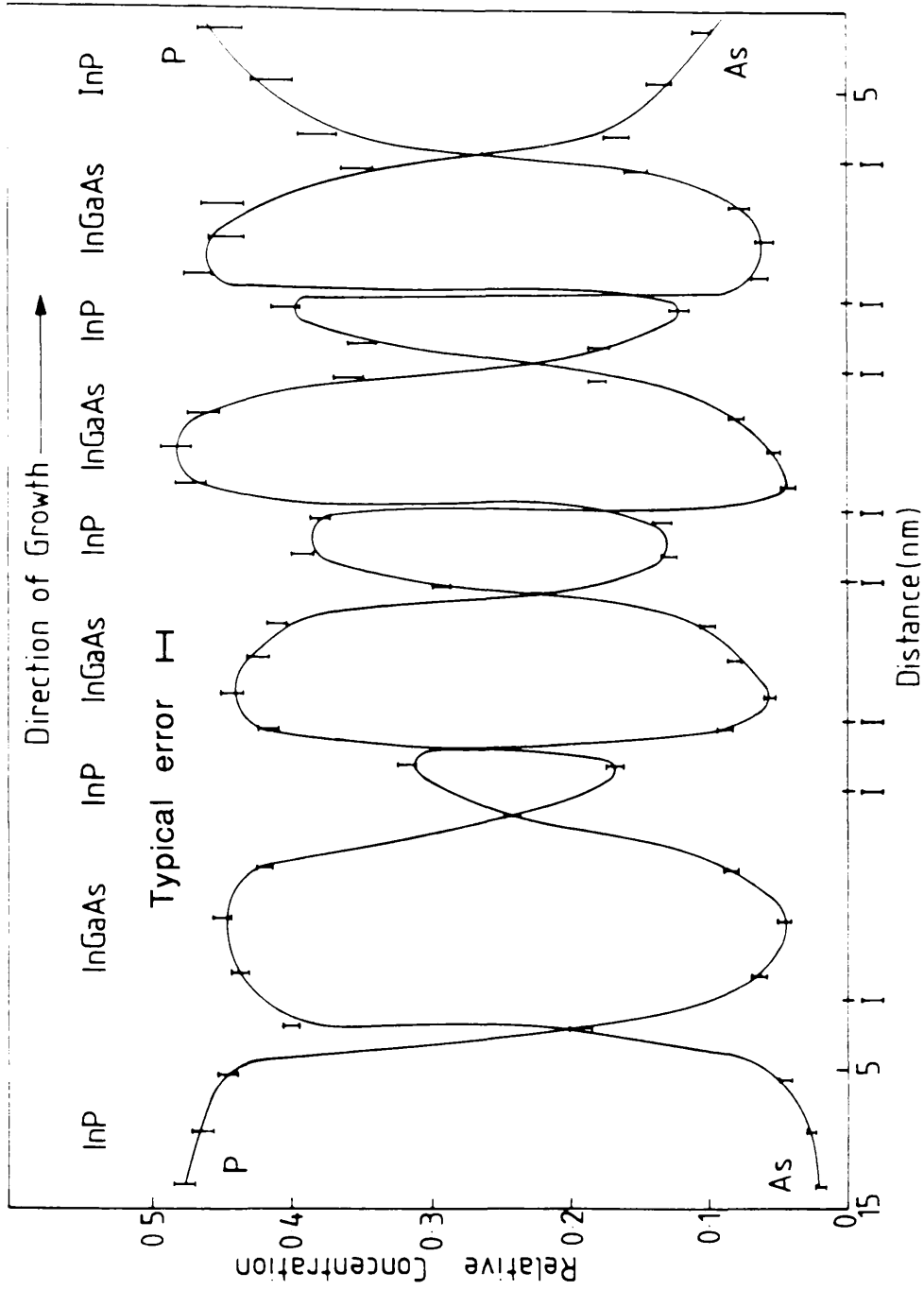


Figure 7.20(d): Graph showing the variation of the atomic fractions for As and P across an InGaAs layer in specimen 2 in the same region as that in (c) and calculated from EDX data

growth direction there is a very substantial As, and to a lesser extent Ga, content in the InP layers which only decays slowly.

As was stressed in chapter 6, detailed interpretation of the detected distributions of the elements in the material using EDX microanalysis should be undertaken with care. This is because of the effect of beam spreading in the specimen across interfaces and into neighbouring layers. Such effects are more noticeable in the data acquired from specimen 2. This can be attributed to two factors: Firstly, as the layers are of smaller dimensions in specimen 2 than in specimen 1. Secondly, the number of characteristic x-ray counts detected indicated that the local film thickness in specimen 2 was ~80nm. The value of t in the areas of specimen 1 examined were found to be in the range 40-50nm. A comparison between the composition changes across the type 2 boundary in figure 19 with the profiles in figure 5.9 that were calculated from Monte Carlo simulations does suggest that the composition transition at this interface is sharply defined. A more quantitative estimate must, however, rely on high-angle ADF data.

The general form of the distributions in figures 7.13 and 7.14 do not depend critically on the K-factors used. However, the magnitudes of the f_i values provide quantitative information on the local compositions. To this end it should be noted that at each position where a spectrum was recorded;

$$f_{\text{Ga}} + f_{\text{In}} = f_{\text{As}} + f_{\text{P}} = 0.5 \quad (7.7)$$

to within experimental error. This is the expected result as the material is known to be structurally perfect and is consistent with there always being a group III atom in one sublattice site and a group V atom in the other. As this condition is in no way forced by the analysis procedure, the above observation serves to validate the method adopted. Although there is a very small amount of As (~0.5%) present in the centre of the 50nm InP layers in specimen 1, the

composition of the InP layer is $\text{In}_{1.0}\text{P}_{1.0}$ to within experimental error. Of greater interest is the composition at the centre of the 10nm InGaAs layers in the same specimen, the mean value of which was found to be $\text{In}_{0.58}\text{Ga}_{0.42}\text{As}_{0.80}\text{P}_{0.20}$ with an error in each index of ± 0.02 . This composition has a corresponding lattice parameter of 0.585nm which was calculated following Furdyna and Kossut (1986). This suggests that there is a small degree of lattice mismatch between the centres of the layers. It should be noted, however, that the detected P content is surprisingly high. As the InGaAs layers in specimen 1 are much narrower than the surrounding InP buffer layers, beam broadening effects could be partly responsible for the P signal, but seem unlikely to account for all of it.

The analytical technique used in chapter 6 to measure layer centre compositions in the presence of tailing effects cannot easily be applied to this system because of the pronounced asymmetry of the concentration distributions. Therefore, to investigate the presence of P in the InGaAs layers further, experiments were carried out on the specimen which possessed InGaAs layer widths of 30nm. A schematic diagram showing the 11 positions at which spectra were acquired across the layers is given in figure 7.21. The results from such a series are plotted in figure 7.22. This graph shows similar interfacial features to those already discussed albeit the local specimen thickness was slightly greater. As a result, the effect of beam broadening was enhanced but the statistical uncertainties were reduced. Of greater interest, however, is the fact that the elemental distribution within the InGaAs layer can now be seen more clearly and, while much lower P concentrations were observed, it appears that P was present throughout the InGaAs layer. From figure 7.16 and other spectra acquired in the centre of the layer, table 7.3 shows that the mean composition well away from the interfaces with the InP layers was found to be $\text{In}_{0.57}\text{Ga}_{0.43}\text{As}_{0.92}\text{P}_{0.08}$. The lattice parameter corresponding to this composition is exactly lattice matched to that of InP (0.587nm).

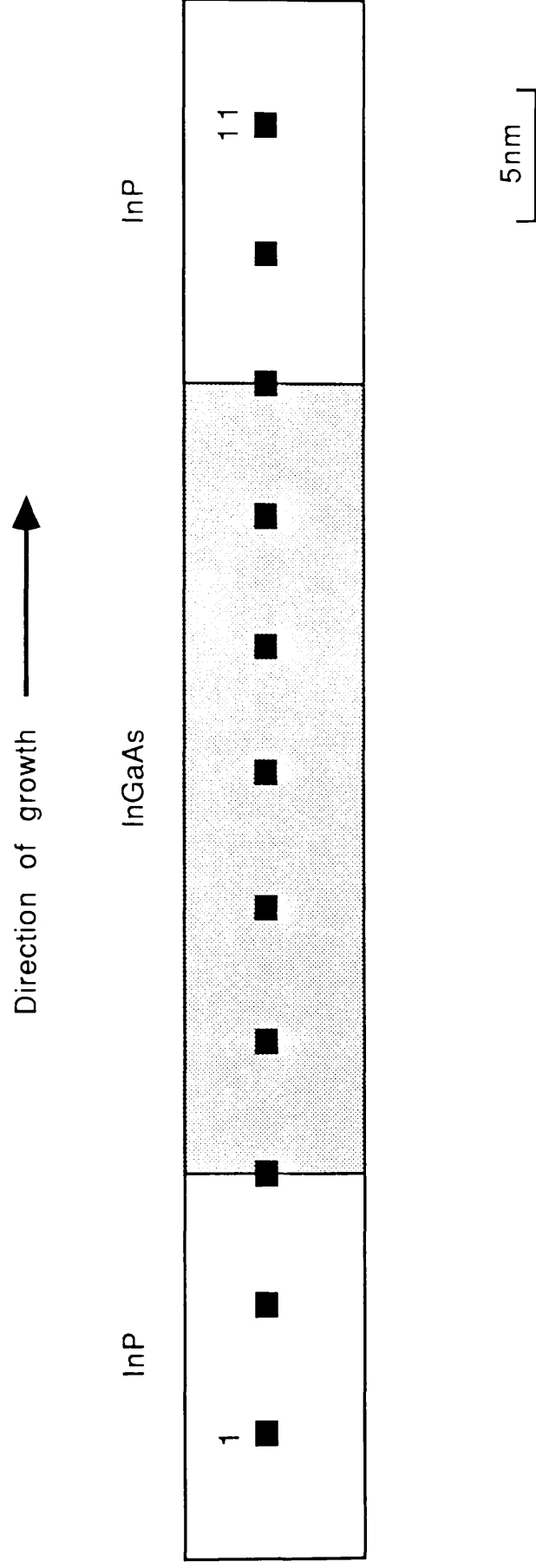


Figure 7.21: Schematic diagram showing the positions at which x-ray spectra were acquired from 30nm InGaAs layer grown by MOCVD at atmospheric pressure.

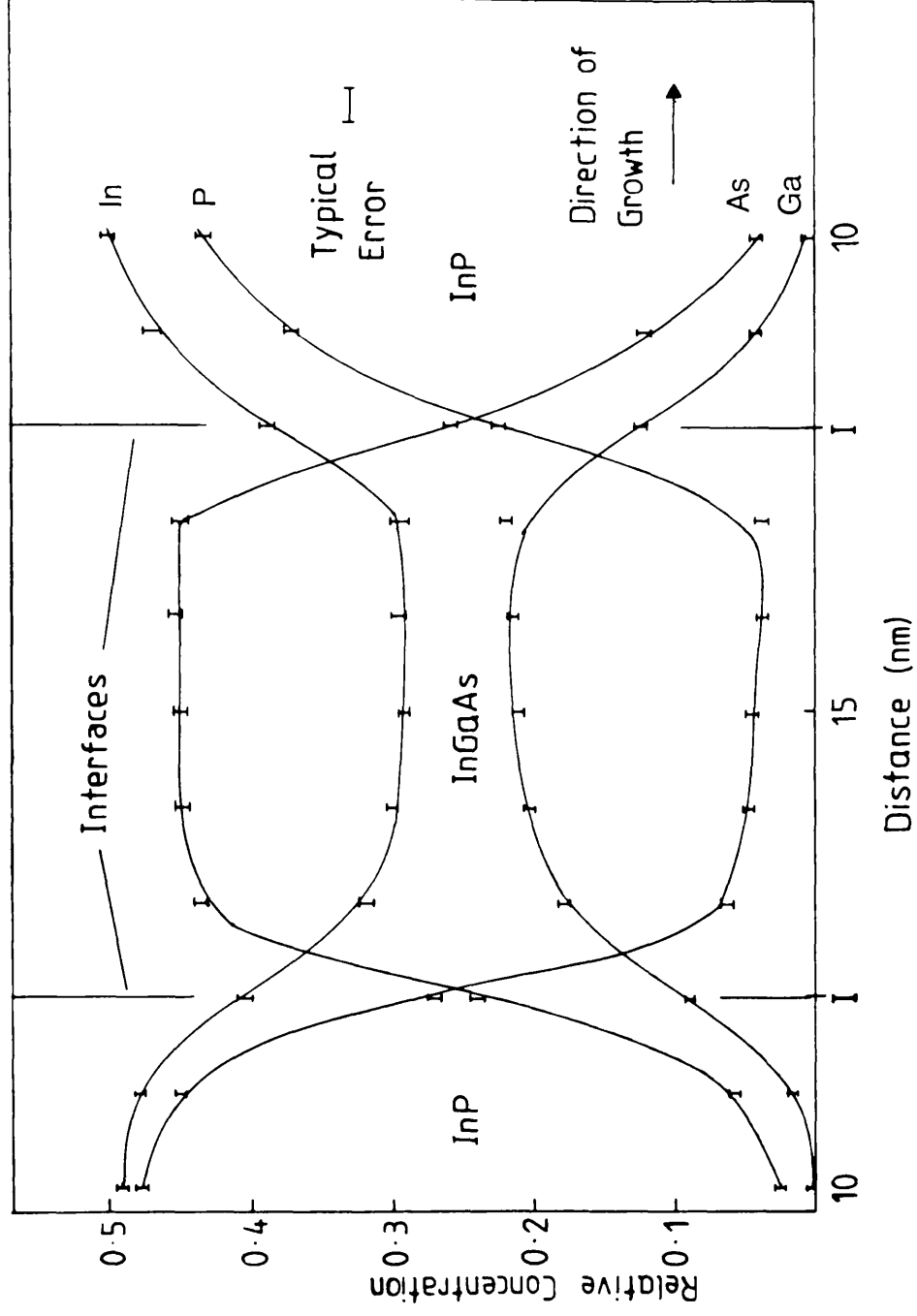


Figure7.22: Graph showing the variation of the atomic fractions across a 30nm InGaAs layer calculated from EDX data

Areas of spectrum acquisition	f_{In}	f_{Ga}	f_{P}	f_{As}	Concentration
InP (50nm layers)	0.502 ± 0.005	0	0.503 ± 0.006	0.004 ± 0.002	$\text{In}_{1.0} \text{P}_{1.0}$
InGaAs (10nm layers)	0.288 ± 0.009	0.211 ± 0.004	0.101 ± 0.004	0.399 ± 0.012	$\text{In}_{0.58} \text{Ga}_{0.42} \text{As}_{0.80} \text{P}_{0.20}$
InGaAs (30nm layers)	0.287 ± 0.003	0.216 ± 0.003	0.041 ± 0.002	0.457 ± 0.004	$\text{In}_{0.57} \text{Ga}_{0.43} \text{As}_{0.92} \text{P}_{0.08}$

Table 7.3: List of the atomic fractions and compositions measured from spectra that were acquired in the centres of layers of InGaAs and InP grown by MOCVD at atmospheric pressure.

7.4 Conclusions

The work described in this chapter has firmly established that there exists a compositional asymmetry across the interfaces in the InGaAs/InP multilayer structures grown by MOCVD at atmospheric pressure that were examined here. In addition, direct quantitative analysis has provided a description of the spatial variation of elements present in the system. In particular, EDX microanalysis has revealed that there is a substantial As carry-over beyond the InGaAs layer into the InP layer. Furthermore, small quantities of As were detected even at the centres of the 50nm InP layers. Cullis (1988) suggested that the build up of the As concentration at the type 2 interface could be attributed to the trapping of As in dead spaces in the MOCVD reactor before being incorporated into the buffer layer even though the arsine supply has been closed. Arsenic is incorporated into InP 50 times more readily than P for a given concentration of hydride (Cullis, loc. cit.). The observation of the presence of As across the type 2 interfaces has been confirmed by x-ray rocking curve simulations (Barnett et al., 1988) which rely upon the measurement of lattice parameter variations. This investigation, however, took no account of the additional Ga and P redistributions which have been identified by EDX microanalysis. The complexity of elemental concentration changes across the type 2 interface hinders the precise interpretation of high-angle ADF profiles acquired from these regions. The studies by Barnett et al. (1988) revealed that there is periodic strain in these materials and so, as postulated earlier in this chapter, the detected increase in high-angle ADF signal in the InGaAs layer ~7nm before the transition does suggest that this is the position at which strain effects reach a level that can be detected under the experimental conditions employed. However, as also pointed out earlier, the relative signal intensities contributed

by strain and \bar{Z} are unknown. It should again be emphasised here that because of the low significance of electron channeling, EDX microanalysis data is essentially unaffected by the presence of strain at interfaces.

The investigations described in this chapter have also confirmed the observation by Chew et. al. (1987) that the InP to InGaAs transition is of a higher quality than that from InGaAs to InP. The signal simulation techniques applied to the high-angle ADF data indicate that the detected transition width is no greater than ~ 5 unit cell dimensions wide. These results are similar to those recorded from the AlGaAs/GaAs interfaces which were discussed in the previous chapter. Consequently, although an upper limit can be placed on the transition width across the type 1 interface, the actual value may be less than that observed. This is in part substantiated by the observation that EDX microanalysis revealed that the compositions at the layer centres are $\text{In}_{1.0}\text{P}_{1.0}$ and $\text{In}_{0.57}\text{Ga}_{0.43}\text{As}_{0.92}\text{P}_{0.08}$ with an error in each index of ± 0.02 . As these compositions are lattice matched, very little strain would be expected at an interface where elemental concentrations change abruptly. This is consistent with the observation that the high-angle ADF intensity varies smoothly across each type 1 interface transition.

The data collected in this chapter can also be utilised to investigate further the accuracy with which direct quantitative analysis of materials can be performed by high-angle ADFI. The Born model for the elastic scattering cross-section (which, in this case, gives the closest agreement between theory and experiment) predicts that the value of layer contrast detected between layers of $\text{In}_{1.0}\text{P}_{1.0}$ and $\text{In}_{0.57}\text{Ga}_{0.43}\text{As}_{0.92}\text{P}_{0.08}$ should be 0.09. This compares to a measured value of 0.07. However, as discussed in the previous chapter, the general disagreement between experiment and theory together with the lack of consistency between individual theoretical models suggests that the use of simple analytical elastic scattering cross-section expressions precludes direct quantitative analysis by high-angle ADFI, and that the use of high-angle ADFI in

conjunction with EDX microanalysis is the most effective and productive approach.

Chapter 8

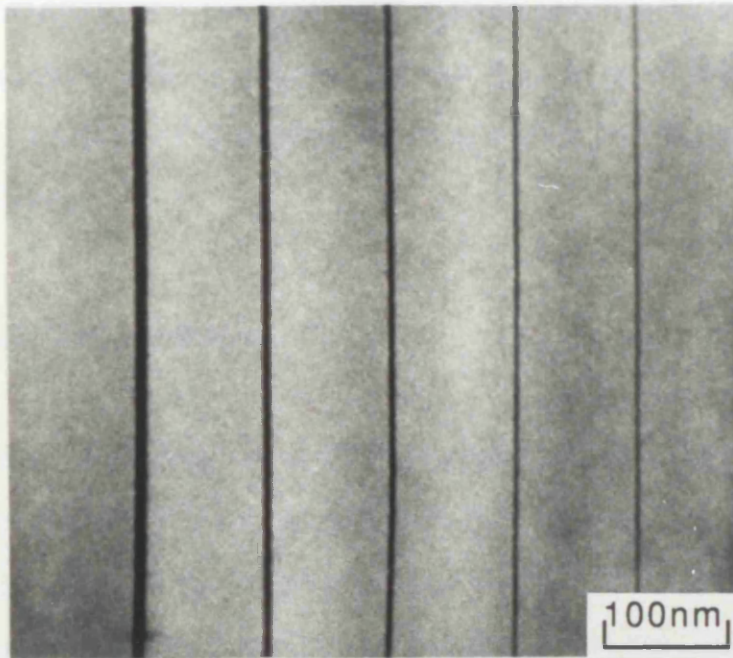
Analysis of the InGaAs/InP system grown by solid source MBE.

8.1 Introduction

In comparison with the previous chapter, in which InGaAs/InP systems grown by MOCVD at atmospheric pressure were examined, this chapter discusses the application of EDX microanalysis and high-angle ADFI to similar materials grown by the more established technique of solid source MBE (e.g Davies and Andrews, 1985; Joyce, 1985). The way in which the InGaAs/InP multilayers analysed here were grown is described in detail by Marsh et. al. (1985) and Claxton et. al. (1987). An (002) dark field image of the specimen examined is given in figure 8.1. The specimen consists of InGaAs wells of 10nm, 5nm, 2.5nm, 2 unit cell dimensions ($\sim 1.2\text{nm}$) and 1 unit cell dimension ($\sim 0.6\text{nm}$). The structure was grown with the narrowest wells towards the surface of the wafer. Each well was separated by a 100nm InP buffer layer. The intended composition of each InGaAs well was $\text{In}_{0.53}\text{Ga}_{0.47}\text{As}$.

In addition to providing information on the specimen that is of interest to the material growers, the geometry of the multilayer structure enables further investigations into the relative merits of high-angle ADFI and EDX microanalysis as applied to multiple quantum well systems. With these aims in mind, sections 8.2 and 8.3 discuss experiments carried out on the specimen of interest by the two techniques. In the final section, the results are assessed and conclusions are drawn on both the compositional variations across the specimen and on the analysis techniques themselves.

Direction of growth \longrightarrow



Light bands: InP

Dark bands: InGaAs

Figure 8.1 Digital (002) dark field image of an InGaAs/InP multilayer grown by MBE. The system comprises 5 InGaAs layers, with widths ranging between ~0.6nm and 10nm.

8.2 High-angle ADFI

This section describes the application of high-angle ADFI to the InGaAs/InP system grown by MBE that is shown in figure 8.1. In addition to providing information on the variation of \bar{Z} across the specimen of interest, the aim of the experiments described here is to use the geometry of the multilayer structure to test the ability of high-angle ADFI to detect the presence of very narrow quantum wells.

8.2.1 Intensity profile analysis

Figure 8.2 shows three profiles (denoted A, B and C) that were taken from a high-angle ADF image of the 10nm InGaAs well. Each profile is an average of 8 consecutive linescans, and the level of noise in each has been reduced by means of an 11-point median filter. The figure shows that the signal detected from the InP buffer layers remained constant over the area scanned and so no thickness correction steps were necessary. Following the profile analysis procedure described in chapter 4, simulations of both the InP to InGaAs growth transition (type 1) and those from InGaAs to InP (type 2) were calculated from models of $f(\bar{Z})$ possessing linearly graded interface transitions spanning widths ranging between 2nm and 5nm.

Figure 8.3 shows comparisons between simulated profiles calculated from transition widths of 3nm and 4nm with those acquired experimentally from the type 1 interface. Similar comparisons are made in figure 8.4 using the profiles acquired across the type 2 interface. The figures demonstrate that whilst the 4nm transition fits selected sections of the profiles, the 3nm transition generally gives the 'best fit'. Figures 8.5 (type 1 interface) and 8.6 (type 2 interface) show that transition widths of 2nm underestimate the signal variations detected,

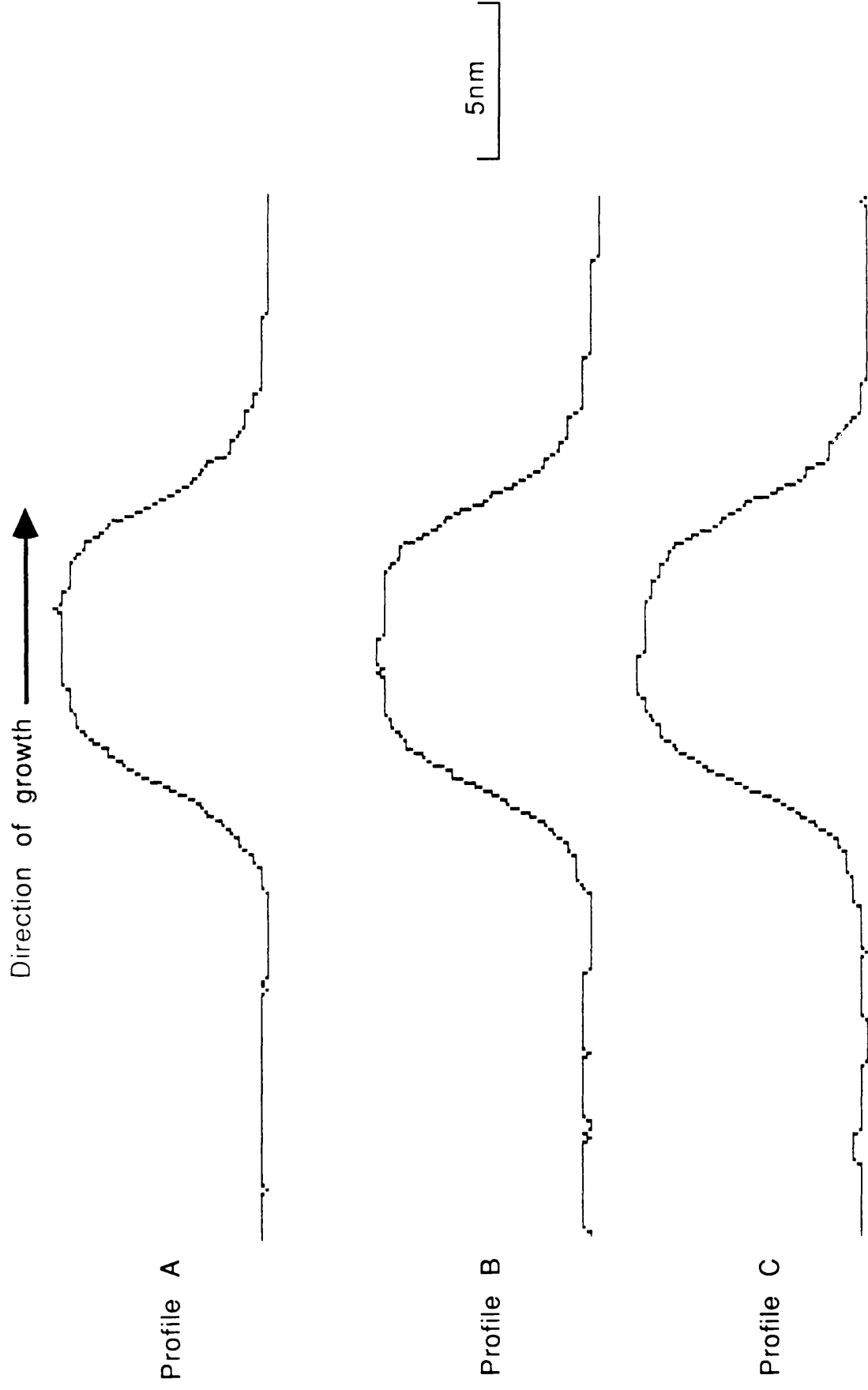


Figure 8.2: 3 processed profiles taken from a high-angle ADF image of the 10nm InGaAs well shown in figure 8.1.

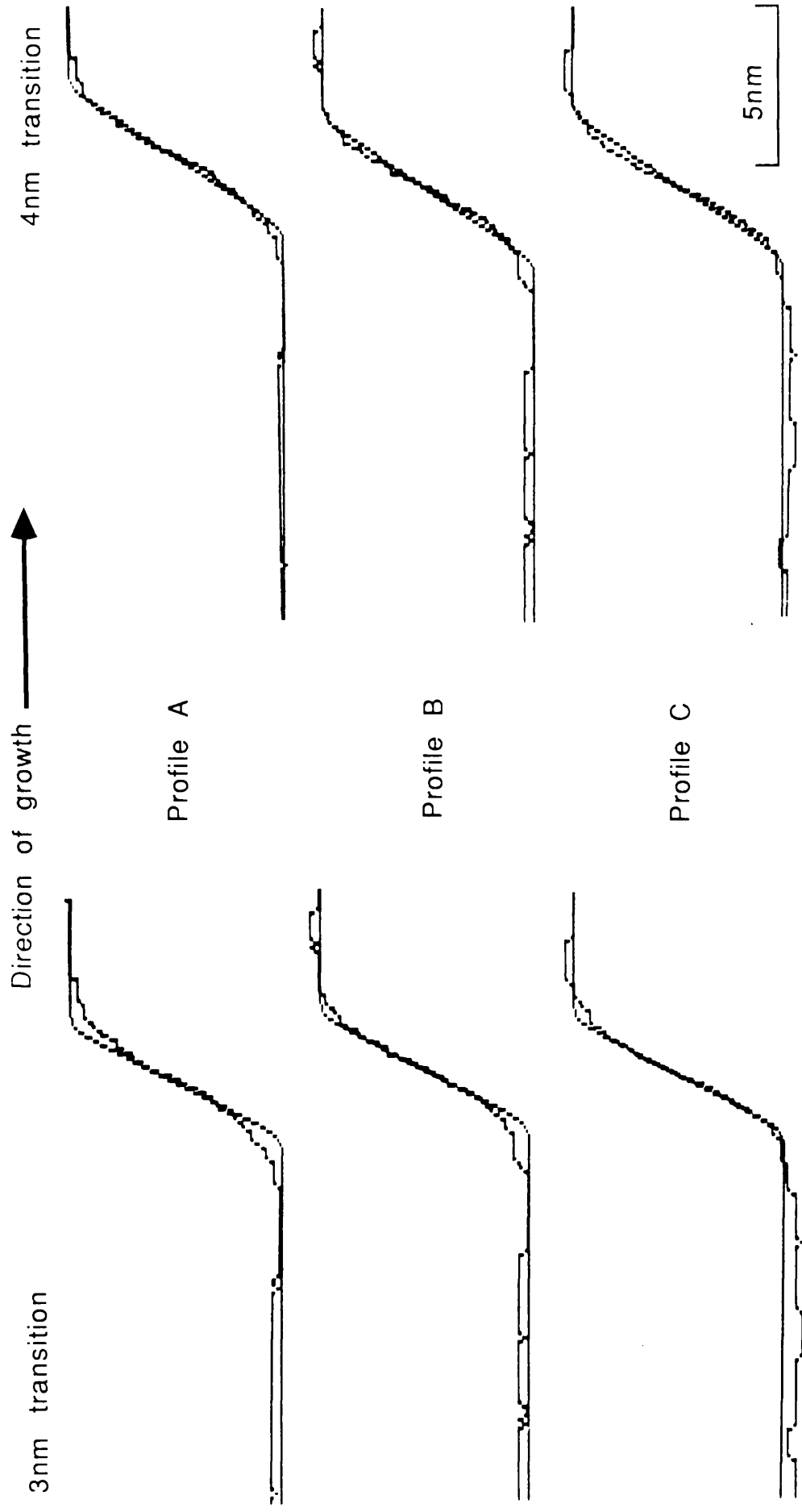


Figure 8.3: Comparison between the type 1 interfaces of profiles A, B and C with simulated profiles calculated from transition widths of 3nm and 4nm.

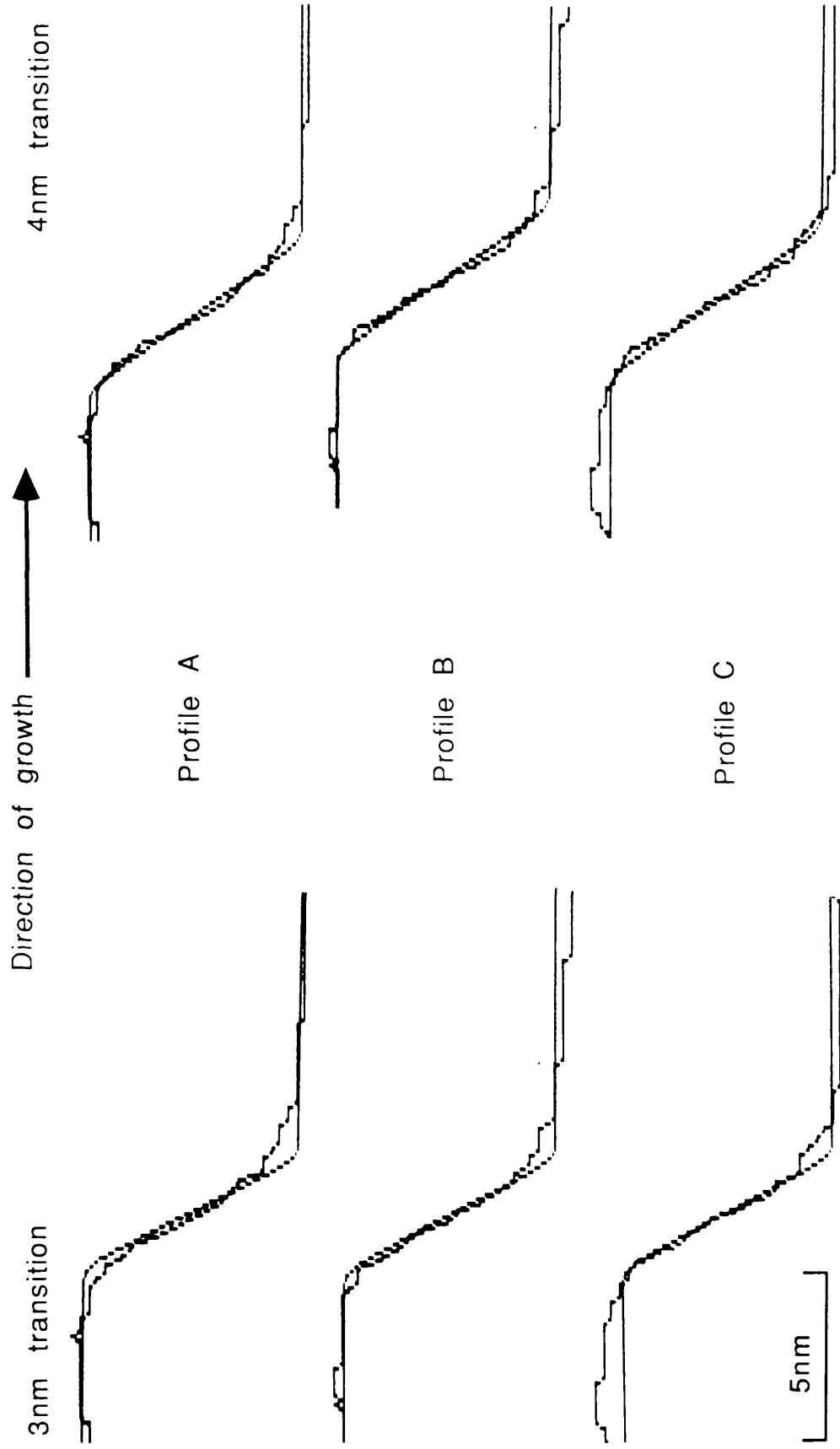


Figure 8.4: Comparison between the type 2 interfaces of profiles A, B and C with simulated profiles calculated from transition widths of 3nm and 4nm.

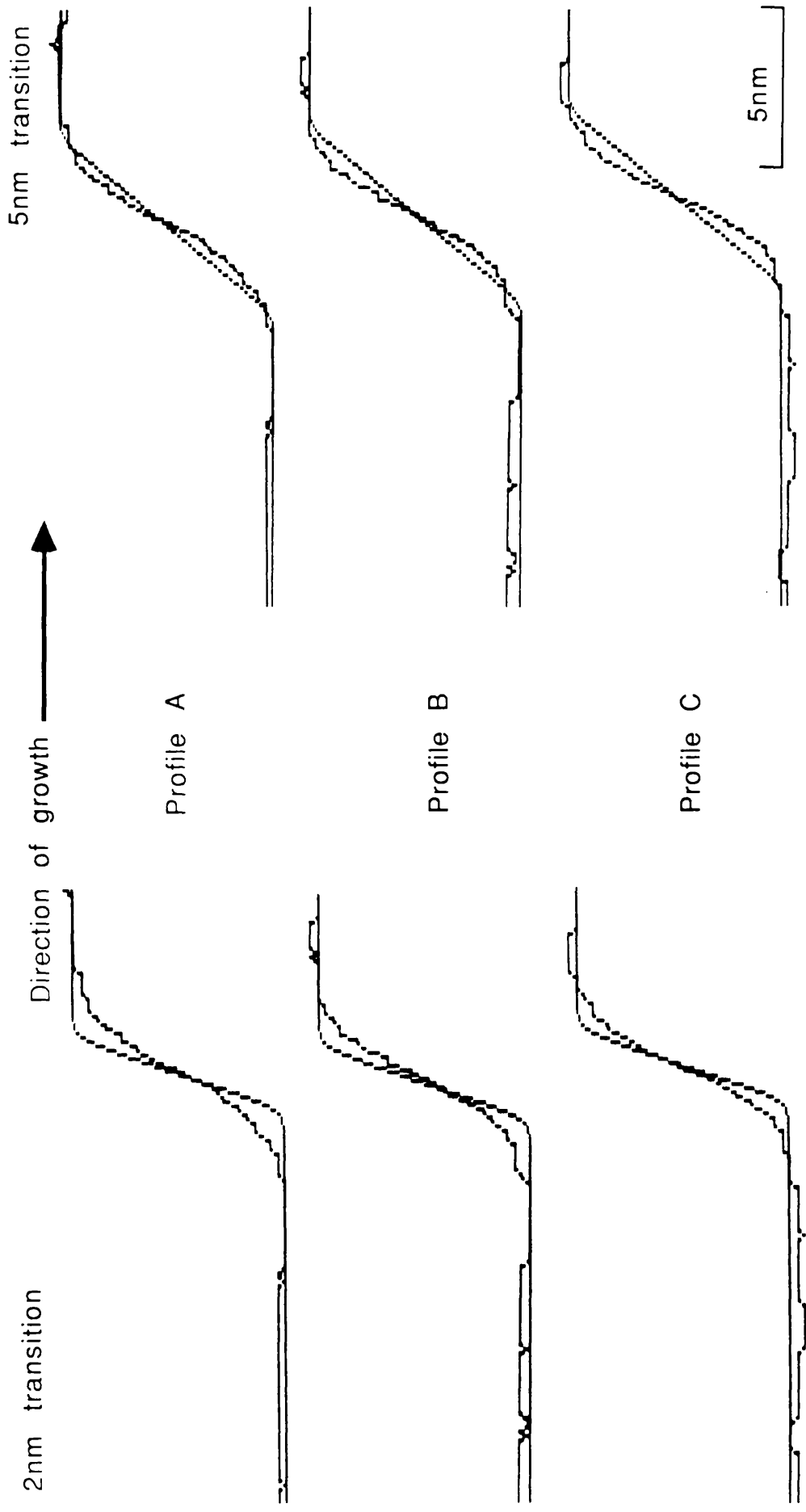


Figure 8.5: Comparison between the type 1 interfaces of profiles A, B and C with simulated profiles calculated from transition widths of 2nm and 5nm.

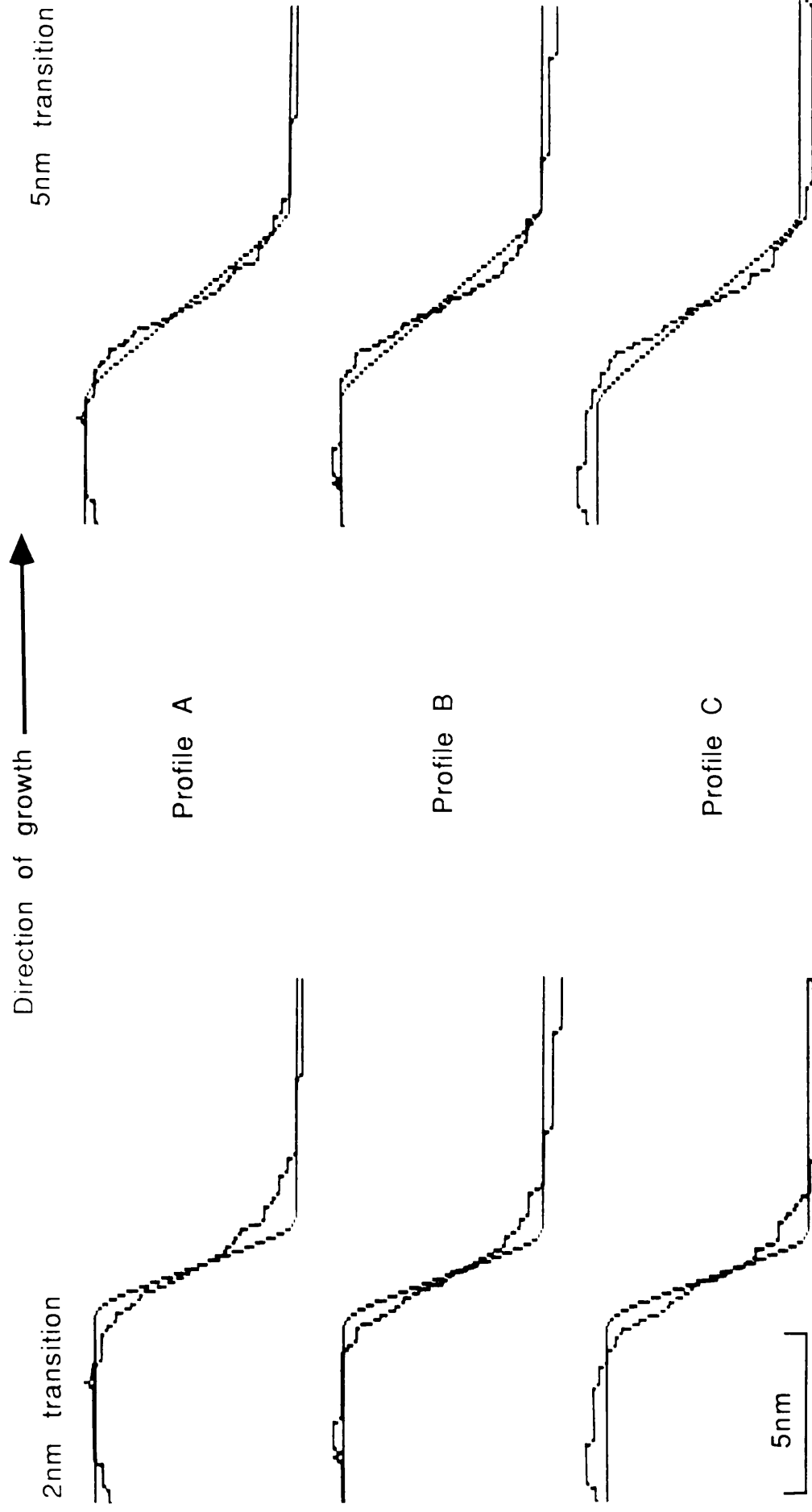


Figure 8.6: Comparison between the type 2 interfaces of profiles A, B and C with simulated profiles calculated from transition widths of 2nm and 5nm.

whereas transition widths of 5nm overestimate the experimentally acquired data in all cases.

Figures 8.7, 8.8, 8.9 and 8.10 each show three profiles taken from high-angle ADF images of the 5nm and 2.5nm InGaAs wells and those spanning 2 and 1 unit cell dimensions respectively. As in figure 8.2, each profile is an average of 8 consecutive linescans. In this case, however, no median filter was used. The reason for this is that the application of such a filter in the regions near the centre of the wells would artificially 'flatten' the peak in the detected signal. The profiles in figures 8.7 to 8.10 are similar to those from the 10nm well in that the detected signal variations are symmetric about the well centres. In figure 8.7, it can be seen that the signal detected from the centre of the 5nm InGaAs layer attains an approximately constant value over a distance of ~1nm. No such constant signal is, however, observed at the centres of the narrower wells analysed in figures 8.8 to 8.10. In these figures, the profiles exhibit strong similarities in terms of the distance over which an increase in signal is detected (~2nm at FWHM), and differ only in terms of the relative effects of signal noise. Such effects were found to be most significant in the narrowest layers where the signal levels detected from the InGaAs were found to be only slightly higher than those detected from the InP. This effect was investigated further by acquiring high-angle ADF images of each well in the system using zero offset and zero black level. Taking dark current contributions into consideration, table 8.1 lists the values of layer contrast C (defined in equation 2.1) that were measured from each image. The table shows that only small differences in C were observed between images of the 10nm, 5nm and 2.5nm InGaAs wells, whilst that measured from the two narrowest wells was approximately a factor of 2 lower.

8.2.2 Discussion

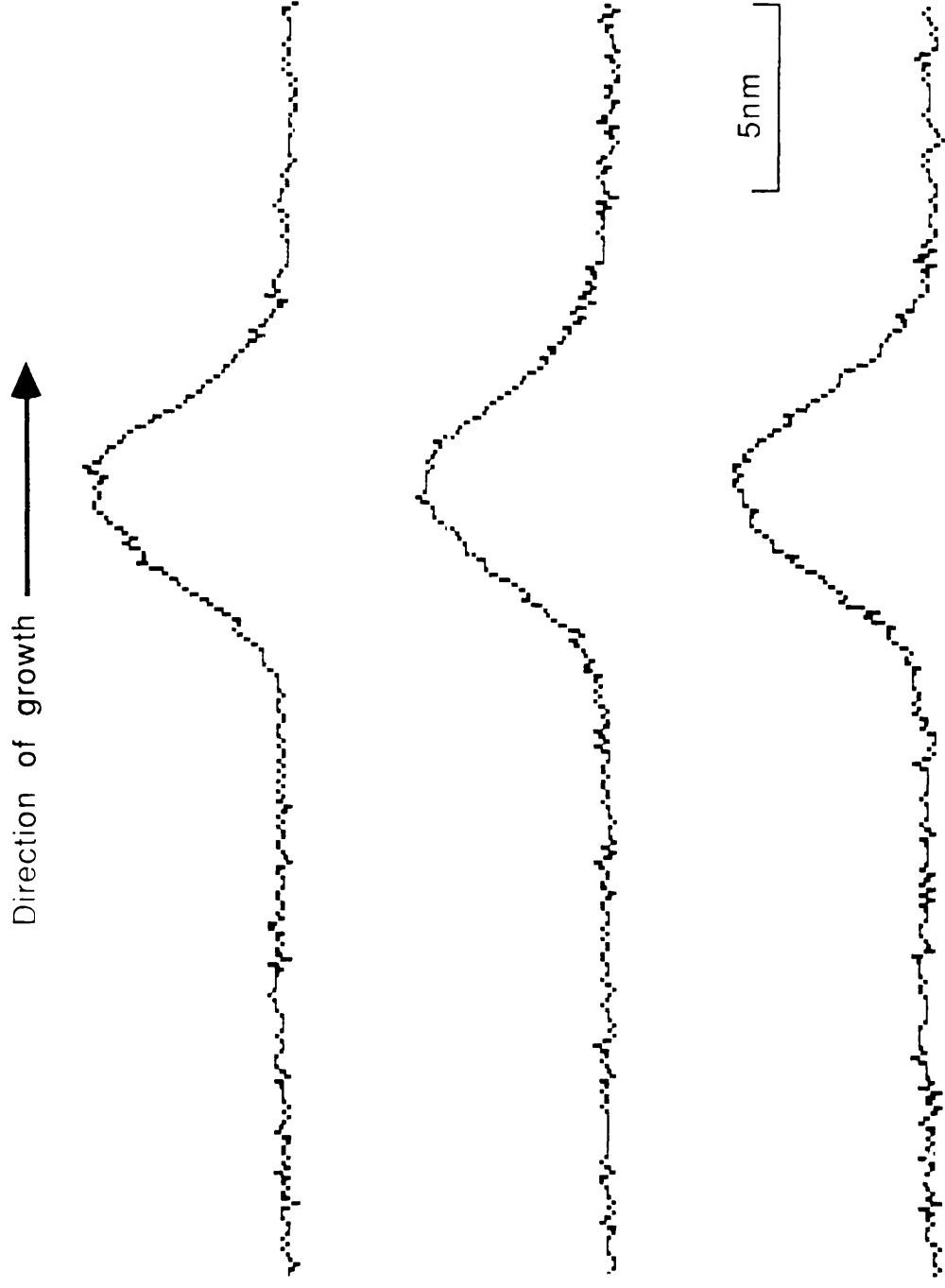


Figure 8.7: 3 processed profiles taken from a high-angle ADF image of the 5nm InGaAs well shown in figure 8.1. No median filter was applied to the profiles.

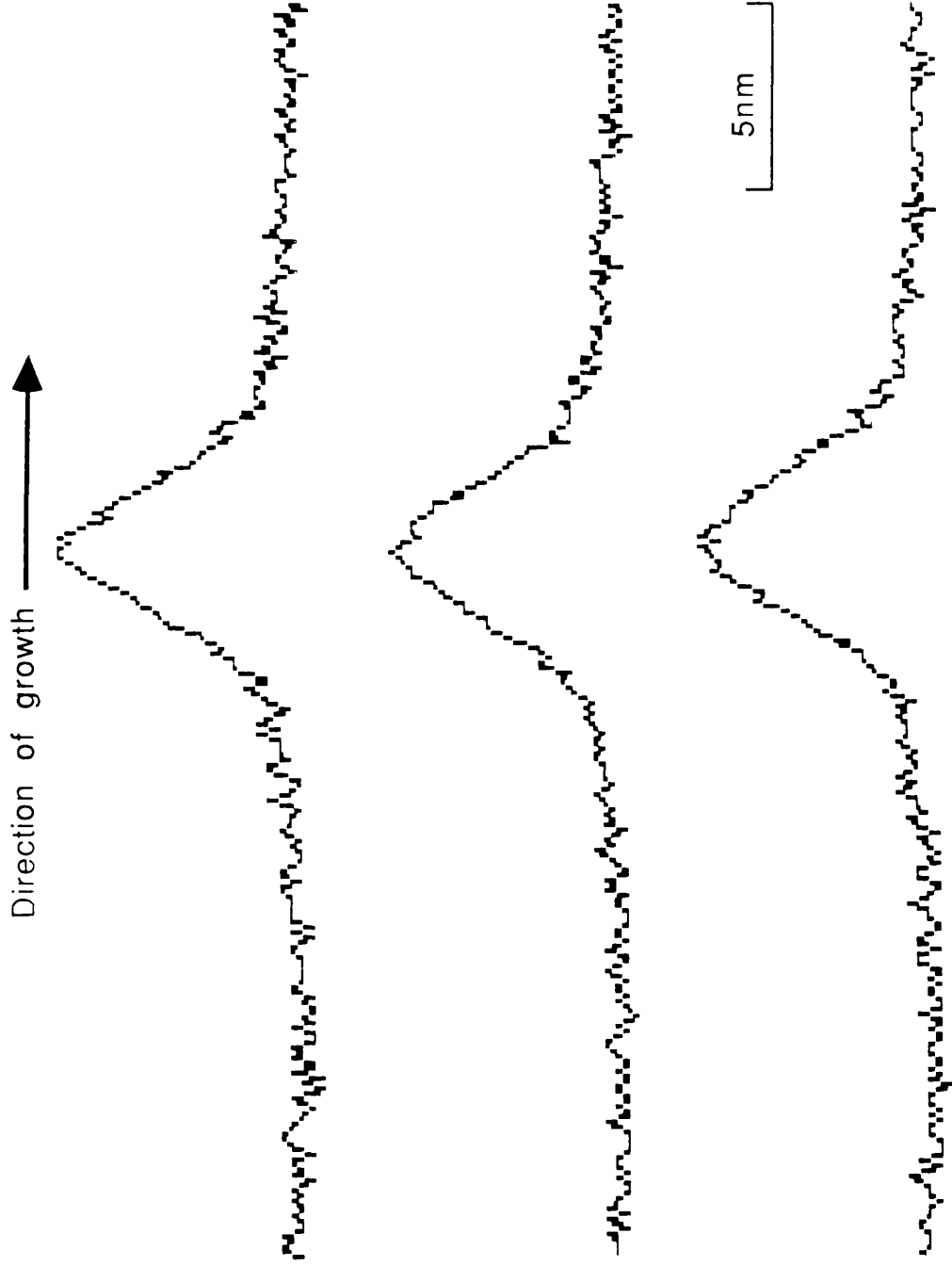


Figure 8.8: 3 processed profiles taken from a high-angle ADF image of the 2.5nm InGaAs well shown in figure 8.1. No median filter was applied to the profiles.

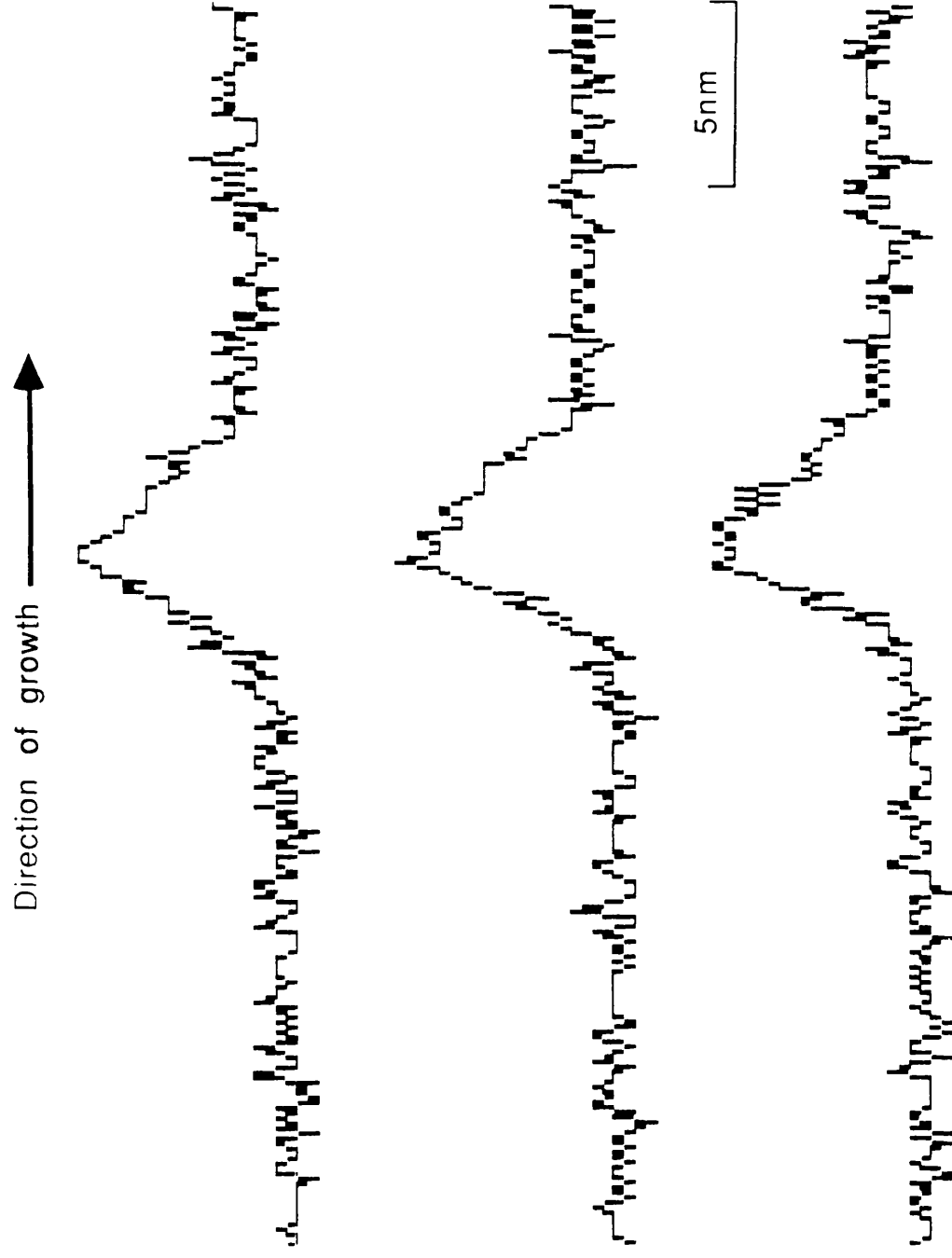


Figure 8.9: 3 processed profiles taken from a high-angle ADF image of the

InGaAs well spanning 2 unit cell dimensions shown in figure 8.1.

No median filter was applied to the profiles.

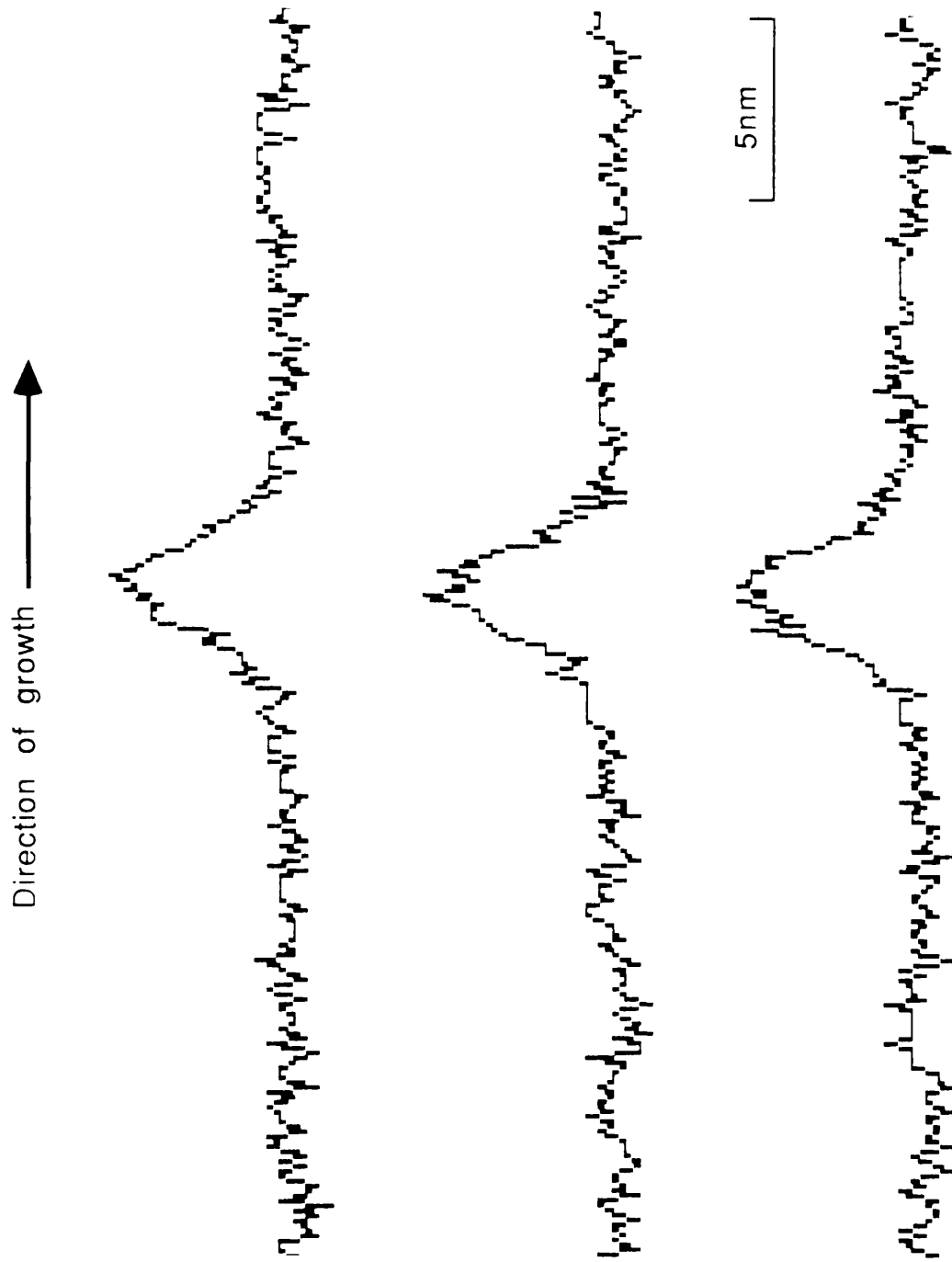


Figure 8.10: 3 processed profiles taken from a high-angle ADF image of the InGaAs well spanning 1 unit cell dimension shown in figure 8.1.
No median filter was applied to the profiles.

InGaAs well width	Contrast
10nm	0.09
5nm	0.09
2.5nm	0.10
2 unit cells	0.05
1 unit cell	0.04

Table 8.1: Values of layer contrast measured between InGaAs wells of varying widths and InP buffer layers from high-angle ADF images acquired with zero offset and zero black level. Dark current contributions have been taken into consideration

Analysis of the profiles acquired across the InGaAs wells revealed that, in all cases, the signal variation detected across the type 1 interface is very similar to that detected across the type 2 interface. This suggests that, to within the spatial resolution of high-angle ADFI, the relative quality of the interfaces is independent of the direction of material growth. Detailed analysis of the high-angle ADF signal from the 10nm InGaAs layer revealed that the 'best fit' of a simulated profile to that acquired experimentally was obtained from transition widths spanning 3nm. However, transition widths of 4nm gave only slightly less satisfactory fits. The previous chapter showed that transition widths of 3nm were also found to give the best agreement with experimentally acquired profiles from the type 1 interfaces in the InGaAs/InP system grown by MOCVD at atmospheric pressure. In this case, the 2nm transition was found to give closer agreement between experiment and theory than that spanning 4nm. However, x-ray count rates reveal that the local thickness (t) in the area of specimen examined in this chapter was $\sim 80\text{nm}$, compared to $\sim 50\text{nm}$ in the previous chapter. Although the effect of film thickness on beam broadening across interfaces is not as significant for high-angle ADFI as EDX microanalysis, t may still have a limited effect on the spatial resolution of the former. Consequently, the small differences in interface abruptness detected between systems grown by MBE and MOCVD cannot conclusively be attributed to differences in the material quality produced by the two techniques. A feature of the profiles acquired from the MBE system that gives credence to the argument that the interfaces are of a high quality is that the detected high-angle ADF signal distributions vary smoothly across each interface and do not exhibit intensity variations that may be associated with the presence of strain.

Analysis of the 2.5nm InGaAs well and those spanning 2 and 1 unit cell dimensions revealed that, whilst the measured contrast between InGaAs and InP decreased as a function of decreasing well width, the spatial distribution of

detected intensity across the profiles changed only slightly. This may imply that the actual dimensions of the wells are considerably greater than intended. However, this seems unlikely when the changes in detected layer contrast are considered along with results from photoluminescence experiments carried out on similar materials (Marsh et. al., loc. cit.). A more likely explanation is that the spatial resolution of the technique, under the experimental conditions used here, limits accurate high-angle ADF analyses to wells possessing dimensions greater than a specified limit. The measured value of C from dark current corrected images of the 10nm, 5nm and 2.5nm wells acquired with zero offset and zero black level attained an approximately constant value. This suggests that the resolution limiting effects only become dominant when examining layers with widths of <2.5nm. This value is consistent with the estimate of the spatial resolution of the technique made in chapter 6. The internal self-consistency observed between the experimentally acquired contrast values from the three widest InGaAs wells also suggests that, although quantitative analysis of layer centre contrast through the use of simple elastic scattering models has been found to be impractical, such analysis may still be feasible through the use of standards of known composition. A final observation that can be made from the data is that the profiles in figure 8.10 demonstrate that changes in the detected high-angle ADF signal can be easily observed from wells that are 1 unit cell wide.

8.3 EDX microanalysis

This section describes EDX microanalysis investigations that were carried out on the MBE grown InGaAs/InP multilayer shown in figure 8.1. The analysis method used for all series of spectra discussed in this chapter follows that outlined in section 7.3.1. All spectra were recorded using a windowless EDX

detector. The K-factors used in the spectral analysis procedures for this detector type are listed in table 7.2. Using the windowless detector, spectrum acquisition times of 10s were found to give ~8000 counts in the In L peak in a spectrum acquired from a region of InP in which t was ~50nm.

The number of counts detected in the characteristic peaks also indicated that, as a consequence of the specimen preparation technique used, t decreased slowly across the specimen in a direction parallel to that of material growth. The values of t were found to be ~80nm in the region of the 10nm well and ~40nm in the region of the narrowest well.

8.3.1 Results

The results discussed here were calculated from series of x-ray spectra acquired across each of the 5 InGaAs wells in the specimen. The positions at which spectra were recorded in each experiment carried out across the 10, 5 and 2.5nm wells and those spanning 2 and 1 unit cell dimensions are illustrated schematically in figures 8.11 to 8.15 respectively. The first and last spectrum in each series was acquired at a distance of 10nm from the nearest interface. Using the analysis procedure described in chapter 7.3.1, figures 8.16 to 8.20 plot the detected variations in the atomic fractions of each element in the material as a function of position across the layers. In addition to analysis of the individual wells, several spectra were acquired in the centres of the InP buffer layers. The average values of the atomic fractions calculated from these spectra are given in table 8.2. Also listed in the table are the atomic fractions for each element calculated from the spectra acquired in the centres of each InGaAs well.

A number of observations on the variation of elemental compositions across the multilayer can be made from the data presented in figures 8.16 to 8.20. A noticeable characteristic of the graphs is that the variations in composition

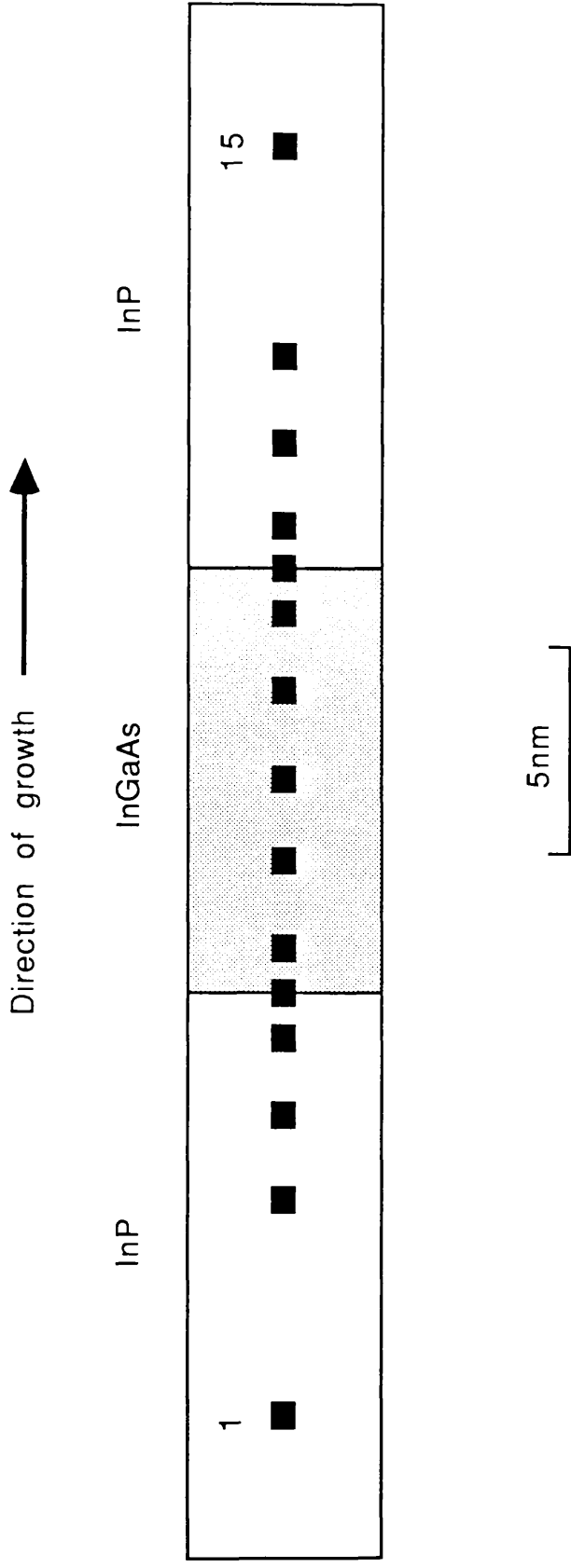


Figure 8.11: Schematic diagram showing the positions at which x-ray spectra were acquired across the 10nm InGaAs well in the MBE grown InGaAs/InP multilayer shown in figure 8.1.

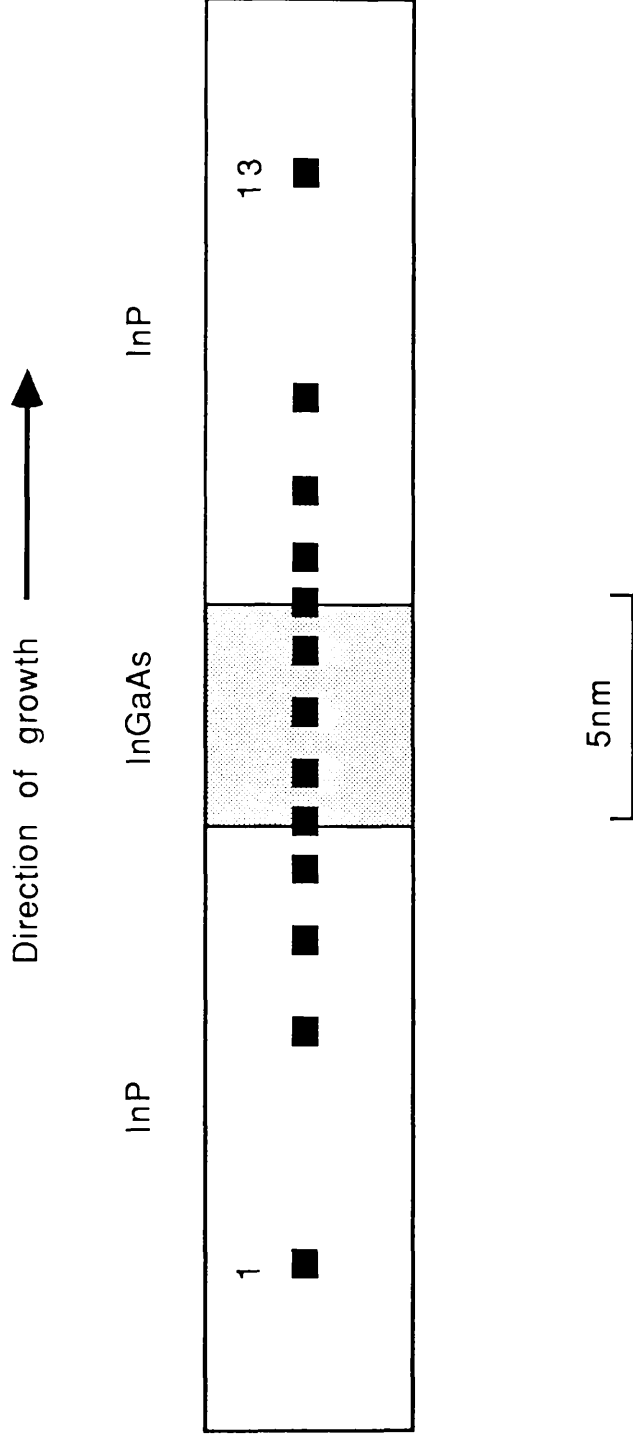


Figure 8.12: Schematic diagram showing the positions at which x-ray spectra were acquired across the 5nm InGaAs well in the MBE grown InGaAs/InP multilayer shown in figure 8.1.

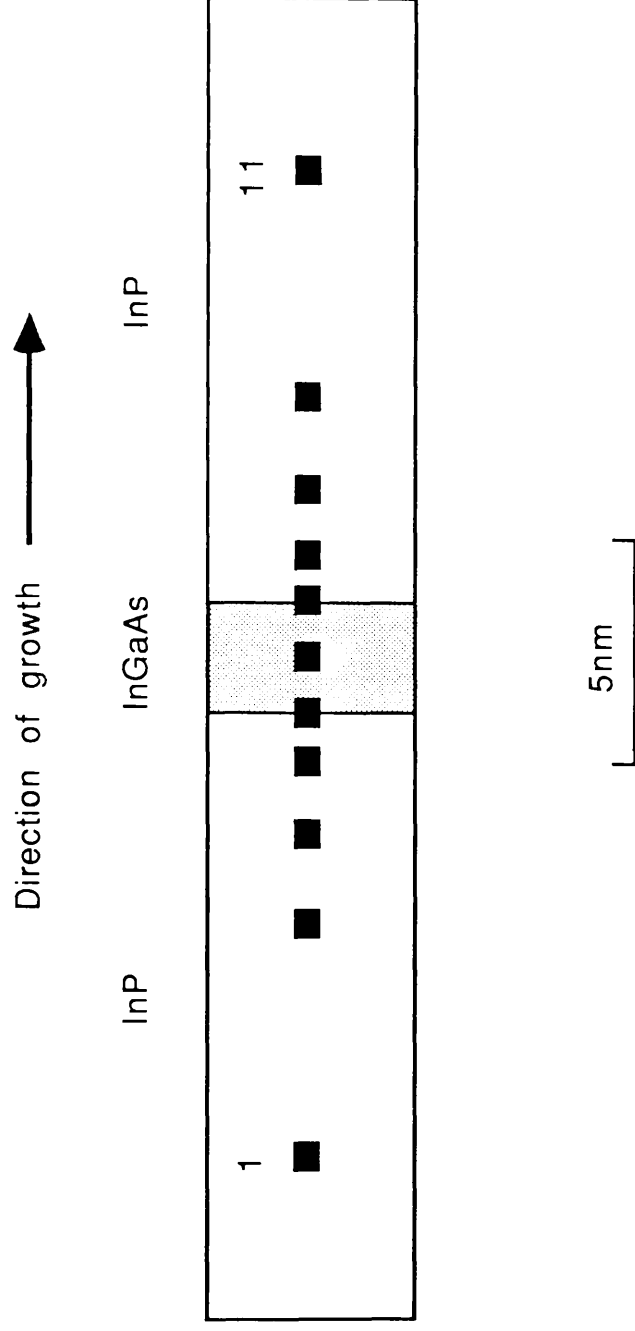


Figure 8.13: Schematic diagram showing the positions at which x-ray spectra were acquired across the 2.5nm InGaAs well in the MBE grown InGaAs/InP multilayer shown in figure 8.1.

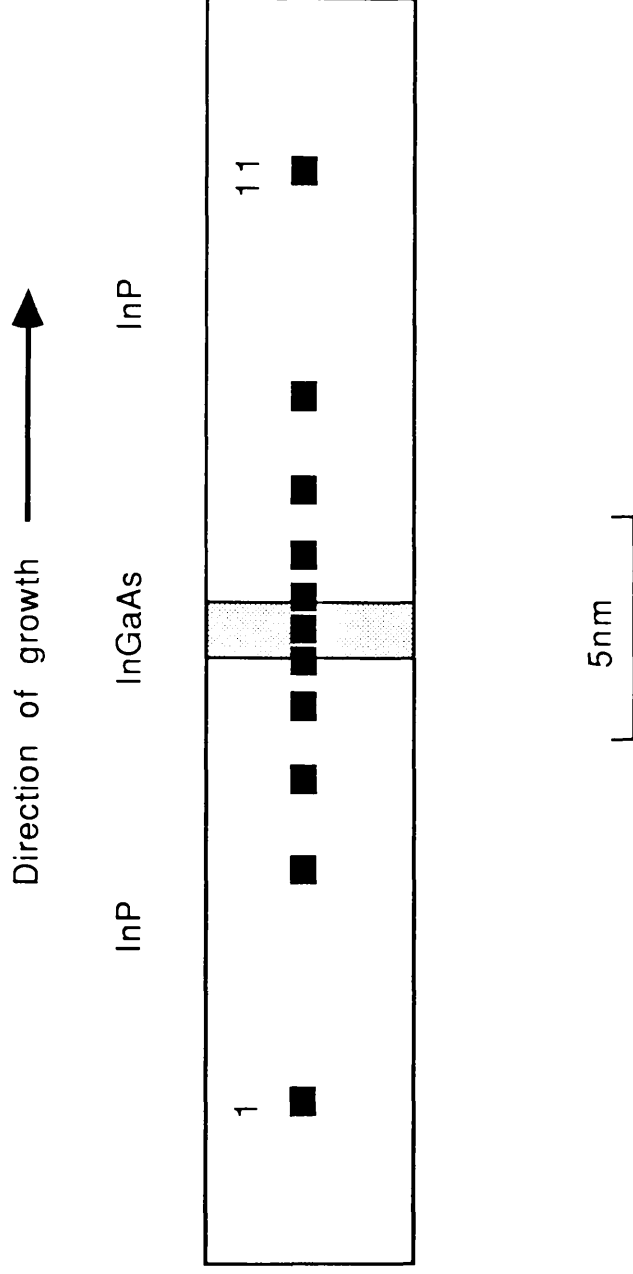


Figure 8.14: Schematic diagram showing the positions at which x-ray spectra were acquired across the InGaAs well spanning 2 unit cell dimensions in the MBE grown InGaAs/InP multilayer shown in figure 8.1.

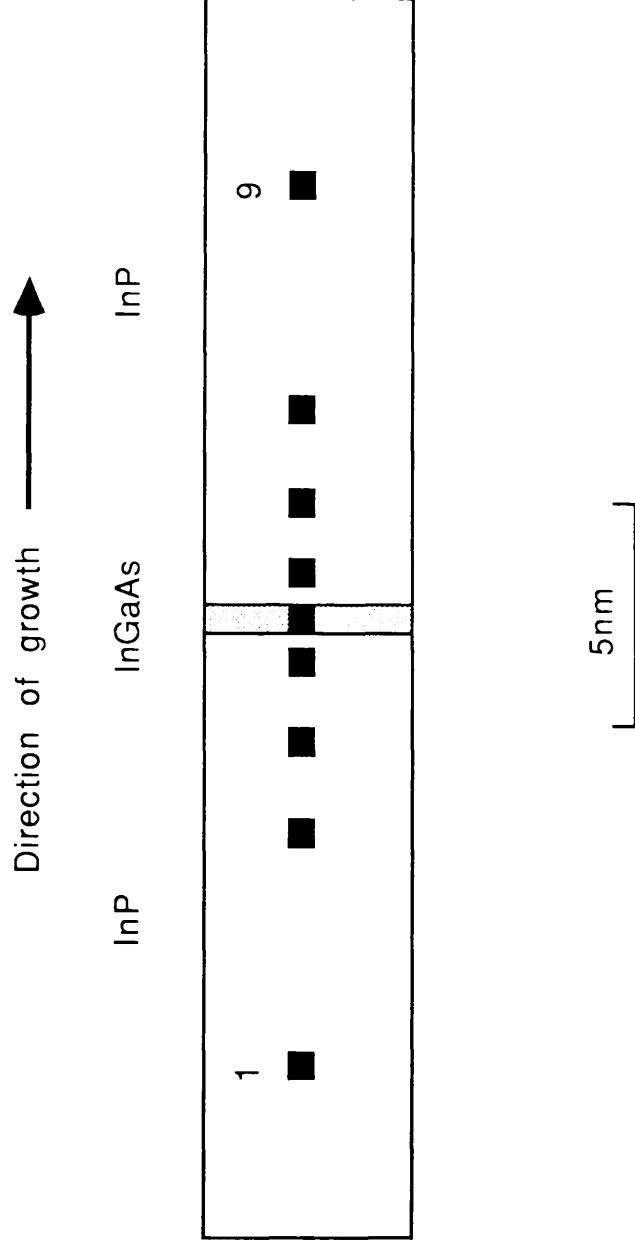


Figure 8.15: Schematic diagram showing the positions at which x-ray spectra were acquired across the InGaAs well spanning 1 unit cell dimension in the MBE grown InGaAs/InP multilayer shown in figure 8.1.

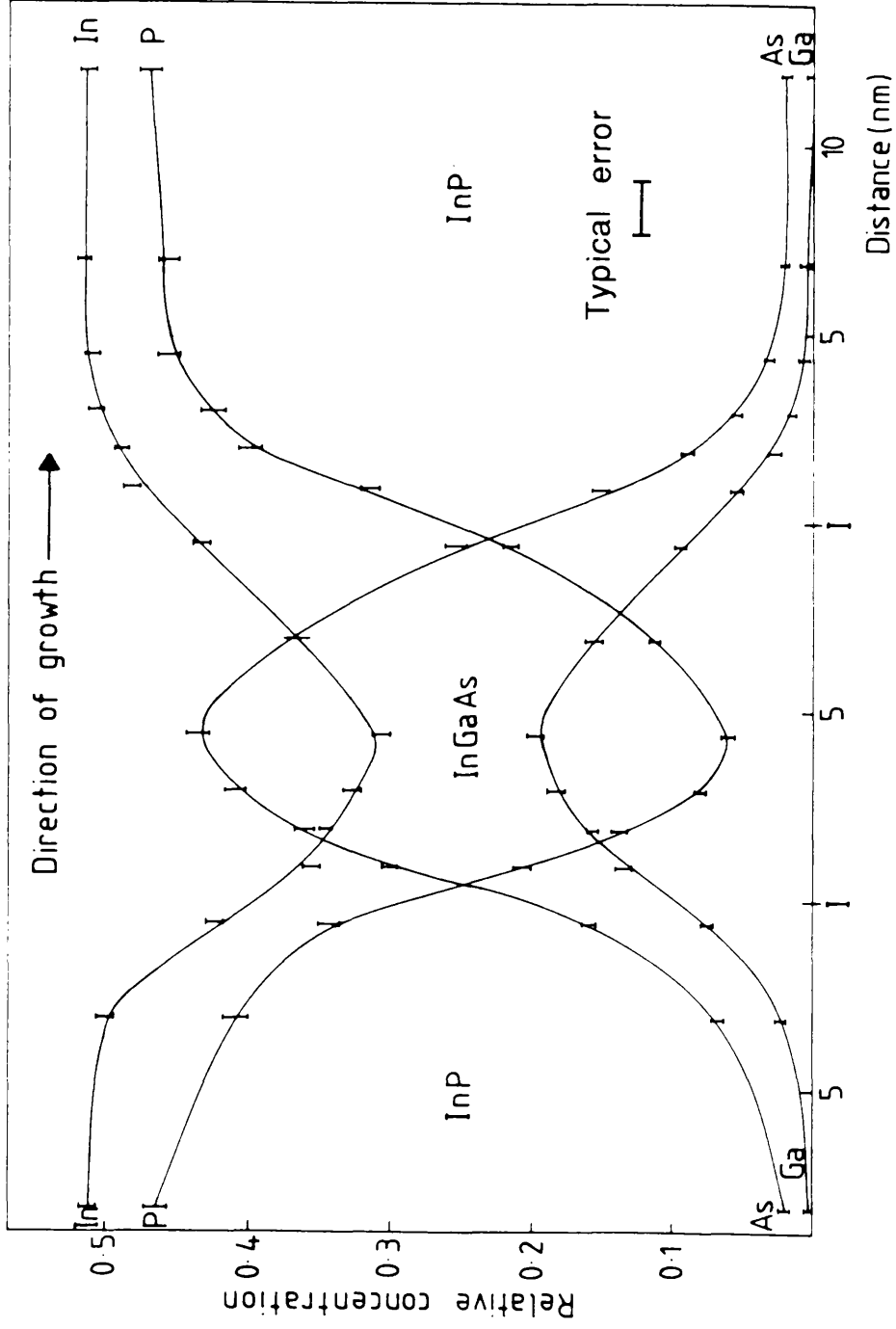


Figure 8.16(a): Graph showing the variation of atomic fractions calculated from EDX data across a 10nm InGaAs layer grown by MBE.

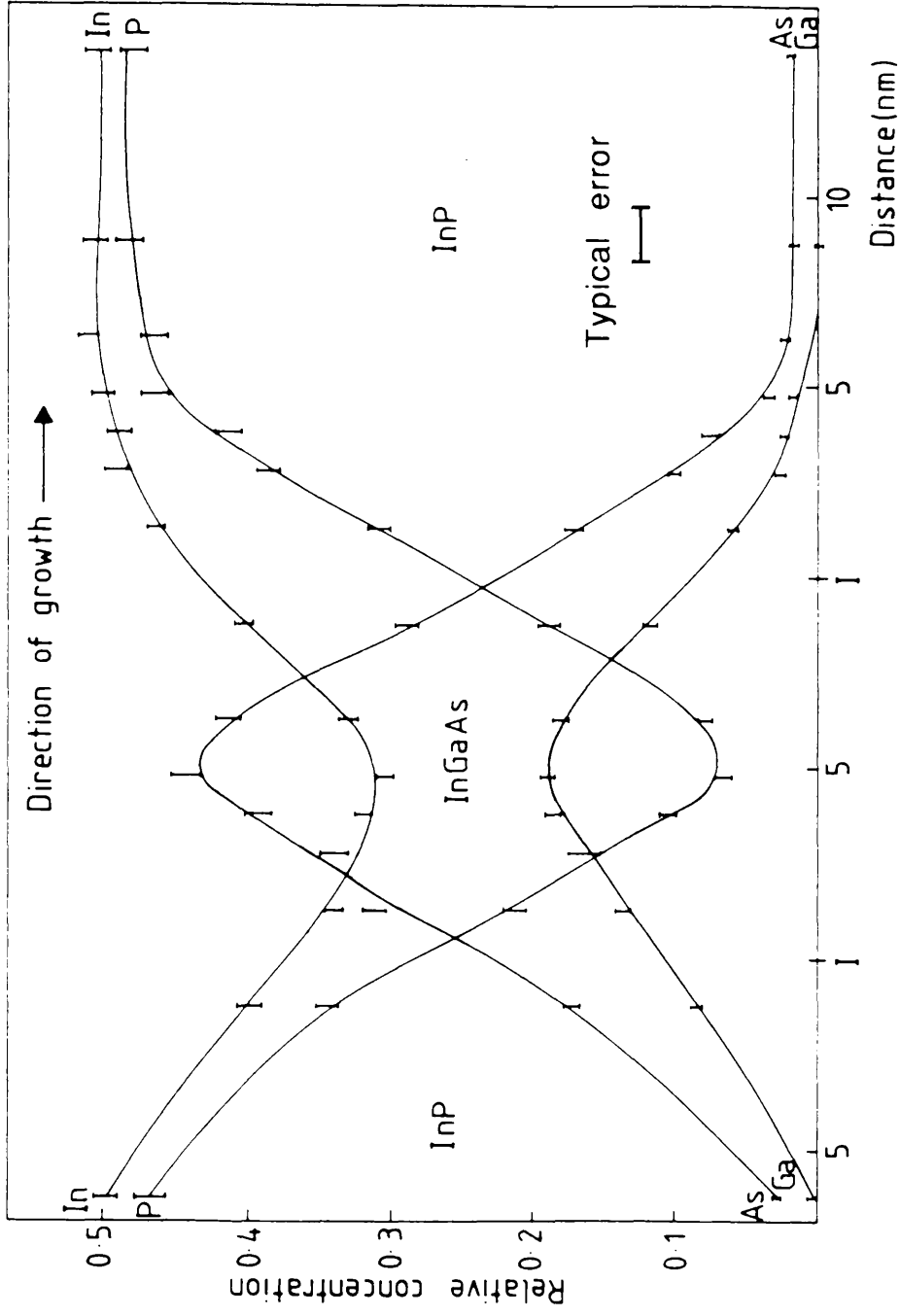


Figure 8.16(b): Graph showing the variation of atomic fractions calculated from EDX data across a different region of the 10nm InGaAs layer analysed in (a).

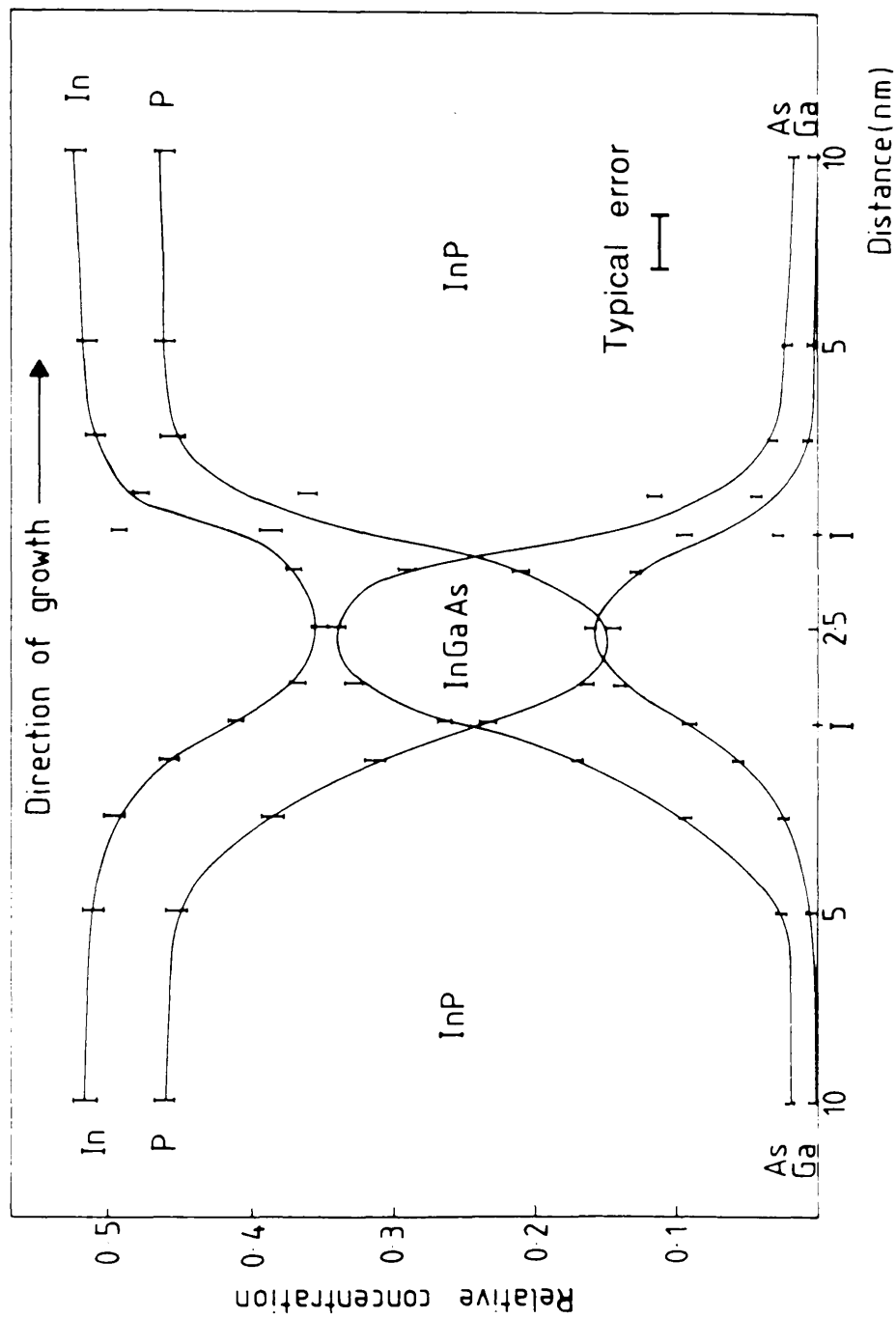


Figure 8.17(a): Graph showing the variation of atomic fractions calculated from EDX data across a 5nm InGaAs layer grown by MBE.

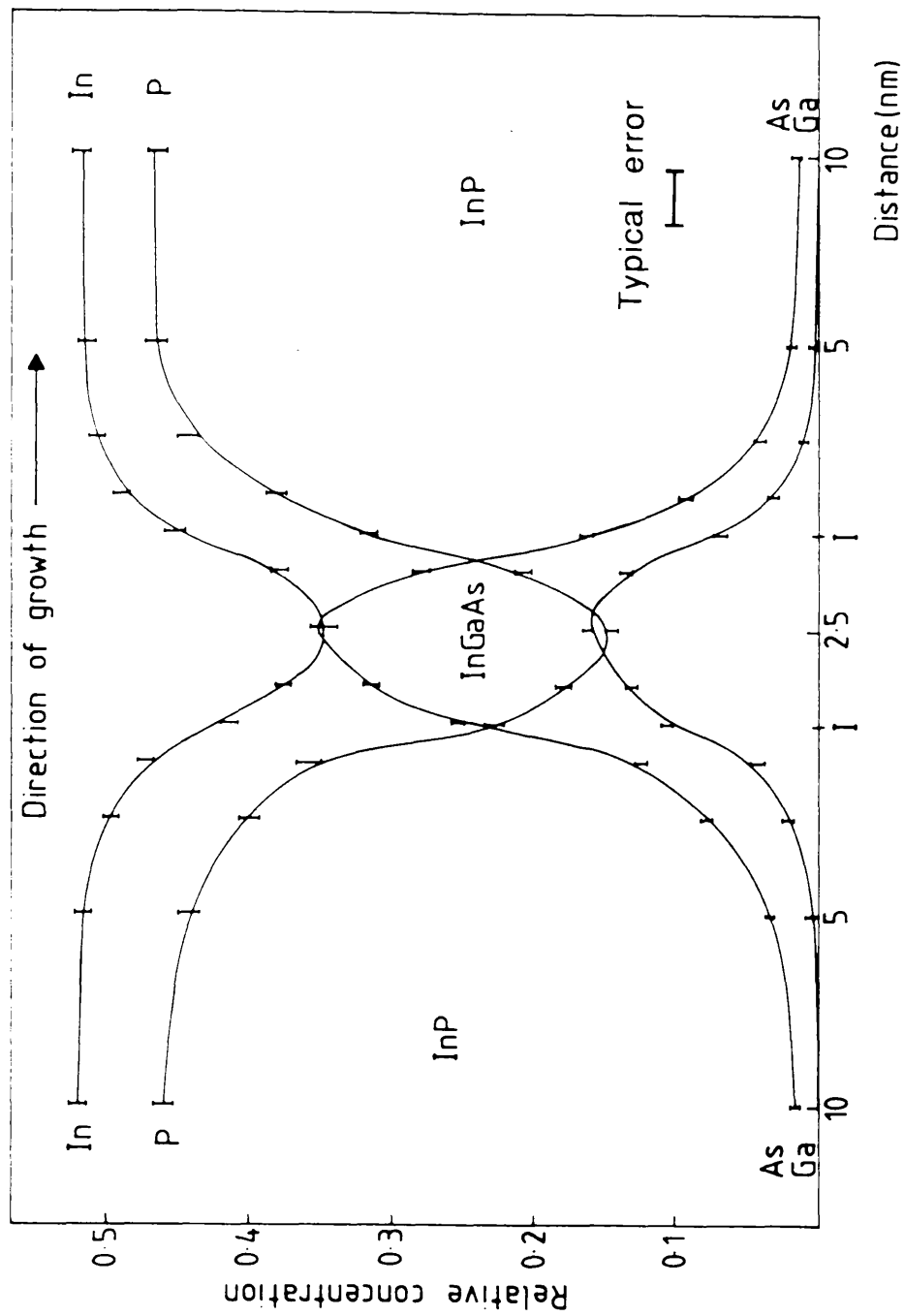


Figure 8.17(b): Graph showing the variation of atomic fractions calculated from EDX data across a different region of the 5nm InGaAs layer analysed in (a).

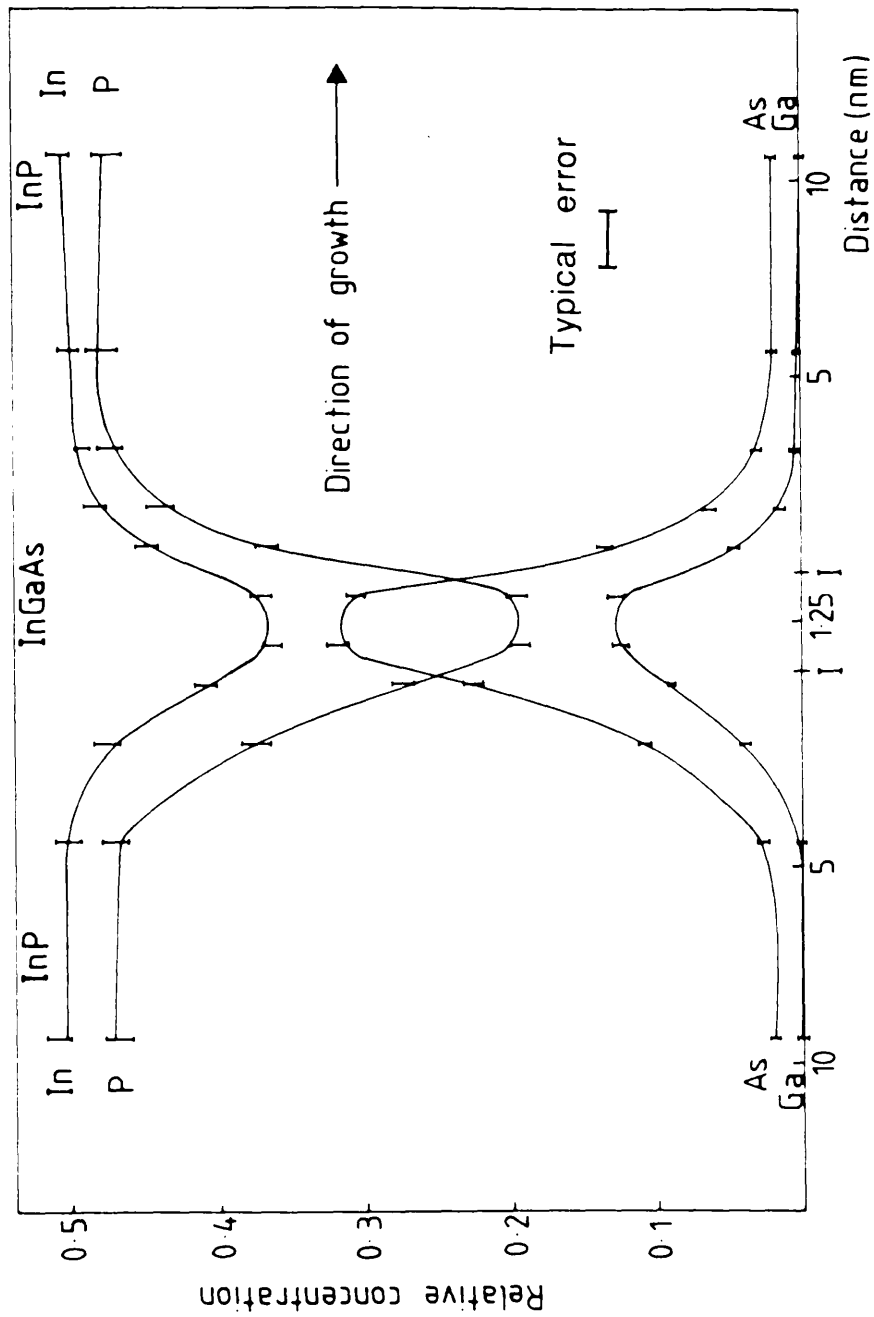


Figure 8.18: Graph showing the variation of atomic fractions calculated from EDX data across a 2.5 nm InGaAs layer grown by MBE.

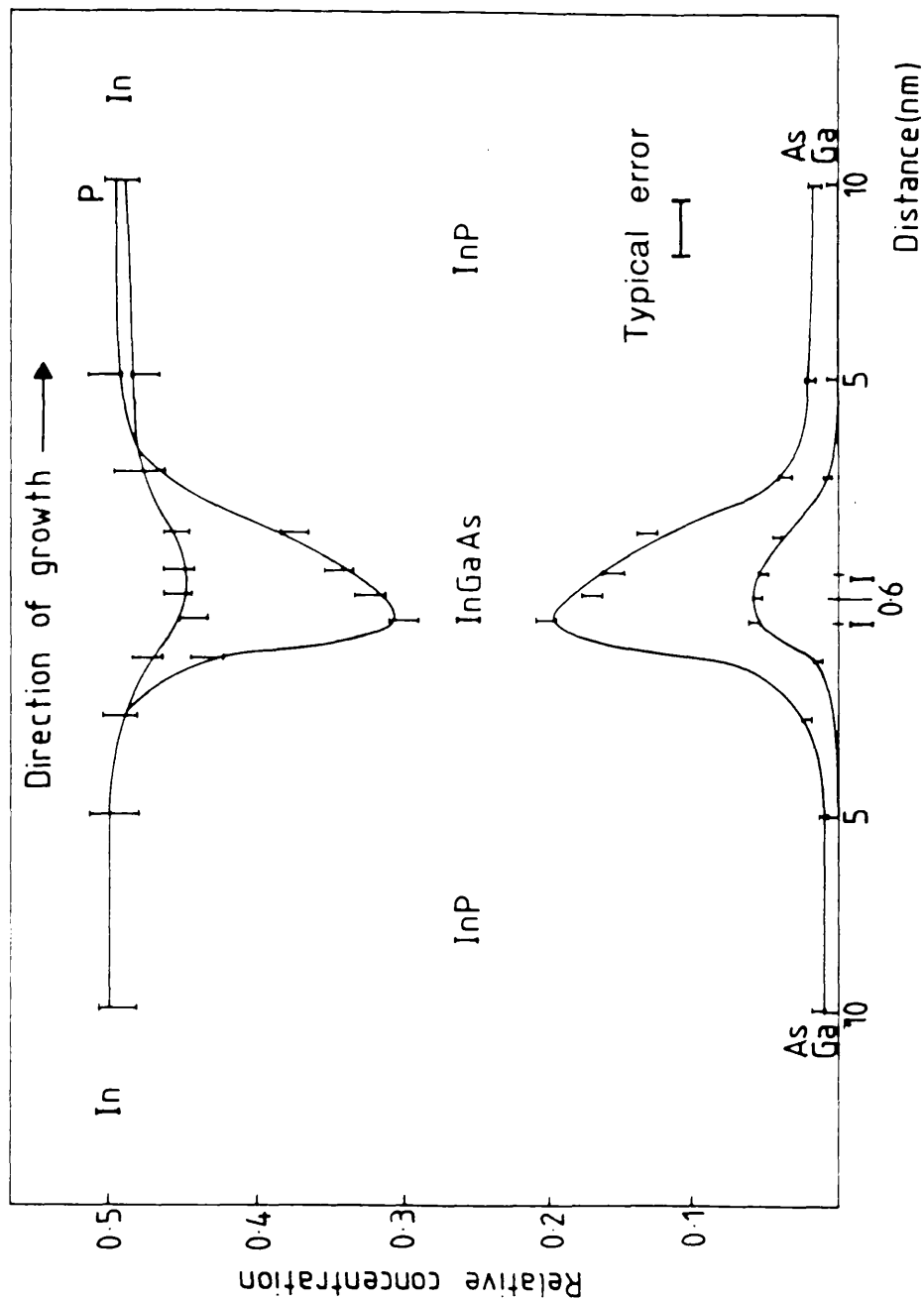


Figure 8.19: Graph showing the variation of atomic fractions calculated from EDX data across an InGaAs layer spanning 2 unit cell dimensions grown by MBE.

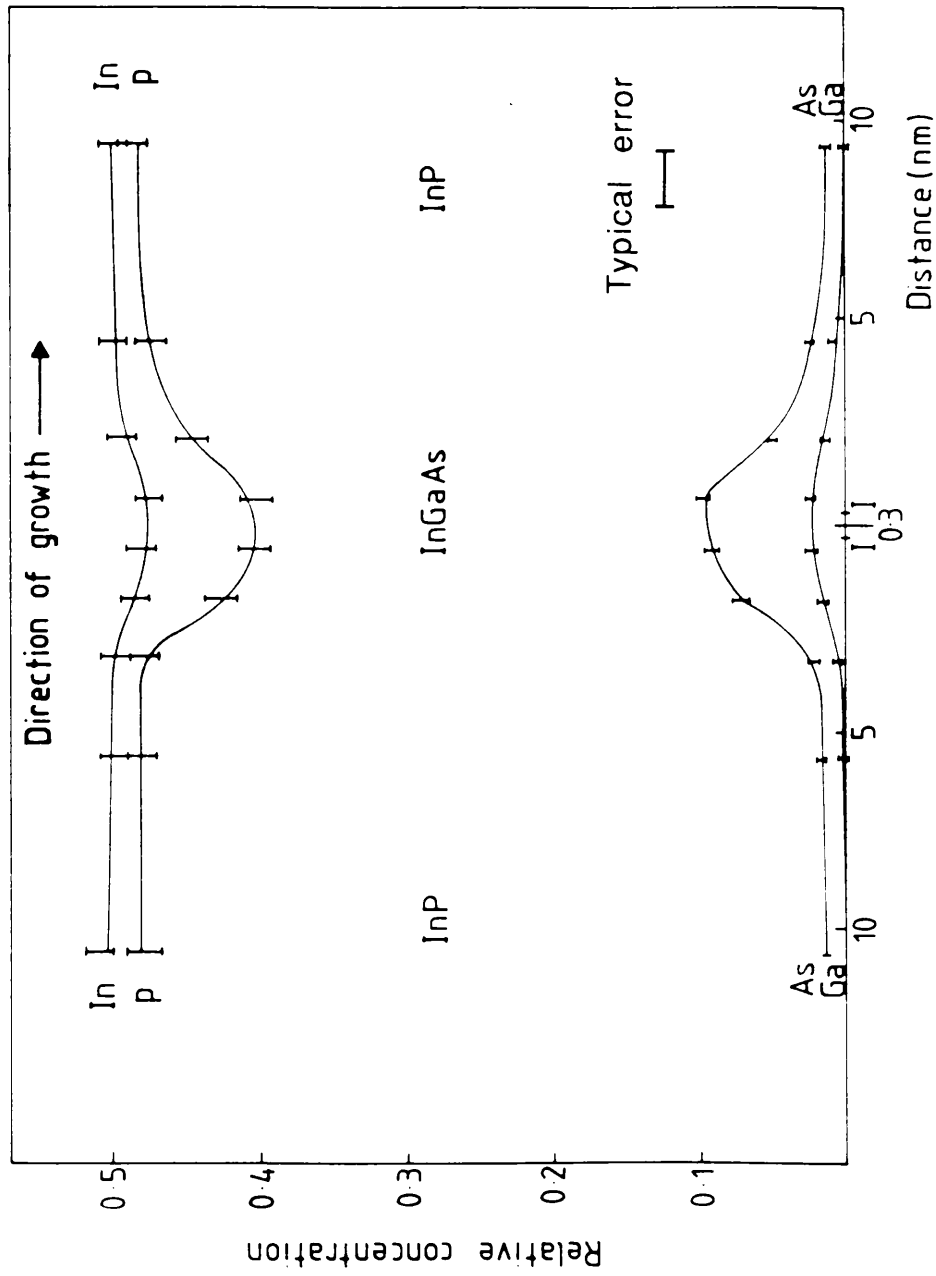


Figure 8.20: Graph showing the variation of atomic fractions calculated from EDX data across an InGaAs layer spanning 1 unit cell dimension grown by MBE.

Areas of spectrum acquisition	f_{In}	f_{Ga}	f_{P}	f_{As}
InP buffers	0.502 ± 0.002	0	0.483 ± 0.002	0.015 ± 0.001
10nm InGaAs	0.306 ± 0.004	0.196 ± 0.004	0.059 ± 0.003	0.436 ± 0.007
5nm InGaAs	0.348 ± 0.004	0.162 ± 0.004	0.144 ± 0.004	0.351 ± 0.006
2.5nm InGaAs	0.364 ± 0.006	0.125 ± 0.004	0.194 ± 0.006	0.318 ± 0.007
1.2nm InGaAs	0.443 ± 0.008	0.050 ± 0.003	0.326 ± 0.008	0.181 ± 0.006
0.6nm InGaAs	0.477 ± 0.008	0.023 ± 0.003	0.403 ± 0.009	0.098 ± 0.004

Table 8.2: List of the atomic fractions and compositions measured from spectra that were acquired in the centres of layers of InGaAs and InP grown by MBE.

across each layer examined are symmetric about the layer centres. The ADF profiles in the previous section showed that t is effectively constant over the distance covered by each individual series. Therefore, to within the spatial resolution of the technique, the type 1 and type 2 transitions are of a similar quality. It can be seen from figures 8.18 to 8.20 that the detected value of f_{Ga} in InP falls below 0.01 at distances of typically 3nm from each interface. This signal distribution is similar to that detected across the type 1 interfaces of specimen 1 in the previous chapter. As the film thicknesses for both sets of results were similar (~40 to 50nm) these data indicate that the compositional variations across layer interfaces in the MBE grown material are comparable to those across the InP to InGaAs transition in the material grown by MOCVD. Furthermore, it was found that for all spectra recorded;

$$f_{\text{In}} + f_{\text{Ga}} = f_{\text{As}} + f_{\text{P}} = 0.5 \quad (8.1)$$

to within experimental error. This is the same result as that observed in chapter 7, and is consistent with there being a group III atom occupying one sublattice site and a group V atom occupying the other. This is the expected result for a crystal of high quality. It should be noted, however, that a high percentage of the signals detected from spectra acquired in the narrowest wells originates from the InP buffer layers. Consequently, any irregularities that may arise in the anion to cation ratio in the InGaAs layers are unlikely to be observed. Information on the MBE growth process is also revealed in figures 8.16 to 8.20 which show that, unlike the type 2 transitions in the MOCVD grown material, there is little evidence of an As 'carry-over' into the InP. There is, however, a constant As concentration in the InP buffer layers. Using the data given in table 8.2, the average composition in the centres of these layers was found to be $\text{InAs}_{0.03}\text{P}_{0.97}$. Such a level of As is consistent with there being desorption of

As from the chamber walls into the material during the growth of the InP layers (Cullis, 1988).

Figures 8.16 to 8.20 show that, in each series acquired, the measured concentrations fail to attain a constant value in the centre of the InGaAs layer. This suggests that the layer centre concentrations listed in table 8.2 are affected by signal contributions from the neighbouring InP layers. As has been mentioned previously, this effect becomes more pronounced in series acquired across the narrowest wells. A knowledge of the specimen geometry together with the data from Monte Carlo analyses described in chapter 5 suggests that the tailing effects observed in the 10nm and 5nm wells are attributable principally to beam broadening in the specimen, whereas the finite probe size becomes the resolution limiting factor as the well dimensions decrease. Table 8.2 shows that the measured value of f_P in the centre of the 10nm InGaAs layer was found to be 0.057. If the assumption is made that no P is actually present in the InGaAs layers, then the concentration of P measured suggests that the contribution from the InP to the total detected signal is ~12%. Section 6.3.2.3 described the method used to estimate layer centre compositions in the presence of tailing effects. Using this technique, the composition in the centre of the 10nm InGaAs layer was estimated to be $\text{In}_{0.56}\text{Ga}_{0.44}\text{As}$, with an error of ± 0.02 associated with each value of x. Such a composition corresponds to a lattice parameter of 0.588nm. This value is exactly matched to the corresponding lattice parameter of $\text{InAs}_{0.03}\text{P}_{0.97}$. The layer centre compositions are consistent with there being abrupt concentration variations at the interfaces. It should be stressed, however, that the estimated composition in the InGaAs layer is based on the assumption that no P is incorporated into the material during the growth of the InGaAs layers. Because of the errors associated with the calculations, the high levels of tailing across the narrower wells (~30% and ~40% in the 5nm and 2.5nm wells respectively) preclude meaningful estimates

of the well centre compositions.

The results have shown that the geometry of the specimen prohibits accurate quantitative analysis on the wells that are <10nm in width. However, the decrease in detected Ga and As signals as a function of decreasing well size shows that EDX microanalysis is sensitive to changes in well width, between (as figures 8.9 and 8.10 show) wells spanning 1 and 2 unit cell dimensions. Furthermore, the existence of detected concentration variations across the narrowest InGaAs well demonstrates that the technique can detect the presence of InGaAs layers down to at least unit cell dimensions.

8.4 Conclusions

The results described in this chapter have shown that the variations in elemental composition across the InGaAs wells in an MBE grown InGaAs/InP system were symmetric about the centres of the layers. Detailed high-angle ADF profile analyses of the system revealed that the detected transition width across each interface was ~3nm. However, the lack of evidence indicating the presence of strain at the interfaces suggests that this value may be in part attributable to resolution limiting factors inherent to the technique and to some instability in the position of the probe at the specimen caused by external interference. The observation that the interface transitions are abrupt or near-abrupt is further supported by noting that firstly, the compositions in the centres of the InGaAs and InP layers were found to be lattice matched and, secondly, that the data acquired from the interfaces are very similar to those recorded from the type 1 interface of the MOCVD grown InGaAs/InP structure examined in the previous chapter. Quantitative analysis showed that the composition in the centres of the InP buffer layers was found to be $\text{InAs}_{0.03}\text{P}_{0.97}$ which, as explained earlier in this chapter, can be attributed to the continued presence of As in the deposition chamber during the growth of the InP layers. Under the

assumption that the flow of P in the chamber can be closely controlled, it was found that the composition in the 10nm well was $\text{In}_{0.56}\text{Ga}_{0.44}\text{As}$. Using the high-angle ADF layer contrast data, it can be deduced that the compositions in the centres of the 5 and 2.5nm wells are the same as that in the 10nm well. When assessed as a whole, the results discussed in this chapter have shown that the specimen examined was of a very high quality, and did not exhibit the same dependence on growth direction observed in the system grown by MOCVD.

The results have also shown that the combination of high-angle ADFI and EDX microanalysis yields important compositional information on wells possessing widths as narrow as 2.5nm. In addition, it has been demonstrated that both techniques are sensitive to the presence of wells that are as narrow as 1 unit cell.

Conclusions and future work

9.1 Conclusions

The work described in this thesis established a firm basis for the examination of compound semiconductor multilayer structures in a STEM using the techniques of high-angle ADFI and EDX microanalysis. It involved the determination of suitable experimental conditions for each technique and the development of analysis procedures designed to yield as much information as possible from acquired data. The techniques were applied to the study of AlGaAs/GaAs specimens grown by MBE and of InGaAs/InP specimens grown by MBE and by atmospheric pressure MOCVD. The work provided valuable information on the variation of elemental composition across the multilayers and led to a greater understanding of material growth processes.

An important consideration in the work carried out in this thesis was the current density distribution of the electron probe at the specimen. It was found that the cross-section for the elastic scattering of electrons into the angular range subtended by the ADF detector was sufficiently high to enable the use of as small a probe as possible for high-angle ADFI. However, to enable the acquisition of EDX spectra with adequate statistical significance over relatively short acquisition times, a compromise was reached between probe current and probe size. Detailed calculations estimating the radial current density distribution in the probe, $j(r)$, for high-angle ADFI and for EDX microanalysis were described in chapter 3. In the analysis of layer interfaces, many of the problems encountered in this project were essentially 1-dimensional. In such cases, it was convenient to express the probe in terms of the linear current

density distribution, $J(x)$. These calculations were also described in chapter 3.

The high spatial resolution characterisation of multilayers in a STEM requires the preparation of high quality cross-sectional specimens to enable microanalysis in a direction parallel to that of material growth. The specimen preparation technique employed in this thesis involved ion beam thinning as the final stage of preparation and was described in detail in chapter 3. Although particular emphasis was given to the preparation of III-V compound semiconductor multilayer specimens, the method can be applied to the preparation of cross-sectional specimens in general.

The results presented in this thesis showed that, although beam broadening in the specimen across interfaces limits the spatial resolution of both high-angle ADFI and EDX microanalysis, the latter named technique is that most seriously affected. It was therefore desirable to obtain a knowledge of the relative effect of probe size and beam broadening on the spatial resolution of EDX microanalysis as a function of specimen thickness, t . Monte Carlo analyses showed that, for 100keV electrons incident on a material in which $Z=32$, the two resolution limiting effects were of comparable magnitude at $t \approx 45\text{nm}$. Below this value, the spatial resolution was principally governed by probe size, whereas the effect of beam spreading became serious as t increased above 45nm. The values of film thickness examined in this thesis were in the range 30 to 80nm. The procedure employed to measure t experimentally in the regions of interest was described in chapter 5 and involved a combination of the CBED technique described by Kelly et. al. (1975) and the analysis of the number of x-ray counts measured in selected characteristic peaks.

Two composition sensitive imaging techniques were employed in this thesis, namely structure factor contrast imaging and high-angle ADFI. The former proved to be an ideal method by which to orient the specimen so that the plane of the layers lay in a direction parallel to that of the incident beam.

However, the interpretation of structure factor contrast in terms of specimen composition requires detailed consideration (Boothroyd and Stobbs, 1988) and so this project looked towards high-angle ADFI as an analytical imaging technique. The discussion on image formation from elastically scattered electrons in chapter 2 showed that, under suitable experimental conditions, the detected signal from high-angle ADF images can be related to the mean atomic number \bar{Z} of the specimen. The experimental conditions used for high-angle ADFI were chosen so that the effect on detected layer contrast of factors such as Bragg scattering and electron channeling in the crystal was minimised. In agreement with Treacy et. al. (1988) it was observed that the presence of strain in materials can also influence the detected high-angle ADF signal distribution. However, this effect was used to provide valuable information on the structural quality of the interfaces in each specimen examined.

The degree to which simple analytical formulae for elastic scattering cross-sections can be used in the quantitative analysis of high-angle ADF images was discussed. A number of elastic scattering models were employed to predict the value of layer contrast detected from images of the InGaAs/InP and AlGaAs/GaAs systems. The values of predicted layer contrast that were obtained varied considerably according to the model used and showed poor agreement with experimentally acquired data. Consequently, image analysis procedures concentrated on the variation of mean atomic number across each specimen, $f(\bar{Z})$, and relied on EDX microanalysis for the provision of quantitative information on elemental composition. The most convenient method found to analyse each image involved the generation of high-angle ADF profile simulations and the comparison of these with profiles acquired experimentally to give the 'best fit' between experiment and theory. Each simulation was calculated by performing a convolution between $J(x)$ and a theoretical estimate of $f(\bar{Z})$ that possessed a linearly varying interface transition of a selected width. Experimental profiles were obtained by taking an average over several

consecutive linescans of an image and applying a median filter to reduce further the effects of signal noise. A correction routine, designed to take into consideration variations in local film thickness over the area scanned by the beam was also described. However, it was stressed that regions of uniform thickness should, if possible be selected for analysis. An advantage of the profile analysis technique used was that comparisons between the measured transition widths allowed conclusions to be drawn on the relative quality of different interface types.

The direct, quantitative technique of EDX microanalysis was employed in this thesis to obtain 'maps' of the variation in elemental composition across the multilayer systems. The experimental procedure employed to obtain such information was described in detail in chapter 5. The chapter also addressed considerations such as those relating to the absorption of characteristic photons before detection. The procedures used in the analysis of spectra acquired from the AlGaAs/GaAs and InGaAs/InP systems were described in chapters 6 and 7 respectively. When possible, the K-factors used in the determination of atomic fractions were measured experimentally. This was of particular importance in analyses involving the conventional EDX detector, as its low energy detection efficiency was, in practice, less than that calculated using a Be window effective thickness of $8.3\mu\text{m}$. In the analysis procedures, elemental compositions in the AlGaAs/GaAs system were deduced directly from the measured Ga to As partial atomic fraction. However, a knowledge of the variation in Al content nevertheless provided much useful information on, for example, the extent of beam spreading across interfaces. In the study of the InGaAs/InP system, the atomic fractions of each of the four elements in the material and their associated errors were calculated for each spectrum acquired.

The Monte Carlo simulation program described in chapter 5 was adapted to estimate the variation in detected x-ray signal across an interface. The aim of

these calculations was to investigate the way in which the detected signal varied with interface transition width. However, the differences between the simulated signal profiles and those measured experimentally were such that only qualitative comparisons could be made. In addition, the Monte Carlo simulations did not predict the extent of signal tailing observed experimentally. Consequently, estimates of the transition width across each interface relied on the high spatial resolution information on the variation of \bar{Z} provided by high-angle ADFI.

The application of high-angle ADFI and EDX microanalysis to the investigation of the AlGaAs/GaAs system grown by MBE was discussed in chapter 6. The experiments described in the chapter were used to assess the resolution capabilities of each technique and to establish a results analysis procedure that utilised the complementarity of the two techniques. High-angle ADF intensity profile analysis of the system demonstrated clear differences in the quality of fit between experiment and theory when the simulated transition width was varied by $\pm 1\text{nm}$. The narrowest detected transition width was found to be 1nm, suggesting that the material was of a high quality. However, in other cases, simulated transition widths of 2.5nm were found to give the best agreement with experiment. It is likely that the variation in detected transition width was attributable in part to some instability in the position of the probe at the specimen caused by the introduction of noise from external sources. Consequently, because of this effect, the profile analysis techniques could not distinguish interfaces possessing actual transition widths of $<2.5\text{nm}$. However, as stated, information on the quality of interfaces can be indicated by an increase in detected high-angle ADF signal that is attributable to the presence of strain. Although this argument cannot be applied in the study of a high quality AlGaAs/GaAs system, it did prove useful in the analysis of the InGaAs/InP system.

The analytical techniques developed in this thesis were applied in chapter 7 to the study of the InGaAs/InP system grown by MOCVD at atmospheric pressure. Both EDX microanalysis and high-angle ADFI showed that interface quality in the material was dependent on the direction of material growth. In particular, the transition from InP to InGaAs was found to be more abrupt than that from InGaAs to InP. Detailed analysis revealed that whilst the InP to InGaAs transition was of a high-quality, a significant As, and to a lesser extent Ga, carry-over at the InGaAs to InP transition led to the presence of strain in these regions. EDX microanalysis revealed that although the compositions at the centers of the InGaAs and InP layers were lattice matched, significant quantities of P were detected in the centre of the InGaAs layers. In the light of the information provided on this multilayer system, steps have been taken to modify MOCVD growth techniques with an aim to improving material quality. For example, in an attempt to decrease the extent of the As carry-over at the InGaAs to InP transition, the pause time between the growth of each layer was increased (Barnett et. al., 1988).

The work carried out on the InGaAs/InP system grown by MBE was described in chapter 8. The results showed that the interface quality in the specimen was very high and did not exhibit the same dependence on growth direction as observed in the system discussed in chapter 7. As in all materials examined in this thesis, the compositions at the layer centres were found (within experimental error) to be lattice matched. However, EDX microanalysis did reveal that, as a result of the growth conditions employed, small quantities of As were present in the InP buffer layers. In addition, the results presented in chapter 8 showed that, when EDX microanalysis is used in conjunction with high-angle ADFI, detailed quantitative analysis can be carried out on wells that are at least as narrow as 2.5nm. Furthermore, it was shown that both techniques are sensitive to the presence of wells that are as narrow as one unit cell.

In conclusion, the work in this thesis has shown that the techniques of EDX

microanalysis and high-angle ADFI that are available on a STEM have a key role to play in the characterisation of semiconductor multilayer structures.

9.2 Future work

A wide variety of components can be used in the growth of semiconductor multilayer structures. The materials can be grown to be lattice matched or, in the case of strained layer superlattices (SLSs) for example, lattice mismatched. The work in this thesis described the application of high-angle ADFI and EDX microanalysis in a STEM to the characterisation of ostensibly lattice matched structures. Consequently, this work has established a foundation for future investigations involving the analysis of lattice matched systems such as CdTe/InSb heterojunctions and superlattices (e.g. Williams et. al., 1985; Chew et. al., 1984).

Provided that principal crystallographic directions are avoided, the data obtained using EDX microanalysis in a STEM is not significantly affected by the presence of strain in materials. Consequently, the technique can be used in the investigation of, for example, elemental compositions at defects in lattice mismatched heterojunctions such as CdTe on GaAs and $\text{Cd}_x\text{Hg}_{1-x}\text{Te}$ on GaAs (Cullis et. al., 1987). Such work would fully utilise the ability of EDX microanalysis to provide quantitative information with high spatial resolution in 2 dimensions. The technique can also provide valuable information on the variation of elemental compositions across strain modulated materials such as SLSs and spinodally decomposed $\text{In}_x\text{Ga}_{1-x}\text{As}_y\text{P}_{1-y}$ layers. EDX studies of the latter named system have been carried out by Glas et. al. (1982).

The work in this thesis demonstrated that simple analytical expressions for elastic scattering cross sections are not of sufficient accuracy to enable quantitative analysis of high-angle ADF images. A possible route by which such

analysis may be achieved could be through high-angle ADF imaging of materials of known composition such as AlAs/GaAs heterojunctions. The detected contrast from such a system could be used to calculate the value of x in high-angle ADF images of $\text{Al}_x\text{Ga}_{1-x}\text{As}/\text{GaAs}$ systems. The accuracy of this technique could be determined by comparing the estimated value of x with that measured using EDX microanalysis.

Unlike EDX microanalysis, the detected high-angle ADF signal can be influenced by the presence of strain in materials. Consequently, careful consideration must be given to the analysis of high-angle ADF images obtained from systems possessing defects and from strain modulated structures. In the latter named materials, the effect of elastic relaxation in the thin specimen on high-angle ADF signal must also be taken into consideration (e.g. Treacy et. al., 1985; Treacy and Gibson, 1986). To enable a greater understanding of the relative contributions of \bar{Z} and the presence of strain to detected signal variations, future work could incorporate lattice parameter measurements across the region of interest. In a STEM, this can be carried out using the technique of microdiffraction. As an alternative to the profile simulation technique used in this thesis, more detailed analysis of high-angle ADF profiles may be aided by the development of profile inversion techniques designed to retrieve information on $f(\bar{Z})$ directly from experimentally acquired data.

Section 1.4 stated that analytical techniques other than high-angle ADFI and EDX microanalysis that are available on a STEM have been employed in the investigation of semiconductor multilayer structures. These include electron energy loss spectroscopy (EELS) and microdiffraction. A STEM technique not previously applied to the characterisation of multilayers is differential phase contrast (DPC) imaging (Dekkers and de Lang, 1977). This technique has been applied successfully to the study of magnetic materials (e.g. Chapman and Morrison, 1983). Variations in elemental concentrations across interfaces in

multilayers signify a change in the mean inner potential of the crystal. On interaction with a cross-sectional specimen, incident electrons will be deviated in a direction perpendicular to the plane of the layers and at an angle related to the rate of change in mean inner potential. Consequently, DPC images formed principally from these electrons will possess signal profiles that can be used to investigate the degree of interface abruptness in materials. Future studies may use the data acquired by DPC imaging to supplement that obtained by the other microanalytical techniques.

Appendix

Notes on software

A1. Programs used to calculate probe current density distributions

Following the method described in section 3.2.2.3, the two programs listed here calculate probe current density distributions at the specimen. Both programs were written in superbasic for use on a Sinclair QL minicomputer.

Program 'J_Dist_Overall' calculates the radial current density distribution at the specimen surface from a monochromatic extended source, $j_o(r)$, by firstly evaluating the radial current density distribution from a monochromatic point source, $j_{mono}(r)$. The discussions in this thesis are restricted to two specific experimental configurations, namely those suitable for EDX microanalysis and for high-angle ADFI. However, by changing the values of the main parameters in the program, 'J_Dist_Overall' can be employed to calculate $j_o(r)$ for a range of experimental conditions. The program listed here is set up to calculate $j_o(r)$ for EDX microanalysis at optimum defocus conditions. $j_o(r)$ and $j_{mono}(r)$ are represented by arrays 'Jover' and 'Jmono' respectively. Included in the calculations of $j_{mono}(r)$ is a subroutine, 'Bessel_F', which can evaluate a Bessel function up to the 50th order. The software also enables the calculation of the percentage of total probe current contained within 0.05nm annuli centered on the origin. These data are used to simulate the probe in the Monte Carlo analyses. As only the relative distributions of current density are calculated in this program, both $j_o(r)$ and $j_{mono}(r)$ are expressed in normalised form. At the completion of the current density calculations, all relevant data is printed out.

It was stated in chapter 3 that, when analysing data acquired across

interfaces, it is convenient to express the probe current density distribution in terms of the linear current density $J(x)$ and so program 'J_Dist_Convert' calculates $J(x)$ from $j_0(r)$. The former is represented by array 'Jx', whereas the latter is represented by array 'Jr'. Included in the program is a database which contains the values of $j_0(r)$ calculated under conditions suitable for high-angle ADFI and for EDX microanalysis.

Program 'J_Dist_Overall'

```
10 REMark J_Dist_overall
20 REMark program to calculate probe profile at specimen for monochromatic
30 REMark extended source for a given aperture size and Cs
40 REMark bessell_f at 310
50 REMark bessell_denominators at 400
60 REMark physical_constants at 500
70 REMark calculate_Jmono at 650
80 REMark mono_radial_distribution at 860
90 REMark print_values at 970
100 REMark normalise_Jmono at 1210
110 REMark calculate_Jover at 1300
120 REMark normalise_Jover at 1500
130 REMark roundnumber(qq) at 1590
140 REMark overall_radial_distribution at 1660
150 REMark *****
160 REMark *****
170 REMark main program
180 MODE 4:WINDOW 512,256,0,0:CLS:AT 20,40:PRINT "Running..."
190 Bessel_denominators
200 physical_constants
210 calculate_Jmono
220 normalise_Jmono
230 calculate_Jover
240 normalise_Jover
250 mono_radial_distribution
260 overall_radial_distribution
270 print_values
280 PRINT "\\!!!!!!!" "FINISHED"
290 REMark *****
300 REMark *****
310 DEFine PROCedure Bessel_F
320 REMark calculate value of Bessel function
330 x=(2*PI*r*alpha)/lamda
340 bess=0
350 FOR qq=1 TO 50
360 bess=bess+((-1)^(qq-1))*(x^(2*(qq-1)))/denom(qq)
370 END FOR qq
380 END DEFine
390 REMark *****
400 DEFine PROCedure Bessel_denominators
410 REMark calculate denominators on Bessel fn. up to 50th order
420 DIM denom(50)
430 num=1:denom(1)=1
440 FOR jj=1 TO 49
450 denom(jj+1)=num*(2*jj)^2
460 num=denom(jj+1)
470 END FOR jj
480 END DEFine
490 REMark *****
500 DEFine PROCedure physical_constants
510 semang=1.1E-2:REMark semi angle for 100 micron VOA in radians
520 Cs=3E-3:REMark Cs estimate in metres
530 lamda=3.7E-12:REMark electron wavelength in metres
540 DIM Jmono(26):REMark array of monochromatic current density values
550 k=2*PI/lamda:REMark electron wavenumber
560 del=5E-5:REMark increment in alpha for integration
570 Ib=2E-10:REMark primary beam current in Amps
580 dz=-1.15E-7:REMark defocus distance in metres
590 DIM Jover(26):REMark array of array of mono extended source Jo values
600 deltrh=.5:REMark radial sampling interval for ext. source convolution
610 sigma=1.2:REMark characteristic width of source in angstroms
620 delth=(2*PI)/50:REMark increment in theta for integration
630 END DEFine
640 REMark *****
650 DEFine PROCedure calculate_Jmono
660 REMark calculate monochromatic point source distribution.
670 FOR r=0 TO 25
680 c=0:s=0
690 r=r*5E-11:REMark convert r to angstroms
700 alpha=0
710 W=(Cs/4)*(alpha*alpha*alpha*alpha)+(dz*alpha*alpha)/2
```

Program 'J_Dist_Overall' (cont.)

```
720 Bessel_F
730 smallc=COS(k*W)*bess*alpha*del
740 smalls=SIN(k*W)*bess*alpha*del
750 c=c+smallc
760 s=s+smalls
770 alpha=alpha+del
780 IF alpha>=semang THEN GO TO 800:END IF
790 GO TO 710
800 r=r*2E10
810 Jo(r+1)=(4*PI*Ib*(c*c+s*s))/(lamda*lamda*semang*semang)
820 AT 10,10:PRINT "Calculated for radius"r/2!"Angstroms.  "
830 END FOR r
840 END DEFine
850 REMark *****
860 DEFine PROCedure mono_radial_distribution
870 REMark Works out current contained within 0.05nm annuli
880 DIM distbn(26)
890 FOR b=1 TO 25
900 avJmono=(Jmono(b)+Jmono(b+1))/2
910 difsqu=((b/2)^2-((b-1)/2)^2)*1E-20
920 perc=100/Ib
930 distbn(b)=PI*avJmono*difsqu*perc
940 END FOR b
950 END DEFine
960 REMark *****
970 DEFine PROCedure print_values
980 REMark dump all data to printer
990 OPEN #5,ser1
1000 PRINT #5,,,"J_Dist_overall"
1010 PRINT #5,\!!"Electron probe profile data for monochromatic extended source.
"
1020 PRINT #5\\,,"Incident semi-angle ="!semang!"radians"
1030 PRINT #5,,,"Cs ="!Cs!"m"
1040 PRINT #5,,,"Electron wavelength ="!lamda!"m"
1050 PRINT #5,,,"Primary beam current ="!Ib!"amps"
1060 PRINT #5,,,"Defocus distance ="!dz!"m"
1070 PRINT #5,,,"Source image characteristic width ="!sigma!"Angstroms"
1080 PRINT #5,\,,"Current density distributions"
1090 PRINT #5,"radius in A",,"monochromatic"!!!!"normalised mono"!!!!"overall"
1100 FOR a=1 TO 26
1110 PRINT #5,,(a-1)/2,,!!!!Jmono(a),!!!!normJmono(a),!!!!Jover(a)
1120 END FOR a
1130 PRINT #5,\,,"Radial current distributions"
1140 PRINT #5,"radial interval",,"monochromatic",!!"overall"
1150 FOR a=1 TO 25
1160 PRINT #5,,(a-1)/2!"to"!a/2!!,,distbn(a),ovdist(a)
1170 END FOR a
1180 CLOSE #5
1190 END DEFine
1200 REMark *****
1210 DEFine PROCedure normalise_Jmono
1220 REMark normalise monochromatic current density distribution
1230 DIM normJmono(26)
1240 Jmax=Jmono(1)
1250 FOR a=1 TO 26
1260 normJmono(a)=Jmono(a)/Jmax
1270 END FOR a
1280 END DEFine
1290 REMark *****
1300 DEFine PROCedure calculate_Jover
1310 REMark calculate monochromatic extended current density distribution
1320 FOR r=0 TO 25
1330 incr=0:x=r/2:REMark correct to angstroms
1340 FOR rho=0 TO 25
1350 y=rho/2:REMark correct to angstroms
1360 FOR theta=1 TO 50
1370 TH=theta*deltth:REMark convert to radians
1380 rr=r*r+rho*rho-2*r*rho*COS(TH)
1390 rr=ABS(rr):rr=SQRT(rr):roundnumber rr:val=rr+1
1400 IF val>26 THEN val=26
1410 gauss=EXP((-y*y)/(2*sigma*sigma))
```

Program 'J_Dist_Overall' (cont.)

```
1420 incr=incr+(2*PI*normJmono(val))*(gauss*v*delt rh)*delt th
1430 END FOR theta
1440 END FOR rho
1450 Jover(r+1)=incr
1460 AT 12.10:PRINT "Jover calculated for"!x!"angstrom radius. "
1470 END FOR r
1480 END DEFine
1490 REMark *****
1500 DEFine PROCedure normalise_Jover
1510 REMark Normalise mono. ext. current density distributionn.
1520 LOCAL a
1530 maxJ=Jover(1)
1540 FOR a=1 TO 26
1550 Jover(a)=Jover(a)/maxJ
1560 END FOR a
1570 END DEFine
1580 REMark *****
1590 DEFine PROCedure roundnumber(qq)
1600 REMark rounds a number to the nearest integer value.
1610 frac=qq-INT(qq)
1620 IF frac<.5 THEN qq=INT(qq):GO TO 1640
1630 qq=INT(qq)+1
1640 END DEFine
1650 REMark *****
1660 DEFine PROCedure overall_radial_distribution
1670 REMark calculate current contained on 0.05nm annuli
1680 DIM ovdist(25)
1690 FOR b=1 TO 25
1700 avJo=(Jover(b)+Jover(b+1))/2
1710 difsqu=((b/2)^2-((b-1)/2)^2)*1E-20
1720 ovdist(b)=PI*avJo*d1+sq
1730 END FOR b
1740 Io=0
1750 FOR b=1 TO 25
1760 Io=Io+ovdist(b)
1770 END FOR b
1780 FOR b=1 TO 25
1790 ovdist(b)=100*ovdist(b)/Io
1800 END FOR b
1810 END DEFine
```

Program 'J_Dist_Convert'

```

10 REMark J_Dist_Convert                      Program to calculate linear
20 REMark define_variables at 170              current density distributions
30 REMark calculate_Jx at 250                  from radial current density
40 REMark normalise_Jx at 420                  distributions.
50 REMark print_values at 500
60 REMark *****
70 REMark *****
80 REMark main program
90 MODE 4:CLS
100 define_variables
110 calculate_Jx
120 normalise_Jx
130 estimate_90r
140 print_values
150 REMark *****
160 REMark *****
170 DEFINE PROCEDURE define_variables
180 DIM Jr(26):REMARK array of radial current density values
190 DIM Jx(23):REMARK array of 1-D current density values
200 FOR j=1 TO 23:Jx(j)=0:END FOR j
210 RESTORE 650
220 FOR j=1 TO 26:READ Jr(j):END FOR j
230 END DEFINE
240 REMark *****
250 DEFINE PROCEDURE calculate_Jx
260 REMark main conversion routine
270 FOR x=0 TO 22
280 n=x+1
290 FOR z=1 TO 50
300 y=z/2
310 rdis=SQRT(x^2+y^2)
320 a=INT(rdis)+1
330 b=a+1
340 IF a>=26:GO TO 360:END IF
350 Jx(n)=Jx(n)+(rdis-a)*(Jr(b)-Jr(a))+Jr(a)
360 END FOR z
370 Jx(n)=2*Jx(n)+Jr(n)
380 AT 5,10:PRINT "Jx("!"n!") calculated.  "
390 END FOR x
400 END DEFINE
410 REMark *****
420 DEFINE PROCEDURE normalise_Jx
430 REMark normalise linear current density distribution
440 Jo=Jx(1)
450 FOR j=1 TO 23
460 Jx(j)=Jx(j)/Jo
470 END FOR j
480 END DEFINE
490 REMark *****
500 DEFINE PROCEDURE print_values
510 OPEN#5,ser1
520 PRINT #5,"Jx current density values for standard ADF probe"\\
530 PRINT #5,TO 5:"distance from probe centre (Angstroms)":TO 35:"normalised cur
rent density"\\
540 FOR j=1 TO 26
550 PRINT #5,TO 14:(j-1)/2;TO 40:Jx(j)
560 END FOR j
570 CLOSE #5
580 END DEFINE
590 REMark *****
600 REMark radial current density distributions
610 REMark standard EDX current density values at .5 Angstrom intervals.
620 DATA 1.,.955,.817,.644,.466,.308,.19,.125,8.9E-2,6.9E-2
630 DATA 5.5E-2,4.5E-2,3.6E-2,2.8E-2,2.4E-2,2.2E-2,2.1E-2,2.1E-2,2E-2
640 DATA 2E-2,1.9E-2,1.8E-2,1.8E-2,1.8E-2,1.7E-2,1.7E-2
650 REMark ADF current density values in .5 Angstrom intervals.
660 DATA 1.,.898,.663,.409,.22,.122,9E-2,8.4E-2,7E-2,4.8E-2,2.7E-2,1.6E-2
670 DATA 1.6E-2,1.4E-2,1.1E-2,9E-3,7E-3,5E-3,4E-3,3E-3,3E-3,3E-3,2E-3
680 DATA 2E-3,1E-3,1E-3

```

A2. High-angle ADFI profile analysis programs

Listed in this section are the programs that were employed in the analysis of high-angle ADF intensity profiles. All acquisition and analysis of profiles was carried out using the Link Systems AN10000 and so each program was written in a version of Fortran 77 that was modified for this particular system. A full description of the analysis steps carried out by each program is given in section 4.4.

Program 'MEDFIL' is an n -point (where n is odd) median filter routine which was employed to reduce the level of noise in experimentally acquired profiles. The value of n most commonly used in the analyses described in this thesis was 11.

Section 4.4 showed that it was sometimes necessary to take into consideration the variation in detected high-angle ADF intensity attributable to changes in specimen thickness over the area scanned by the electron beam. Such corrections were carried out using program 'CUBFIT', which generates a profile in the form of a cubic polynomial. This profile is calculated using information on the number of counts in each pixel in regions or 'windows' of the experimentally acquired profile that possess intensity variations attributable to changes in specimen thickness only. The software enables the selection of up to 5 such windows. By evaluating each element in equation 4.10, 'CUBFIT' can perform a matrix inversion routine which is used to calculate values of the coefficients a , b , c and d of the polynomial given in equation 4.9. In the course of the calculations, subroutine 'ADET' (a program which evaluates the determinant of a 4×4 matrix) is employed on several occasions. The final stage of 'CUBFIT' involves the evaluation of the number of counts in each pixel of the fitted polynomial profile using the relation given in equation 4.9. All relevant data is stored on disc.

Profiles simulating those acquired experimentally by high-angle ADFI were calculated by performing a convolution between an idealised variation in \bar{Z} , $f(\bar{Z})$, and the linear current density distribution, $J(x)$. Such calculations were carried out using program 'CONVO'. The particular version of 'CONVO' listed here was employed to simulate signal intensity distributions across an AlGaAs well. The distributions $f(\bar{Z})$ and $J(x)$ are represented by arrays 'RSPEC' and 'PROBE' respectively. Each element in 'PROBE' is matched to the standard pixel size used in this thesis, corresponding to a sampling interval of 0.13nm. The software enables the free selection of both the pixel position at which each interface occurs and the transition width of the interface. It should be noted that all interface transitions calculated using 'CONVO' vary linearly. Before being stored on disc, all profiles calculated in the program are scaled to the experimentally acquired profile. This enables a direct comparisons to be made between experiment and simulation when using the 'DIGIPAD' and 'AN10' analysis software.

Program 'MEDFIL'

```
C PROGRAM MEDFIL
C MEDIAN FILTER LINE PROFILES
C
C DEFINE ARRAYS
  DIMENSION ISPEC(512),ISPEC2(512),RSPEC(512),RSPEC2(512)
  DIMENSION RANARR(20),ORDARR(20)
C
C DEFINE FILES AND FILTER SIZE
  CALL MESS(" PROGRAM TO MEDIAN FILTER A LINE PROFILE.")
  CALL CRLF
  CALL MESS(" NO. OF POINTS IN FILTER (MUST BE ODD) = ")
  CALL IGETNO(N)
  CALL CRLF
C
C READ IN PROFILE AND CONVERT TO FLOATING POINT ARRAY
  CALL MESS("INPUT SPECTRUM = ")
  CALL GSTRING(PRI)
  CALL CRLF
  CALL OPEN(1,PRI,2,NERR,$10000)
  CALL RDBLK(1,1,ISPEC(1),2,NERR,$10000)
  DO 10 I=1,512
    RSPEC(I)=FLOAT(ISPEC(I))
    RSPEC2(I)=RSPEC(I)
10  CONTINUE
C
C PERFORM FILTER
  N2=(N-1)/2
  DO 110 I=1+N2,512-N2
    DO 30 J=1,N
      RANARR(J)=RSPEC(I-N2-1+J)
30  CONTINUE
      DO 100 K=1,N2+1
        VMAX=RANARR(1)
          DO 90 J=2,N
            IF (RANARR(J).GT.VMAX) GOTO 40
            GO TO 90
          VMAX=RANARR(J)
          CONTINUE
        ORDARR(K)=VMAX
        L=1
93  IF (RANARR(L).EQ.VMAX) GO TO 95
        L=L+1
        GO TO 93
95  RANARR(L)=0.0
100 CONTINUE
    RSPEC2(I)=ORDARR(N2+1)
110 CONTINUE
C
C CONVERT ARRAY INTO INTEGER FORM AND STORE
  DO 150 I=1,512
    ISPEC2(I)=IFIX(RSPEC2(I))
150 CONTINUE
  CALL MESS("OUTPUT SPECTRUM = ")
  CALL GSTRING(PRO)
  CALL OPEN(2,PRO,2,NERR,$10000)
  CALL WRBLK(2,1,ISPEC2(1),2,NERR,$10000)
C
1000 STOP
END
```

Program 'CUBFIT'

```
C  PROGRAM CUBFIT
C  FIT CUBIC THICKNESS CORRECTION TO LINE PROFILES
C  PREVIOUS DATA IS OVERWRITTEN
C  PROGRAM CALLS SUBROUTINE ADET(A)
C
C  DEFINE PARAMETERS
      COMMON DET
      INTEGER ISPEC(0:511),IHED(0,255),IWINST(5),IWINFI(5)
      REAL XVALS(512),YVALS(512),S(11),RSPEC(512)
      REAL AMAT(4,4),MAT0(4,4),MAT1(4,4),MAT2(4,4),MAT3(4,4),MAT4(4,4)
C
      CALL MESS("PROGRAM TO FIT CUBIC POLYNOMIAL TO SPECTRUM")
C
C  SET BACKGROUND WINDOWS
      CALL CRLF
      CALL MESS("NO. OF WINDOWS = ")
      CALL IGETNO(IWINNO)
      DO 5 I=1,IWINNO
      CALL IPUTNO(I)
      CALL MESS("  START NO. = ")
      CALL IGETNO(IWINST(I))
      CALL CRLF
      CALL MESS("  END NO. = ")
      CALL IGETNO(IWINFI(I))
      CALL CRLF
5     CONTINUE
C
C  READ IN SPECTRUM
      CALL MESS("INPUT SPECTRUM = ")
      CALL GSTRING(PRI)
      CALL CRLF
      CALL OPEN(1,PRI,2,NERR,$10000)
      CALL RDBLK(1,1,ISPEC(0),2,NERR,$10000)
C
C  CONVERT DATA TO REAL FLOATING POINT ARRAY
      DO 10 I=0,511
      J=I+1
      RSPEC(J)=FLOAT(ISPEC(I))
10     CONTINUE
C
C  CALCULATE ARRAY OF CONSTANTS FOR BACKGROUND FITTING
      NOCHAS=0
      DO 20 I=1,IWINNO
      IDUM=IWINST(I)
15     NOCHAS=NOCHAS+1
      XVALS(NOCHAS)=FLOAT(IDUM)
      YVALS(NOCHAS)=RSPEC(IDUM)
      IDUM=IDUM+1
      IF (IDUM.GT.IWINFI(I)) GO TO 20
      GO TO 15
20     CONTINUE
C
C  CALCULATE ARRAY OF CONSTANTS
      DO 30 I=1,11
      S(I)=0.0
30     CONTINUE
      S(1)=FLOAT(NOCHAS)
      DO 40 I=1,NOCHAS
      S(2)=S(2)+XVALS(I)
      S(3)=S(3)+XVALS(I)**2
```

Program 'CUBFIT' (cont.)

```

      S(4)=S(4)+XVALS(I)**3
      S(5)=S(5)+XVALS(I)**4
      S(6)=S(6)+XVALS(I)**5
      S(7)=S(7)+XVALS(I)**6
      S(8)=S(8)+YVALS(I)
      S(9)=S(9)+YVALS(I)*XVALS(I)
      S(10)=S(10)+YVALS(I)*XVALS(I)**2
      S(11)=S(11)+YVALS(I)*XVALS(I)**3
40    CONTINUE
C
C    SET UP MATRICES FROM ARRAY VALUES
      DO 70 I=1,4
        DO 60 J=1,4
          K=I+(J-1)
          AMAT(J,I)=S(K)
60    CONTINUE
70    CONTINUE
      DO 90 I=1,4
        DO 80 J=1,4
          MAT0(I,J)=AMAT(I,J)
          MAT1(I,J)=AMAT(I,J)
          MAT2(I,J)=AMAT(I,J)
          MAT3(I,J)=AMAT(I,J)
          MAT4(I,J)=AMAT(I,J)
80    CONTINUE
90    CONTINUE
      DO 100 I=1,4
        J=I+7
        MAT1(I,1)=S(J)
        MAT2(I,2)=S(J)
        MAT3(I,3)=S(J)
        MAT4(I,4)=S(J)
100   CONTINUE
C
C    EVALUATE MATRIX DETERMINANTS
      CALL ADET(MAT0)
      DET0=DET
      CALL ADET(MAT1)
      DET1=DET
      CALL ADET(MAT2)
      DET2=DET
      CALL ADET(MAT3)
      DET3=DET
      CALL ADET(MAT4)
      DET4=DET
C
C    CALCULATE CUBIC FITTING CONSTANTS
      A=DET1/DET0
      B=DET2/DET0
      C=DET3/DET0
      D=DET4/DET0
C
C    PRINT OUT CONSTANTS
      CALL CRLF
      CALL PUTNO(A,30,10)
      CALL CRLF
      CALL PUTNO(B,30,10)
      CALL CRLF
      CALL PUTNO(C,30,10)
      CALL CRLF
```

Program 'CUBFIT' (cont.)

```
      CALL PUTNO(D,30,10)
      CALL CRLF
C
C   CALCULATE CUBIC POLYNOMIAL
      DO 110 I=1,512
      F=FLOAT(I)
      RSPEC(I)=A+(B*F)+(C*(F**2))+(D*(F**3))
110   CONTINUE
C
C   CONVERT BACK TO INTEGER ARRAY
      DO 500 I=0,511
      J=I+1
      ISPEC(I)=IFIX(RSPEC(J))
500   CONTINUE
      CALL MESS("OUTPUT SPECTRUM = ")
      CALL GSTRING(PRO)
      CALL OPEN(2,PRO,2,NERR,$10000)
      CALL WRBLK(2,1,ISPEC(0),2,NERR,$10000)
C
10000  STOP
      END
```

Subroutine 'ADET'

```
C   SUBROUTINE TO DETERMINE THE DETERMINANT OF 4X4 MATRIX A
C
      SUBROUTINE ADET(A)
      DIMENSION A(4,4)
      COMMON DET
C
      B1=A(2,2)*(A(3,3)*A(4,4)-A(3,4)*A(4,3))
      B2=A(2,3)*(A(3,2)*A(4,4)-A(3,4)*A(4,2))
      B3=A(2,4)*(A(3,2)*A(4,3)-A(3,3)*A(4,2))
      B4=A(2,1)*(A(3,3)*A(4,4)-A(3,4)*A(4,3))
      B5=A(2,3)*(A(3,1)*A(4,4)-A(3,4)*A(4,1))
      B6=A(2,4)*(A(3,1)*A(4,3)-A(3,3)*A(4,1))
      B7=A(2,1)*(A(3,2)*A(4,4)-A(3,4)*A(4,2))
      B8=A(2,2)*(A(3,1)*A(4,4)-A(3,4)*A(4,1))
      B9=A(2,4)*(A(3,1)*A(4,2)-A(4,1)*A(3,2))
      B10=A(2,1)*(A(3,2)*A(4,3)-A(4,2)*A(3,3))
      B11=A(2,2)*(A(3,1)*A(4,3)-A(4,1)*A(3,3))
      B12=A(2,3)*(A(3,1)*A(4,2)-A(4,1)*A(3,2))
C
      C1=A(1,1)*(B1-B2+B3)
      C2=A(1,2)*(B4-B5+B6)
      C3=A(1,3)*(B7-B8+B9)
      C4=A(1,4)*(B10-B11+B12)
C
      DET=C1-C2+C3-C4
C
      RETURN
      END
```

Program 'CONVO'

```
C PROGRAM CONVO
C CONVOLUTE PROBE DATA WITH CONCENTRATION PROFILES TO
C SIMULATE HIGH-ANGLE ADF INTENSITY PROFILES
C
      DIMENSION RSPEC(512),ICSPEC(512),PROBE(21),CSPEC(512),IDSPEC(512)
      DIMENSION DUMSP(512)
C
      CALL MESS("PROGRAM TO DESIGN PROFILE FOR SINGLE ALGAAS WELL")
      CALL CRLF
      CALL MESS("AND CONVOLUTE THE RESULT WITH ADF PROBE DATA")
      CALL CRLF
C
C DEFINE SPECTRUM SCALERS
      CALL MESS("AVERAGE COUNTS IN ALGAAS LAYER = ")
      CALL GETNO(B)
      CALL CRLF
      CALL MESS("AVERAGE COUNTS IN GAAS BACKGROUND = ")
      CALL GETNO(H)
      CALL CRLF
      CALL MESS("POSITIONS OF COMPOSITION CHANGES ARE;")
      CALL CRLF
      CALL IGETNO(K1)
      CALL CRLF
      CALL IGETNO(K2)
      CALL CRLF
C
C DEFINE TRANSITION WIDTHS (MUST BE EVEN)
      CALL MESS("WIDTHS OF COMPOSITION CHANGES ARE;")
      CALL CRLF
      CALL IGETNO(M1)
      CALL CRLF
      CALL IGETNO(M2)
      CALL CRLF
C
C DESIGN BASIC PROFILE
      DO 10 I=1,K1
10      RSPEC(I)=1.0
      DO 20 I=K1+1,K2
20      RSPEC(I)=0.0
      DO 30 I=K2+1,512
30      RSPEC(I)=1.0
C
C DESIGN DIFFUSE INTERFACES
      IF (M1.EQ.0) GO TO 55
      AM=FLOAT(M1)
      CRE=1/(AM+1)
      X=0.0
      L1=K1+1-(M1/2)
      L2=K1+(M1/2)
      DO 53 I=L1,L2
      X=X+1.0
      RSPEC(I)=1.0-CRE*X
C
53      CONTINUE
55      IF (M2.EQ.0) GO TO 60
      AM=FLOAT(M2)
      CRE=1/(AM+1)
      X=0.0
      L1=K2+1-(M2/2)
      L2=K2+(M2/2)
```

Program 'CONVO' (cont.)

```

      DO 58 I=L1,L2
      X=X+1.0
      RSPEC(I)=CRE*X
58    CONTINUE
60    CONTINUE
C
C   SCALE SPECTRUM AND STORE CONC PROFILE
      DO 100 I=1,512
      DUMSF(I)=RSPEC(I)
      DUMSF(I)=B+(H-B)*DUMSF(I)
      ICSPEC(I)=IFIX(DUMSF(I))
100   CONTINUE
      CALL MESS("COMPOSITION PROFILE TO BE STORED AS;")
      CALL CRLF
      CALL GSTRING(PRI)
      CALL CRLF
      CALL OPEN(1,PRI,2,NERR,$10000)
      CALL WRBLK(1,1,ICSPEC(1),2,NERR,$10000)
C
C   DEFINE PROBE DATA
      PROBE(11)=1.0
      PROBE(12)=.814
      PROBE(13)=.449
      PROBE(14)=.215
      PROBE(15)=.112
      PROBE(16)=.057
      PROBE(17)=.035
      PROBE(18)=.022
      PROBE(19)=.014
      PROBE(20)=.008
      PROBE(21)=.004
      DO 110 I=1,10
110   PROBE(11-I)=PROBE(I+11)
C
C   PERFORM CONVOLUTION
      DO 120 I=1,512
120   CSPEC(I)=0.0
      DO 150 I=13,499
      DO 140 J=1,21
      CSPEC(I)=CSPEC(I)+PROBE(J)*RSPEC(I-10+J)
140   CONTINUE
150   CONTINUE
C
C   TIDY, NORMALISE AND SCALE CSPEC
      DO 160 I=1,12
160   CSPEC(I)=CSPEC(13)
      DO 170 I=500,512
170   CSPEC(I)=CSPEC(13)
      CMAX=CSPEC(13)
      DO 180 I=1,512
180   CSPEC(I)=CSPEC(I)/CMAX
      DO 190 I=1,512
      CSPEC(I)=B+(H-B)*CSPEC(I)
190   IDSPEC(I)=IFIX(CSPEC(I))
C
C   STORE CONVOLUTED SPECTRUM
      CALL MESS("CONVOLUTED PROFILE TO BE STORED AS;")
      CALL CRLF
      CALL GSTRING(PRO)
      CALL OPEN(2,PRO,2,NERR,$10000)
      CALL WRBLK(2,1,IDSPEC(1),2,NERR,$10000)
C
1000  STOP
      END
```

A3. Monte Carlo simulations

This section lists the Monte Carlo program 'Monty', written in superbasic for use on a Sinclair QL minicomputer. A full and detailed description of the Monte Carlo calculations and of the modifications made to estimate the distribution of trajectory path lengths within the specimen is given in chapter 5.

The desired probe current density distribution for each simulation can be chosen from the database listed at the end of the program. The user is also free to choose the composition of the target material (always single element), the film thickness and the number of electrons in each complete simulation (typically 2000). The software also enables several different simulations to be run consecutively. For example, the program listed here is set up to perform 5 simulations, with 2000 electrons in each. The incident probe is a δ -function positioned at the origin, the target material is Ge, the values of film thickness for the simulations range between 10 and 90nm, and the incident electron energy is 100keV. The principal calculations involved in each scattering event are included in subroutine 'trajectories'. At the completion of each scattering event, the subroutine 'pathlengths' is implemented to record both the total distance travelled by the electron in the specimen and that travelled through each 0.2nm wide section. At the completion of each run of 'Monty', both the path length distributions and the radial distribution of transmitted electrons at the exit surface are recorded on microdrive or floppy disc. The program also enable graphical representations of these data to be printed on the VDU screen and 'dumped' to a printer.

Program 'Monty'

```
10 REMark Monty - calculates electron distribution
20 REMark opening_page at 370 for selected probe across abrupt or
30 REMark second_page at 600 diffuse interfaces using pathlength
40 REMark starting_variables at 900 or radial distribution data. All
50 REMark mainscreen at 1100 data is stored in microdrive.
60 REMark trajectories at 1310
70 REMark countback at 1790
80 REMark counttrans at 1900
90 REMark graphpage at 2080
100 REMark clocksub at 2380
110 REMark roundnumber at 2480
120 REMark displaynumbers at 2540
130 REMark pathlengths at 2640
140 REMark displaypathnos at 2950
150 REMark store_data at 3040
160 REMark scr_dump at 3210
170 REMark define_first_angles at 3290
180 REMark first_path at 3500
190 REMark choose_radius at 3650
200 REMark *****
210 REMark *****
220 REMark main program
230 opening_page
240 FOR xxx=1 TO nogos
250 second_page
260 starting_variables
270 mainscreen
280 trajectories
290 graphpage
300 displaynumbers
310 displaypathnos
320 store_data
330 END FOR xxx
340 CLS:AT 10,10:PRINT "End of program."
350 REMark *****
360 REMark *****
370 DEFine PROCedure opening_page
380 REMark set up initial parameters
390 dump=RESPR(1312)
400 LBYTES mdv1_gprint_prt,dump
410 PAPER 4:INK 7
420 MODE 4:CLS
430 AT 10,10:PRINT "Ensure data_store cartridge is in mdv2_."
440 AT 19,20:PRINT "Press 'SPACE' to continue..."
450 IF KEYROW(1)=64 THEN CLS:GO TO 470
460 GO TO 450
470 BLOCK 250,150,94,30.0
480 OPEN #3,con_250a150a130x40 : PAPER #3,2:INK #3,7
490 CLS #3
500 DIM ex%(100)
510 CSIZE #3,1,0
520 CURSOR #3,30,10:UNDER #3,1 :PRINT #3,"Monte Carlo Simulation":UNDER #3,0
530 UNDER #3,1:CURSOR #3,50,20:PRINT #3,"for thin films":UNDER #3,0
540 PRINT #3,\\\\" NBS program modified for QL\\\\"
550 CLOSE #3
560 PAUSE 200
570 RESTORE 3780:READ nogos: REMark No. of times monty is to be run
580 END DEFine
590 REMark *****
600 DEFine PROCedure second_page
610 REMark read in initial data
620 MODE 4:PAPER 3:INK 7:CLS
630 RESTORE 3790+10*(xxx-1)
640 READ na$,EI,TH,prolin,counts,dy,file$
650 REMark read element, initial energy, film thickness, probe data line
660 REMark . no. of counts, sampling interval and file to be stored as
670 CSIZE 1,1 :CURSOR 110,0:UNDER 1
680 PRINT "Experimental Conditions": CSIZE 0,0:UNDER 0
690 PRINT \\\", " Element= " na$
700 RESTORE prolin
710 READ probe$
```

Program 'Monty' (cont.)

```

720 DIM distbn(26)
730 FOR I1=1 TO 26 :READ distbn(I1):END FOR I1
740 RESTORE 4020
750 FOR j=1 TO 30
760 READ nm$,z,aa,rh
770 REMark read element, atomic number, atomic weight, density.
780 zzz=z
790 IF nm$=na$ THEN GO TO B10
800 NEXT j
810 AT 10,5:PRINT ","      Atomic Number  "Iz\,,"      Atomic weight  "Iaa\,,"
      Density gm/cc  "Irh
820 PRINT ","      Beam KV = "IEI\,,"      Foil thickness (nm) = "ITH\,,probe$
830 PRINT ","      No. of counts = "Icounts
840 q=100
850 PRINT ","      No. of windows for conc. gradient = "Iq
860 PRINT ","      Window length (nm) = "Idy:dy=10*dy
870 PAUSE 300
880 END DEFine
890 REMark *****
900 DEFine PROCedure starting_variables
910 TH=TH*10: REMark convert thickness to angstroms
920 REMark set up initial parameters
930 AL=(z^.67)*3.4E-3/EI:AK=AL*(1+AL)
940 ER=((EI+511)*(EI+511)/((EI+1022)*(EI+1022)))
950 SG=(z*z)*12.56*5.21E-21*ER
960 SG=SG/(EI*EI*AK):REMark CROSS-SECTION
970 L1=aa/(rh*SG*6.023E23):REMark MFP IN CM
980 L1=L1*1E8*(1+(z/300)):REMark MFP IN ANGSTROMS
990 ES=EI
1000 JB=9.76*z+(58.5/((z)^.19)):JB=JB*1E-3
1010 DQ=78500*rh*z/aa
1020 ELS=DQ*LN(1.166*ES/JB)*1E-8*TH/ES
1030 dbeg=DATE
1040 REMark pathlength calculation arrays
1050 DIM lboxt(q):FOR j=1 TO q:lboxt(j)=0:NEXT j
1060 DIM lbox(q):FOR j=1 TO q:lbox(j)=0:NEXT j
1070 totlen=0
1080 alphas=0:REMark incident semiangle for d-function probe in rads
1090 END DEFine
1100 REMark *****
1110 DEFine PROCedure mainscreen
1120 REMark set up Monte Carlo simulation page
1130 PAPER 0:WINDOW 512,256,0,0:CLS:PAPER 0:INK 7
1140 WINDOW 430,230,50,15:CLS
1150 SCALE 1000,0,0
1160 zs=1:IF TH>500 THEN zs=TH/500
1170 ne=0:bs=0:tr=0
1180 zz=900-TH/zs
1190 CURSOR 50,150:PRINT "Beam normal"\      "IES!"KV beam"\probe$
1200 LINE 0,900 TO 1450,900:LINE 0,zz TO 1450,zz
1210 PAPER 7:LINE 680,950 TO 680,900:FILL 1:LINE TO 660,920 TO 700,920 TO 680,90
0:FILL 0:PAPER 3
1220 STRIP 0
1230 AT 15,40:PRINT "Total"
1240 AT 16,40:PRINT "BS"
1250 AT 17,40:PRINT "Trans"
1260 AT 19,40:PRINT "Energy (KeV)"
1270 AT 20,40:PRINT TH/10!"nm"!na$!"foil"
1280 AT 21,40:PRINT "Time="
1290 END DEFine
1300 REMark *****
1310 DEFine PROCedure trajectories
1320 REMark main Monte Carlo calculations are in this subroutine.
1330 IF ne>=counts THEN GO TO 1770
1340 INK 7:clocksub
1350 choose_radius:re=RND*PI*2:x=r1*SIN(re):y=r1*COS(re)
1360 lam=L1/EI:ES=ES:re=RND:define_first_angles:first_path:firstz=z
1370 IF y=0 THEN y=-1E-4*RND(0 TO 1)
1380 IF z>TH THEN LINE 680-y/zs,900 TO 680-yn/zs,zz-S:z=0:zn=TH:counttrans:GO TO
1320
1390 LINE 680-y/zs,900 TO 680-yn/zs,900-z/zs

```

Program 'Monty' (cont.)

```

1400 zn=z:z=0:pathlengths
1410 z=firstz:x=xn:y=yn
1420 y1=680-y/zs:z1=900-z/zs
1430 r1=RND
1440 st=-1am*LN(r1)
1450 r1=RND
1460 cp=1-((2*AL*r1)/(1+AL-r1))
1470 sp=SQRT(ABS(1-cp*cp))
1480 r2=RND:ga=PI*r2*2
1490 m=ATAN(-cx/cz)
1500 IF cx=0 THEN cx=1.1E-4
1510 n=ATAN(-cz/cx)
1520 REMark calculate new coordinates
1530 xn=x+(st*cx*cp)+(st*COS(m)*sp*COS(ga))+(st*cy*COS(n)*sp*SIN(ga))
1540 yn=y+(st*cy*cp)+(st*sp*SIN(ga)*(cz*COS(m)-cx*COS(n)))
1550 zn=z+(st*cz*cp)+(st*COS(n)*COS(ga))-(st*cy*COS(m)*SIN(ga))
1560 y2=INT(680-(yn/zs)):z2=INT(900-(zn/zs))
1570 REMark check if electron is still within film
1580 IF y2<1 THEN LINE TO 1,z1:counttrans:GO TO 1320
1590 IF y2>1380 THEN LINE TO 1380,z1:counttrans:GO TO 1320
1600 IF z2>900 THEN LINE y1,z1 TO y2,925:countback:GO TO 1320
1610 IF z2<zz THEN LINE y1,z1 TO y2,zz-5:counttrans:GO TO 1320
1620 LINE y1,z1 TO y2,z2:y1=y2:z1=z2
1630 vc=SQRT((xn-x)*(xn-x)+(yn-y)*(yn-y)+(zn-z)*(zn-z))
1640 cx=(xn-x)/vc:cy=(yn-y)/vc:cz=(zn-z)/vc
1650 pathlengths
1660 x=xn:y=yn:z=zn
1670 REMark re-evaluate electron energy
1680 de=D0*LN(1.166*EI/JB):de=de/EI
1690 EI=EI-st*1E-8*de
1700 INK 7:AT 19,57:PRINT INT(EI*10)/10
1710 IF EI<ES AND EI>ES-ELS*.333 THEN INK 7
1720 IF EI<ES-ELS*.333 AND EI>ES-ELS*.67 THEN INK 5
1730 IF EI<ES-ELS*.67 AND EI>ES-ELS THEN INK 3
1740 lam=L1*EI/ES
1750 IF EI<25 THEN INK 7:ne=ne+1:AT 15,50:PRINT ne:GO TO 1320
1760 GO TO 1430
1770 END DEFine
1780 REMark *****
1790 DEFine PROCedure countback
1800 REMark count no. of backscattered electrons
1810 bs=bs+1:ne=ne+1
1820 INK 7:AT 15,50:PRINT ne
1830 AT 16,50:PRINT bs
1840 vc=SQRT((xn-x)*(xn-x)+(yn-y)*(yn-y)+(zn-z)*(zn-z))
1850 cx=(xn-x)/vc:cy=(yn-y)/vc:cz=(zn-z)/vc
1860 ll=(-z)/cz:xe=x+ll*cx:ye=y+ll*cy
1870 xn=xe:yn=ye:zn=0:pathlengths
1880 DEFine
1890 REMark *****
1900 DEFine PROCedure counttrans
1910 REMark count no. of transmitted electrons
1920 ne=ne+1:tr=tr+1
1930 AT 15,50:PRINT ne
1940 AT 17,50:PRINT tr
1950 vc=SQRT((xn-x)*(xn-x)+(yn-y)*(yn-y)+(zn-z)*(zn-z))
1960 IF vc=0 THEN rn=0:GO TO 2020
1970 cx=(xn-x)/vc:cy=(yn-y)/vc:cz=(zn-z)/vc
1980 ll=(TH-z)/cz:xe=x+ll*cx:ye=y+ll*cy
1990 rn=SQRT((xe*xe)+(ye*ye))
2000 r=rn/(2*zs)
2010 roundnumber r
2020 r=r+1:IF r>100 THEN r=100
2030 ex%(r)=ex%(r)+1
2040 REMark evaluate pathlengths for final leg of trajectory
2050 xn=xe:yn=ye:zn=TH:pathlengths
2060 END DEFine
2070 REMark *****
2080 DEFine PROCedure graphpage

```

Program 'Monty' (cont.)

```
2090 REMark output radial transmitted data to screen
2100 PAUSE 200
2110 PAPER 0:INK 7:CLS
2120 LINE 1300,400 TO 100,400:em%=0
2130 FOR j=1 TO 100
2140 IF ex%(j)>em% THEN em%=ex%(j)
2150 NEXT j
2160 FOR j=1 TO 100:ex%(j)=INT(ex%(j)*500/em%):NEXT j
2170 FOR j=1 TO 99
2180 LINE 100+(j*6-6)*2,400 TO 100+(j*6-6)*2,ex%(j)+400 TO 100+j*12,ex%(j)+400 T
O 100+j*12,400
2190 NEXT j
2200 UNDER 1
2210 AT 0,5:PRINT "Radial intensity distribution at exit surface of specimen"
2220 UNDER 0
2230 ss=INT(2*zs)/10:AT 16,20:PRINT ss!"nm bars"
2240 wa=0:wb=0
2250 FOR j=1 TO 100
2260 wb=wb+ex%(j)
2270 NEXT j
2280 FOR j=1 TO 100
2290 wa=wa+ex%(j)
2300 IF wa>(.9*wb) THEN GO TO 2320
2310 NEXT j
2320 AT 17,20:PRINT "90% radius is"!j*ss!"nm"
2330 AT 18,20:PRINT "in"!TH/10!"nm of"!na$!"at"!ES!"KV"
2340 AT 19,20:PRINT probe$
2350 AT 20,25:PRINT "Storing all relevant data..."
2360 END DEFINE
2370 REMark *****
2380 DEFINE PROCEDURE clocksub
2390 dend=DATE
2400 ddiff=dend-dbeg
2410 nohrs=INT(ddiff/3600)
2420 nomins=INT((ddiff-nohrs*3600)/60)
2430 noseecs=ddiff-nohrs*3600-nomins*60
2440 AT 21,50:PRINT " "
2450 AT 21,50:PRINT nohrs!"":!nomins!"":!noseecs
2460 END DEFINE
2470 REMark *****
2480 DEFINE PROCEDURE roundnumber (qq)
2490 frac=qq-INT(qq)
2500 IF frac<.5 THEN qq=INT(qq):GO TO 2520
2510 qq=INT(qq)+1
2520 END DEFINE
2530 REMark *****
2540 DEFINE PROCEDURE displaynumbers
2550 REMark evaluate radial transmitted distribution array
2560 DIM radis(100)
2570 FOR j=1 TO 100
2580 i=100*ex%(j)/wb
2590 roundnumber i
2600 radis(j)=i
2610 NEXT j
2620 END DEFINE
2630 REMark *****
2640 DEFINE PROCEDURE pathlengths
2650 REMark calculate pathlengths in each window through which
2660 REMark a trajectory has passed.
2670 xmem=xn:ymem=yn:zmem=zn
2680 IF yn>=y THEN GO TO 2710
2690 xn=x:yn=y:zn=z
2700 x=xmem:y=ymem:z=zmem
2710 IF yn<-(q/2)*dy OR y>=(q/2)*dy : GO TO 2880
2720 m=INT(y/dy):IF m<-(q/2) THEN m=-(q/2)
2730 mn=INT(yn/dy):IF mn>(q/2)-1 THEN mn=(q/2)-1
2740 IF mn=m THEN lbox(m+(q/2)+1)=SQRT((x-xn)*(x-xn)+(y-yn)*(y-yn)+(z-zn)*(z-zn)
)
2750 IF mn=m THEN lboxt(m+(q/2)+1)=lboxt(m+(q/2)+1)+lbox(m+(q/2)+1):totlen=totle
n+lbox(m+(q/2)+1):GO TO 2920
2760 mx=(xn-x)/(yn-y):mz=(zn-z)/(yn-y)
```

Program 'Monty' (cont.)

```
2770 dx=mx*dy:dz=mz*dy
2780 IF y<-(q/2)*dy THEN y=-(q/2)*dy:x=x+mx*(-(q/2)*dy-y):z=z+mz*(-(q/2)*dy-y)
2790 IF yn>=(q/2)*dy THEN yn=(q/2)*dy-1E-4:xn=xn-mx*(yn-(q/2)*dy):zn=zn-mz*(yn-(
q/2)*dy)
2800 boxlen=SQRT(dx*dx+dy*dy+dz*dz)
2810 FOR j=m+(q/2)+1 TO mn+(q/2)+1
2820 IF (j>m+(q/2)+1) AND j<(mn+(q/2)+1) THEN lbox(j)=boxlen
2830 END FOR j
2840 dely=(m+1)*dy-y
2850 lbox(m+(q/2)+1)=SQRT((mx*dely)*(mx*dely)+dely*dely+(mz*dely)*(mz*dely))
2860 delyn=yn-(mn*dy)
2870 lbox(mn+(q/2)+1)=SQRT((mx*delyn)*(mx*delyn)+delyn*delyn+(mz*delyn)*(mz*delyn))
2880 FOR j=m+(q/2)+1 TO mn+(q/2)+1
2890 lboxt(j)=lboxt(j)+lbox(j)
2900 totlen=totlen+lbox(j)
2910 END FOR j
2920 xn=xmem:yn=yem:zn=zmem
2930 END DEFine
2940 REMark *****
2950 DEFine PROCedure displaypathnos
2960 REMark evaluate pathlength distribution array.
2970 DIM perpat(q):FOR j=1 TO q:perpat(j)=0:NEXT j
2980 FOR j=1 TO 100
2990 i=100*lboxt(j)/totlen
3000 perpat(j)=i
3010 NEXT j
3020 END DEFine
3030 REMark *****
3040 DEFine PROCedure store_data
3050 REMark store all relevant data on microdrive.
3060 OPEN_NEW #7,file$
3070 PRINT #7,na$
3080 PRINT #7,zzz
3090 PRINT #7,aa
3100 PRINT #7,rh
3110 PRINT #7,probe$
3120 PRINT #7,TH
3130 PRINT #7,dy
3140 PRINT #7,totlen
3150 FOR a=1 TO 100:PRINT #7,lboxt(a):END FOR a
3160 FOR a=1 TO 100:PRINT #7,perpat(a):END FOR a
3170 FOR a=1 TO 100:PRINT #7,radis(a):END FOR a
3180 CLOSE #7
3190 END DEFine
3200 REMark *****
3210 DEFine PROCedure scr_dump
3220 REMark subroutine used for screendumps
3230 CALL dump
3240 OPEN #5,ser1
3250 PRINT #5,\\
3260 CLOSE #5
3270 END DEFine
3280 REMark *****
3290 DEFine PROCedure define_first_angles
3300 REMark allow for a finite spread of incident electron angle up
3310 REMark to alpha nought.
3320 phi=2*PI*RND
3330 prob=15*RND
3340 REMark incident angle probability varies as alpha with |alpha|<alphao
3350 IF prob<1
3360 theta=alphao/10:GO TO 3480
3370 END IF
3380 IF prob<3
3390 theta=3*alphao/10:GO TO 3480
3400 END IF
3410 IF prob<6
3420 theta=5*alphao/10:GO TO 3480
3430 END IF
3440 IF prob<10
3450 theta=7*alphao/10:GO TO 3480
```

Program 'Monty' (cont.)

```

3460 END IF
3470 theta=9*alphao/10
3480 END DEFine
3490 REMark *****
3500 DEFine PROCedure first_path
3510 len1=-lam*LN(re):REMark initial pathlength into specimen
3520 z=len1*COS(theta):REMark initial z coordinate
3530 IF z>TH
3540 len1=TH/COS(theta)
3550 xn=x+len1*SIN(theta)*COS(phi)
3560 yn=y+len1*SIN(theta)*SIN(phi)
3570 GO TO 3620
3580 END IF
3590 xn=x+len1*SIN(theta)*COS(phi)
3600 yn=y+len1*SIN(theta)*SIN(phi)
3610 cx=(xn-x)/len1:cy=(yn-y)/len1:cz=z/len1
3620 END DEFine
3630 REMark *****
3640 DEFine PROCedure choose_radius
3650 REMark chose initial radial distance from probe centre at which the
3660 REMark incident electron enters (based on probe data)
3670 ff=0
3680 FOR ee=1 TO 40
3690 ii=distbn(ee)*counts/100:roundnumber ii
3700 ff=ii+ff
3710 IF ne<=ff THEN gg=.5*(ee-1):GO TO 3740
3720 END FOR ee
3730 IF ne>ff THEN r1=SQRT(-7.28*LN(RND)):GO TO 3750
3740 hh=RND/2:r1=gg+hh
3750 END DEFine
3760 REMark *****
3770 REMark data required for the running of each simulation
3780 DATA 5
3790 DATA "ge",100,10,18000,2000,.2,"mdv2_delta10"
3800 DATA "ge",100,30,18000,2000,.2,"mdv2_delta30"
3810 DATA "ge",100,50,18000,2000,.2,"mdv2_delta50"
3820 DATA "ge",100,70,18000,2000,.2,"mdv2_delta70"
3830 DATA "ge",100,90,18000,2000,.2,"mdv2_delta90"
3840 REMark *****
3850 REMark Probe data
3860 DATA "Incoherent probe, 500m VOA, C1 only"
3870 DATA 3.256,9.067,13.093,14.863,14.341,12.073,9.144,6.332
3880 DATA 4.135,2.712,1.871,1.44,1.208,1.032,.861,.709,.6,.536
3890 DATA .492,.446,.394,.35,.329,.338,.33,.3
3900 DATA "Gaussian probe, 4.5 Angstrom FWHM."
3910 DATA 3.6,9.4,13.7,15.7,15.3,13.3,10.5,7.5,4.9,3,1.7,.9
3920 DATA .4,.2,.1,5E-2,5E-2,2E-2,2E-2,1E-2,1E-2
3930 DATA "Incoherent probe, 1000m VOA, C1 only"
3940 DATA 2.699,10.05,10.659,9.546,7.551,5.774,4.694,3.997
3950 DATA 3.507,3.119,2.734,2.357,2.11,2.052,2.088,2.119,2.148
3960 DATA 2.168,2.188,2.217,2.246,2.278,2.27,2.5,2.2,2
3970 DATA "Delta function probe"
3980 DATA 100,0,0,0,0,0,0,0,0,0,0,0,0,0,0,0
3990 DATA 0,0,0,0,0,0,0,0,0,0,0,0,0,0,0,0
4000 REMark *****
4010 REMark elemental species database.
4020 DATA "be",4,9.01,1.848,"b",5,10.81,2.5,"c",6,12.01,2.34,"na",11,22.99,.97,"
mg",12,24.31,1.74
4030 DATA "al",13,26.98,2.7,"si",14,28.09,2.34,"p",15,30.97,2.2,"ca",20,40,1.54,
"ti",22,47.9,4.5,"v",23,50.94,6.1,"cr",24,52,7.1
4040 DATA "mn",25,54.94,7.4,"fe",26,55.85,7.87,"co",27,58.93,8.9,"ni",28,58.71,8
.9,"cu",29,63.55,8.96,"zn",30,65.37,7.14
4050 DATA "ga",31,69.72,5.91,"ge",32,72.59,5.32,"nb",41,92.91,8.6,"mo",42,95.94,
10.2,"pd",46,106.4,12,"ag",47,107.9,10.5
4060 DATA "cd",48,112.4,8.64,"sn",50,118.7,7.3,"w",74,183.9,19.3,"pt",78,195.1,2
1.45,"au",79,197,19.3,"pb",82,207.2,11.34

```

A4. Analysis programs for series of x-ray spectra.

The programs listed in this section were used to calculate the relative concentrations of elemental species from x-ray spectra. For analyses of the AlGaAs/GaAs system, program 'AlGaAs_Analyse' was employed, whereas 'InGaAs_Analyse' was used to process spectra acquired from InGaAs/InP multilayers. Each program was written in suberbasic for use on a Sinclair QL minicomputer. Detailed descriptions of the methods followed by 'AlGaAs_Analyse' and 'InGaAs_Analyse' are given in chapters 6 and 7 respectively. Both programs are designed to calculate and store the number of characteristic counts in each x-ray peak of interest. This includes, for example, corrections that take into consideration the overlap of the Ga K_{β} peak with the As K_{α} peak. From the characteristic signal information, the corresponding atomic fractions (or partial atomic fractions in the case of the AlGaAs/GaAs system) and their associated errors are calculated. After all calculations have been performed, all relevant data can be stored on microdrive.

Program 'AlGaAs_Analyse'

```
10 REMark AlGaAs_analyse
20 REMark input_title at 220
30 REMark define_variables at 310
40 REMark input_data at 410
50 REMark write_data at 720
60 REMark read_data at 950
70 REMark print_counts at 1270
80 REMark calculate_concs at 1410
90 REMark print_concs at 1600
100 REMark print_errors at 6500
110 REMark *****
120 REMark *****
130 REMark main program
140 MODE 4:CLS
150 read_data
160 calculate_concs
170 print_concs
180 print_errors
190 REMark *****
200 REMark *****
210 DEFINE PROCEDURE input_title
220 REMark specify filenames
230 CLS
240 AT 5,5:PRINT "Give title of data run - "
250 AT 7,5:INPUT title$
260 AT 10,5:PRINT "File to be save as - "
270 AT 12,5:INPUT file$
280 AT 14,5:INPUT "No. of spectra in data run = ";q
290 END DEFINE
300 REMark *****
310 DEFINE PROCEDURE define_variables
320 REMark set up arrays
330 CLS
340 RESTORE 1860
350 READ ALB1W,GALW,ASLW,ALKW,SIKW,ALB2W,GABW,GAKW,GASBW,ASKW,ASBW
360 DIM LGa(q):DIM LAs(q):DIM Al(q):DIM Ga(q):DIM As(q):DIM Si(q)
370 DIM LGa2(q):DIM LAs2(q):DIM Al2(q):DIM Ga2(q):DIM As2(q):DIM Si2(q):DIM Alb(
q)
380 DIM spec$(q,10)
390 END DEFINE
400 REMark *****
410 DEFINE PROCEDURE input_data
420 REMark calculate no. of counts in characteristic peaks
430 FOR a=1 TO q
440 CLS
450 AT 2,5:INPUT "Spectrum No. : ";spec$(a)
460 AT 4,5:INPUT "ALB1 = ";ALB1: REMark Al lower energy background
470 AT 5,5:INPUT "GAL = ";GAL: REMark Ga L peak
480 AT 6,5:INPUT "ASL = ";ASL: REMark As L peak
490 AT 7,5:INPUT "ALK = ";ALK: REMark Al K peak
500 AT 8,5:INPUT "SIK = ";SIK: REMark Si K peak
510 AT 9,5:INPUT "ALB2 = ";ALB2: REMark Al higher energy background
520 AT 10,5:INPUT "GAB = ";GAB: REMark Ga lower energy background
530 AT 11,5:INPUT "GAK = ";GAK: REMark Ga K peak
540 AT 12,5:INPUT "GASB = ";GASB: REMark background for Ga and As
550 AT 13,5:INPUT "ASK = ";ASK: REMark As K peak
560 AT 14,5:INPUT "ASB = ";ASB: REMark As higher energy background
570 bigbac=INT((ALB1+ALB2)/(ALB1W+ALB2W))
580 f=ALKW/(ALB1W+ALB2W): Alb(a)=ALB1+ALB2
590 LGa(a)=GAL-GALW*bigbac
600 LAs(a)=ASL-ASLW*bigbac
610 Al(a)=ALK-ALKW*bigbac: Si(a)=SIK-SIKW*bigbac
620 LGa2(a)=GAL:LAs2(a)=ASL:Al2(a)=ALK:Si2(a)=SIK
630 Ga(a)=GAK-INT(GAKW*((GAB+GASB)/(GABW+GASBW)))
640 Kbeta=INT((Ga(a)/.873))-Ga(a)
650 As(a)=ASK-INT(ASKW*((GASB+ASB)/(GASBW+ASBW)))
660 As(a)=As(a)-Kbeta
670 Ga2(a)=GAK:As2(a)=ASK-Kbeta
680 print_counts
690 END FOR a
700 END DEFINE
```

Program to analyse series of
spectra acquired from AlGaAs
/GaAs multilayers using the
windowless EDX detector.

Program 'AlGaAs_Analyse' (cont.)

```

710 REMark *****
720 DEFine PROCedure write_data
730 REMark store all relevant data on microdrive
740 OPEN_NEW #7,file$
750 PRINT #7,title$
760 PRINT #7,f
770 PRINT #7,q
780 FOR a=1 TO q:PRINT #7,spec$(a):END FOR a
790 FOR a=1 TO q:PRINT #7,LGa(a):END FOR a
800 FOR a=1 TO q:PRINT #7,LGa2(a):END FOR a
810 FOR a=1 TO q:PRINT #7,LAs(a):END FOR a
820 FOR a=1 TO q:PRINT #7,LAs2(a):END FOR a
830 FOR a=1 TO q:PRINT #7,Al(a):END FOR a
840 FOR a=1 TO q:PRINT #7,Al2(a):END FOR a
850 FOR a=1 TO q:PRINT #7,Si(a):END FOR a
860 FOR a=1 TO q:PRINT #7,Si2(a):END FOR a
870 FOR a=1 TO q:PRINT #7,Ga(a):END FOR a
880 FOR a=1 TO q:PRINT #7,Ga2(a):END FOR a
890 FOR a=1 TO q:PRINT #7,As(a):END FOR a
900 FOR a=1 TO q:PRINT #7,As2(a):END FOR a
910 FOR a=1 TO q:PRINT AlB(q):END FOR a
920 CLOSE #7
930 END DEFine
940 REMark *****
950 DEFine PROCedure read_data
960 REMark retrieve all relevant data from microdrive
970 CLS
980 AT 9,5:PRINT "Give source and title of file to be examined."
990 AT 11,5:INPUT file$
1000 OPEN #7,file$
1010 INPUT #7,title$
1020 INPUT #7,q
1030 INPUT #7,f
1040 DIM LGa(q):DIM LAs(q):DIM Al(q):DIM Ga(q):DIM As(q):DIM Si(q):DIM AlB(q)
1050 DIM LGa2(q):DIM LAs2(q):DIM Al2(q):DIM Ga2(q):DIM As2(q):DIM Si2(q)
1060 DIM spec$(q,10)
1070 FOR a=1 TO q:INPUT #7,spec$(a):END FOR a
1080 FOR a=1 TO q:INPUT #7,LGa(a):END FOR a
1090 FOR a=1 TO q:INPUT #7,LGa2(a):END FOR a
1100 FOR a=1 TO q:INPUT #7,LAs(a):END FOR a
1110 FOR a=1 TO q:INPUT #7,LAs2(a):END FOR a
1120 FOR a=1 TO q:INPUT #7,Al(a):END FOR a
1130 FOR a=1 TO q:INPUT #7,Al2(a):END FOR a
1140 FOR a=1 TO q:INPUT #7,Si(a):END FOR a
1150 FOR a=1 TO q:INPUT #7,Si2(a):END FOR a
1160 FOR a=1 TO q:INPUT #7,Ga(a):END FOR a
1170 FOR a=1 TO q:INPUT #7,Ga2(a):END FOR a
1180 FOR a=1 TO q:INPUT #7,As(a):END FOR a
1190 FOR a=1 TO q:INPUT #7,As2(a):END FOR a
1200 FOR a=1 TO q:INPUT #7, AlB(q):END FOR a
1210 CLOSE #7
1220 FOR a=1 TO q
1230 Al(a)=2*Al(a):Al2(a)=2*Al2(a)
1240 END FOR a
1250 END DEFine
1260 REMark *****
1270 DEFine PROCedure print_counts
1280 REMark output characteristic peak data to printer
1290 OPEN #5,ser1
1300 PRINT #5,\\,,"Spectrum No.    "!,spec$(a)\\
1310 PRINT #5,TO 5;"Peak";TO 23;"gross counts";TO 43;"net counts"\\
1320 PRINT #5,TO 3;"Gallium L";TO 28;LGa2(a);TO 48;LGa(a)
1330 PRINT #5,TO 3;"Arsenic L";TO 28;LAs2(a);TO 48;LAs(a)
1340 PRINT #5,TO 3;"Aluminium K";TO 28;Al2(a);TO 48;Al(a)
1350 PRINT #5,TO 3;"Silicon K";TO 28;Si2(a);TO 48;Si(a)
1360 PRINT #5,TO 3;"Gallium K";TO 28;Ga2(a);TO 48;Ga(a)
1370 PRINT #5,TO 3;"Arsenic K";TO 28;As2(a);TO 48;As(a)
1380 CLOSE #5
1390 END DEFine
1400 REMark *****
1410 DEFine PROCedure calculate_concs

```

Program 'AlGaAs_Analyse' (cont.)

```
1420 REMark calculate partial atomic fractions and associated errors
1430 DIM fGa(q):DIM fGaerr(q):DIM fAl(q):DIM fAlerr(q):DIM fT(q):DIM fTerr(q)
1440 KGaAs=.901:KAsGa=1/KGaAs
1450 KAlAs=1.14:KAlAs=1/KAlAs
1460 FOR a=1 TO q
1470 fGa(a)=(Ga(a)/As(a))*KGaAs
1480 fAl(a)=(Al(a)/As(a))*KAlAs
1490 fT(a)=fGa(a)+fAl(a)
1500 END FOR a
1510 FOR a=1 TO q
1520 dum=Ga2(a)/(Ga(a)*Ga(a))+As2(a)/(As(a)*As(a))
1530 fGaerr(a)=SQRT(fGa(a)*fGa(a)*ABS(dum))
1540 dum=(Al2(a)+f*f*AlB(a))/(Al(a)*Al(a))+(KAlAs*KAlAs*As2(a))/(As2(a)*As2(a))
1550 fAlerr(a)=SQRT(fAl(a)*fAl(a)*ABS(dum))
1560 fTerr(a)=SQRT(fGaerr(a)*fGaerr(a)+fAlerr(a)*fAlerr(a))
1570 END FOR a
1580 END DEFine
1590 REMark *****
1600 DEFine PROCedure print_concs
1610 REMark output concentration data to printer
1620 OPEN #5,ser1
1630 PRINT #5,\\,title$
1640 PRINT #5,\\,"Relative concentrations calculated from spectra."
1650 PRINT #5,\\,"KGaAs = ";KGaAs,"KAlAs = ";KAlAs
1660 PRINT #5,TO 3;\\ "Spectrum No.";TO 23;"Al/As";TO 37;"Ga/As";TO 51;"(Ga/Al)+(G
a/As)"\\
1670 FOR a=1 TO q
1680 PRINT #5,TO 3;spec$(a);TO 21;fAl(a);TO 35;fGa(a);TO 49;fT(a)
1690 END FOR a
1700 CLOSE #5
1710 END DEFine
1720 DEFine PROCedure print_errors
1730 REMark output error data to printer
1740 OPEN #5,ser1
1750 PRINT #5,\\,title$
1760 PRINT #5,\\,"Relative concentration errors calculated from spectra."
1770 PRINT #5,\\,"KGaAs = ";KGaAs,"KAlAs = ";KAlAs
1780 PRINT #5,TO 3;\\ "Spectrum No.";TO 23;"Al/As";TO 37;"Ga/As";TO 51;"(Ga/Al)+(G
a/As)"\\
1790 FOR a=1 TO q
1800 PRINT #5,TO 3;spec$(a);TO 21;fAlerr(a);TO 35;fGaerr(a);TO 49;fTerr(a)
1810 END FOR a
1820 CLOSE #5
1830 END DEFine
1840 REMark *****
1850 REMark no. of channels in each window
1860 DATA 11,14,13,7,11,15,16,25,16,37,12
```

Program 'InGaAs_Analyse'

```

10 REMark InGaAs_analyse          Program to analyse series of spectra
20 REMark initial_parameters at 210 acquired from InGaAs/InP multilayers
30 REMark window_counts at 390
40 REMark calculate_concs at 790
50 REMark read_data at 1320
60 REMark file_data at 1420
70 REMark retrieve_data at 1690
80 REMark *****
90 REMark *****
100 REMark main program
110 MODE 4:CLS
120 initial_parameters
130 FOR a=1 TO q
140 window_counts
150 END FOR a
160 read_data
170 calculate_concs
180 file_data
190 REMark *****
200 REMark *****
210 DEFINE PROCEDURE initial_parameters
220 REMark set up data arrays
230 RESTORE 2070
240 REMark read in channel widths of windows
250 READ PB1W,SIKW,PKW,PB2W,INLW,INBW,GAB1W,GAKW,GAB2W,ASKW,ASBW
260 AT 4,5:PRINT "Give title of experimental run to be analysed."
270 AT 6,5:INPUT title$
280 AT 9,5:PRINT "Give title of file to store data in cartridge."
290 AT 11,5:INPUT file$
300 REMark calculate atomic fractions
310 AT 15,5:INPUT "No. of spectra in run = ";q
320 AT 17,5 :INPUT "Percentage transmitted of P signal = ";Pabs
330 Pabs=Pabs/100
340 DIM Fp(q):DIM In(q):DIM Ga(q):DIM As(q):DIM Si(q)
350 DIM grosPp(q):DIM grosIn(q):DIM grosGa(q):DIM grosAs(q):DIM grosSi(q)
360 DIM spectra$(q,10)
370 END DEFINE
380 REMark *****
390 DEFINE PROCEDURE window_counts
400 REMark calculate no. of characteristic counts in each peak
410 CLS
420 AT 1,10:INPUT "Spectrum no. = ";spectra$(a)
430 REMark and output data to printer.
440 AT 3,10:PRINT "Give gross counts in each window"
450 AT 5,10:INPUT "PB1 = ";pb1:REMARK P lower energy background
460 AT 6,10:INPUT "SIK = ";sik:REMARK Si K peak
470 AT 7,10:INPUT "PK = ";PK:REMARK P K peak
480 AT 8,10:INPUT "PB2 = ";PB2:REMARK P higher energy background
490 AT 9,10:INPUT "INL = ";INL:REMARK In L peak
500 AT 10,10:INPUT "INB = ";INB:REMARK In higher energy background
510 AT 11,10:INPUT "GAB1 = ";GAB1:REMARK Ga low energy background
520 AT 12,10:INPUT "GAK = ";GAK:REMARK Ga K peak
530 AT 13,10:INPUT "GAB2 = ";GAB2:REMARK background for Ga and As
540 AT 14,10:INPUT "ASK = ";ASK:REMARK As K peak
550 AT 15,10:INPUT "ASB = ";ASB:REMARK As high energy background
560 sik2=sik-INT(SIKW*((pb1+PB2)/(PB1W+PB2W)))
570 PK2= PK-INT(PKW*((pb1+PB2)/(PB1W+PB2W)))
580 Pdiff=INT((PK2/Pabs)-PK2):PK2=PK2+Pdiff:PK=PK+Pdiff
590 INL2=INL-INT(INLW*((PB2+INB)/(PB2W+INBW)))
600 GAK2=GAK-INT(GAKW*((GAB1+GAB2)/(GAB1W+GAB2W)))
610 ASK2=ASK-INT(ASKW*((GAB2+ASB)/(GAB2W+ASBW)))
620 DIFF=INT(((GAK2/.873)-GAK2)):ASK2=ASK2-DIFF
630 ASK=ASK-DIFF
640 IF GAK2=0 THEN GAK2=1:IF ASK2=0 THEN ASK2=1
650 OPEN #5,ser1
660 PRINT #5,\\,"Spectrum No. ";spectra$(a)
670 PRINT #5,,"Window",,"Gross counts",,"Net counts"
680 PRINT #5,,"Si K",,sik,,,sik2
690 PRINT #5,,"P K",,PK,,,PK2
700 PRINT #5,,"In L",,INL,,,INL2
710 PRINT #5,,"Ga K",,GAK,,,GAK2

```

Program 'InGaAs_Analyse' (cont.)

```

720 PRINT #5,,"As K",,ASK,,ASK2
730 CLOSE #5
740 REMark fill up arrays for concentration calculations
750 Pp(a)=PK2:In(a)=INL2:Ga(a)=GAK2:As(a)=ASK2:Si(a)=sik2
760 grosPp(a)=PK:grosIn(a)=INL:grosGa(a)=GAK:grosAs(a)=ASK:grosSi(a)=sik
770 END DEFINE
780 REMark *****
790 DEFINE PROCEDURE calculate_concs
800 REMark calculate concentration distributions and associated errors
810 OPEN #5,ser1
820 REMark calculate all K-factors
830 kCB=1/kBC:kAC=1/kCA:kBD=1/kDB
840 kBA=kBC*kCA:kDC=kDB*kBC:kDA=kDC*kCA
850 kAB=1/kBA:kCD=1/kDC:kAD=1/kDA
860 FOR a=1 TO q
870 ratIn(a)=In(a)/(In(a)+(kBA*Ga(a))+(kCA*Pp(a))+(kDA*As(a)))
880 ratGa(a)=Ga(a)/(Ga(a)+(kAB*In(a))+(kCB*Pp(a))+(kDB*As(a)))
890 ratPp(a)=Pp(a)/(Pp(a)+(kAC*In(a))+(kBC*Ga(a))+(kDC*As(a)))
900 ratAs(a)=As(a)/(As(a)+(kAD*In(a))+(kBD*Ga(a))+(kCD*Pp(a)))
910 IF ratGa(a)<0 THEN ratGa(a)=0
920 IF ratAs(a)<0 THEN ratAs(a)=0
930 END FOR a
940 REMark calculate errors
950 FOR a=1 TO q
960 derrIn(a)=In(a)+(kBA*kBA*Ga(a))+(kCA*kCA*Pp(a))+(kDA*kDA*As(a))
970 derrGa(a)=Ga(a)+(kAB*kAB*In(a))+(kCB*kCB*Pp(a))+(kDB*kDB*As(a))
980 derrPp(a)=Pp(a)+(kAC*kAC*In(a))+(kBC*kBC*Ga(a))+(kDC*kDC*As(a))
990 derrAs(a)=As(a)+(kAD*kAD*In(a))+(kBD*kBD*Ga(a))+(kCD*kCD*Pp(a))
1000 END FOR a
1010 FOR a=1 TO q
1020 dIn(a)=(In(a)+(kBA*Ga(a))+(kCA*Pp(a))+(kDA*As(a)))^2
1030 dGa(a)=(Ga(a)+(kAB*In(a))+(kCB*Pp(a))+(kDB*As(a)))^2
1040 dPp(a)=(Pp(a)+(kAC*In(a))+(kBC*Ga(a))+(kDC*As(a)))^2
1050 dAs(a)=(As(a)+(kAD*In(a))+(kBD*Ga(a))+(kCD*Pp(a)))^2
1060 END FOR a
1070 FOR a=1 TO q
1080 errIn(a)=SQRT((grosIn(a)/(In(a)^2))+(derrIn(a)/dIn(a))*ratIn(a))
1090 errGa(a)=SQRT((grosGa(a)/(Ga(a)^2))+(derrGa(a)/dGa(a))*ratGa(a))
1100 errPp(a)=SQRT((grosPp(a)/(Pp(a)^2))+(derrPp(a)/dPp(a))*ratPp(a))
1110 errAs(a)=SQRT((grosAs(a)/(As(a)^2))+(derrAs(a)/dAs(a))*ratAs(a))
1120 END FOR a
1130 REMark output values yo printer
1140 PRINT #5,\\title$
1150 PRINT #5,"KEY : A = Indium B = Gallium C = Phosphorus D = Arsenic"\\
1160 PRINT #5,"kAB="!kAB!"kBA="!kBA!"kAC="!kAC!"kCA="!kCA
1170 PRINT #5,"kAD="!kAD!"kDA="!kDA!"kBD="!kBD!"kDB="!kDB
1180 PRINT #5,"kBC="!kBC!"kCB="!kCB!"kCD="!kCD!"kDC="!kDC
1190 PRINT #5,\\,,"Concentration ratios"
1200 PRINT #5,\\Indium",,\\!Gallium",,\\!Phosphorus",,\\!Arsenic"\\
1210 FOR x=1 TO q
1220 PRINT #5,ratIn(x),\\!ratGa(x),\\!ratPp(x),\\!ratAs(x),\\!spectra$(x)
1230 END FOR x
1240 PRINT #5,\\,,"Concentration ratio errors"
1250 PRINT #5,\\Indium",,\\!Gallium",,\\!Phosphorus",,\\!Arsenic"\\
1260 FOR x=1 TO q
1270 PRINT #5,errIn(x),\\!errGa(x),\\!errPp(x),\\!errAs(x),\\!spectra$(x)
1280 END FOR x
1290 CLOSE #5
1300 END DEFINE
1310 REMark *****
1320 DEFINE PROCEDURE read_data
1330 REMark read in data that has been previously stored
1340 DIM ratPp(q):DIM ratIn(q):DIM ratGa(q):DIM ratAs(q)
1350 DIM derrPp(q):DIM derrAs(q):DIM derrIn(q):DIM derrGa(q)
1360 DIM dPp(q):DIM dAs(q):DIM dIn(q):DIM dGa(q)
1370 DIM errPp(q):DIM errAs(q):DIM errIn(q):DIM errGa(q)
1380 RESTORE 2090
1390 READ kBC,kCA,kDB
1400 END DEFINE
1410 REMark *****
1420 DEFINE PROCEDURE file_data

```

Program 'InGaAs_Analyse' (cont.)

```
1430 REMark store all relevant data on microdrive
1440 OPEN_NEW #7,file$
1450 PRINT #7,title$
1460 PRINT #7,q
1470 FOR a=1 TO q:PRINT #7,spectra$(a):END FOR a
1480 FOR a=1 TO q:PRINT #7,Si(a):END FOR a
1490 FOR a=1 TO q:PRINT #7,Pp(a):END FOR a
1500 FOR a=1 TO q:PRINT #7,In(a):END FOR a
1510 FOR a=1 TO q:PRINT #7,Ga(a):END FOR a
1520 FOR a=1 TO q:PRINT #7,As(a):END FOR a
1530 FOR a=1 TO q:PRINT #7,grosSi(a):END FOR a
1540 FOR a=1 TO q:PRINT #7,grosPp(a):END FOR a
1550 FOR a=1 TO q:PRINT #7,grosIn(a):END FOR a
1560 FOR a=1 TO q:PRINT #7,grosGa(a):END FOR a
1570 FOR a=1 TO q:PRINT #7,grosAs(a):END FOR a
1580 FOR a=1 TO q:PRINT #7,ratPp(a):END FOR a
1590 FOR a=1 TO q:PRINT #7,ratIn(a):END FOR a
1600 FOR a=1 TO q:PRINT #7,ratGa(a):END FOR a
1610 FOR a=1 TO q:PRINT #7,ratAs(a):END FOR a
1620 FOR a=1 TO q:PRINT #7,errPp(a):END FOR a
1630 FOR a=1 TO q:PRINT #7,errIn(a):END FOR a
1640 FOR a=1 TO q:PRINT #7,errGa(a):END FOR a
1650 FOR a=1 TO q:PRINT #7,errAs(a):END FOR a
1660 CLOSE #7
1670 END Define
1680 REMark *****
1690 Define PROCEDURE retrieve_data
1700 CLS
1710 AT 9,5:PRINT "Give title of file to be examined from cartridge."
1720 AT 11,5:INPUT file$
1730 OPEN #7,file$
1740 INPUT #7,title$
1750 INPUT #7,q
1760 DIM Pp(q):DIM In(q):DIM Ga(q):DIM As(q):DIM Si(q)
1770 DIM grosPp(q):DIM grosIn(q):DIM grosGa(q):DIM grosAs(q):DIM grosSi(q)
1780 DIM spectra$(q,10)
1790 DIM ratPp(q):DIM ratIn(q):DIM ratGa(q):DIM ratAs(q)
1800 DIM derrPp(q):DIM derrAs(q):DIM derrIn(q):DIM derrGa(q)
1810 DIM dPp(q):DIM dAs(q):DIM dIn(q):DIM dGa(q)
1820 DIM errPp(q):DIM errAs(q):DIM errIn(q):DIM errGa(q)
1830 FOR a=1 TO q:INPUT #7,spectra$(a):END FOR a
1840 FOR a=1 TO q:INPUT #7,Si(a):END FOR a
1850 FOR a=1 TO q:INPUT #7,Pp(a):END FOR a
1860 FOR a=1 TO q:INPUT #7,In(a):END FOR a
1870 FOR a=1 TO q:INPUT #7,Ga(a):END FOR a
1880 FOR a=1 TO q:INPUT #7,As(a):END FOR a
1890 FOR a=1 TO q:INPUT #7,grosSi(a):END FOR a
1900 FOR a=1 TO q:INPUT #7,grosPp(a):END FOR a
1910 FOR a=1 TO q:INPUT #7,grosIn(a):END FOR a
1920 FOR a=1 TO q:INPUT #7,grosGa(a):END FOR a
1930 FOR a=1 TO q:INPUT #7,grosAs(a):END FOR a
1940 FOR a=1 TO q:INPUT #7,ratPp(a):END FOR a
1950 FOR a=1 TO q:INPUT #7,ratIn(a):END FOR a
1960 FOR a=1 TO q:INPUT #7,ratGa(a):END FOR a
1970 FOR a=1 TO q:INPUT #7,ratAs(a):END FOR a
1980 FOR a=1 TO q:INPUT #7,errPp(a):END FOR a
1990 FOR a=1 TO q:INPUT #7,errIn(a):END FOR a
2000 FOR a=1 TO q:INPUT #7,errGa(a):END FOR a
2010 FOR a=1 TO q:INPUT #7,errAs(a):END FOR a
2020 CLOSE #7
2030 RESTORE 2090:READ kBC,kCA,kDB
2040 END Define
2050 REMark *****
2060 REMark no. of channels in each window
2070 DATA 4,11,16,17,34,31,16,25,16,37,32,12
2080 REMark K-factors for windowless detector
2090 DATA 1.2,0.4,1.11
```

References

K Alavi, P M Petroff, W R Wagner and A Y Cho, J. Vac. Sci. Technol. B 1 146 (1983)

U Bangert and P Charsley, Phil. Mag. A 59 629 (1989)

N C Barford, Experimental Measurements: Precision, Error and Truth (Addison Wesley, London) (1967)

S J Barnett, G T Brown, S J Courtney, S J Bass and L L Taylor, J. Appl. Phys. 64 1185 (1988)

S J Bass, S J Barnett, G T Brown, N G Chew, A G Cullis, A D Pitt and M S Skolnick, J. Cryst. Growth 79 378 (1986)

S J Bass, S J Barnett, G T Brown, N G Chew, A G Cullis, M S Skolnick and L L Taylor, Thin Film Growth Techniques for Low-Dimensional Structures, eds. R F C Farrow, S S P Parkin, P J Dobson, J H Neave and A S Arnott (Plenum, New York) 137 (1987)

J C Bean, L C Feldman, A T Fiory, S Nakahara and I K Robinson, J. Vac. Sci. Technol. A 2 436 (1984)

M J Berger and S M Selzer, Nat. Acad. Sci. Natl. Res. Council Publ. 1133 205 (1964)

S D Berger and S J Pennycook, AEM proceedings, Manchester, 1987, (Inst. of Metals, ed. G W Lorimer) 219 (1987)

H A Bethe Annalen de. Phys. 5 325 (1930)

H E Bishop in use of Monte Carlo Calculations in Electron Probe Microanalysis and Scanning Electron Microscopy, eds. K F J Heinrich et. al. (NBS special publication 460) 5 (1976)

D Berenyi and G Hock, Jap. J. Appl. Phys. 12 (2) 78 (1978)

C B Boothroyd and W M Stobbs, Ultramicrosc. 26 361 (1988)

M Born and E Wolf, "Principles of Optics", Pergamon Press, Oxford (1959)

L M Brown, J M Rodenburg and W T Pike, EUREM 88 Proceedings (Inst. Phys. Conf. Ser. No. 93, Adam Hilger Ltd., Bristol) 2 3 (1988)

T P Buggy, Ph.D. Thesis, University of Glasgow (1985)

J F Bullock, J M Titchmarsh and C J Humphreys, Semicond. Sci. Technol. 1 343 (1986)

J F Bullock, C J Humphreys, A G Norman and J M Titchmarsh, Microscopy of Semiconducting materials 1987 (Inst. Phys. Conf. Ser. No. 87, Adam Hilger Ltd., Bristol) 643 (1987)

J Burgeat, M Quillec, J Primot, G Le Roux and H Launois, Appl. Phys. Lett. 38 542 (1981)

J Cazaux, P Etienne and M Razeghi, J. Appl. Phys. 59 3598 (1986)

J N Chapman, C C Gray, B W Robertson and W A P Nicholson, X-ray Spectrom. 12 (4) 153 (1983)

J N Chapman and G R Morrison, J. Magn. Magn. Mat. 35 254 (1983)

J N Chapman, W A P Nicholson and P A Crozier, J Microsc. 136 (2) 179 (1984)

N G Chew and A G Cullis, Appl. Phys. Lett. 44(1) (1984)

N G Chew, A G Cullis and G M Williams, Appl. Phys. Lett. 45 1090 (1984)

N G Chew and A G Cullis, Ultramicrosc. 23 175 (1987)

N G Chew, A G Cullis, S J Bass, L L Taylor, M S Skolnick and A D Pitt, Microscopy of Semiconducting materials 1987 (Inst. Phys. Conf. Ser. No. 87, Adam Hilger Ltd., Bristol) 231 (1987)

P A Claxton, J S Roberts, J P R David, C M Sotomayor-Torres, M S Skolnick, P R Tapster and K J Nash, J. Cryst. Growth 81 288 (1987)

J M Cole, L G Earwaker, A G Cullis, N G Chew and S J Bass, J. Appl. Phys. 64 1185 (1988)

C Colliex and C Mory in Quantitative Electron Microscopy, eds. J N Chapman and A J Craven (SUSSP No. 25) ch4 (1983)

J M Cowley, Ultramicrosc. 2 3 (1976)

A J Craven and P Buggy, J. Microsc. 136 (2) 227 (1984)

A V Crewe in Electron Microscopy and Material Science, ed. U Valdre 162 (1971)

A V Crewe, J P Langmore and M S Isaacson in Physical aspects of electron microscopy and microbeam analysis, eds. B M Siegel and D R Beam (Wiley, New York) 47 (1975)

P A Crozier, Ph.D. Thesis (1985)

A G Cullis, Private communication (1988)

A G Cullis and N G Chew, Proc. Electron Microscopy and Analysis 1985 (Inst. Phys. Conf. Ser. No. 78, ed. G J Tatlock. Adam Hilger Ltd., Bristol) 143 (1985)

A G Cullis, N G Chew and J L Hutchison, Ultramicrosc. 17 203 (1985)

A G Cullis, N G Chew, S J C Irvine and J Geiss, Microscopy of Semiconducting materials 1987 (Inst. Phys. Conf. Ser. No. 87, Adam Hilger Ltd., Bristol) 141 (1987)

G J Davies and D A Andrews, Br. Telecom. Technol. J. 3 59 (1985)

N H Dekkers and H de Lang, Philips. Tech, Rev. 37 1 (1977)

M A DiGiuseppe, H Temkin, L Peticolas and W A Bonner, Appl. Phys. Lett. 43 906 (1983)

M A DiGiuseppe, H Temkin and W A Bonner, J. Cryst. Growth 58 279 (1982)

A Donald and A J Craven, Phil. Mag. A 39 1 (1979)

P A Doyle and P S Turner, Acta Cryst. A 24 390 (1967)

L Esaki and R Tsu, IBM J. Res. Dev. 14 61 (1970)

H Fleischmann, Z. Naturforsch. 15a 1090 (1960)

J K Furdyna and J Kossut, Superlattices and Microstructures 2 89 (1986)

F Glas, Ph.D. Thesis, Universite de Paris-Sud (1986)

F Glas, M M J Treacy, M Quillec and H Launois, J. de Physique 43 C5-11 (1982)

J I Goldstein, J L Costley, G W Lorimer and S J B Reed, SEM 1977, ed. O Johari (IITRI, Chicago) 315 (1977)

P J Goodhew (a), Proc. Electron Microscopy and Analysis 1985 (Inst. Phys. Conf. Ser. No. 78, ed. G J Tatlock. Adam Hilger Ltd., Bristol) 183 (1985)

P J Goodhew (b) in Thin Foil Preparation for Electron Microscopy (ed. A M Glauert, Elsevier, Oxford) (1985)

C C Gray, Ph.D. Thesis, University of Glasgow (1981)

C C Gray, J N Chapman, W A P Nicholson, B W Robertson and R P Ferrier, X-ray Spectrom. 12 163 (1983)

R J M Griffiths, N G Chew, A G Cullis and G C Joyce, Electr. Lett. 19 988 (1983)

C R M Grovenor, A Cerezo, J A Liddle and G D W Smith, Microscopy of Semiconducting materials 1987 (Inst. Phys. Conf. Ser. No. 87, Adam Hilger Ltd., Bristol) 665 (1987)

C R Hall and P B Hirsch, Proc. Roy. Soc. A 286 158 (1965)

T A Hall and B L Gupta in Introduction to Analytical Electron Microscopy, eds. J J Hren, J C Goldstein and D C Joy (Plenum) (1979)

K F J Heinrich, in EMSA proceedings (1987)

P B Hirsch, A Howie, R B Nicholson, D W Pashley and M J Whelan, Electron Microscopy of Thin Crystals (Krieger, New York) (1977)

A Howie, J. Microsc. 117 11 (1979)

- R Hull, K W Carey, J E Fouquet, G A Reid, S J Rosner, D Bimberg and D Oertel**, Proc. GaAs and related compounds, Las Vegas, Nevada (Inst. Phys. Conf. Ser. No. 83) 209 (1986)
- C J Humphreys**, Proc. ICEM XI (eds. T Imura, S Maruse and T Suzuki, Jap. Soc. of EM, Tokyo) 1 105 (1986)
- C J Humphreys, D J Eaglesham, D M Maher and H L Fraser**, Ultramicrosc. 26 13 (1988)
- C J Humphreys, D M Maher, H L Fraser and D J Eaglesham**, Phil. Mag. A 58 787 (1988)
- J L Hutchison**, Microscopy of Semiconducting materials 1987 (Inst. Phys. Conf. Ser. No. 87, Adam Hilger Ltd., Bristol) 1 (1987)
- M Inokuti**, Rev. Mod. Phys. 43 297 (1971)
- M S Isaacson, J P Langmore, N W Parker, D Kopf and M. Utlaut**, Ultramicrosc. 1 359 (1976)
- A F de Jong and K T F Janssen**, EUREM 88 Proceedings (Inst. Phys. Conf. Ser. No. 93, Adam Hilger Ltd., Bristol) 2 153 (1988)
- D C Joy**, EUREM 88 Proceedings (Inst. Phys. Conf. Ser. No. 93, Adam Hilger Ltd., Bristol) 1 23 (1988)
- B A Joyce**, Rep. Prog. Phys. 48 1637 (1985)
- H Kakibayashi and F Nagata**, Jap. J. Appl. Phys. 24 L905 (1985)
- H Kakibayashi and F Nagata**, Jap. J. Appl. Phys. 25 1644 (1986)
- M J Kane, D A Anderson, L L Taylor and S J Bass**, J. Appl. Phys. 60 (2) 657 (1986)
- P M Kelly, A Jostens, R G Blake and J G Napier**, Phys. Stat. Sol. A 81 771 (1975)
- K Kodama, M Ozeki and J Komeno**, J. Vac. Sci. Technol. B 1 696 (1983)
- D Kyser** in Introduction to Analytical Electron Microscopy, eds. J J Hren, J I

Goldstein and D C Joy (Plenum) ch 6 (1979)

F Lenz, Z. Naturforsch 9a 185 (1954)

M H Loretto, Microscopy of Semiconducting materials 1987 (Inst. Phys. Conf. Ser. No. 87, Adam Hilger Ltd., Bristol) 633 (1987)

G W Lorimer in Quantitative Electron Microscopy, eds. J N Chapman and A J Craven (SUSSP No. 25) ch 4 (1983)

R E Mallard, W G Waddington and P C Spurdens, Microscopy of Semiconducting materials 1987 (Inst. Phys. Conf. Ser. No. 87, Adam Hilger Ltd., Bristol) 21 (1987)

J H Marsh, J S Roberts and P A Claxton. Appl. Phys. Lett. 46 1161 (1985)

C H McGillavry, Physica 7 329 (1940)

T Mimura, S Hiyamizu, T Fujii and K Nambu, Jap. J. Appl. Phys. 19 L225 (1980)

G Moliere, Z. Naturforsch. 2a 133 (1947)

G R Morrison, Ph.D. Thesis (1981)

C Mory, M Tence and C Colliex, J. Microsc. Spectrosc. Electron. 10 381 (1985)

S B Newcomb, C S Baxter and E G Bithell, EUREM 88 Proceedings (Inst. Phys. Conf. Ser. No. 93, Adam Hilger Ltd., Bristol) 1 43 (1988)

M Ohtsuki, Ultramicrosc. 5 317 (1980)

G C Osbourne, R M Biefeld and P L Gourley, Appl. Phys. Lett. 41 172 (1982)

G C Osbourne, Phys. Rev. B 27 5126 (1983)

M B Panish, H Temkin, R A Hamm and S N G Chu, Appl. Phys. Lett. 49 164 (1986)

J H Paterson, J N Chapman, W A P Nicholson and J M Titchmarsh, J Microsc. to be published (1989)

S J Pennycook, J. Microsc. 124 15 (1981)

S J Pennycook, S G Berger and R J Culbertson, J. Microsc. 144 229 (1986)

A K Petford-Long and N J Long, AEM proceedings, Manchester, 1987, (Inst. of Metals, ed. G W Lorimer) 201 (1987)

P M Petroff, J. Vac. Sci. Technol. 14 157 (1977)

M Razeghi, J P Hirtz, U D Ziemelis, C Delalande, B Etienne and M Voos, Appl. Phys. Lett. 43 585 (1983)

M Razeghi, J Nagle, P Maurel, F Omnes and J P Pocholle, Appl. Phys. Lett. 49 1110 (1986)

P Rez, X-ray Spectrom. 13 55 (1984)

J P Rosbeck and M E Harper, J. Appl. Phys. 62 1717 (1987)

F M Ross, E G Britton and W M Stobbs, AEM proceedings, Manchester, 1987, (Inst. of Metals, ed. G W Lorimer) 205 (1987)

J H Scofield, Phys. Rev. A 9 1041 (1974)

W T Scott, Rev. Mod. Phys. 35 231 (1963)

M S Skolnick, L L Taylor, S J Bass, A D Pitt, D J Mowbray, A G Cullis and N G Chew, Appl. Phys. Lett. 51 24 (1987)

J D Steele, J N Chapman and P F Adam, Electron Microscopy 1984, eds. A Csanady, P Rohlich and D Szabo (Programme Committee 8th Eur. Cong. on EM) 1 373 (1984)

M M J Treacy, J. Microsc. Spectrosc. Electron. 7 511 (1982)

M M J Treacy and J M Gibson, J. Vac. Sci. Technol. B 4 1458 (1986)

M M J Treacy, J M Gibson and A Howie, Phil. Mag. A 51 389 (1985)

M M J Treacy, J Gibson, K T Short and S B Rice, Ultramicrosc. 26 133 (1988)

W T Tsang, Appl. Phys. Lett. 39 786 (1981)

W T Tsang and E F Schubert, Appl. Phys. Lett. 49 220 (1986)

M E Twigg, S N G Chu, D C Joy, D M Maher, A T Macrander and A K Chin, J. Appl. Phys. 62 3156 (1987)

G Wentzel, Z. Phys. 40 590 (1927)

G M Williams, C R Whitehouse, N G Chew and A G Cullis, J. Vac. Sci. Technol. B 3 704 (1985)

E Zeitler and G R Thomson, Optik 31 258 (1970)